Optimal Design of Miniature Flexural and Soft Robotic Mechanisms

Submitted in partial fulfillment of the requirements for

the degree of

Doctor of Philosophy

in

Department of Mechanical Engineering

Guo Zhan Lum

B.Eng., Mechanical Engineering, Nanyang Technological University
M.S., Mechanical Engineering, Carnegie Mellon University

Carnegie Mellon University
Pittsburgh, PA

December, 2017

Abstract

Compliant mechanisms are flexible structures that utilize elastic deformation to achieve their desired motions. Using this unique mode of actuation, the compliant mechanisms have two distinct advantages over traditional rigid machines: (1) They can create highly repeatable motions that are critical for many high precision applications. (2) Their high degrees-of-freedom motions have the potential to achieve mechanical functionalities that are beyond traditional machines, making them especially appealing for miniature robots that are currently limited to only having simple rigid-body-motions and gripping functionalities. Unfortunately, despite the potential of compliant mechanisms, there are still several key challenges that restrict them from realizing their full potential. To facilitate this discussion, we first divide the compliant mechanisms into two categories: (1) the stiffer flexural mechanisms that are ideal for high precision applications, and (2) the more compliant miniature soft robots that can reshape their geometries to achieve highly complex mechanical functionalities.

The key limitation for existing flexural mechanisms is that their stiffness and dynamic properties cannot be optimized when they have multi-degrees-of-freedom. This limitation has severely crippled the performance of flexural mechanisms because their stiffness and dynamic properties dictate their workspace, transient responses and capabilities to reject disturbances. On the other hand, miniature soft robots that have overall dimensions smaller than 1 cm, are unable to achieve their full potential because existing works do not have a systematic approach to determine the required design and control signals for the robots to generate their desired time-varying shapes.

This thesis addresses these limitations by developing two design methodologies: The first methodology is developed for synthesizing optimal flexural mechanisms, while the second is a universal programming method for designing and controlling miniature soft robots that can generate desired time-varying shapes. The first methodology is implemented by first employing a kinematic approach to select suitable parallel-kinematic configurations for the flexural mechanisms, i.e. determine their required number and type of sub-chains. Subsequently, a structural optimization approach is used to automatically synthesize and optimize the sub-chains' structural topology, shape and size. In order to integrate the kinematic and structural optimization approaches, a new topological optimization algorithm termed the mechanism-based approach has been created. In comparison with existing algorithms, a notable benefit for the mechanism-based approach is that it can eliminate infeasible solutions that have no physical meanings while having a flexible way to change its topology during the optimization process. This algorithm has been shown to be able to develop various devices such as a μ-gripper, a compliant prismatic joint, and a compliant prismatic-revolute joint. A generic semi-analytical dynamic model that can accurately predict the fundamental natural frequency for compliant mechanisms with parallel-kinematic configurations has also been developed for the proposed integrated design methodology.

The effectiveness of the first methodology is demonstrated by synthesizing a planar-motioned X–Y–θ_z flexure-based parallel mechanism (FPM). This FPM has a large workspace of 1.2 mm$\times$ 1.2 mm$\times 6^\circ$, bandwidth of 117 Hz, and translational and rotational stiffness ratios of 130 and 108, respectively. The achieved stiffness and dynamic properties show significant improvement over existing 3-degrees-of-freedom, centimeter-scale compliant mechanisms that can deflect more than 0.5 mm and 0.5°. These compliant mechanisms typically only have stiffness ratios and

bandwidth that are less than 50 and 45 Hz, respectively. The stiffness and dynamic properties of the optimal FPM were validated experimentally and they deviated less than 9% from the simulation results.

Our second design methodology is a universal programming methodology that can magnetically program small-scale materials to generate a series of desirable time-varying shapes. More specifically, this method allows scientists and engineers to automatically generate the required magnetization profile and actuating magnetic fields for the robots. The effectiveness of the second methodology is demonstrated via creating various miniature devices that are difficult to realize with existing technologies, and this includes a spermatozoid-like undulating swimmer and an artificial cilium that could mimic the complex beating patterns of its biological counterparts. In comparison to existing previous works that rely solely on human intuition and can only program these materials for a limited number of applications, our universal methodology has the potential to allow scientists and engineers to fully capitalize shape-programming technologies.

We envision that the first methodology can inspire engineers to develop a variety of high precision machines that have optimal performances while the second methodology has paved the way for novel miniature devices that are critical in robotics, for smart engineering surfaces or materials, and for biomedical devices.

Acknowledgments

I would like to express my sincere gratitude to my thesis committee: Professor Metin Sitti, Professor Yeo Song Huat, Professor Jessica Zhang and Professor Carmel Majidi (Committee Chair) for their time, efforts and advises. In particular, I would like to thank my advisors, Professor Metin Sitti and Professor Yeo Song Huat, for their support, encouragement and advice. They have motivated me to do my best for my graduate study and have also provided me an ideal environment to work in. I would also like to thank Dr. Yang Guilin for his informative comments and advices that had been so instrumental in my research. My gratitude is also extended to Professor Tai Kang for his help in topological optimization, and also to Daniel Teo Tat Joo for his help in flexure mechanisms.

My graduate studies had started in Nanyang Technological University (NTU) and I had received tremendous amount of help from my colleagues in Robotics Research Centre (RRC). I would first like to thank my seniors Lim Wen Bin, Mustafa Shabbir Kurbanhusen and Wong Choon Yue for sharing their Ph.D. experiences with me. They have given me many valuable advices and their encouragements had given me the courage to persevere in my studies. Special thanks also go to Yuan Qilong, Gu Yuan Long, Do Thanh Nho, Li Lei, Ahmad Khairyanto, Chi Wan Chao, Sun Zhenglong, Wang Zenan, Liu Shi Cong, Song Chaoyang, Dong Huixu, Lim Eng Cheng, Agnes Tan Siok Kuan, You Kim San and Pham Minh Tuan for their friendship and constant encouragements. They have always given me a warm welcome whenever I return from overseas.

When I came to CMU for my third and fourth year of studies, I had the privilege to work with many colleagues in the NanoRobotics Lab. Members of the NanoRobotics lab have provided constant encouragement, critique and ideas throughout my PhD study, and I am deeply grateful to them. In particular, I would like to thank my seniors Ye Zhou, Hamid Marvi, Eric Diller, and Sehyuk Yim for sharing their experiences and expertises with me. They have helped me to shape and strengthen my research perspective. Special thanks also go to Lindsey Hines, Dong Xiaoguang, Rika Wright, Steven Rich and Matthew Woodward for their helpful discussions. I would also like to thank my fellow Singaporean friends in CMU: Ang Wei Sin, Goh Chun Fan, Ong Wee Liat, Zhang Juanjuan, Jing Wei and Wu Yingying. They have given me alot of support and encouragements when I was in Pittsburgh. In my final year of studies, I had the privilege to work in Max Planck Institute (MPI) with many other researchers. I would especially like to thank Wenqi Hu for his selfless help. Special thanks also go to Zeinab Hosseini-Doust and Janina Sieber for their help, suggestions and advice. I would also like to thank Wendong Wang for helping me to settle down in Stuttgart.

I would also like to thank NTU, Singapore Economic Development Board (EDB) and MPI for providing me the scholarship to pursue my Ph.D. studies. Finally, I thank all my family and friends for their support. I would especially like to thank my parents, Lum Sang and Peng Hsiu Feng, my god-sister, Katherine Yeo, my brother, Lum Guo Sheng and his family, and my wife, Tan Shi Hua. They provided me a balanced life and constant encouragement through all of my years of education. I cherish their love and support.

Contents

List of Figures

List of Tables

Nomenclature

α Parameter for defining $x_{L,\text{max}}$ for the cubic curve

$\bar{\mathbf{u}}_e$ Translational deformation of any arbitrary point within a finite element

β Parameter for defining $y_{L,\text{max}}$ for the cubic curve

$\boldsymbol{\epsilon}_e$ Strain vector of an arbitrary point

$\dot{\mathbf{r}}_{\text{ee},6\times1}$ The FPM's end-effector twist

$\dot{\mathbf{u}}_{\text{SC},n\times1,j}$ Rate of change of nodal deformation with respect to time for sub-chain j (FEA format)

γ Variable for selecting solid elements

$\hat{\mathbf{p}}_j$ The position vector from the FPM's end-effector to the j^{th} sub-chain (in skew-symmetric matrix format)

$\hat{\mathbf{r}}_j$ Skew-symmetry matrix of the $\mathbf{r}_j$ position vector

λ Wavelength of harmonic curve

μ-gripper Small-scale mobile gripper

ω_n Natural frequencies of the FPM

$\omega_{n,1}$ Fundamental natural frequency of the FPM

ϕ_j The rotational angle between sub-chain j with the global frame

ρ The density of the FPM

τ_m Magnetic torque

$\mathbf{0}_{3\times3}$ 3×3 zero matrix

$\mathbf{Ad}_{\mathbf{T},j}$ Adjoint matrix for sub-chain j

$\mathbf{A}$ Matrix that extracts the necessary information from the global nodal deflections to obtain the 6×6 compliance matrix

$\mathbf{B}(t)$ Magnetic fields

$\mathbf{B}_x$ Magnetic field along the x-axis

$\mathbf{C}_{\text{Int},6\times6}$ The 6×6 compliance matrix of a μ-gripper created via human intuition

$\mathbf{C}_{\text{Opt},6\times6}$ The 6×6 compliance matrix of the optimized μ-gripper

$\mathbf{C}_{\text{upscale, experiments, }6\times6}$ Experimental compliance matrix for the up-scale μ-gripper

$\mathbf{C}_{\text{upscale, FEA, }6\times6}$ FEA prediction for the compliance matrix of the up-scale μ-gripper

$\mathbf{C}_{\text{con},ee,6\times6}$ The conventional 3$\underline{\text{P}}$PR's 6×6 compliance matrix (at the end-effector)
$\mathbf{C}_{\text{gripper},\,6\times6}$ The 6×6 compliance matrix of the μ-gripper
$\mathbf{C}_{\text{opt},ee,6\times6}$ The optimal 3$\underline{\text{P}}$PR's 6×6 compliance matrix (at the end-effector)
$\mathbf{C}_{\text{PR},6\times6}$ The 6×6 compliance matrix for the PR joint
$\mathbf{C}_{\text{P},6\times6}$ The 6×6 compliance matrix for the P joint
$\mathbf{C}_{\text{SC},j,6\times6}$ The 6×6 compliance matrix of the j^{th} sub-chain
$\mathbf{f}_m$ Magnetic force
$\mathbf{f}_x$ Unit x-axis force on the end-effector (FEA format)
$\mathbf{f}_y$ Unit y-axis force on the end-effector (FEA format)
$\mathbf{f}_z$ Unit z-axis force on the end-effector (FEA format)
$\mathbf{I}_{3\times3}$ 3×3 identity matrix
$\mathbf{J}_j$ Jacobian matrix for sub-chain j
$\mathbf{K}_{\text{gripper}}$ Stiffness matrix for the μ-gripper
$\mathbf{K}_{\text{con},ee,6\times6}$ The conventional 3$\underline{\text{P}}$PR's 6×6 stiffness matrix (at the end-effector)
$\mathbf{K}_{\text{FE}}$ Stiffness matrix for the finite element
$\mathbf{K}_{\text{opt},ee,6\times6}$ The optimal 3$\underline{\text{P}}$PR's 6×6 stiffness matrix (at the end-effector)
$\mathbf{K}_{\text{PR},6\times6}$ The 6×6 stiffness matrix for the PR joint
$\mathbf{K}_{\text{P},6\times6}$ The 6×6 stiffness matrix for the P joint
$\mathbf{K}_{\text{SC},j,6\times6}$ The 6×6 stiffness matrix of the j^{th} sub-chain
$\mathbf{K}_{ee,6\times6}$ End-effector's 6×6 stiffness matrix
$\mathbf{m}(s)$ Magnetization profile
$\mathbf{m}_x$ Unit x-axis torque about the end-effector (FEA format)
$\mathbf{m}_y$ Unit y-axis torque about the end-effector (FEA format)
$\mathbf{M}_z$ Magnetic torque about the z-axis
$\mathbf{m}_z$ Unit z-axis torque about the end-effector (FEA format)
$\mathbf{M}_{\text{FE},i}$ The mass matrix of one finite element in FEA format
$\mathbf{M}_{\text{platform},6\times6}$ The 6×6 mass matrix of the platform
$\mathbf{M}_{\text{SC},j,6\times6}$ The 6×6 mass matrix of the j^{th} sub-chain
$\mathbf{M}_{\text{SC},j,n\times n}$ The $n\times n$ mass matrix of the j^{th} sub-chain in FEA format
$\mathbf{M}_{ee,6\times6}$ The effective 6×6 mass matrix of the FPM
$\mathbf{N}$ Shape function matrix
$\mathbf{q}$ A weighting vector for the bases of wrenches
$\mathbf{r}_j$ Displacement vector from the loading point of PR joint to the loading point of $\underline{\text{P}}$ joint
$\mathbf{R}_{\text{comp}}$ A matrix that computes the ratio between the components of $\mathbf{C}_{\text{opt},ee,6\times6}$ to $\mathbf{C}_{\text{con},ee,6\times6}$

$\mathbf{r}_{\text{ee},6\times1}$ The FPM's end-effector deflection

$\mathbf{R}_z$ Rotational matrix about the z-axis

$\mathbf{u}_e$ Nodal deformation vector for a finite element

$\mathbf{u}_{\text{SC},n\times1,j}$ Nodal deformation for sub-chain j (FEA format)

$\mathbf{w}_{\text{SC},n\times1,j}$ External wrench acting on the FPM's end-effector

θ_x Rotary deflection about the x-axis

θ_y Rotary deflection about the y-axis

θ_z Rotary deflection about the z-axis

A Cross-sectional area of beam

e_h Variable for defining the ending position of the harmonic curve

h Amplitude of the harmonic curve

i Variable to represent the i^{th} finite element

J det($\mathbf{F}$)

j Variable to represent the j^{th} sub-chain

L Link length

l The total number of sub-chains for a FPM

L_3 Variable that determines the space distribution between the compliant $\underline{\text{P}}$ and PR joints

m Variable for selecting a seed

M_b Bending moment of beam

n_h Number of troughs and peaks for the harmonic curve

p_1 Displacement for the first leg's active prismatic joint

p_2 Displacement for the second leg's active prismatic joint

p_3 Displacement for the third leg's active prismatic joint

r Distance between the 3$\underline{\text{P}}$PR FPM's end-effector and the PR joint's loading point

s State of the finite element - $s = 1$ if it is solid, $s = 10^{-6}$ if it is void

S_e Total strain energy for one finite element

s_h Variable for defining the starting position of the harmonic curve

S_{total} Total strain energy for the FPM

T_j Total kinetic energy for sub-chain j

T_{total} Total kinetic energy for the FPM

u Deflection along the x-axis

V Volume of the finite element

v Deflection along the y-axis

W Total work done by external wrench $\mathbf{w}_{\text{ee},6\times1}$

w	Deflection along the z-axis
x_L	x-axis coordinate of the cubic curve's stationary point
y_L	y-axis coordinate of the cubic curve's stationary point
3$\underline{\text{P}}$PR	3-legged-prismatic-prismatic-revolute parallel mechanism. The underlined $\underline{\text{P}}$ represents the active prismatic joint
$\mathbf{B}$	Deformation matrix in FEA format
$\mathbf{D}$	Compliance matrix in solid mechanics
$\mathbf{F}$	The deformation gradient tensor
$\mathbf{S}$	The stress tensor in Lagrangian description (2nd Piola-Kirchhoff stress)
$\underline{\text{P}}$	Active prismatic joint
$\{\text{g}\}$	The global frame
ESO	Evolutionary structure optimization
FPM	Flexure-based parallel mechanism
G.A.	Genetic algorithm
PR	Passive prismatic-revolute joint
SIMP	Solid isotropic material with penalization

Chapter 1

Introduction

1.1 Motivation

Compliant mechanisms are flexible structures that utilize elastic deformation to achieve their desired motions. This unique mode of actuation effectively eliminates dry friction, mechanical play, backlash and wear-and-tear [1, 2, 3, 4, 5], allowing compliant mechanisms to achieve highly repeatable motions. As a result, compliant mechanisms have become the ideal candidates for a wide range of high precision applications such as positional mechanisms for high-resolution imaging systems [6], industrial nano-imprint and nano-alignment applications [7, 8, 9, 10, 11], and numerous other micro/nano-manipulation tasks [12, 13, 14, 15, 16, 17, 18, 19].

Compliant mechanisms can also be used for MEMS and other miniature soft robots as they can be easily manufactured at small-scale [20, 21, 22, 23, 24, 25]. The soft characteristics of compliant mechanisms are especially appealing to miniature robotic applications as their continuous deformations can achieve relatively high degrees-of-freedom, creating a larger feasible range of motions. By exploiting their large range of motions, these soft robots could significantly enhance the mechanical functionalities of traditional miniature robots that are currently limited to only having basic rigid-body-motions [26, 27, 28] and gripping capabilities [29].

Unfortunately, despite the potential of compliant mechanisms, there are still several key challenges that restrict compliant mechanisms from realizing their full potential. For ease of this discussion, we will divide the available compliant mechanisms into two categories - the stiffer flexural mechanisms and the more compliant soft robots.

The relative high stiffness characteristics of flexural mechanisms are ideal for high precision applications as they have sufficiently high off-axis stiffness to resist disturbances. However, since flexural mechanisms also achieve their desired motions via elastic deformation, it is desirable to have low actuating stiffness because this allows the flexural mechanisms to deflect more easily in their desired motions, allowing them to achieve a larger workspace. As a result, the performance of flexural mechanisms is highly dependent on their stiffness properties and it is desirable to maximize the flexural mechanisms' stiffness ratio, i.e. the ratio of off-axis to actuating stiffness, to optimize their workspace and capabilities to resist disturbances. In addition to attaining good stiffness properties, it is also essential for flexural mechanisms to achieve a fast dynamic response. However, higher bandwidth requires higher stiffness, and this will generally reduce the workspace and compromise the stiffness ratio of the flexural mechanisms. Because of the conflicting requirements of stiffness ratios and dynamic properties, it is still a great challenge to synthesize flexural mechanisms with optimal stiffness and dynamic properties. This is especially true when the flexure mechanisms have multi-degrees-of-freedom.

On the other hand, the more compliant soft robots are favorable for miniature robotic applications. As these robots can produce sufficiently larger deflections to change their shapes, they could achieve mechanical functionalities beyond traditional small-scale machines. Among these robots, the magnetically-actuated ones have significant potential to achieve very complex functionalities as the control signals for these robots can be specified not only in their magnitude but also in their direction and spatial gradients. Despite the potential of these soft robots, existing works could only created a limited number of such robots since they can only rely on human intuition to guess the required magnetization profile and actuating fields to realize the necessary functions. As a result, scientists and engineers are still unable to fully capitalize the potential of miniature soft robots and it remains a great challenge to develop a universal programming method for miniature soft robots that are smaller than 1 cm.

1.2 Literature Review

To understand the challenges for compliant mechanisms better, this section provides a detail review for the available methods to synthesize flexural mechanisms and miniature soft robots. There are two general approaches to synthesize flexural mechanism and they are known as the kinematic and structural optimization approaches. These two approaches will be discussed in sections 1.2.1 and 1.2.2, respectively, while the design methods for miniature soft robots will be discussed in 1.2.3.

1.2.1 Kinematic approach

The kinematic approach uses a combination of flexural and rigid-body components such that the flexural mechanisms can achieve their desired kinematics. An advantage of the kinematic approach is that it can easily synthesize flexural mechanisms with multi-degrees-of-freedom. The main drawback of the kinematic approach, however, is that while the selected topology is feasible, it is not necessarily optimal [30, 31]. Two main methods, the rigid-body-replacement and the constraint-based design methods, are established synthesis procedures that can select suitable kinematic configurations for their flexural mechanisms.

Rigid-body-replacement method

The rigid-body-replacement method synthesizes flexural mechanisms by mimicking the motions of traditional mechanisms [1, 32]. This is achieved by replacing the joints of the traditional mechanisms with suitable flexures known as compliant joints. The elastic deformation characteristics of these compliant joints are designed to mimic motions achieved by corresponding

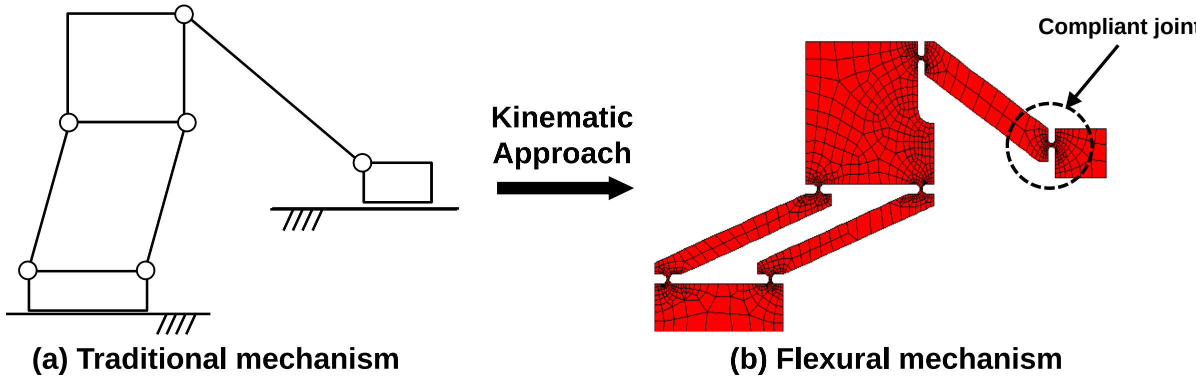

Figure 1.1: An example that illustrates the kinematic approach. A flexural mechanism, shown in (b), is synthesized by replacing the joints of a traditional mechanism, shown in (a), with elastic-bodies called compliant joints. As an example, a compliant joint located on the extreme right of (b) is highlighted.

traditional joints. Thus, by assembling corresponding compliant joints with "rigid" bodies, the motions of these flexural mechanisms can be similar to the traditional mechanisms. This resemblance allows the rigid-body-replacement method to predict its end-effector's motion accurately by using traditional inverse kinematics and stiffness analyses [33, 34]. Furthermore, similar to traditional mechanisms, well-developed Lagrangian equations can be used to describe the dynamic behavior of these flexural mechanisms. By using these valuable analyzes, a vast variety of flexural mechanisms had been developed by the rigid-body-replacement method. An example of the kinematic approach is illustrated in Fig. 1.1 where the joints of a traditional mechanism's joints are replaced with compliant joints.

Unfortunately, while the rigid-body-replacement method can select a feasible kinematic configuration, its topology is not necessarily optimal. As a result, the performance of these flexural mechanisms, i.e. their stiffness and dynamic properties, are generally not optimal.

Constraint-based design method

The constraint-based design method models the off-axis stiffness axes of the flexures as constraint lines, which can restrict specific motions on the rigid components [4, 5, 34, 35]. Each constraint line is assumed to be able to provide infinite resistive force, restricting the rigid components from moving along it. Once a topology of constraint lines has been set, a line that can intersect all these constraint lines is known as a freedom line. This line represents a permitted rotational axis for the rigid component because all the resisting forces do not have an effective moment arm that can supply a resisting torque along that axis. This argument is also true for translational motions as they can be represented by rotations about axes that are located infinitely away from the rigid component. As a result, the number of linearly independent freedom lines that a rigid component possesses, dictates its degrees-of-freedom. Thus, by properly designing the constraint topologies, the desired kinematics for the flexural mechanism can be realized. Although it seems difficult to use intuition to create a suitable constraint topology, all feasible constraint topologies can now be visualized by the freedom and constraint topology (FACT) method [36, 37, 38]. Furthermore, this design process can be further simplified by using the screw theory to mathematically represent the FACT method [39]. As an illustration, Fig. (1.2) shows a flexural mechanism that is synthesized by using five wire flexures (rods) to constrain the end-effector.

Ideally, if all the constraint lines can indeed provide infinite resistive forces to the rigid components, any selected constraint topology would have perfect performance. Unfortunately, this assumption is not true because the off-axis stiffness of the flexures are not infinite, and as the constraint-based design method cannot determine an optimal topology for the flexural mechanism, the overall performance of these flexural mechanisms are not necessarily optimal too.

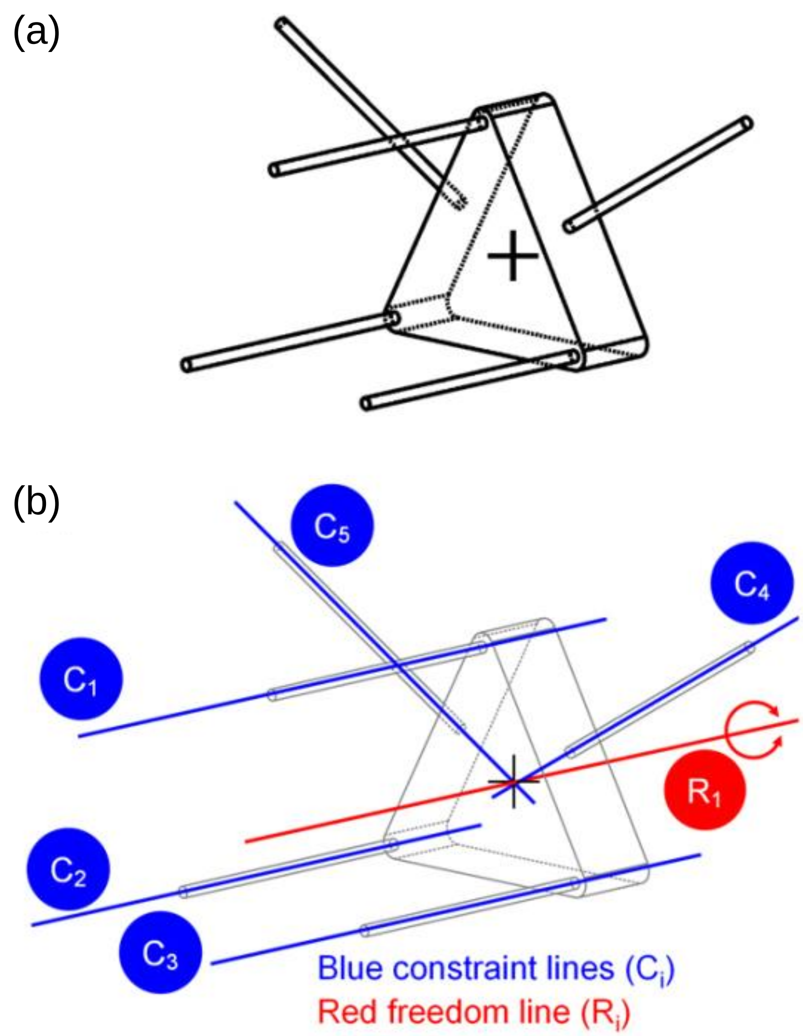

Figure 1.2: An example for the constraint-based method where a flexural mechanism is constrained by five wire flexures [36]. (a) A rigid-body (triangular prism) is constrained by five wire flexures (rods). (b) Each wire flexure can be represented as a constraint line that is indicated by a blue line. The freedom line, which is represented in red, shows the permitted rotation achievable by the rigid-body.

Compliant joints

In addition to the wire flexures that are shown in Fig. (1.2), there are two other types of elementary compliant joints - the leaf-spring design and the notched-type design (Fig. 1.3 [2, 40, 41]). The leaf-spring compliant joints, also known as blade flexures, are simple beam designs where the flexural thickness and width of the beam are intentionally reduced and increased respectively as shown in Fig. 1.3. By having this configuration, certain planes of this design would have low area moment of inertia while other planes would have high area moment of inertia. Thus, this allows the leaf-spring compliant joint to bend easily in the high compliance directions as shown in Fig. (1.3). This actuating compliance of the leaf-spring designs can be determined by using the classical Euler-Bernoulli equations. In comparison with the notch-type design, the leaf-spring design have higher actuating compliance but with lower off-axis stiffness. Thus, the leaf-spring compliant joints can achieve a larger workspace but at the expense of compromising their off-axis stiffness characteristics.

The last elementary compliant joint, the notched-type design, has cutouts on both sides of a blank to form a necked-down section. While there are various types of notch shaped joints, we have presented three examples in Fig. 1.4. Extensive studies have been carried out to determine the actuating stiffness for different types of compliant joints [2, 41]. The notch-type compliant joints are ideal for applications that only require small workspace where the flexural mechanism does not have to compromise its off-axis stiffness.

Compliant joints with more complex deformation characteristics can be obtained by amalgamating the elementary compliant joints. Some examples of such compliant joints include the cart-wheel and prismatic joints that are shown in Fig. 1.5(a) and (b), respectively. It should, however, be noted that the stiffness characteristics of these elementary compliant joints may not be optimal because their selected topology did not undergo an optimization process.

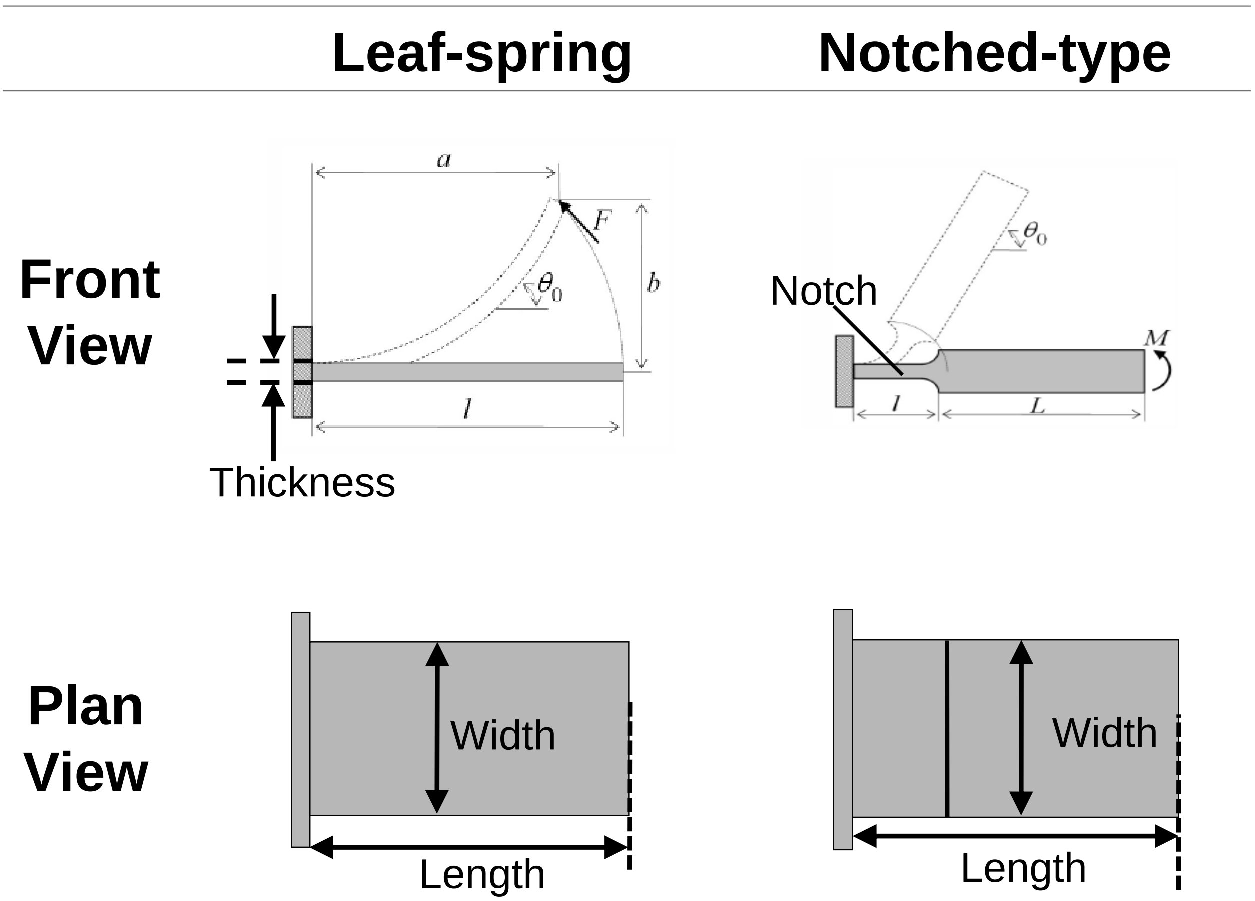

Figure 1.3: The elementary leaf-spring and notched-type compliant joints. The leaf-spring design is a simple beam design that has a high width to thickness ratio. The notch-type design has cutouts on both sides of a blank to form a necked-down section.

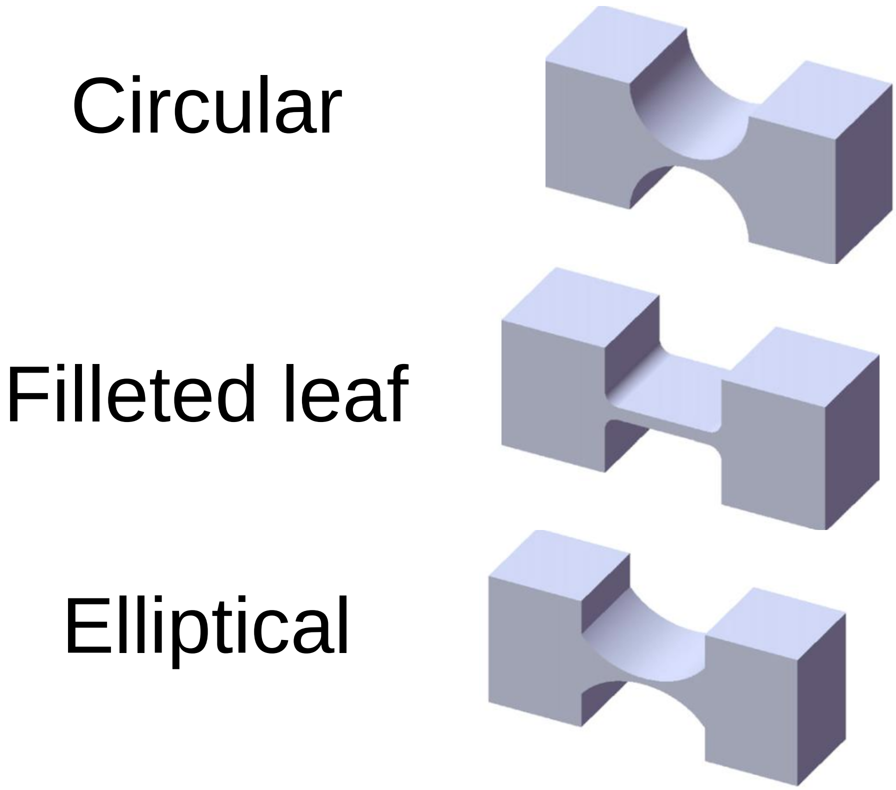

Figure 1.4: Examples of some notch-type compliant joints: the circular, the filleted leaf and elliptical notch-type joints [2, 41].

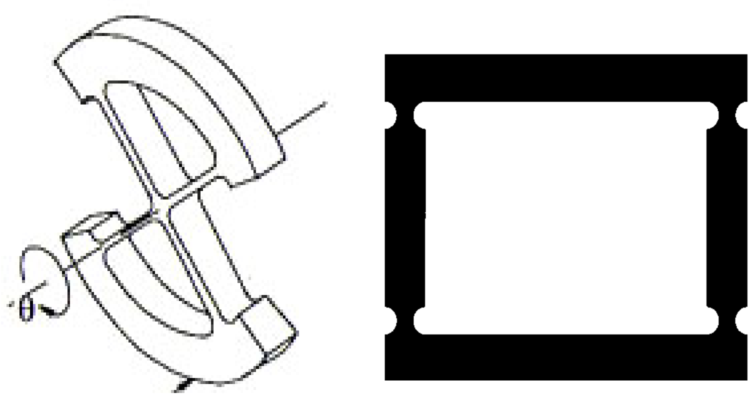

(a) Cartwheel (b) Prismatic

Figure 1.5: Based on the elementary compliant joints, complex compliant joints such as the (a) cartwheel and (b) prismatic compliant joints can be constructed.

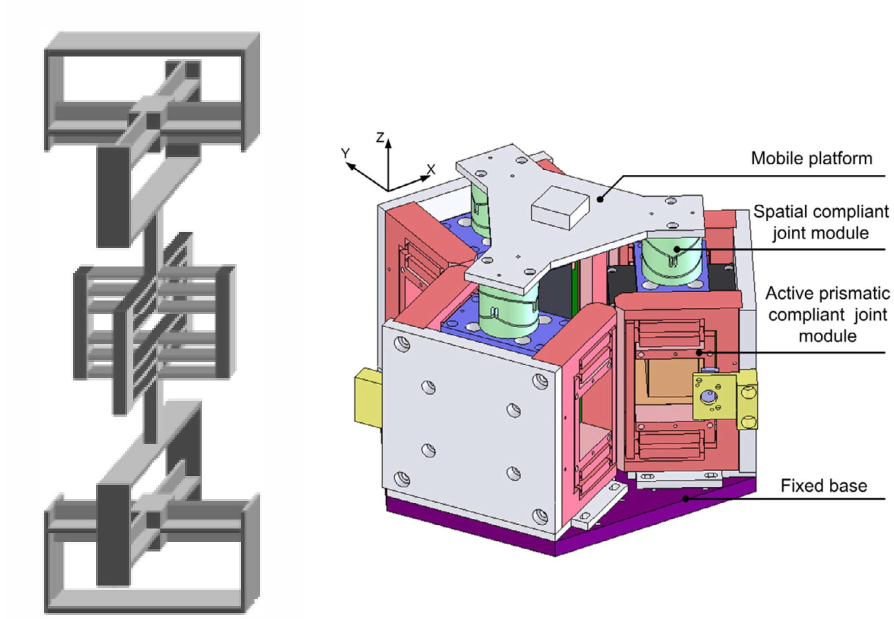

(a) Serial configuration (b) FPM configuration

Figure 1.6: There are generally two types of kinematic configurations. (a) A serial configured flexural mechanism has a chain of compliant joints and rigid linkages that are serially connected to one another [40]. (b) A FPM has an end-effector that is articulated by several parallel sub-chains [7]. As an example, a sub-chain of a FPM is highlighted.

Kinematic configurations

The overall topology of the flexural mechanism, i.e. the connectivity between the compliant joints and the rigid linkages, can be classified into either the serial or parallel kinematic configurations. A flexural mechanism with a serial configuration consists of a chain of compliant joints and rigid linkages that are serially connected to one another. Conversely, a flexural mechanism with a parallel configuration has an end-effector that is articulated by several parallel sub-chains. The parallel-kinematic flexural mechanisms are also commonly termed as a flexure-based parallel mechanism (FPM). An example of a flexural mechanism with a serial configuration is shown in Fig. 1.6(a) while an example of a FPM is illustrated in Fig. 1.6(b).

In comparison, flexural mechanisms with the serial kinematic configuration generally have a larger workspace compared to the FPMs. This is because the elastic deflections of the compliant joints are accumulated for a flexural mechanism with serial kinematic configuration, while the overall stiffness of the FPM is accumulated by the stiffness of each sub-chain. The FPMs, however, have several advantages over their serial counterparts. These include having superior dynamic responses, lower sensitivity towards disturbances and higher off-axis stiffness.

Performances for existing centimeter-scale $X - Y - \theta_z$ flexural mechanisms

The kinematic approach had been used to develop a variety of flexural mechanisms with multi-degrees-of-freedom. Examples of such flexural mechanisms include those with X–Y [35, 42, 43, 44, 45], X– Y– θ_z [9, 10, 12], θ_X– θ_Y–Z [7, 8], X– Y–Z [46, 47, 48] motions, or high precision grippers [17, 18]. As this report illustrates the proposed integrated design approach via the synthesis of a X– Y– θ_z flexural mechanism, this sub-section will discuss the performances of such existing structures in detail.

In the literature, X– Y– θ_z flexural mechanisms can be synthesized with either the serial or FPM configurations as shown in Fig (1.7). In comparison, the FPMs are more popular as they have superior dynamic responses, lower sensitivity towards disturbances and higher off-axis stiffness. Among the developed X– Y– θ_z FPMs, many are synthesized by replacing the traditional revolute joints with compliant notch joints [9, 10, 14, 15]. Due to the high actuating stiffness of the notch-type compliant joints, the resultant workspaces for these FPMs are small. The allowable translational and rotational motions of these FPMs are only within hundreds of micrometers and arcseconds, respectively. The small workspace characteristics for these FPMs are primarily restricted by the high actuating stiffness nature of the notch joints.

Larger workspace FPMs, however, can be obtained by replacing the compliant notch joints with the more compliant beam joints [11, 49]. For example, the beam-type $X - Y - \theta_z$ FPM constructed by Yang et al. can achieve a large workspace of ± 2.5 mm$\times \pm 2.5$ mm$\times \pm 2.5°$[11]. However, the non-actuating stiffness of these FPMs are lower than their notch joint counterparts and this results in lower resistance towards unwanted external disturbances. Thus, the stiffness

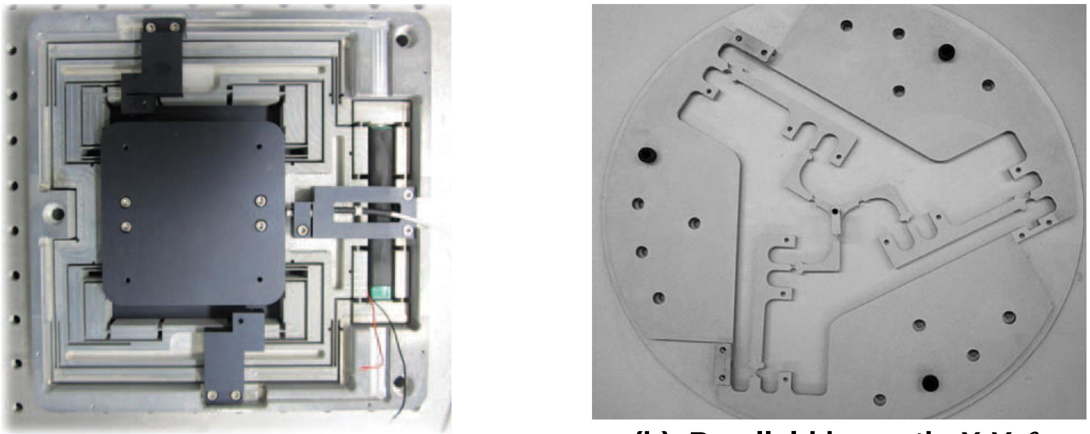

(a) Serial-kinematic X-Y-θ_z (b) Parallel-kinematic X-Y-θ_z

Figure 1.7: (a) A $X-Y-\theta_z$ flexural mechanism with a serial kinematic configuration [12]. (b) A FPM constructed by Yi et al. that can achieve X-Y-θ_z [13].

characteristics for both the notch-type and beam-type FPMs are not optimal as the former is too stiff while the latter is too compliant. Furthermore, the typical stiffness ratio of their end-effector only range between 0.5-50, regardless of the type of elementary compliant joints the $X-Y-\theta_z$ FPM utilized [7, 8, 9, 10, 11, 12, 13, 14, 49, 50]. Although it is possible to increase the FPMs' stiffness ratio by increasing the aspect ratio of their compliant joints (the flexures' width to thickness ratio), the maximum achievable aspect ratio is constrained by two factors. Firstly, in order to operate the FPM within its elastic regime, the induced stress on the compliant joints must not exceed their fatigue stress. This dictates that the flexural thickness of the compliant joints cannot be too small. Secondly, if the flexural width of the compliant joints is too large, the FPM's actuating stiffness might become too high for the FPM to achieve its required workspace. Therefore, the development of a X– Y– θ_z FPM that has a high stiffness ratio greater than 100 is still a great challenge.

In addition to attaining good stiffness properties, it is also essential for the X– Y– θ_z flexural mechanism to obtain a fast dynamic response. However, higher bandwidth requires higher stiffness, and this will reduce the workspace of the flexural mechanism. As an example, the bandwidth for the X– Y– θ_z flexural mechanisms that have workspace of 0.22 mm$\times$0.22 mm$\times$0.22° and 0.52 mm$\times$0.6 mm$\times$0.3° are reported to be 84 Hz [14] and 45 Hz [12] respectively. Large workspace 3-degrees-of-freedom flexural mechanisms that can deflect more than 0.5 mm and $0.5°$, have yet to achieve a high bandwidth that is greater than 45 Hz [7, 8, 12, 49].

1.2.2 Structural optimization approach

The structural optimization approach synthesizes compliant mechanisms automatically via numerical methods such as optimization algorithms and finite element analysis (FEA). By following the structural hierarchy of the compliant mechanism, this synthesis approach will sequentially determine the structure's topology, shape and size. A compliant mechanism's topology can be described as its overall connectivity. For a selected topology, the curvature of a segment that connects different portions of the compliant mechanism can be described as shape. Lastly, based on the selected topology and shape, the physical dimensions of the compliant mechanism can be described as size. In particular, the topological optimization is the most essential component in the structural optimization method and it will be discussed in detail in this section.

Topological optimization determines the compliant mechanisms' optimal overall connectivity via optimization algorithms. This is achieved by first defining the fitness function, loading and boundary conditions of the design domain. Subsequently, the design domain is discretized into a mesh of finite elements and the aim is to identify the state of the elements. Note that topological optimization is a discrete natured optimization problem as the state of the elements can only either be solid or void. The final state of the elements is determined after the performance of the compliant mechanism had gone through iterations of evolution. Performance is quantitatively defined by the fitness value, which is in turned evaluated via FEA.

Unfortunately, the structural optimization approach has its limitations too. For example many established topological optimization algorithms may produce infeasible final designs such as having disconnected solid elements, or elements that are neither solid nor void. Furthermore, unlike the kinematic approach, formulation for the structural optimization problem becomes difficult for compliant mechanisms with more than 1-degree-of-freedom [24, 25, 51, 52] and thus

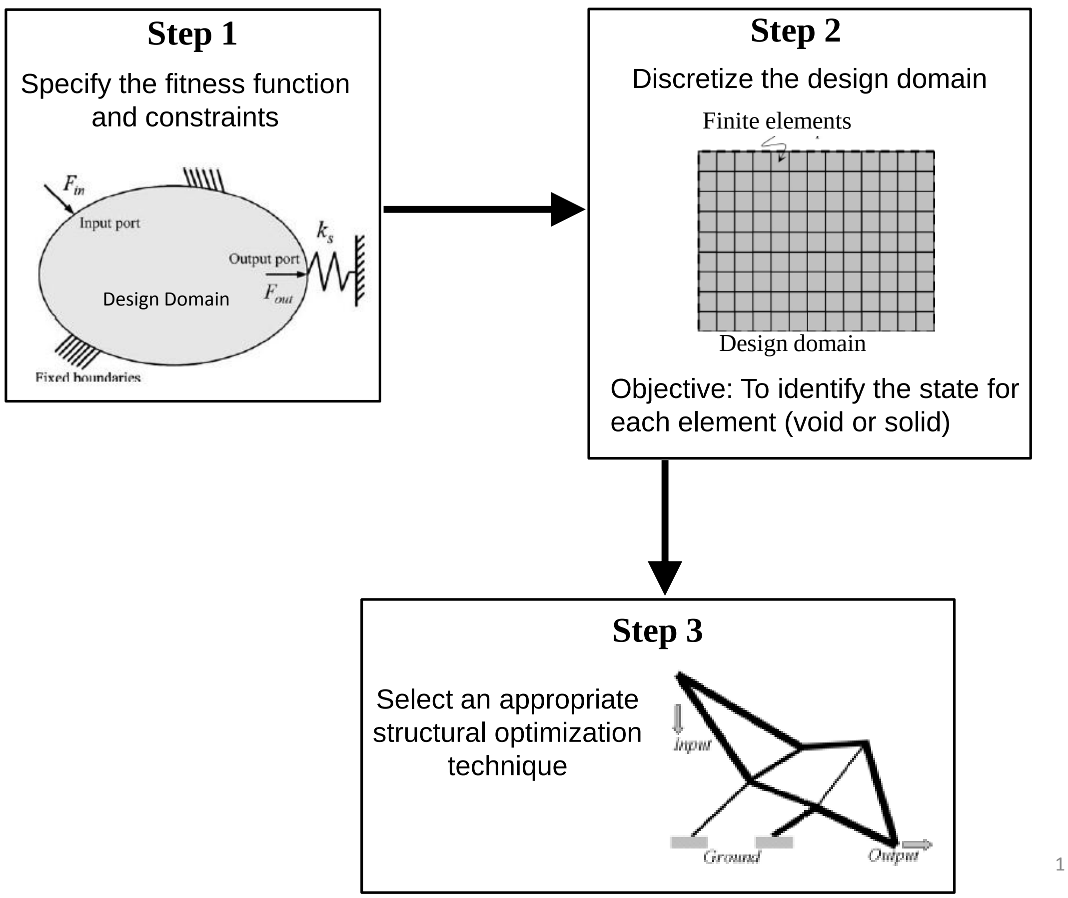

Figure 1.8: The general procedure to implement topological optimization method. Step 1 formulates the optimization problem by specifying the fitness function, constraints, and loading and boundary conditions. This is followed by step 2 where the design domain/space of the compliant mechanism is discretized into a mesh of finite elements. The state of each element can only either be solid or void. Lastly, step 3 uses an appropriate algorithm to perform the structural optimization method, and eventually an optimized design can be obtained.

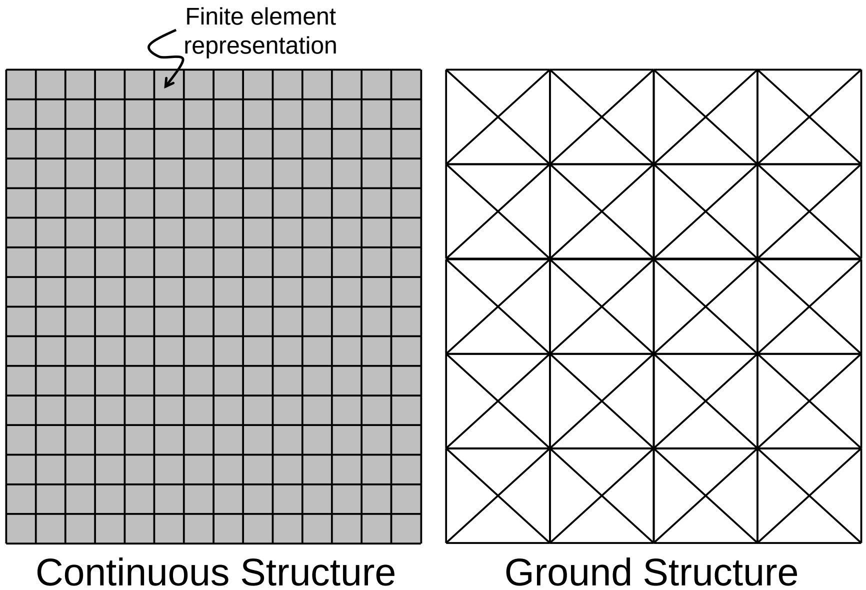

Figure 1.9: Comparison between continuous structure and ground structure topology. The design domain of a ground structure topology is made of discrete components such as bars, beams or frames.

majority of them have only one degree-of-freedom.

From the current literature, there are a number of algorithms developed to perform topological optimization. These include the homogeneous [40, 53, 54], simple isotropic material with penalization (SIMP) [55, 56, 57, 58, 59, 60, 61, 62], evolutionary structural optimization (ESO/BESO) [63, 64, 65], genetic algorithm (G.A.) based algorithms [52, 66, 67, 68, 69, 70], level set methods [71, 72, 73, 74], ground-structure [51, 75, 76, 77, 78, 79, 80] and building block algorithms [81, 82]. Continuum structure topologies can be optimized by homogeneous, SIMP, BESO, level set and G.A. based algorithms. Ground structure algorithms, on the other hand, optimize the topology that is composed by discrete bars/beams/frames. The comparison between the topology of continuous structure and ground structure is illustrated in Fig. 1.9.

As these algorithms differ from one another in their modeling and optimization schemes, each of them has their corresponding benefits and limitations. The following sub-sections will describe these various algorithms.

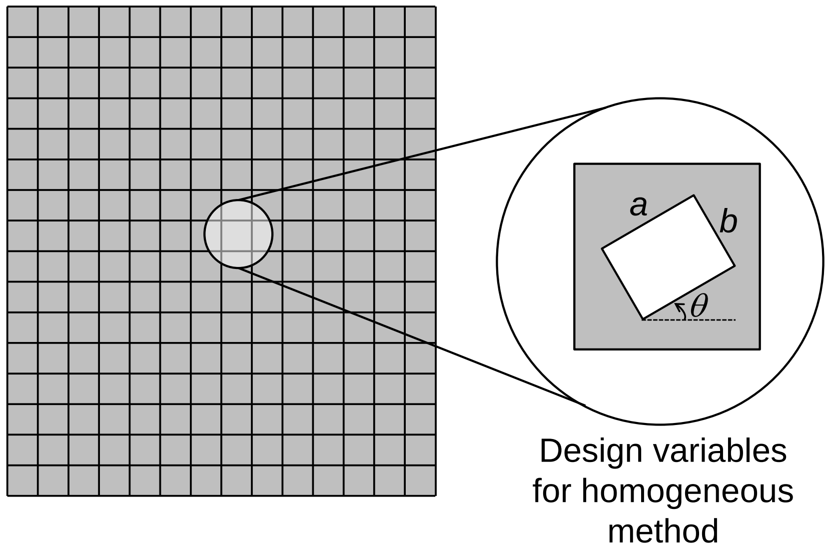

Figure 1.10: Illustration of the design variables for homogeneous method. Within each finite element, a void with the size of $a \times b$ is introduced. The orientation of each void can be specified by the angle θ.

Homogeneous

The homogeneous algorithm introduces a hole within every finite element in the design domain [53]. This is illustrated in Fig. 1.10 where the variables a and b determine the size of the hole and θ determines its orientation. Performance of the topology will change when the size and orientation of the holes vary. Thus, by doing a size optimization on the holes, the optimal topology can be determined. If the size of the hole is as big as the element, this element is considered as a void element. Likewise, if the hole vanishes, it means that this element is considered as a solid element. As the design variables are continuous, the optimization problem can be converted from a discrete natured one into a continuous one. This simplifies the optimization problem and allows the homogeneous algorithm to utilize a gradient-based solver. Note that gradient-based solvers can only be used for continuous optimization problems. Based on the fitness function, the solver will iteratively search for a new solution until the fitness value converges to a solution. The resultant topology will be deemed as the optimal topology.

The homogeneous algorithm has two advantages. Firstly, it has good convergence as it uses a

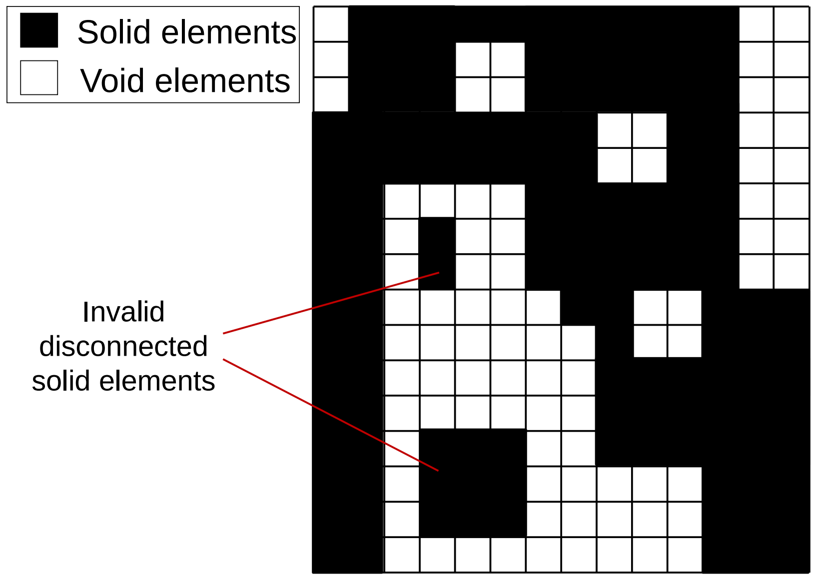

Figure 1.11: Illustration of an infeasible design that consists of disconnected solid elements. In this illustration, the final design is composed of three solid pieces which are disconnected to one another.

gradient-based solver. Secondly, as the homogeneous algorithm factors in the orientation of the inner hole, this optimization can be extended to composite materials as well.

However, this algorithm has also two drawbacks. The homogeneous algorithm may produce infeasible designs such as having microscopic sized holes and disconnected solid elements. Figure 1.11 illustrates an example of a topology, which consists of disconnected solid elements. In addition, since the homogeneous method uses gradient-based solvers, the optimal topology is very sensitive to the initial guess. This implies that there is a higher probability to converge to a local solution, instead of the global one.

Solid isotropic material with penalization (SIMP)

The SIMP algorithm assigns each element with an artificial density [55]. These densities are continuous design variables that range between '0' and '1'. Elements with density values of '1' and '0' represent solid (black) and void (white) elements, respectively. As the densities are

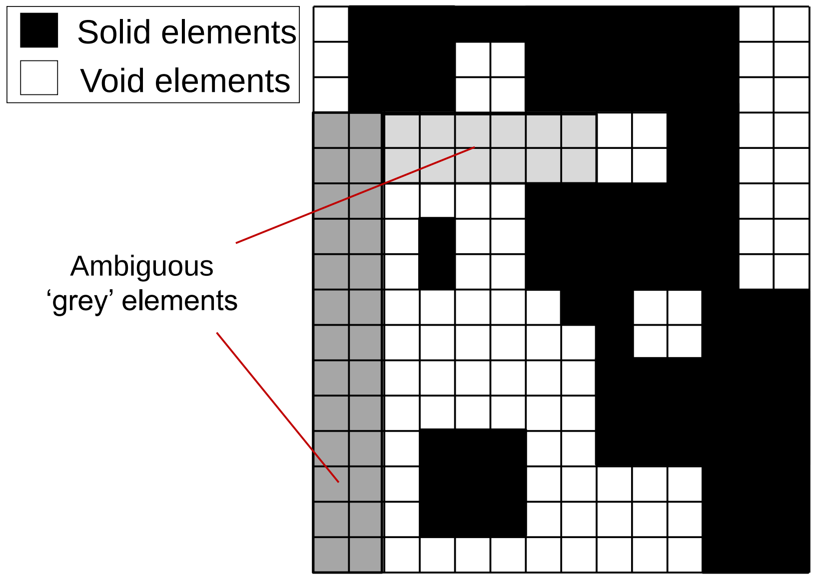

Figure 1.12: Ambiguous 'grey' elements that maybe produced by SIMP. Ideally, all the elements in the mesh should either be solid or void. The 'grey' elements are ambiguous as they are neither solid nor void.

continuous design variables, SIMP can also convert the discrete natured topological optimization problem into a continuous one too. Gradient-based solvers can thus be utilized to perform a "size" optimization on the densities to obtain the optimal topology. The gradient for the fitness function can be obtained from the FEA.

Ideally, all the elements in the optimal topology should be either '1' or '0'. However, in actual implementations, SIMP will usually generate elements that are in between '0' and '1'. These are termed as 'grey' elements and they do not have any physical representations. Thus, designers would have to use their intuition to determine the final state of these 'grey' elements. As a result, the performance of the topology usually deteriorates. Figure 1.12 illustrates the 'grey' elements that are produced by SIMP. In addition to having ambiguous 'grey' elements, SIMP may also produce disconnected solid elements that are invalid too.

Despite the shortcomings of SIMP, it is important to note that SIMP is able to demonstrate good converge capability [55, 57]. It is also an established topological optimization algorithm that is highly robust, and has been utilized for a vast range of applications.

Evolutionary structure optimization/bi-directional evolutionary structure optimization (ESO/BESO)

The ESO/BESO algorithm uses identical design variables as SIMP, where each element is assigned a continuous artificial density. Similarly, the gradient of the fitness function is evaluated via FEA. However, in contrast to SIMP, ESO/BESO does not rely on mathematical programming. Instead, it relies on a set of rules to determine the state of the elements [63, 64, 65]. The earlier version of ESO has only rules to remove solid elements [63] while recent progress allows BESO to add solid elements back to the structure [65]. As ESO/BESO uses a rule-based approach, the artificial densities for all elements remain either a 'zero' or a 'one' at all times. Thus, the possibility of having 'grey' elements does not occur for BESO.

Nevertheless, ESO/BESO was largely criticized for its heuristic approach to perform the optimization process. It has been illustrated that on several occasions, the ESO/BESO algorithm is unable to converge into a solution [83]. Furthermore, similar to homogeneous and SIMP, the ESO/BESO algorithm may produce disconnected solid elements as well.

Genetic algorithm based algorithm

Genetic algorithm (G.A.) is a search and find optimization solver and it will create an initial population of random chromosomes to represent the design parameters. By employing the concept of "survival of the fittest", G.A. can evolve the population gradually until the optimal solution is obtained. When G.A. was first employed for topological optimization, each chromosome maps a corresponding topology by assigning every element in the design domain with a binary number of either a '0' or a '1'. A value '1' corresponds to a solid element while a '0' indicates a void. As genetic algorithm is a discrete solver in nature, it can tackle the topological optimization efficiently and thus it does not produce any 'grey' elements like SIMP [84]. However, this modeling

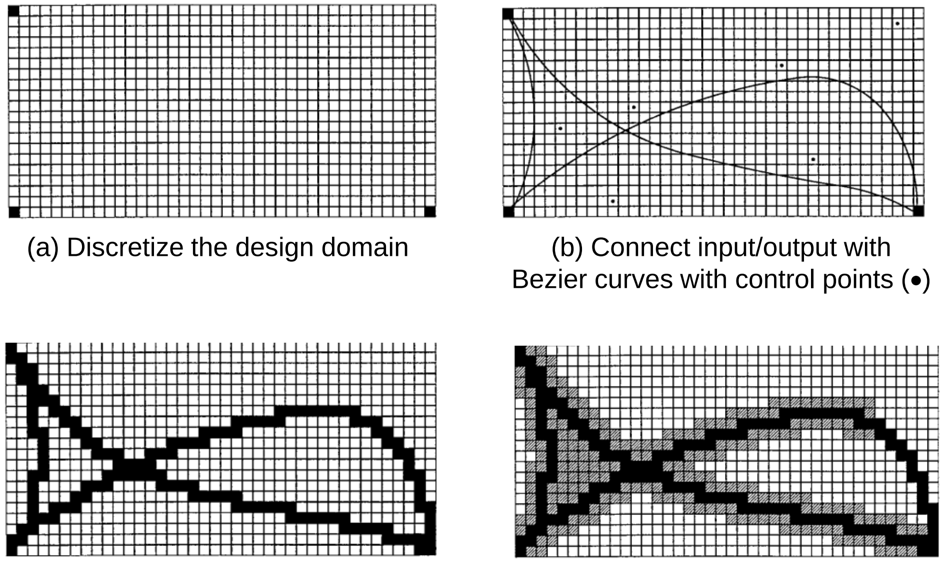

(a) Discretize the design domain

(b) Connect input/output with Bezier curves with control points (•)

(c) Skeleton made of elements along the curves

(d) Add flesh to the skeleton to form the final structure

Figure 1.13: A typical mapping for the morphological method [66]. The output, input and fixed points are connected to one another via a skeleton that is formed by various Bezier curves. Subsequently, additional flesh are added to the skeleton to form a corresponding compliant mechanism.

has a high possibility to produce disconnected solid elements. Fortunately, this issue was eventually resolved when the morphological method was introduced. Instead of using the state of every element as the design variables, the chromosomes of the morphological methodology use the geometrical structure of animals to represent a topology [52, 66, 67, 68, 69]. Each topology differs from one another in terms of the locations of their loading, support and output points and the Bezier curves that connect these points. These Bezier curves form the skeleton of the 'animal' and corresponding flesh are added onto the skeleton to form a corresponding topology. Figure 1.13 shows a typical mapping for the morphological method. The solver will continue to evolve the population of chromosomes until the fitness function converges to a minimum. With the mutation function, the G.A. solver has a higher chance to search for the global minimum while exhibiting good convergence capability [67]. Furthermore, it is important to highlight that the solution is always feasible as it does not produce checkerboard, ambiguous 'grey' elements and disconnected solid elements.

Recent advances of this method introduce the concept of "passive" and "active" Bezier curves [52, 69]. The "passive" curves are curves that do not appear on the topologies while the "active" curves do appear. Based on the performance, all the Bezier curves have the option to switch between "active" and "passive". This essentially increases the search space for the optimization and adds more flexibility in choosing the number of curves. However, the main drawback of this method is that the designer would not know the maximum number of Bezier curves required (active plus passive). In addition, new holes cannot be introduced within each Bezier curve as all elements within the "flesh" components are always solid. Lastly, it requires more computational time and power to implement this algorithm.

Level set method

The level set method uses moving boundaries as its design variables. Elements that are within the boundaries are considered solid while others are void. This effectively allows the optimization process to be performed discretely and eliminates the possibility of having ambiguous "grey" elements. The moving boundaries are represented by a scalar function of a higher dimensionality known as the level set function [71, 72, 73, 74]. This function allows the topology/shape of the compliant mechanism to undergo drastic changes while it remains simple and continuous. A speed function is used to represent the motion of the moving boundaries and it can be determined by FEA. One notable advantage of using the level set method is that it does not require a seed; thus, it does not have limited sets of solutions. When the boundaries move, a boundary can be spilt to form more boundaries or several boundaries may form into one. By using the topological derivatives in conjunction with the level set method, new holes can be generated [72].

As the optimization is usually solved by using steepest descent, it is very sensitive on the initial guess. Thus, it is very likely that the final design will converge to a local minimum instead of the global solution. In terms of the computational power, the level set method is computationally more expensive than SIMP and homogeneous algorithms. Similar to other algorithms, the level

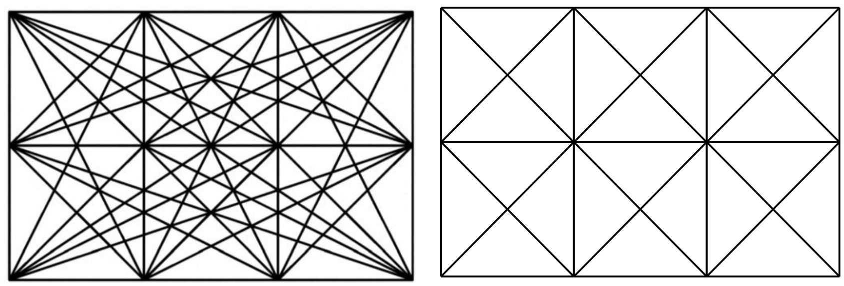

Figure 1.14: The two types of ground structure topology. The fully connected topology has a more inclusive topology compared to its reduced/partially connected counterpart.

set method may produce disconnected solid elements as well.

Ground structure algorithms

As mentioned earlier, the ground structure algorithm differs from all of the above methods as it uses a discrete form of topology to represent its design domain [51, 75, 76, 77, 78, 79, 80]. In general, there are two different types of ground structure topology - the reduced/partial topology and the fully connected topology as shown in Fig. 1.14. Regardless if it is fully- or partially-connected, each connecting element is typically modeled as a bar, beam, or frame.

The fully connected topology will allow the user to have a more inclusive topology. However, this will also increase the complexity of the problem and the optimal topology is usually harder to be manufactured. Solutions obtained from the fully-connected topology are also generally stiffer than the ones obtained from the reduced connected topology.

Once the design domain has been selected, the cross-sectional area of the elements will be optimized by the ground structure algorithm. This allows both topological and size optimization to be carried out simultaneously. The major drawback of this method is that even if one is using a fully-connected ground structure topology, it is still not as inclusive as the ones obtained via continuous structure. In addition, ground structure topology is highly sensitive to the modeling of each element. Based on different types of modeling, the optimized topology will change accordingly.

Building block algorithms

There are generally two types of building block algorithms. The first algorithm uses the concept of ‘divide and conquer’ to synthesize their compliant mechanisms [81]. This is achieved by first pre-defining the required stiffness properties of the compliant mechanisms and decomposing the synthesis process into multiple sub-problems. The objective of each sub-problem is to match specific stiffness ratios by using a combination of basic building blocks. Based on this approach, the building block method is similar to the kinematic approach because it aims to identify feasible topologies for the compliant mechanism. Thus, there may exist multiple feasible topologies, and the selected topology may not have optimal performance.

The second algorithm uses the reduced connected topology to represent the design domain [82]. Instead of using elementary bars, beams or frames, however, this algorithm uses a library of basic blocks to represent each sub-block in the design domain. Similar to other topological optimization algorithms, it is difficult to use this algorithm to construct compliant mechanisms with multi-degrees-of-freedom. Furthermore, similar to the ground structure algorithms, the represented topology is not as inclusive as the ones obtained via continuous structure.

Fitness functions for topological optimization

In addition to the fitness function mentioned for the building block algorithm, other available fitness functions for topological optimization include the geometric advantage, mechanical advantage, energy efficiency and reduced path error [54]. Geometric advantage fitness functions minimize the ratio of the input displacement against the output displacement while the mechanical advantage minimizes the ratio of the input force against the output force. If the designer considers both geometric and mechanical advantage concurrently, the energy efficiency fitness function can be used. The reduced path error fitness function is used when one tries to design a compliant mechanism, which can follow a prescribed path indicated by the designer. In addition to these fitness functions that focus on the static behavior of the compliant mechanisms, the topological optimization method has been shown to be able to optimize their dynamic responses too. The popular approach for dynamic optimization is to maximize the fundamental natural frequencies of the compliant mechanism by using the Rayleigh principle. Despite the variety of available fitness functions, it should be noted that most of these functions are only valid for compliant mechanisms with 1-degree-of-freedom, and the optimization formulations become difficult when multi-degrees-of-freedom are required.

1.2.3 Miniature soft robots

In contrast to the flexural mechanisms, the achievable deformations for the soft robots are much larger, and thus they can achieve their desired functionalities by controlling their shapes to generate desired folding or bending. By reshaping their geometries, the soft robots have the potential to create mechanical functionalities that are beyond traditional rigid machines (especially at small-scale). An example of such functionalities include the recent work by Felton et al. where they were able to program a flat sheet to self-fold into a functional crawling robot [85] (see Fig. 1.15(d)).

These soft robots typically have at least two types of components - the active and the passive components. The active components are the materials that can create a physical change in size or stiffness when they are subjected to stimulants like heat [85, 86, 87, 88, 89, 90], light [91, 92], chemicals [93, 94, 95, 96, 97, 98], pressure [99, 100] or magnetic fields [101, 102, 103, 104, 105, 106, 107, 108, 109, 110, 111, 112]. On the other hand, the passive components are much less responsive toward such stimulants, and their size and stiffness remain relatively unchanged when the active components are actuated. Thus, when both the active and passive components are present within the soft robots, it is possible to create desirable foldings or bending only at specific locations. By properly designing the distribution of the active and passive components, engineers can precisely design the desired shapes for their soft robots.

A common strategy to design the distribution of active and passive components is to place the active components at the compliant joints, allowing the robot to produce desirable folding at those locations when the stimulants are applied [86, 91]. The magnitude of these deflections can be tuned by adjusting the amount of active components, stiffness of the compliant joints and the magnitude of the stimulants. Similarly, the deflecting directions can be controlled by placing the compliant joints in the right orientations. Using this strategy, multiple soft robots have been able to fold into origami structures. Although it seems difficult to determine the required orientation and magnitude for the joints' deflections to achieve the robot's desired shape i.e. to design the required crease pattern of the robot, there exists systematic computational methods that can guide scientists and engineers to determine this crease pattern. These computation methods are modified algorithms that are inspired by the traditional motion-planning algorithms for self-reconfiguring module robots [86, 89]. The connecting joints between the modules of the self-reconfiguring modular robots are similar to the crease/folding lines on the robot. The main difference between the shape-programming algorithms and the traditional algorithms is that there is no relative motions between the underlying modules provided by the crease pattern for the soft robots. Using this computational method, researchers have been able to pattern the distribution of active and passive components correctly, creating a variety of small-scale soft robots (see some examples in Fig. 1.15).

Key challenges

While there are systematic approaches to design the soft robots, the difficulty of designing such robots become exponentially more difficult when their overall dimensions reach approximately 1 cm or smaller. This is because due to the size of such miniature soft robots, the stimulants become

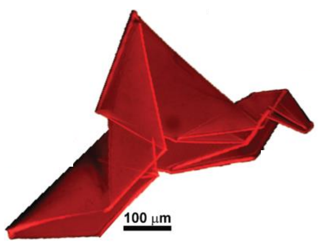

(a) Na et al. (2015)

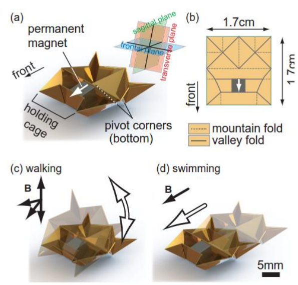

(b) Miyashita et al. (2015)

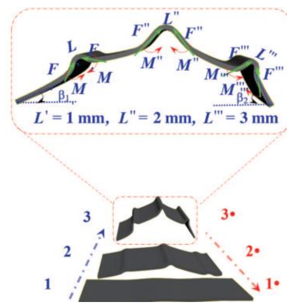

(c) Mu et al. (2015)

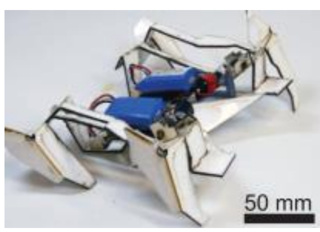

(d) Felton et al. (2014)

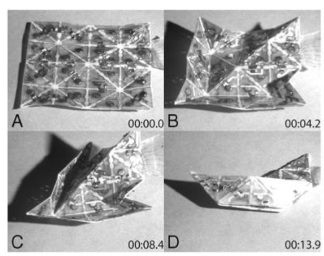

(e) Hawkes et al. (2009)

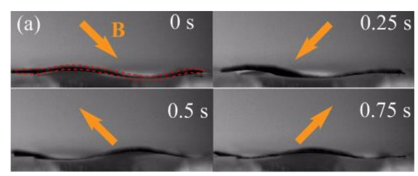

(f) Diller et al. (2014)

Figure 1.15: Examples of some small-scale soft robots. (a) The micron-scale origami crane presented by Na et al. [89]. (b) A millimeter-scale origami ship by Miyashita et al. [87]. (c) The millimeter-scale crawling robot by Mu et al. [92]. (d) The centimeter-scale functional crawling robot by Felton et al. [85]. (e) The centimeter-scale foldable ship by Hawkes et al. [86]. (f) The Talyor swimming sheet by Diller et al. [101].

global actuating signals that can not be varied spatially, enabling all the folding and bending to occur concurrently. This makes the design process to create more shapes exponentially more difficult, and as a result the number of shapes achievable by many of such soft robots are limited to one.

To increase the number of programmable shapes, several research had suggested incorporating two types of active materials within the soft robots. As each active component would only react to a specific stimulant, it is possible to achieve two independent shapes in this manner. However, the benefits of this strategy cannot be further extended for creating more than two shapes because it is difficult to incorporate multiple types of active components within a miniature soft robot from the fabrication perspective (thus many soft robots can only achieve 1-2 shape changes [87, 88, 89, 91, 93, 96, 97, 98]). Having a maximum of one two shapes imply that the temporal resolution of the achievable time-varying shapes for the soft robots are low, and this has severely limited their capabilities. Although many miniature soft robots have time-varying shapes with low temporal resolutions, it is possible for them to achieve shape changes that have high spatial resolutions. An example for such complex geometries is shown by Na et al. where they were able to program a sheet that is several microns long to self-fold into a complex crane-shape origami [89] (see Fig. 1.15(a)).

We would also like to point out that there are also exists soft robots that allow researchers to achieve more than two shapes. For example, Xie et al. were able to create shape-memory-polymers that can program four shapes [90]. Although the work of Xie et al. is impressive, their materials' responses were very slow as they require at least tens of minutes to induce a shape change, making them impractical for many small-scale applications that require fast dynamics. Another two examples that can achieve more two shapes include the work by Mu et al. [92] where they were able to program their graphene paper to achieve four distinct shapes, and the small-scale undulating crawling robot presented by Maeda et al [95]. Although the response of these two works were fast, enabling them to achieve their desired shape change within seconds, their achievable spatial resolutions for their achievable shapes were low, restricting them to achieve relatively simple shapes. In general, many of these soft robots that can achieve more than two shapes have either slow responses [90] or they can only achieve simple shapes for basic crawling [92, 95], gripping [92] and swimming functionalities [107, 111].

Amongst the miniature soft robots, the magnetic-actuated ones have the highest potential to create complex time-varying shapes that have both high spatial and temporal resolutions because the magnetic field control inputs can be specified not only in their magnitude but also in their directions. Unfortunately, despite the potential of these magnetic materials, their state-of-the-art programming method can only rely on a trial-and-error approach to approximate the required magnetization profile and actuating magnetic fields for their desired time-varying shapes. It will be, however, very difficult to use such random processes to deduce the required magnetization profile and actuating fields for numerous other unexplored complex time-varying shapes. As a result, the potential of magnetic shape-programmable materials had been severely underdeveloped because previous works had either only demonstrated simple deformations [102, 103, 104, 105, 108, 110] or were only able to program these magnetic materials for very specific applications [101, 107, 109, 111, 112]. Furthermore, the achievable range of shapes for existing works had been severely limited by their relatively simple magnetization profiles, which are either non-programmable in both directions and magnitude [102, 103, 104, 105, 107, 108, 110, 111, 112], or are only be programmable in directions [101, 109]. The limited range of achievable shapes has thus further reduced restricted scientists and engineers to fully capitalize on this technology.

1.3 Research Objectives

The objective of this research is to propose two new design methodologies that can synthesize optimal compliant mechanisms. The first methodology aims to provide generic steps for engineers to create multi-degrees-of-freedom flexural mechanisms with optimal stiffness and dynamic properties - enabling engineers to synthesize a variety of high precision machines that have optimal performances. To achieve our objectives, we propose an integrate design methodology that can incorporate the benefits of both the kinematic and structural optimization approaches. This can be achieved by first using the kinematic approach to select suitable parallel-kinematic configurations for the compliant mechanism, i.e. determine their required number and type of sub-chains. Subsequently, the sub-chains are automatically synthesized as a whole via a structural optimization method. By integrating these two approaches, the performance of multi-degrees-of-freedom compliant mechanism has the potential to be significantly improved.

To facilitate the design methodology for the flexural mechanisms, we also proposed a new topological optimization algorithm that can eliminate infeasible final designs that have disconnected solid elements or ambiguous 'gray' elements, while having a flexible way to alter their topologies during the optimization process. We will also develop a generic dynamic model that can accurately predict the fundamental natural frequency for flexural mechanisms with parallel-kinematic configurations. This model will help to evaluate the dynamic properties of the flexural mechanism during the design optimization process. The accuracy of the model will be evaluated by validating various compliant mechanisms with random geometries.

Our second methodology aims to provide a universal programming method that can enable scientists and engineers to magnetically program miniature soft robots to achieve desired time-varying shapes with high spatial and temporal resolutions. The universality of the proposed method can therefore inspire a vast number of miniature soft devices that are critical in robotics, smart engineering surfaces and materials, and biomedical devices. Our proposed method includes theoretical formulations, computational strategies, and fabrication procedures for programming magnetic soft matter. The presented theory and computational method are universal for programming 2D or 3D time-varying shapes, whereas the fabrication technique is generic only for creating planar beams.

1.4 Organization of the Report

The following chapters are organized in the following manner:

Chapter 2 introduces a new topological optimization algorithm. The performance of this algorithm will be evaluated via the synthesis of a small-scale gripper, various compliant joints that can be assembled into a 3$\underline{\text{P}}$PR flexural mechanism.

Chapter 3 introduces the proposed integrated design approach for optimal flexural mechanisms that have multi-degrees-of-freedom. This will be demonstrated via the development of an optimal $X - Y - \theta_z$ planar-motioned compliant mechanism.

Chapter 4 introduces the proposed programming methodology that can universally program miniature soft robots (overall dimensions approximately 1 cm or smaller) to achieve desired time-varying shapes. The proposed method includes theoretical formulations, computational strategies and fabrication procedures for miniature soft robots. The effectiveness of this proposed computational methodology will be demonstrated via the synthesis of several miniature soft robots.

Chapter 5 provides the conclusion of this thesis and discusses about possible future works.

1.5 Contributions

The main contributions of this work are to develop novel design methodologies that are generic for synthesizing optimal compliant mechanisms. We provide two methodologies and the first one can be used for the stiffer flexural mechanisms while the second is developed for the more compliant miniature soft robots. The expected contributions for these methodologies can be summarized as:

- We proposed an integrated design methodology for multi-degrees-of-freedom flexural mechanisms with optimal stiffness and dynamic properties. To implement and illustrate the steps of the proposed methodology, we also made the following contributions:
    - A new topological optimization algorithm is developed for designing flexural mechanisms. This algorithm will eliminate the possibly of having infeasible designs while having a flexible way to alter their topologies during the optimization processes.
    - A new semi-analytical dynamic model is developed for evaluating the fundamental natural frequencies of flexure-based parallel mechanisms. The proposed model is generic and can be used universally across flexural mechanisms with arbitrary geometries.
    - We developed a series of flexural mechanisms with optimal performances. In particular, an optimal $X - Y - \theta_z$ with optimal stiffness and dynamic properties had been developed to illustrate the benefits of the proposed methodology.
- We proposed a universal programming methodology for programming miniature (overall dimensions approximately 1 cm or smaller) soft robots to achieve desired time-varying shapes with high spatial and temporal resolutions. The contributions for this methodology include:
    - We provide the theory and optimization algorithm to implement the proposed methodology. As the theory and optimization algorithm are universal, they can guide scientists and engineers to develop a wide range of soft robots that are critical in robots, smart surfaces and biomedical devices.
    - We proposed a new fabrication method that can not only program the directions of the magnetization profile but also its magnitude. This creates an extra dimension of programmable parameter, enabling scientists and engineers to create a larger range

of achievable shapes.

- We developed a series of miniature soft robots with desired time-varying shapes. Examples of these soft robots include the jellyfish-like robot, spermatozoid-like robot and an artificial cilium.

Chapter 2

Two-Dimensional Topological Optimization Algorithm

This chapter introduces a new topological optimization algorithm termed the mechanism-based approach. This algorithm is specifically created for the proposed integrated design methodology. The procedure to carry out the mechanism-based approach will be discussed in section 2.1. Subsequently, the performance of the proposed algorithm will be evaluated by synthesizing a miniature mobile gripper, a compliant prismatic joint and a compliant prismatic-revolute joint. After the compliant joints are synthesized, they will also be assembled into a 3$\underline{\text{P}}$PR FPM. The synthesis of the mobile gripper will be presented in section 2.2 and the synthesis and assembly of the compliant joints will be presented in section 2.3. Lastly, a summary for this chapter will be provided in section 2.4.

2.1 Geometrical Mapping for the Mechanism-based Approach

Inspired by the morphological algorithm that can eliminate infeasible solutions, we develop a new topological optimization termed the mechanism-based approach. This algorithm uses traditional mechanisms as seeds to represent the topology of the continuum flexural mechanism. In order to implement the mechanism-based approach, traditional mechanisms that have the same degrees-of-freedom as the flexural mechanism are selected as seeds. If there are multiple seeds, a discrete variable, m, will be used to select a seed to superimpose onto a design domain where all the finite elements are initially selected as void. The position of links' tip for the selected seed will be defined by other design variables.

Once the seed has been superimposed, there are two ways to represent its links. The first way is to represent each link with a straight line and all the finite elements that are in contact with the selected seed are converted into solid elements. As the solid elements are selected in a discrete manner, no ambiguous "grey" elements can be formed.

Alternatively, the second way represents each link of the mechanism with one cubic curve, one harmonic curve, and their reflected curves about the link. As an example, the second way of mapping is illustrated with a four-bar linkage seed in Fig. 2.1. The four curves form the boundaries used in the selection of solid elements. Based on the value of γ assigned to each link $(\gamma \in \mathbb{Z}^+, 1 \leq \gamma \leq 3)$, different combinations of solid elements can be generated. If $\gamma = 1$, all the elements bounded between the original curves and the link are solid. When $\gamma = 2$, all the elements bounded by the reflected curves and the link are solid. When $\gamma = 3$, the solid elements will be the combined elements of $\gamma = 1$ and $\gamma = 2$ cases. Similar to the first way of mapping, the second way selects their solid elements in a discrete manner and this prevents any ambiguous "grey" elements from forming.

Using the second way of mapping, the cubic curves are designed to have one stationary point

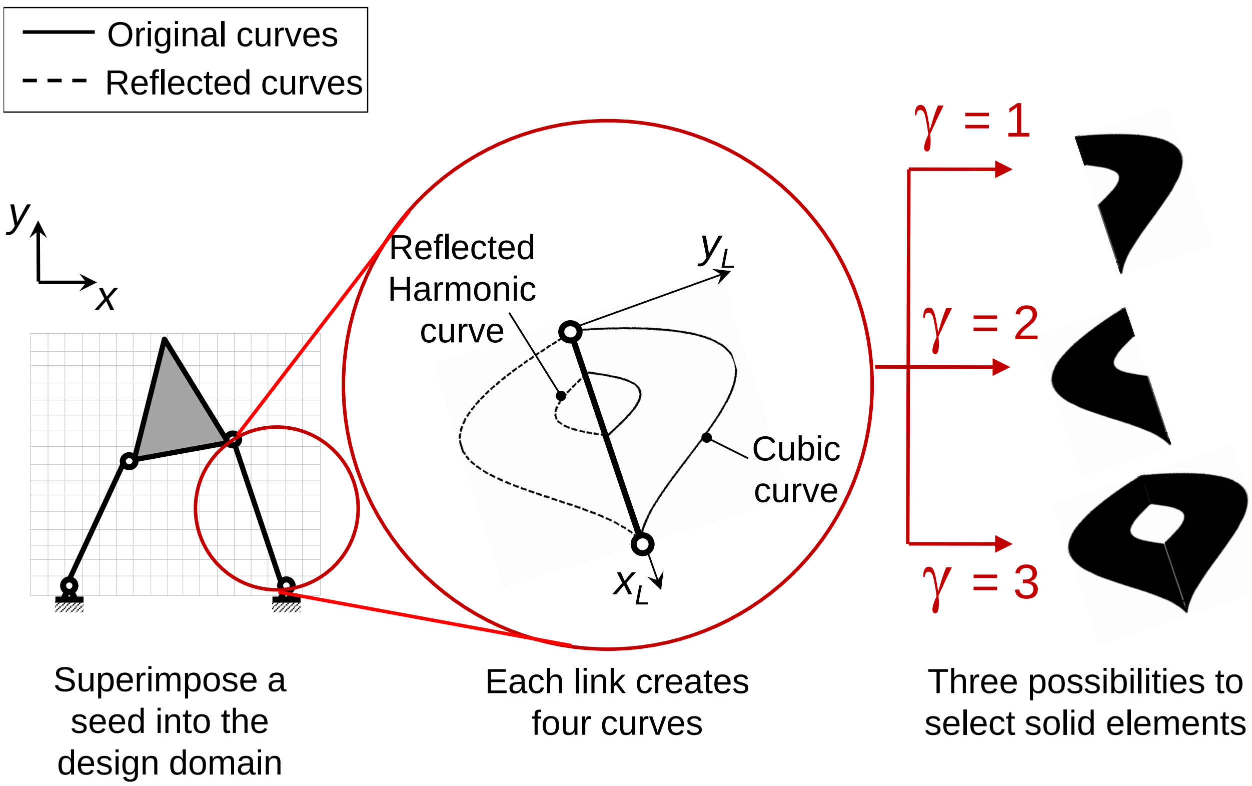

Figure 2.1: The procedure to implement the mechanism-based approach. In this example, a four-bar linkage seed is superimposed onto a mesh of void elements. Each link of the seed is represented with four curves and based on the value of the variable γ, different combinations of solid elements can be generated.

within the link length so that the harmonic curves can be enclosed. With this configuration, it is possible to create holes within each link. The number of holes for $\gamma = 3$ is equal to $2n_h - 1$ where n_h is a positive integer that represents the number of troughs and peaks of the harmonic curve. The cubic curves can be described by using three parameters - the link length, L, and another two parameters, α and β. These three parameters define the coordinates of the stationary point $(x_{L,\max}, y_{L,\max})$ such that $x_{L,\max} = \alpha_c L$ and $y_{L,\max} = \beta_c L$. With the boundary conditions $(0,0)$ and $(L,0)$ in the $x_1 - y_1$ frame, the cubic curves' equations are:

$$\begin{aligned} y_L = \pm(a_c x_L^3 + b_c x_L^2 + c_c x_L + d_c) \ \text{ where} \\ a_c = -\beta_c \frac{2\alpha_c - 1}{(\alpha_c(\alpha_c - 1))^2}, \\ b_c = \beta_c \frac{3\alpha_c^2 - 1}{(\alpha_c(\alpha_c - 1))^2 L} \\ c_c = -(a_c L^2 + b_c L) \ \text{ and } \ d_c = 0. \end{aligned} \tag{2.1}$$

Equation (2.1) with the plus sign represents the original cubic curves. Four independent parameters s_h, n_h, e_h and h are used to define the harmonic curves. The parameters s_h and e_h determine the starting and ending point of the curve respectively and h determines the amplitude of the curve. If $(s_h + e_h) \geq 1$ or $h = 0$, no harmonic curves are produced and thus no holes are formed. Figure 2.2 shows the corresponding parameters for the original curves and $n_h = 1$ for the harmonic curve as there is only one peak. The equations of the harmonic curves for $s_h L \leq x_1 \leq L - e_h L$ are:

$$y_L = \pm h \sin\left[\frac{2\pi}{\lambda_h}(x_L - s_h L)\right] \tag{2.2}$$

where λ_h is the wavelength and it is expressed as:

$$\lambda_h = 2\frac{L - (s_h L + e_h L)}{n_h}. \tag{2.3}$$

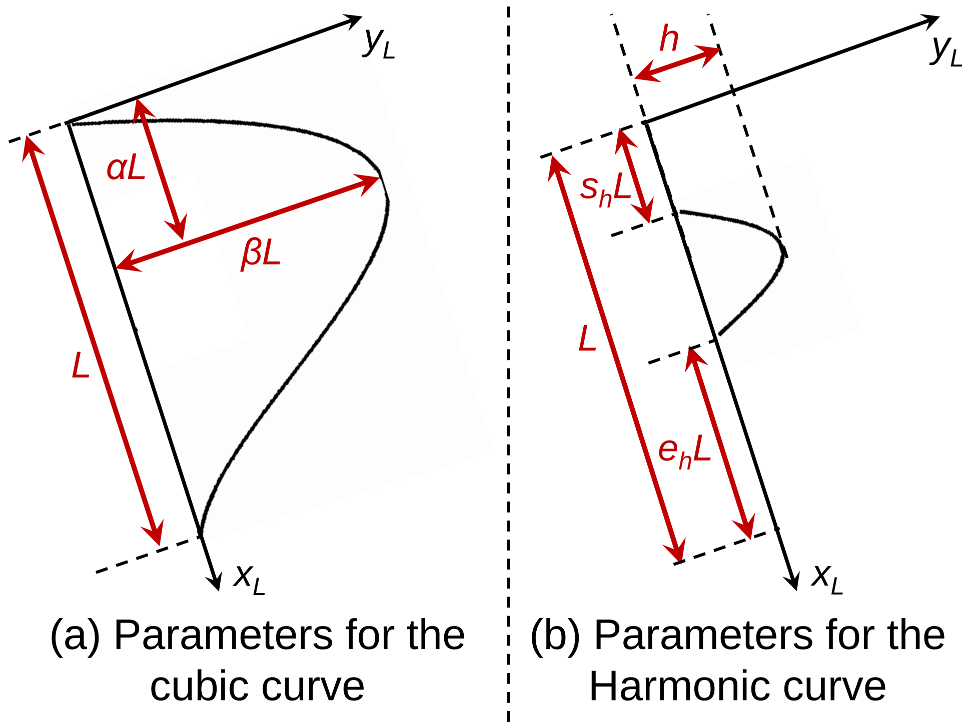

Figure 2.2: The design variables required to map the cubic and harmonic curves. (a) The design variables, α, β and L, will define the curvature of the cubic curves. (b) The design variables, h, s_h, e_h and L, will define the curvature of the harmonic curves.

Note that Eq. (2.2) with the plus sign represents the original harmonic curves. A corresponding topology is produced when all the links follow the above-mentioned description and an example is shown in Fig. 2.3. In comparison, the second mapping has the potential to create topologies that are more complex but this will require more computational time and resources. Thus, if the computational resources permits, the second mapping might be a better option to represent the linkages of the seed.

Regardless of the way to represent the links, this algorithm will not produce disconnected solid elements because the links of the traditional mechanism are always physically connected to one another. In addition, topologies created via the mechanism-based approach are not limited by its seeds because if any links' length approaches zero during the optimization process, even the seeds' "topology" can be changed. This effectively allows the mechanism-based approach to have a more flexible way to perform the optimization process. The optimization problem will be solved by using G.A. and each chromosome contains the information of the design variables (the

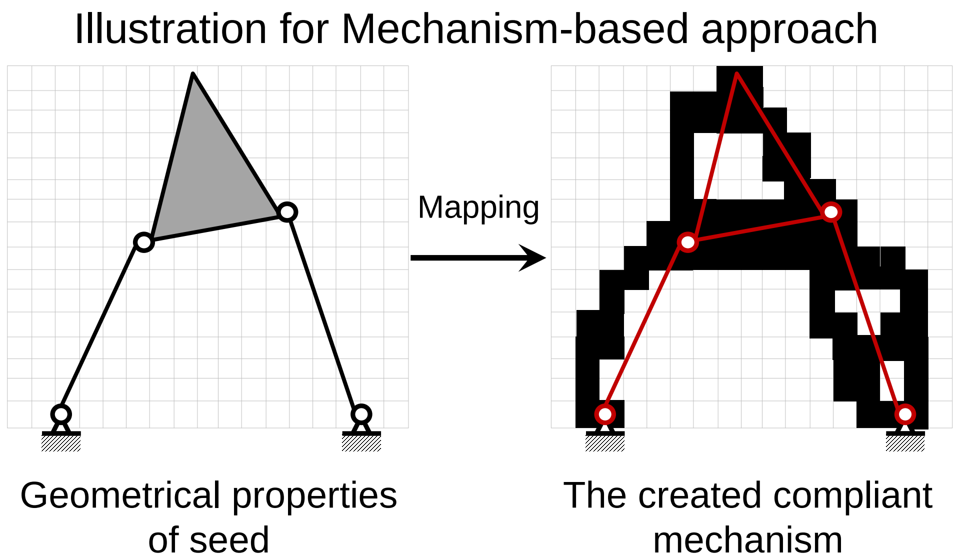

Figure 2.3: A corresponding flexural mechanism is formed based on the curves' parameters, and the seed's topology and posture. The black and white elements represent the solid and void elements, respectively.

position of the links' tip, and possibly the curves' parameters). Based on the specified fitness function, G.A. will gradually evolve these solutions until an optimum solution is found. As G.A. is used as the solver, the possibility of arriving at the global solution is higher than the gradient-based methods. However, it should also be noted that in comparison to gradient-based methods, more computational time and power are required to achieve this.

2.2 Design of a Small Scale Flexure-based Mobile μ-grippers

The performance of the mechanism-based approach is investigated via a test problem - synthesizing a millimeter-scale mobile gripper known as a μ-gripper . The conceptual design of the μ-gripper is shown in Fig. 2.4, where each arm of the μ-gripper has a rigid component and a flexure (flexural mechanism). The function of the rigid component is to grab and manipulate micro-objects while the flexural mechanism allows the μ-gripper to achieve its desired deflections.

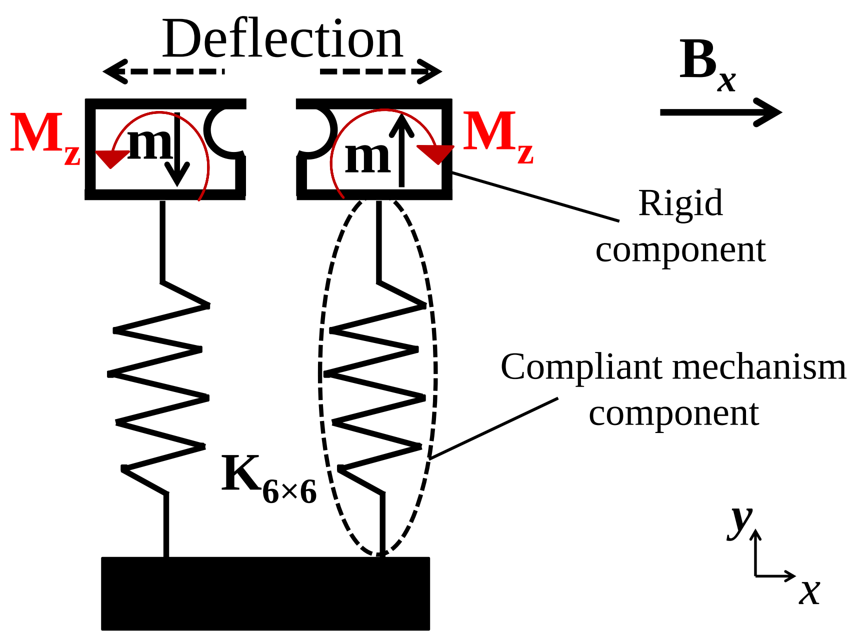

Figure 2.4: The conceptual design of the μ-gripper. The gripper has two arms and each arm has a rigid and a flexural mechanism component. The flexural mechanism component is represented by a spring with stiffness in all 6 axes. The rigid component is magnetized in the body frame's y-axis direction and it will experience a torque about the z-axis when a magnetic field that is along the body frame's x-axis is applied. Ideally, upon actuated, the flexural mechanism component should have a large translational deflection along the body frame's x-axis. Furthermore, the flexural mechanism component should have high stiffness for all other directions.

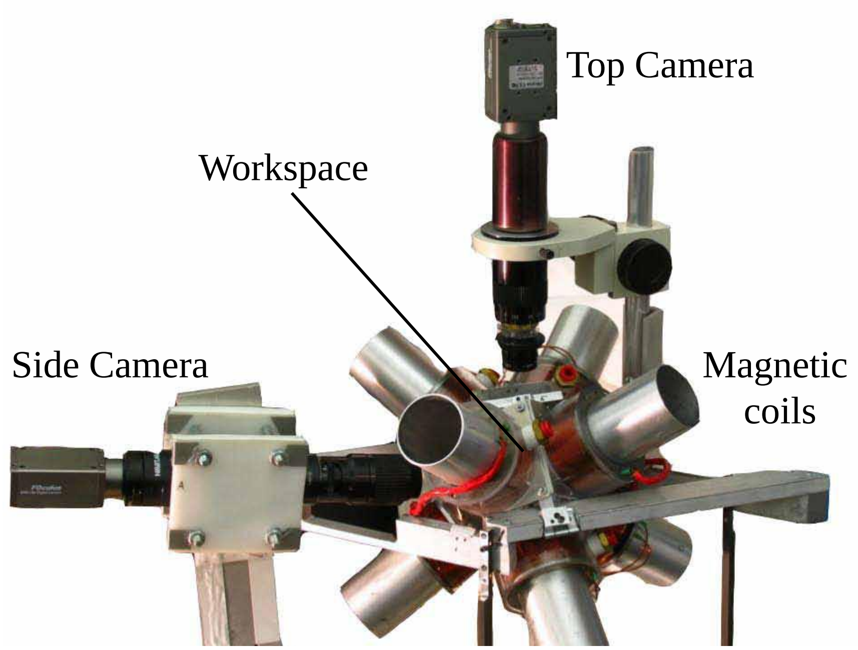

Figure 2.5: The magnetic coil system that is used to actuate the μ-grippers. The μ-grippers are located within the workspace indicated in the figure. There are two cameras - side and top, to provide vision feedback.

The desired motion of the flexural mechanism can be seen in Fig. 2.4 where the flexure can provide a large x-axis translational deflection when it is subjected to a torque in the z-axis. In order to create this torque, $\mathbf{M}_z$, via magnetic actuation, the rigid component has a magnetic moment that is parallel to its y-axis body frame (Fig. 2.4); the actuating torque can be generated by using the electromagnetic coil system shown in Fig. 2.5 to supply an external magnetic field that is parallel to the x-direction ($\mathbf{B}_x$). Other than the desired compliance, the μ-gripper should exhibit high stiffness in all other directions so that it can easily reject mechanical disturbances when it is grabbing and transporting other objects; this implies that the flexure has only 1-degree-of-freedom.

Based on the degree-of-freedom of the flexure, we have used the Grübler equation [113] to select two appropriate traditional mechanisms as seeds. The selected seeds are the 6-bar Watt- and Stephenson-Chains, and their topologies can be seen in Fig. 2.6(b). These mechanisms are chosen because they can be constrained to generate flexural mechanisms with symmetrical features that can help to reduce the parasitic compliances.

During the optimization process, the topologies can be evolved by varying the position of the seeds' link tip. The topology of the seeds can also be changed if any link lengths are reduced to zero. As the position of the links' tip are the design variables, they are encoded in G.A.'s chromosomes. To reduce computational resources, we represent the linkages of the seeds with straight lines in this test problem (first way of mapping).

The design domain for each of the μ-gripper's flexural mechanism component is bounded within an area of 1.25 mm $\times$ 1.25 mm with 50 μm thickness. The design domain's dimensions is chosen to facilitate fabrication via photolithography and replica molding. The utilized material is a flexible elastomer material (ST-1087, BJB Enterprises), with Young's modulus and Poisson ratio estimated to be 9.8 MPa and 0.45 respectively. The design domain is discretized into a mesh of 25×25 identical 20-node quadratic finite element where each element can only be either solid or void, and they are all initially selected as void.

The stiffness characteristics of the μ-gripper can be evaluated by using FEA to determine the deformation characteristics of its loading point (indicated by the point where an arbitrary wrench, $\mathbf{w}$, is applied on the gripper (see Fig. 2.6)). To implement FEA, we shall first define the translational deformation of any arbitrary point within a finite element, $\bar{\mathbf{u}}_e$, to be the product of the shape function matrix, $\mathbf{N}$, and the nodal deformation vector $\mathbf{u}_e$:

$$\bar{\mathbf{u}}_e = \begin{bmatrix} u \\ v \\ w \end{bmatrix} = \begin{bmatrix} N_1 & 0 & 0 & ... & 0 \\ 0 & N_1 & 0 & ... & 0 \\ 0 & 0 & N_1 & ... & N_{20} \end{bmatrix} = \begin{bmatrix} u_1 \\ v_1 \\ w_1 \\ \vdots \\ w_{20} \end{bmatrix} = \mathbf{N}\mathbf{u}_e \tag{2.4}$$

Note that u, v and w represent the deformation in the $x-$, $y-$ and $z-$axis respectively. Subsequently, the strain vector of the point, $\boldsymbol{\epsilon}_e$, can be obtained by partial differentiating corresponding

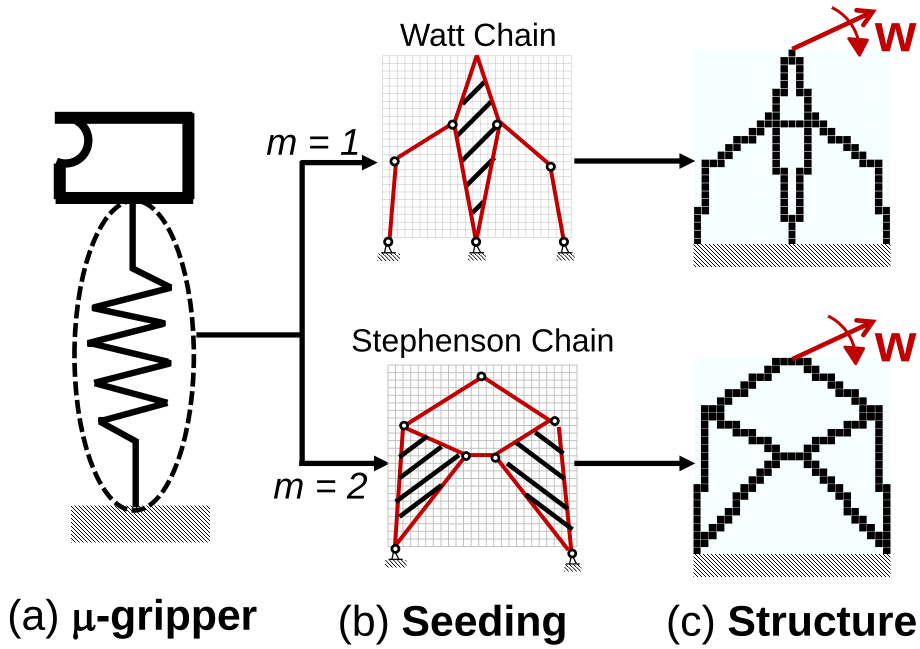

Figure 2.6: Implementing the mechanism-based approach on the (a) μ-gripper. (b) shows the design domain of the flexure being discretized into a mesh of 25×25 identical finite elements. The area of the design domain is 1.25 mm $\times$ 1.25 mm. Based on the valuable of m , different seeds will be used to represent the flexure. A Watt chain seed is used when $m = 1$ while a Stephenson chain is used when $m = 2$. (c) shows the obtained structure created via their corresponding seed.

rows in Eq. (2.4):

$$\boldsymbol{\epsilon}_e = \begin{bmatrix} \frac{\partial u}{\partial x} \\ \frac{\partial v}{\partial y} \\ \frac{\partial w}{\partial z} \\ \frac{\partial v}{\partial z} + \frac{\partial w}{\partial y} \\ \frac{\partial u}{\partial z} + \frac{\partial w}{\partial x} \\ \frac{\partial v}{\partial x} + \frac{\partial u}{\partial y} \end{bmatrix} = \mathbf{B}\mathbf{u}_e \tag{2.5}$$

where **B** is the commonly used deformation matrix in FEA. By using Hooke's law, the stress vector at that point, $\boldsymbol{\tau}_e$, can be expressed as:

$$\boldsymbol{\tau}_e = \mathbf{D}\boldsymbol{\epsilon}_e = \mathbf{D}\mathbf{B}\mathbf{u}_e \tag{2.6}$$

where **D** is the compliance matrix in solid mechanics. The element's total strain energy, S_e, is:

$$S_e = \frac{1}{2}\iiint \boldsymbol{\tau}_e^{\mathrm{T}}\boldsymbol{\epsilon}_e \,\mathrm{d}V = \frac{1}{2}\mathbf{u}_e^{\mathrm{T}}\left[\iiint \mathbf{B}^{\mathrm{T}}\mathbf{D}\mathbf{B}\mathrm{d}V\right]\mathbf{u}_e = \frac{1}{2}\mathbf{u}_e^{\mathrm{T}}\mathbf{K}_{\mathrm{FE}}\mathbf{u}_e. \tag{2.7}$$

where V represents the volume of the finite element and $\mathbf{K}_{\mathrm{FE}}$ represents the stiffness matrix for one element. The FEA global stiffness matrix for the gripper, $\mathbf{K}_{\text{gripper}}$, can then be obtained by summing all elements' stiffness matrix:

$$\mathbf{K}_{\text{gripper}} = \sum_{i=1}^{\text{all elements}} \left(s_i \mathbf{K}_{\mathrm{FE},i}\right). \tag{2.8}$$

The variable s represents the state of the finite element, if element i is solid, s_i = 1; if it is void, $s_i = 10^{-6}$ (to prevent numerical instabilities). Since the six loadings are unit wrenches, their corresponding work functions are simply the deformation of the loading point that is parallel to the unit wrench. Note that the rotational deformation of the loading point can be derived from

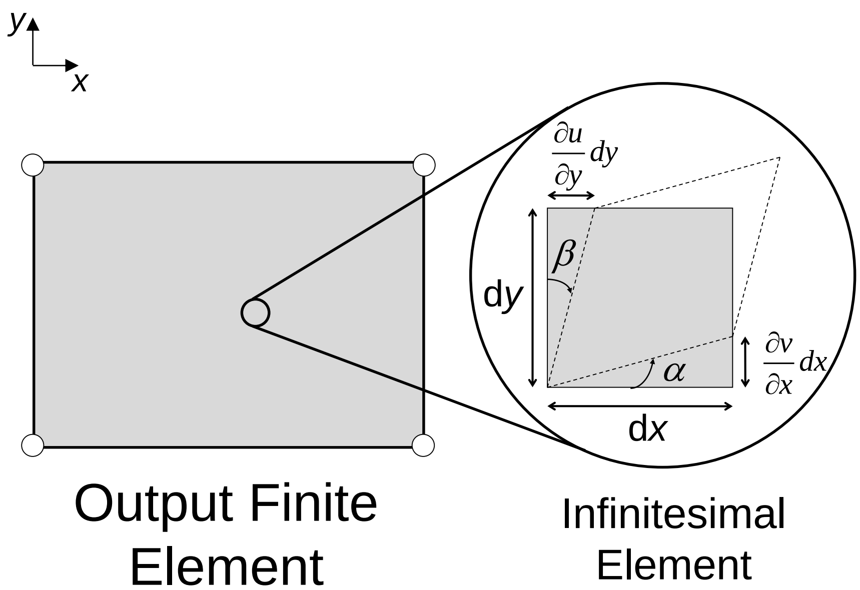

Figure 2.7: A graphical representation of rotary deflection for any point within the finite element. By zooming into the infinitesimal element of a finite element, the average rotary deflections about the z-axis of any given point is $\frac{1}{2}(\alpha - \beta)$.

the infinitesimal element. Using Fig. 2.7 as illustration aid, the angular displacement in the z-direction of the loading point is:

$$\begin{aligned} \theta_z &= \frac{1}{2}(\alpha - \beta) = \frac{1}{2}(\frac{\partial v}{\partial x} - \frac{\partial u}{\partial y}) \\ \therefore \theta_z &= \frac{1}{2}\left[\sum_{i=1}^{8}\left(\frac{\partial N_i}{\partial x}v_i - \frac{\partial N_i}{\partial y}u_i\right)\right]. \end{aligned} \tag{2.9}$$

Likewise, the rotational displacement in the x and y-axes can be obtained as:

$$\begin{aligned} \theta_x &= \frac{1}{2}\left[\sum_{i=1}^{8}\left(\frac{\partial N_i}{\partial y}w_i - \frac{\partial N_i}{\partial z}v_i\right)\right] \\ \theta_y &= \frac{1}{2}\left[\sum_{i=1}^{8}\left(\frac{\partial N_i}{\partial z}u_i - \frac{\partial N_i}{\partial x}w_i\right)\right]. \end{aligned} \tag{2.10}$$

The translation and rotational work functions are represented by $\phi_{\mathrm{T},j}$ and $\phi_{\mathrm{R},j}$, $j \in [x, y, z]$, respectively. The global nodal deformation vector is represented by $\mathbf{u}_{\text{gripper}}$ and thus the six work functions are expressed as:

$$\begin{aligned}
\phi_{\text{T},x} &= \mathbf{u}_{\text{gripper}}^{\text{T}}\mathbf{f}_x \quad \phi_{\text{R},x} = \mathbf{u}_{\text{gripper}}^{\text{T}}\mathbf{m}_x \\
\phi_{\text{T},y} &= \mathbf{u}_{\text{gripper}}^{\text{T}}\mathbf{f}_y \quad \phi_{\text{R},y} = \mathbf{u}_{\text{gripper}}^{\text{T}}\mathbf{m}_y \\
\phi_{\text{T},z} &= \mathbf{u}_{\text{gripper}}^{\text{T}}\mathbf{f}_z \quad \phi_{\text{R},z} = \mathbf{u}_{\text{gripper}}^{\text{T}}\mathbf{m}_z.
\end{aligned} \tag{2.11}$$

By partial-differentiating the work functions with respect to the global nodal deflections, the six loading vectors are represented in FEA format as $\mathbf{f}_x$, $\mathbf{f}_y$, $\mathbf{f}_z$, $\mathbf{m}_x$, $\mathbf{m}_y$ and $\mathbf{m}_z$, respectively. After applying the boundary conditions, the corresponding deformation vectors are obtained by pre-multiplying the six loading vectors with the structure's inverse stiffness matrix. The six 6×1 position vectors which describe the position and orientation deformations at the loading point can be obtained by using N_i, and u_i, v_i and w_i from the corresponding global nodal deformation vectors. This is represented by pre-multiplying the six global nodal deformations vectors with a constant matrix $\mathbf{A}$.

$$\therefore \mathbf{C}_{\text{gripper, } 6\times 6} = \mathbf{A}\mathbf{K}_{\text{gripper}}^{-1}[\mathbf{f}_x \;\; \mathbf{f}_y \;\; \mathbf{f}_z \;\; \mathbf{m}_x \;\; \mathbf{m}_y \;\; \mathbf{m}_z]. \tag{2.12}$$

The matrix, $\mathbf{C}_{\text{gripper, } 6\times 6}$, represents the compliance matrix of the flexural mechanism. The six columns of the matrix represent the rigid-body deflections induced by corresponding loadings. The first three rows of $\mathbf{C}_{\text{gripper, } 6\times 6}$ represent the translational deflection while the last three rows represent the rotary deflection. As the actuating compliance of the μ-gripper is represented by C_{61} in $\mathbf{C}_{\text{gripper, } 6\times 6}$, we will use the following fitness function to optimize its stiffness characteristics:

$$\text{minimize } F_{\textbf{gripper}} = \frac{C_{51}C_{15}\left[\prod_{\delta=1}^{3} C_{\delta\delta}\right]\left[\prod_{\eta=4}^{6} C_{\eta\eta}^{2}\right]}{|C_{61}|^{8}} \tag{2.13}$$

$$\text{subject to: } \mathbf{K}_{\text{gripper}}\mathbf{u}_{\text{gripper}} = \mathbf{f}_{\text{gripper}},$$

The numerator of the fitness function is composed by the product of prominent off-axis compliances that will be minimized by the optimization process. The rotary parasitic compliances, i.e. C_{44}, C_{55} and C_{66}, are regarded as more important for robust gripper operations, thus they have a higher exponential to represent a greater emphasis. The denominator of the fitness function aims to maximize the actuating compliance, C_{61}, and its exponent is raised to eight because there are eight different components in the numerator. The governing FEA equation for evaluating the stiffness characteristics of the μ-gripper is represented by the equality constraint. This optimization process is conducted with a population of 100 chromosomes and it converges within 50 generations as shown in Fig. 2.8. The optimization process took 4-5 hours and the solution is shown in Fig. 2.9(b). Thanks to the nature of the mechanism-based approach, the obtained solution did not have any 'grey' or disconnected solid elements. Furthermore, it is interesting to note that the topology has evolved from the six-bar seeds into a non-uniform thickness beam; this implies that the search space of the mechanism-based approach is not limited by the topologies of the initial seeds. Finally, by smoothening the jagged edges to remove the stress concentration, we obtained the final design of the μ-gripper (Fig. 2.9(c)).

The performance of the gripper is evaluated by comparing it with a thin-beam design that is developed via human intuition (Fig. 2.9(d)). The thickness of the thin-beam was adjusted to match the actuating compliance with the gripper; this allows an easier comparison between these two designs. The compliance matrices of the optimized design, $\mathbf{C}_{\text{Opt},6\times6}$, and the intuitively-designed beam-type μ-gripper, $\mathbf{C}_{\text{Int},6\times6}$, are evaluated via FEA to be:

$$\mathbf{C}_{\text{Opt},6\times6} = \begin{bmatrix} 19.3 & & & & & \\ 0 & 3.57\times10^{-2} & & & \textbf{SYM} & \\ 0 & 0 & 7.81 & & & \\ 0 & -530 & 8.06\times10^{3} & 1.17\times10^{7} & & \\ 900 & 0 & 0 & 0 & 1.87\times10^{7} & \\ -1.71\times10^{4} & 0 & 0 & 0 & 0 & 1.77\times10^{7} \end{bmatrix}$$

$$\mathbf{C}_{\text{Int},6\times6} = \begin{bmatrix} 14.0 & & & & & \\ 0 & 6.22\times10^{-2} & & & \textbf{SYM} & \\ 0 & 0 & 9.11 & & & \\ 0 & -941 & 1.12\times10^{4} & 2.00\times10^{7} & & \\ 1.72\times10^{3} & 0 & 0 & 0 & 3.55\times10^{7} & \\ -1.71\times10^{4} & 0 & 0 & 0 & 0 & 3.04\times10^{7} \end{bmatrix} \tag{2.14}$$

A superior design is one that has more components with lower magnitude in their compliance matrix as this implies that it can better reject disturbances. Based on the compliance matrices for both designs, it is apparent that the optimal structure have better stiffness characteristics as eight out of nine components are better(smaller). Some of these components are even approximately two times better - demonstrating the effectiveness of the mechanism-based approach.

2.2.1 Experimental results for the μ-gripper

In order to evaluate the accuracy of the FEA comparison in Eq. (2.14), an up-scale prototype had been constructed as shown in Fig. 2.10(a). We had selected a larger prototype because it would be easier to measure its deflections and input forces experimentally. As the accuracy of the FEA will not be affected by the size of the prototype, this implies that if the compliances of

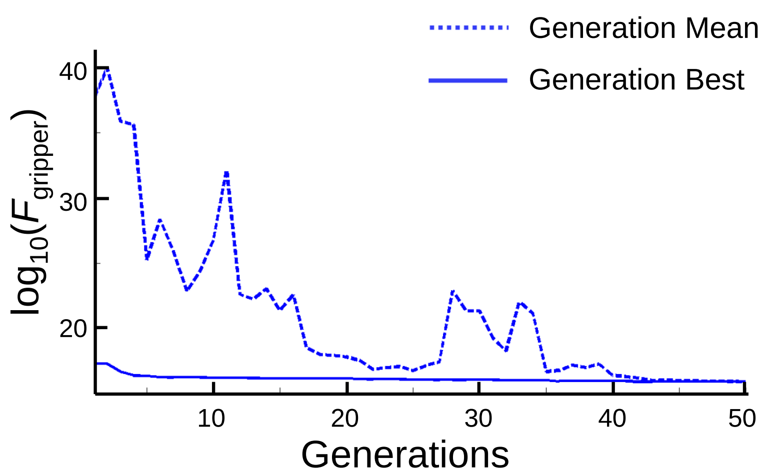

Figure 2.8: The convergence plot for the μ-gripper. The optimization process is shown to converge as the fitness value for the generation mean and generation best converges to one another eventually.

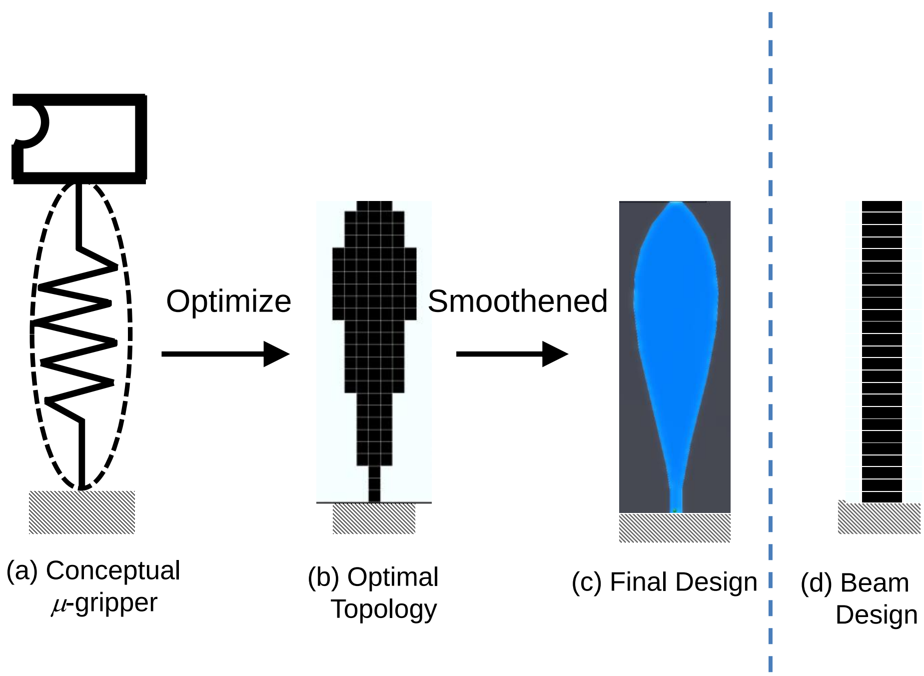

Figure 2.9: A comparison between the optimized gripper with an human-intuitively created beam design. (b) is the optimized gripper. (c) smoothen the sharp corners of (b) to prevent stress concentration. (d) is the human-intuitively created beam design.

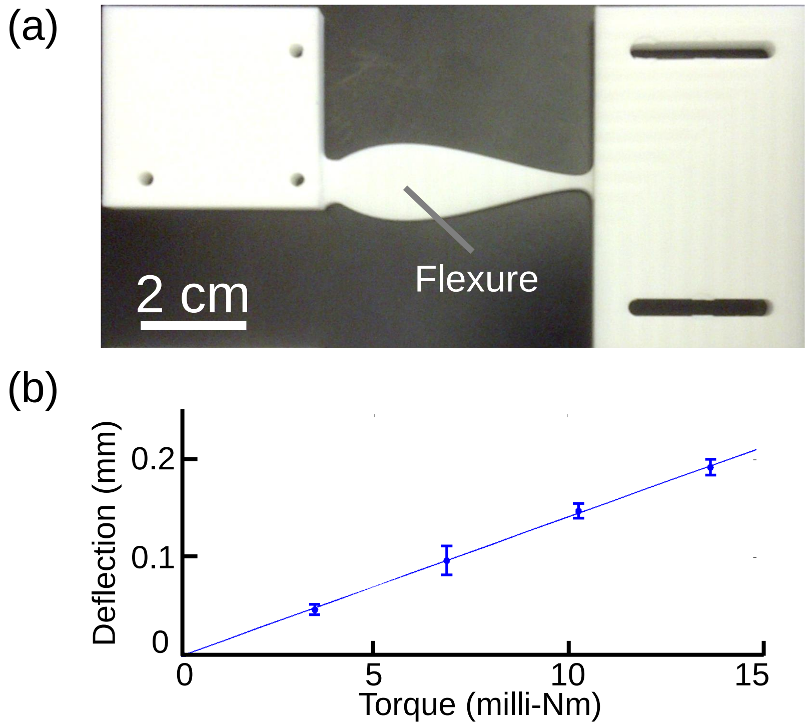

Figure 2.10: The experimental result for the large-scale prototype shown in (a). (b) Experimental data for the actuating compliance of the prototype is shown as an example. The slope of the plot represents the experimental actuating compliance is -14.1$\times 10^{-3}$ m/(Nm) and it agrees with the FEA prediction of -16.1$\times 10^{-3}$ m/(Nm) within 12% deviation. Each datapoint represents the mean from three measurements, and error bars indicate standard deviation.

the up-scale prototype can match its FEA prediction, the FEA comparison for the μ-grippers' stiffness characteristics will be valid too.

The up-scale prototype was constructed with acetal, and its Young's modulus and Poisson ratio were estimated to be 3.1 GPa and 0.45, respectively. Precise force loading was applied on the prototype by hanging calibrated weights, and the induced deflections were measured by a dial gauge indicator. The compliances of the prototype were determined experimentally from the slope of their load against deflection plots. By changing the orientation of the prototype and the location of the dial, different compliances could be evaluated. Eight compliances, C_{11}, C_{22}, C_{33}, C_{44}, C_{55}, C_{66}, C_{61} and C_{43} had been validated. For all the evaluated compliances, three sets of data were collected and each set had 5 data points. As an example, Fig. 2.10(b) showed the deflection plot for the prototype's actuating compliance, and the complete experimental data and simulation results were shown in the following two equations:

$$\mathbf{C}_{\text{upscale, experiments, } 6\times 6} = \begin{bmatrix} 0.98\times 10^{-3} & & & & & \\ 0 & 1.50\times 10^{-6} & & & & \\ 0 & 0 & 0.434\times 10^{-3} & & & \\ 0 & 0 & 8.56\times 10^{-3} & 0.27 & & \\ 0 & 0 & 0 & 0 & 0.402 & \\ -16.1\times 10^{-3} & 0 & 0 & 0 & 0 & 0.35 \end{bmatrix} \tag{2.15}$$

$$\mathbf{C}_{\text{upscale, FEA, } 6\times 6} = \begin{bmatrix} 0.834\times 10^{-3} & & & & & \\ 0 & 1.85\times 10^{-6} & & & & \\ 0 & 0 & 0.471\times 10^{-3} & & & \\ 0 & 0 & 8.40\times 10^{-3} & 0.335 & & \\ 0 & 0 & 0 & 0 & 0.343 & \\ -14.1\times 10^{-3} & 0 & 0 & 0 & 0 & 0.423 \end{bmatrix}. \tag{2.16}$$

Based on the experimental results, the maximum deviation between the experiments and FEA predictions was 20%, and the mean deviation was computed to be 15%. The small deviation between the experiments and predictions for the up-scale prototype suggested that the comparison made in Eq. (2.14) for the at-scale μ-gripper was accurate as well - suggesting the superior stiffness characteristics of the optimal flexural mechanism over the thin-beam design.

While we did not evaluate the stiffness characteristics of the at-scale grippers, we had constructed these grippers with photolithography and replica molding. To fabricate μ-grippers from soft elastomer with included magnetic particles, a replica molding technique was used. The process included shape definition by photolithography, replica molding to achieve flexible elas-

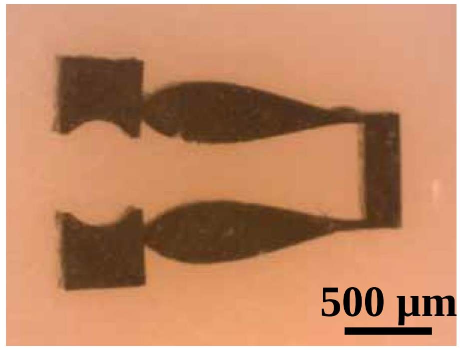

Figure 2.11: At-scale fabricated μ-grippers with optimized flexure designs.

tomer gripper shapes, and a magnetization process. The μ-grippers were made from a flexible elastomer material (ST-1087, BJB Enterprises) to allow for larger deflections given the same magnetic actuation. The design required that each gripper tip be magnetized in opposite directions, which is accomplished at the magnetization step by deforming the μ-gripper arms 90° prior to magnetization. The manufactured μ-gripper was shown in Fig. 2.11.

The fabricated μ-gripper was magnetized and actuated in a magnetic coil system. The gripper could move on a planar surface by using a rolling locomotion, and it could create gripping motions when it was subjected to a magnitude fields of 10 mT. Some snapshots during the actuation are shown in Fig. 2.12 .

2.3 Design and Experiments of a 3-legged-Prismatic-Prismatic-Revolute Flexure-based Parallel Mechanism

This section further investigates the effectiveness of the proposed topological optimization algorithm - the mechanism-based approach. In particular, the algorithm will create compliant joints that can be assembled into a $X - Y - \theta_z$ FPM. The effectiveness of the algorithm will be evaluated by comparing the synthesized FPM's stiffness characteristics with a similar FPM that is

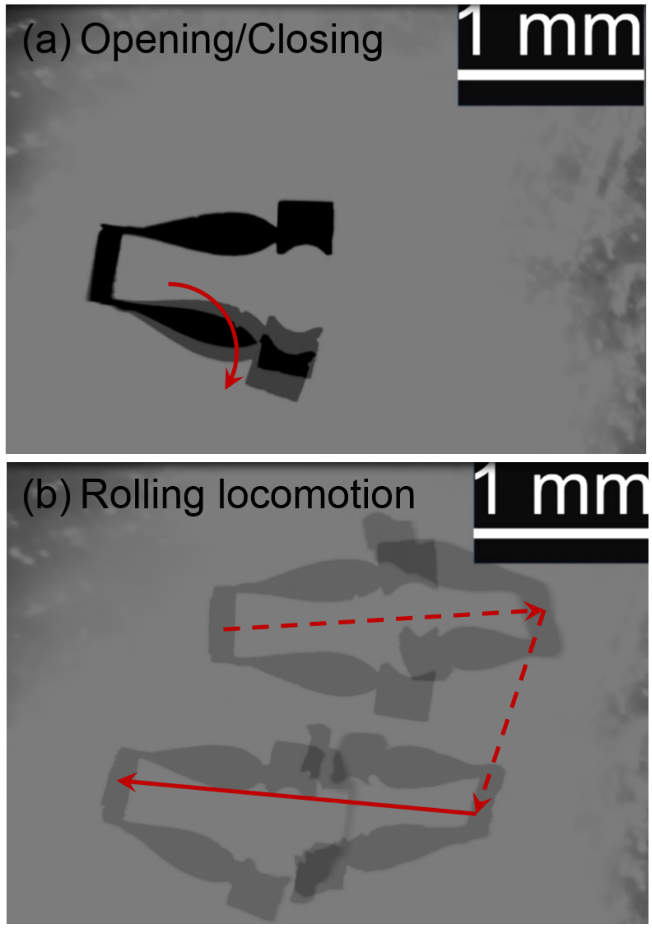

Figure 2.12: At-scale fabricated μ-grippers (a) opening and closing its grippers and (b) rolling on the substrate.

composed by traditional complinat joints.

2.3.1 Overall Configuration

Based on the rigid-body-replacement method, there are three possible parallel-kinematic configurations that can realize a $X - Y - \theta_z$ FPM. The three configurations are the 3-legged revolute-revolute-revolute (3RRR), the 3-legged prismatic-revolute-revolute (3PRR), and the 3-legged prismatic-prismatic-revolute (3PPR). We will select the 3PPR configuration because compliant prismatic joints are generally more deterministic than the compliant revolute joints. The schematic of the 3PPR architecture is shown in Fig. 2.13 where the end-effector is articulated by three identical parallel sub-chains that are arranged in a rotary symmetrical manner. Each sub-chain has an active prismatic joint ($\underline{\text{P}}$) that is serially connected to a passive prismatic-revolute (PR) joint. The active $\underline{\text{P}}$ joint is placed nearer to the fixed base to prevent the weight of the actuator from contributing to the overall moving masses of the FPM. Based on this configuration, the relationship between the end-effector's output motion, x, y, and θ_z, and the displacement of the active prismatic joints, p_1, p_2, and p_3, can be obtained via traditional inverse kinematics analysis:

$$\begin{bmatrix} p_1 \\ p_2 \\ p_3 \end{bmatrix} = \begin{bmatrix} \frac{1}{2} & \frac{\sqrt{3}}{2} & r \\ -1 & 0 & r \\ \frac{1}{2} & -\frac{\sqrt{3}}{2} & r \end{bmatrix} \begin{bmatrix} x \\ y \\ \theta_z \end{bmatrix}, \tag{2.17}$$

where r is the distance between the end-effector and the PR joint's loading point. Note that p_j refers to the displacement of the active joint in sub-chain j.

2.3.2 Synthesizing the compliant PR and $\underline{\text{P}}$ joints

Based on the selected 3$\underline{\text{P}}$PR FPM configuration, there are two types of compliant joints - the PR and P joints. Thus, in this section, we will show that they can be synthesized via the mechanism-based approach.

Synthesis of a PR compliant joint

An ideal PR compliant joint can provide a large x-axis translation and also a large z-axis rotation when its loading point is subjected to a F_x force and a M_z torque, respectively. Mathematically, this implies that its actuating compliances, C_{11} and C_{66}, should be maximized while other off-axis components in the $\mathbf{C}_{\text{PR},6\times 6}$ must be minimized to achieve optimal stiffness properties. As the PR joint has 2-degrees-of-freedom (2 actuating compliances), we have selected a 5-bar linkage as the seed for the mechanism-based approach. The coupler point of the seed, which is also its loading point, is constrained to move along the top row elements while two fixed points were

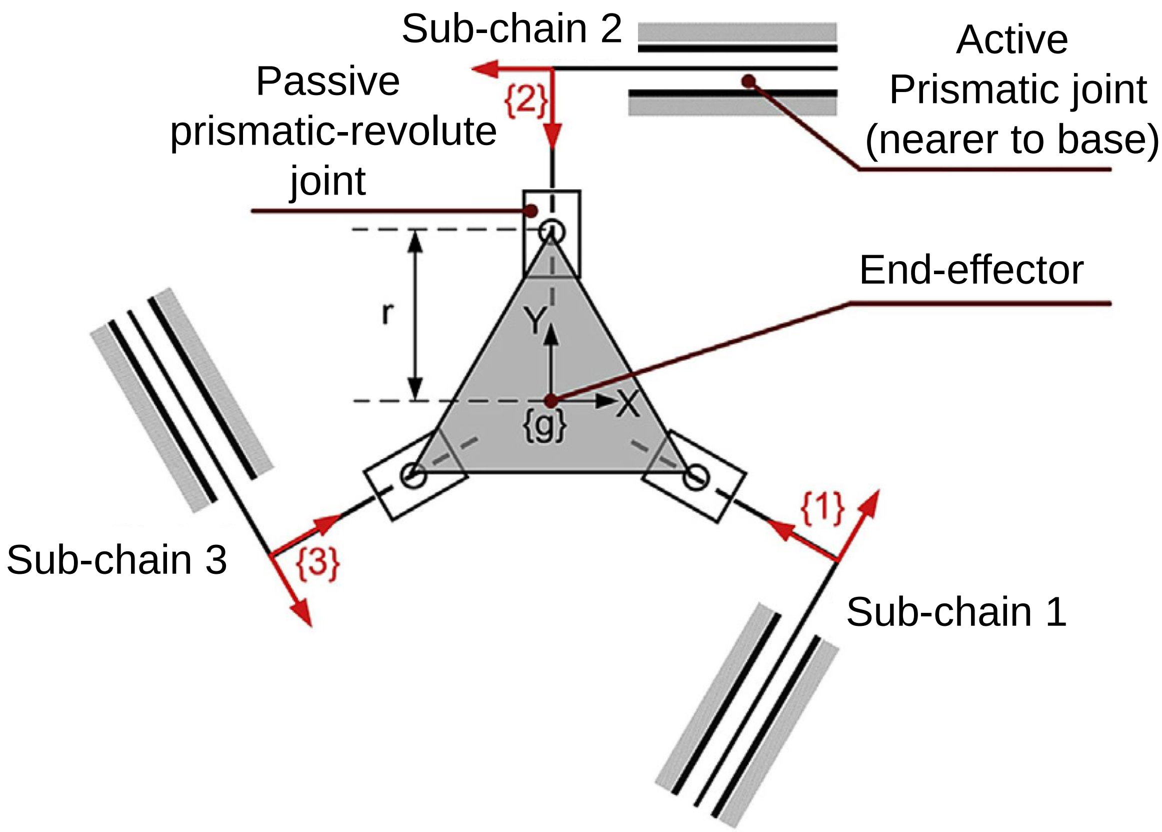

Figure 2.13: The selected overall configuration for the FPM: A 3$\underline{\text{P}}$PR configuration. The FPM has three symmetrical sub-chains that are arranged in a rotary symmetrical manner. Each sub-chain consists of an active $\underline{\text{P}}$ joint and a passive PR joint. The active joint is placed closer to the fixed base. The variable r represents the distance between the end-effector and the PR joint.

located at the base (Fig. 2.14(a)).

The synthesis of the PR compliant joint was broken down into two stages to reduce the computational time. The first stage was performed through a coarse mesh while the second stage will further refine the design with a fine mesh. In both stages, the design domain of the PR joint is constrained within a 50 mm $\times$ 20 mm $\times$ 10 mm volume, which is discretized into a mesh of 3-D 8-node bilinear finite elements. The utilized material is assumed to be aluminum, and its Young's Modulus and Poisson ratio are estimated to be 71 GPa and 0.33, respectively. Thus, the stiffness matrices in FEA format for one finite element, $\mathbf{K}_{\text{FE},i}$, and the overall structure of the PR joint, $\mathbf{K}_{\text{PR},n\times n}$, are given as:

$$\mathbf{K}_{\text{FE},i} = \iiint \mathbf{B}^{\text{T}}\mathbf{D}\mathbf{B}\ \mathrm{d}V, \quad \mathbf{K}_{\text{PR},n\times n} = \sum_{i=1}^{\text{all elements}} s_i \mathbf{K}_{\text{FE},i}, \tag{2.18}$$

where s_i represents the state of the i^{th} finite element in the design domain - s_i = 1 represents a solid element and $s_i = 10^{-6}$ represents a void element. To optimize the stiffness characteristics, we use the following fitness function for both stages:

$$\begin{aligned} &\text{minimize } F_{\text{pr}}(\mathbf{x}_{\text{PR}}) = \frac{\Pi_{\delta=2}^{6}\Pi_{\eta=1}^{\delta} C_{\delta\eta}}{[C_{11}]^{19}\,[C_{66}]^{19}}, \\ &\text{subject to: } \mathbf{K}_{\text{PR},n\times n}\mathbf{u}_{\text{PR},n\times 1} = \mathbf{f}_{\text{PR},n\times 1}. \end{aligned} \tag{2.19}$$

The numerator in the fitness function aims to minimize the off-axis compliance components while the denominator will maximize the actuating compliances. As there are 19 off-axis stiffness, the $C_{11}$and C_{66} components are raised to the exponential of 19. The vector $\mathbf{x}_{\text{PR}}$ represents the variables for the mechanism-based approach and the equality constraint represents the FEA governing equation.

By evolving 500 chromosomes via 100 generations, the initial 5-bar linkage gradually evolves into a 3-bar topology during the first stage of optimization Fig. 2.14(b). By refining the design domain in the second stage of optimization, the optimized PR compliant joint is obtained after evolving 200 chromosomes via 50 generations (Fig. 2.14c). The optimal PR joint resembles a non-uniform beam supported by an arch. To further reduce the magnitude of the non-diagonal off-axis compliances, we adopted a symmetrical design for the final compliant PR joint (Fig. 2.14(d)). Note that both optimization processes have shown to converge as the mean fitness values in the convergence plots managed to converge with the best fitness values (Fig. 2.15).

The obtained stiffness matrix of the compliant PR joint (inverse of $\mathbf{C}_{\text{PR, }6\times 6}$) is given as:

$$\mathbf{K}_{\text{PR},6\times 6} = \begin{bmatrix} 1544 & & & & & \\ 0 & 1.16\times 10^{7} & & & \textbf{SYM} & \\ 0 & 0 & 4.89\times 10^{5} & & & \\ 0 & 2.63\times 10^{4} & 0 & 232 & & \\ 0 & 0 & 0 & 0 & 1.32 & \\ 0 & 0 & 0 & 0 & 0 & 1.10 \end{bmatrix}. \tag{2.20}$$

Synthesis of P̲ joint

Similar to the synthesis of the PR joint, the active P̲ compliant joint is synthesized via two optimization stages. In both stages, the Young's Modulus, Poisson ratio and utilized finite elements are similar to those of the PR compliant joint. The width of the design domain, however, is changed to 25 mm. As the active P̲ compliant joint needs to deliver a large $x-$axis translation motion when its loading point is subjected to a F_x force, its actuating compliance, C_{11}, must be high while the rest of the components in the $\mathbf{C}_{\underline{P},6\times 6}$ must be low. Thus, we use the following fitness function to optimize the compliant P̲ joint's stiffness characteristics:

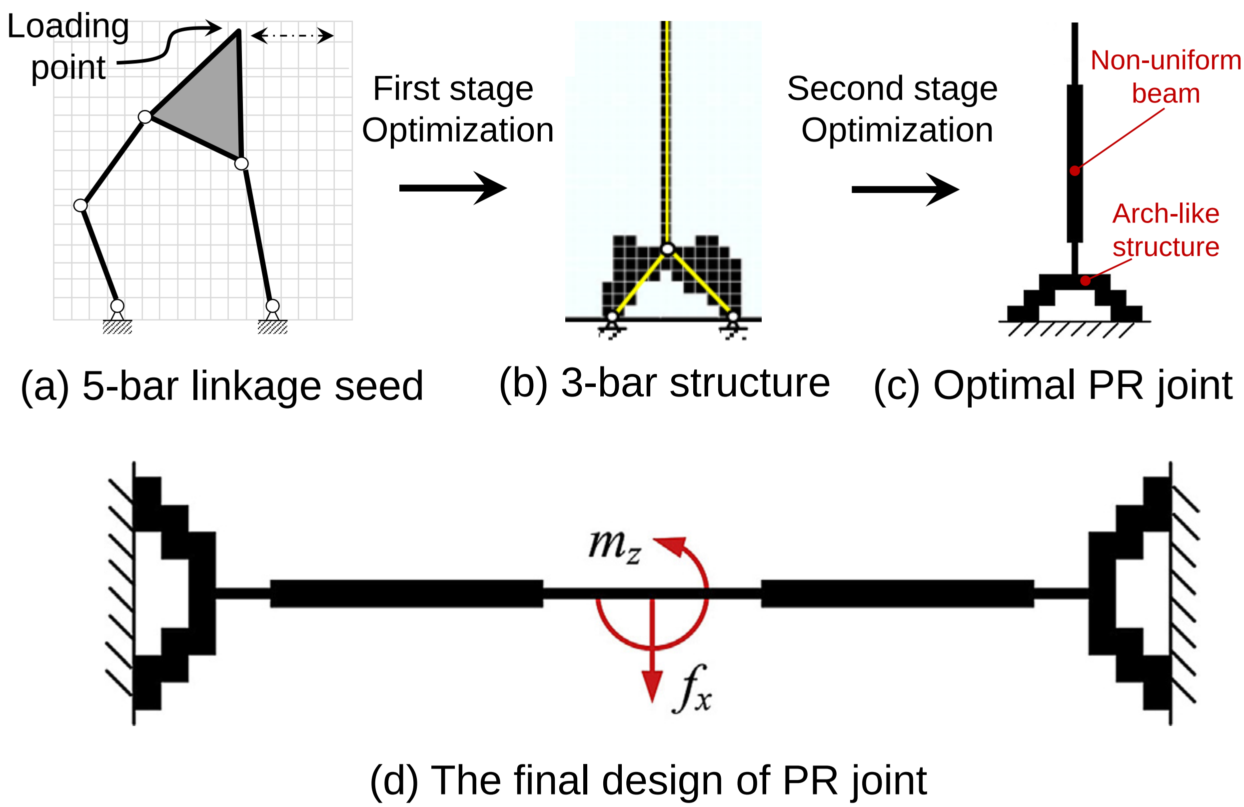

Figure 2.14: The synthesis process for the PR compliant joint. (a) A 5-bar linkage seed is used for the mechanism-based approach. (b) The topology of the PR joint has evolved from the 5-bar linkage into a 3-bar linkage after the first stage of optimization. Two link lengths has been reduced to zero, changing the topology of the seed. (c) The design has been further refined via the second stage optimization. The solution resembles a non-uniform beam, which is supported by an arch. (d) The final design of the PR joint. The joint is made symmetrical to further reduce the non-diagonal off-axis compliances.

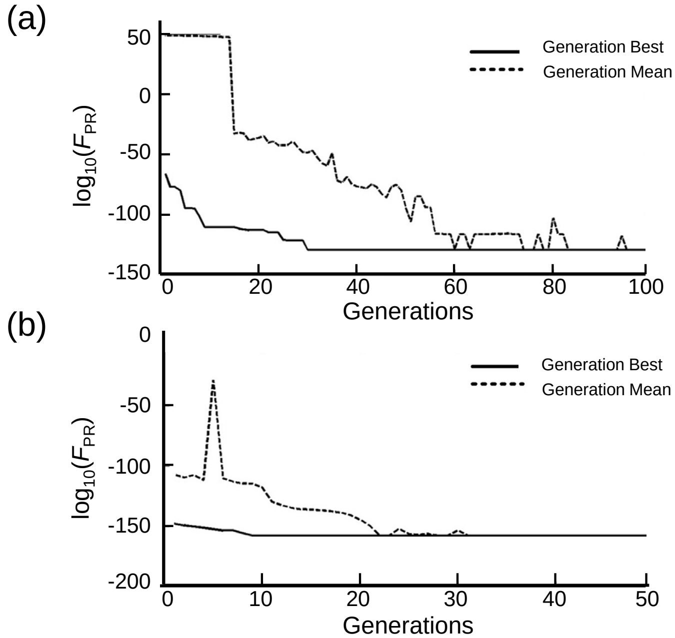

Figure 2.15: The convergence plot for the two stages of optimization processes for the compliant PR joint. (a) and (b) represent the convergence plots for the first and second stages of optimization, respectively. The optimization processes were shown to converge as both plots show that their mean and best fitness values managed to converge.

$$\begin{aligned} &\text{minimize } F_{\mathrm{p}}(\mathbf{x}_p) = \frac{\Pi_{\delta=2}^{6}\Pi_{\eta=1}^{\delta} C_{\delta\eta}}{[C_{11}]^{20}} \\ &\text{subject to: } \mathbf{K}_{\mathrm{P},n\times n}\mathbf{u}_{\mathrm{P},n\times 1} = \mathbf{f}_{\mathrm{P},n\times 1}. \end{aligned} \tag{2.21}$$

The actuating compliance, C_{11}, has an exponent of 20 because there are 20 off-axis stiffness components. The vector $\mathbf{x}_{\mathrm{P}}$ represents the variables while the equality constraint represents the FEA governing equation. As the compliant P has only 1-degree-of-freedom, we will use a 4-bar linkage as the seed for the mechanism-based approach (Fig. 2.16(a)). The coupler point of the seed, which is also its loading point, is located at the top row's central element. The seed is fixed by two points that are located at the bottom row. The first stage of optimization was carried out by evolving a population of 400 chromosomes via 100 generations. From Fig. 2.16(b), the solution still has a 4-bar topology but the limbs had become parallel with one another. Subsequently, the second stage of optimization further refines the solution with a finer mesh. Consequently, the optimal $\underline{\mathrm{P}}$ compliant joint is obtained after the G.A. solver has evolved a population of 200 chromosomes via 50 generations. As shown in Fig. 2.16(c),the optimal $\underline{\mathrm{P}}$ compliant joint resembles a tapered-shape rigid-link supported by two thin beams. The optimization processes have converged and their convergence plots are plotted in Fig. 2.17.

The obtained stiffness matrix of the compliant $\underline{\mathrm{P}}$ joint (inverse of $\mathbf{C}_{\underline{\mathrm{P}},\,6\times6}$) is given as:

$$\mathbf{K}_{\mathrm{P},6\times6} = \begin{bmatrix} 1338 & & & & & \\ 0 & 9.72\times10^{6} & & & \textbf{SYM} & \\ 0 & 5.94\times10^{5} & 3.92\times10^{5} & & & \\ 0 & 2.84\times10^{4} & -6205 & 350 & & \\ 0 & 0 & 0 & 0 & 53.6 & \\ 0 & 0 & 0 & 0 & 0 & 90.3 \end{bmatrix}. \quad (2.22)$$

Experimental results

As the effectiveness of the optimization processes depends heavily on the accuracy of the FEA, we would experimentally evaluate the actuating stiffness characteristics of the compliant joints here. In particular, the translational compliances for both the compliant $\underline{\mathrm{P}}$ and PR joints would be characterized. Likewise, the actuating rotational compliance of the PR joint would also be evaluated. Note that as these experiments were only used to evaluate the accuracy of the FEA, we did not smoothen the sharp edges of the joints yet.

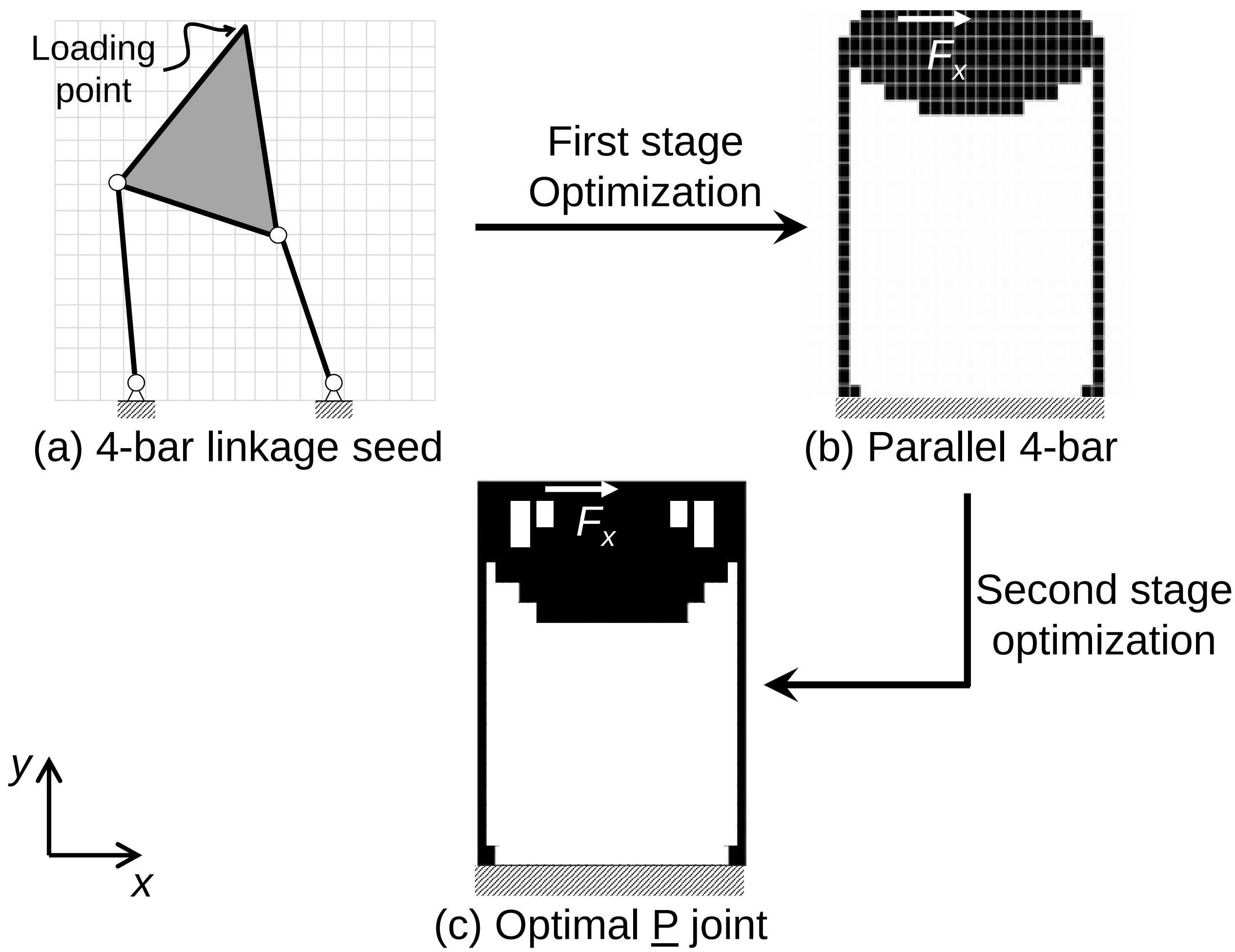

Figure 2.16: The synthesis process for the compliant P joint. (a) A 4-bar linkage seed is used for the mechanism-based approach. (b) The solution obtained after the first stage of optimization. (c) The optimized design after the second stage optimization.

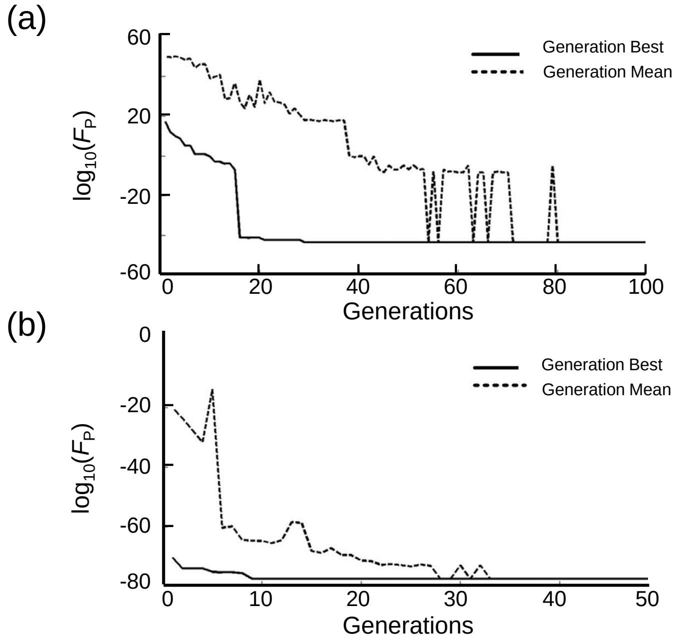

Figure 2.17: The convergence plot for the two stages of optimization processes for the active compliant P̲ joint. (a) and (b) represent the convergence plots for the first and second stages of optimization, respectively. The optimization processes were shown to converge as both plots show that their mean and best fitness values managed to converge.

Evaluation for translational compliance of compliant joints

In these experiments, we would evaluate the translational compliance of the joints. The fixed points of the compliant joints were constrained by a fixed plate and their loading points were mounted by an linear actuator. By varying the input current to the actuator, different magnitudes of force could be applied to the joints. Upon loading, the applied force and linear deflections of the joints would be measured by a force sensor and a linear probe, respectively (see Fig. 2.18 for the experimental setup). Note that the force sensor was located between the joints and the actuator.

For both experiments, three sets of data were collected; each set consisted of 10 data points. The compiled data for the PR and P̲ joints' experiments were shown via the scatter plots that had a corresponding best fit line in Fig. 2.19(a) and (b), respectively. Based on the gradient of the best fit lines, the PR and P̲ joints had a compliance of $6.00\times\ 10^{-4}$ m/N and $7.04\times\ 10^{-4}$ m/N,

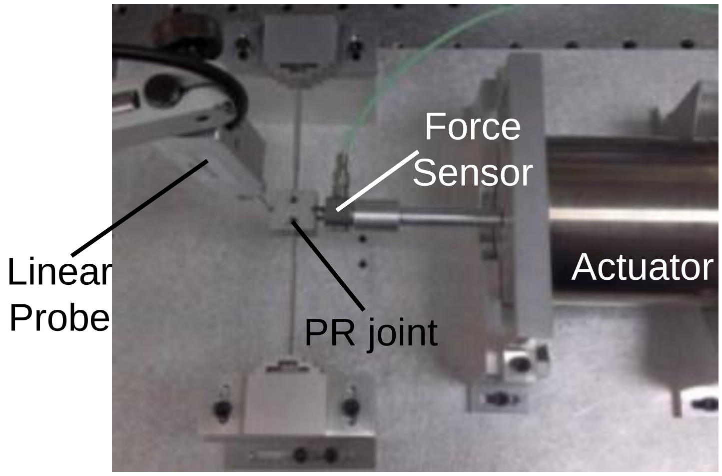

Figure 2.18: The experimental setup to evaluate the translational compliance of the joints. The setup for the compliant PR joint was used as an example. The joint would produce a translational deflection when the actuator supplied an input force. The deflection and magnitude of the input force would be measured by the linear probe and the force sensor, respectively.

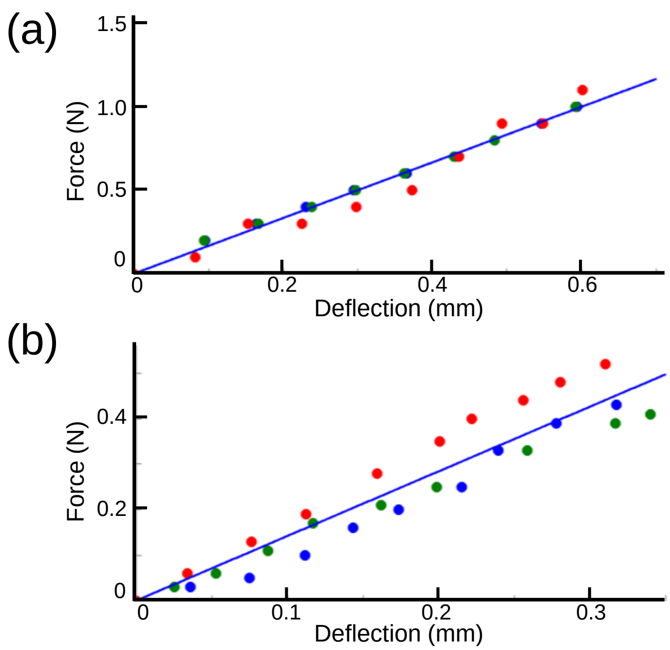

Figure 2.19: The experimental data for evaluating the translational compliance of the joints. (a) Experimental results for PR joint's linear deflection where the input force was plotted against the deflection. The slope of the best fit line was 1.66 N/mm. (b) Experimental results for P joint's linear deflection where the input force was plotted against the deflection. The slope of the best fit line is 1.42 N/mm.

respectively. These experimental results agreed with the FEA simulation where the predicted compliance for the PR and $\underline{\text{P}}$ joints were 6.68×10^{-4} m/N and 7.47×10^{-4} m/N (based on Eq. (2.20) and Eq. (2.22)), respectively. The deviation between the FEA predictions and experimental results for the PR and $\underline{\text{P}}$ joints were 10% and 6% respectively and they may be caused by manufacturing errors. However, these deviations were negligible and this suggested that the FEA predictions had high credibility for the translational compliance.

Evaluation for angular compliance of PR joint The actuating angular compliance of the PR joint was investigated with these experiments. Similar to the previous experiments, the fixed points of the PR joint were constrained by a fixed plate. In order to apply an external torque to the loading point, we used a stepper motor to replace the linear actuator (Fig. 2.20). Different magnitudes of torques could be applied to the joint by varying the current supplied to the actuator. During the experiments, the linear deflections of a specific point (defined as point A) and the applied torque would be measured by using a linear probe and a torque sensor, respectively. By dividing point A's linear deflection with a prior known moment arm (20 mm), the angular deflection could be obtained.

In these experiments, three sets of 10 data points had been collected. The compiled data was represented by the scatter plot, and a best fit line had been plotted (Fig. 2.21). Based on the gradient of the best fit line, the angular compliance of the PR joint was evaluated to be 0.834 rad/(Nm) and this agreed with the FEA prediction of 0.909 rad/(Nm) (based on Eq. (2.20)). The deviation between the experiments and FEA simulation was only 9%, and could simply be due to manufacturing errors. However, since the deviation was small, this suggested that the FEA accuracy had relatively high credibility.

2.3.3 Assembly of the 3$\underline{\text{P}}$PR FPM

The optimal compliant joints obtained from the previous section will be assembled into a 3$\underline{\text{P}}$PR FPM as shown in Fig. 2.22. For practical issues, we have smoothened out the sharp edges of

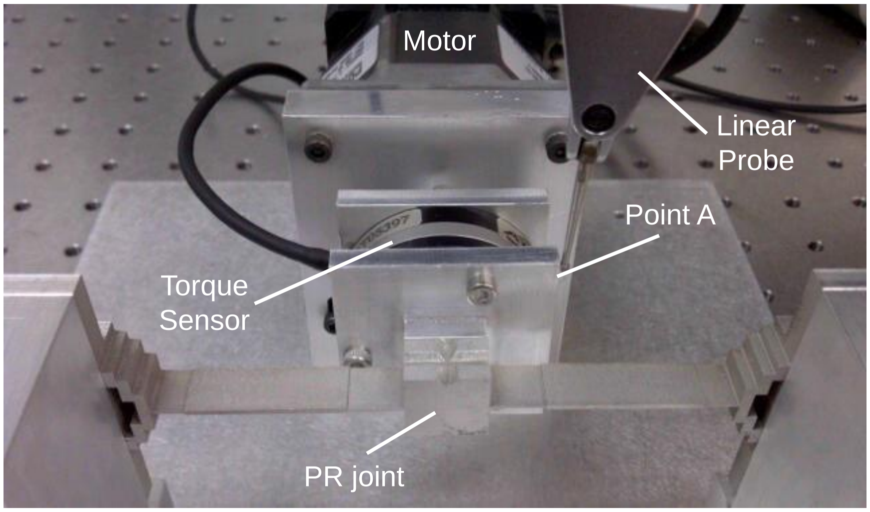

Figure 2.20: The experimental setup to evaluate the rotational compliance of the PR joint. The joint would produce a rotational deflection when the actuator supplied an input torque. The linear deflection and magnitude of the input torque would be measured by the linear probe and the force sensor, respectively. By dividing the linear deflection with a prior known moment arm, the angular deflection could be determined.

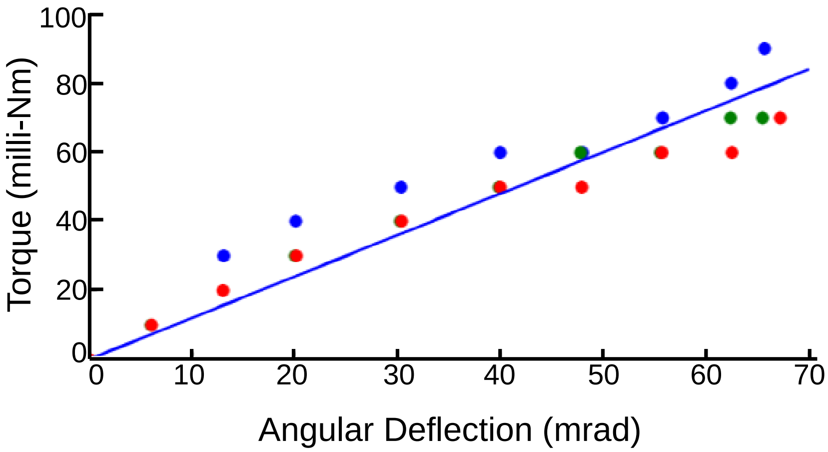

Figure 2.21: Experimental results for PR joint's angular deflection where the input torque was plotted against the angular deflection. The slope of the best fit line was 1.19 N m/rad.

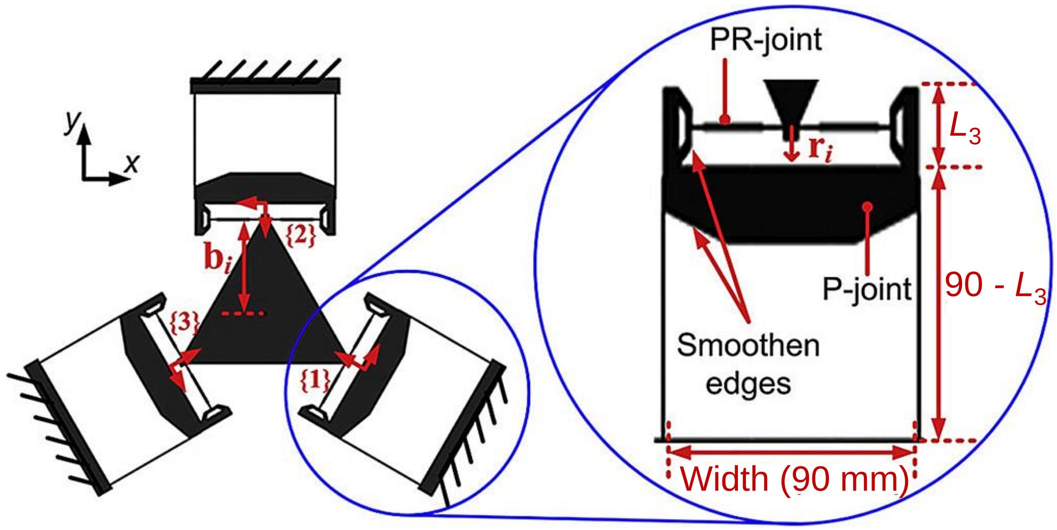

Figure 2.22: The schematic drawing for the 3<u>P</u>PR FPM. The values L_3 and r_j are shown.

the joints to prevent stress concentration. In order to achieve millimeters stroke range, we have selected electromagnetic voice-coil (VC) as our linear actuators. It is estimated that each VC actuator needs to generate a continuous force of at least 30 N, and the required dimensions of such a VC actuator is estimated to be at least $\varnothing$ 60 mm $\times$ 60 mm. Thus, the dimensions of each sub-chain has been assigned to a design domain of 90 mm $\times$ 90 mm so that it can encase a VC actuator. The proposed FPM will be monolithically cut from a SUS316 stainless steel workpiece (19 mm thickness), and the Young's Modulus and Poisson ratio of the material are estimated to be 200 GPa and 0.33, respectively.

To optimize the stiffness characteristics for the end-effector, a size optimization is used to determine the optimal space distribution between the compliant joints. This is because by increasing L_3, it will increase the off-axis stiffness of the PR joints but will also decrease the actuating compliance of the active compliant <u>P</u> joint (refer to Fig. 2.22). In order to retain the actuating compliance of these joints, this optimization does not alter the thickness of the beams.

Based on the configuration shown in 2.13, the stiffness matrix of each compliant joint obtained via the proposed topology optimization technique are expressed in terms of their local sub-chain frame. These sub-chain frames are illustrated in Fig. 2.13 where $\{1\}$, $\{2\}$, and $\{3\}$ have a z-axis rotation angle of $[\phi_1 \;\; \phi_2 \;\; \phi_3] = [\pi/3 \;\; \pi \;\; \pi/3]$ with respect to the global frame {g}, respectively. Based on the classical mechanism stiffness modeling approach [14,22], the compliance matrix of sub-chain j, $\mathbf{C}_{\text{SC},j,6\times6}$, at the PR joint loading point can be determined by:

$$\mathbf{C}_{\text{SC},j,6\times6} = \mathbf{C}_{\text{PR},j,6\times6} + \mathbf{J}_j \left[\mathbf{C}_{\text{P},j,6\times6}\right] \mathbf{J}_j^{\text{T}}, \text{where} \quad \mathbf{J}_j = \begin{bmatrix} \mathbf{I}_{3\times3} & \hat{\mathbf{r}}_j \\ \mathbf{0}_{3\times3} & \mathbf{I}_{3\times3} \end{bmatrix}. \tag{2.23}$$

The matrix $\mathbf{J}_j$ refers to the Jacobian matrix, and the matrices $\mathbf{I}_{3\times3}$, $\mathbf{0}_{3\times3}$ and $\hat{\mathbf{r}}_j$ represent the identity, zero and the skew-symmetry matrices of the position vector, $\mathbf{r}_j$, respectively. Note that $\mathbf{r}_j$ represents the displacement vector from the loading point of sub-chain j to its compliant P joint's loading point (Fig. 2.22). After the chains' stiffness matrices are identified, the stiffness matrix of the end-effector, $\mathbf{K}_{\text{ee},6\times6}$, can be computed:

$$\mathbf{K}_{\text{ee},6\times6} = \sum_{j=1}^{3} \mathbf{Ad}_{\mathbf{T},j}^{-\text{T}} \left[\mathbf{C}_{\text{SC},j,6\times6}\right]^{-1} \mathbf{Ad}_{\mathbf{T},j}^{-1}, \quad \text{where} \;\; \mathbf{Ad}_{\mathbf{T},j} = \begin{bmatrix} \mathbf{R}_z(\phi(j)) & \hat{\mathbf{b}}_j \mathbf{R}_z(\phi(j)) \\ \mathbf{0}_{3\times3} & \mathbf{R}_z(\phi(j)) \end{bmatrix}. \tag{2.24}$$

The matrix $\mathbf{Ad}_{\mathbf{T},j}$ refers to the adjoint matrix, which consists of a rotational matrix $\mathbf{R}_z$ and a skew-symmetry matrix $\hat{\mathbf{b}}_j$ that represents the displacement vector from the end-effector to the loading point of the j^{th} sub-chain (Fig. 2.22). As the main objective is to optimize the stiffness ratio of the proposed FPM, i.e. maximizing off-axis diagonal stiffness while minimizing the actuating stiffness in $\mathbf{K}_{ee,6\times6}$, the fitness function becomes

$$\text{minimize } F_{\text{ee}}(L_3) = \frac{K_{xx} K_{yy} K_{\theta z\,\theta z}}{K_{zz} K_{\theta x\,\theta x} K_{\theta y\,\theta y}} \tag{2.25}$$

After using G.A to evolve a population of 10 chromosomes via 10 generations, the optimal

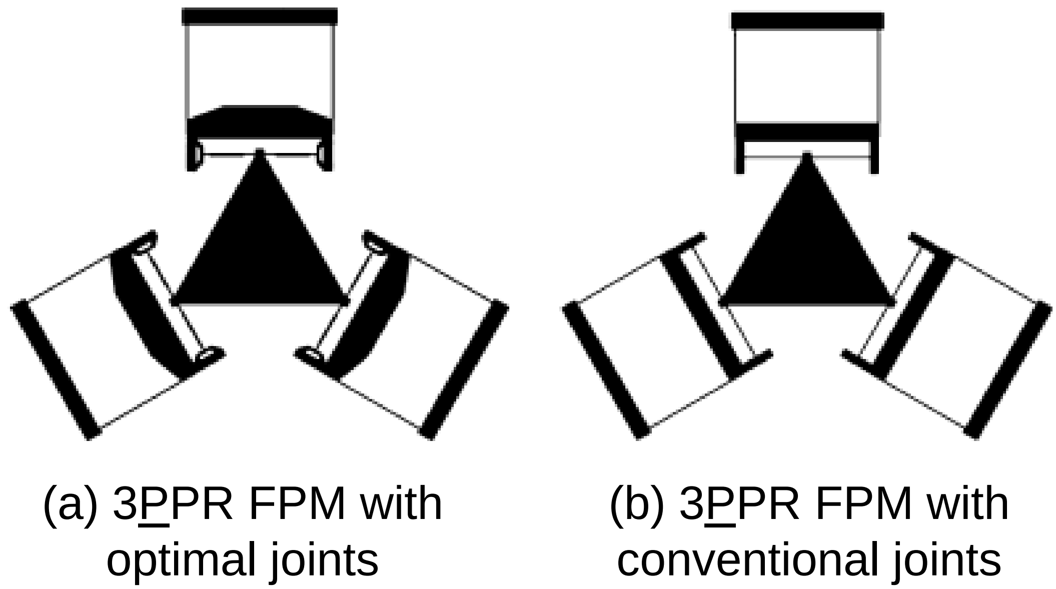

Figure 2.23: 3PPR FPMs articulated by compliant joints with (a) optimized topologies versus and (b) conventional topologies.

solution of L_3 was found to be 20 mm. The final stiffness matrix of the optimized FPM, $\mathbf{K}_{\text{opt, ee}}$, is given as:

$$\mathbf{K}_{\text{opt,ee},6\times6} = \begin{bmatrix} 2.82\times10^4 & & & & & \\ 0 & 2.82\times10^4 & & & \textbf{SYM} & \\ 0 & 0 & 8.93\times10^5 & & & \\ 0 & -250 & 0 & 2.46\times10^3 & & \\ 250 & 0 & 0 & 0 & 2.46\times10^3 & \\ 0 & 0 & 0 & 0 & 0 & 41.4 \end{bmatrix}. \tag{2.26}$$

Discussion

In comparison with the stiffness ratios obtained in the literature (0.5-50), the optimized FPM's translational and rotational stiffness ratio are considered high as they are computed to be $\frac{K_{zz}}{K_{xx}} =$

$\frac{K_{zz}}{K_{yy}} = \frac{8.93\times10^5}{2.82\times10^4} = 32$ and $\frac{K_{\theta_x\theta_x}}{K_{\theta_z\theta_z}} = \frac{K_{\theta_y\theta_y}}{K_{\theta_z\theta_z}} = \frac{2.46\times10^3}{41.4} = 60$, respectively. However, as we specifically like to compare the effectiveness of the synthesized compliant joints compared to traditional compliant joints, we have created a similar 3$\underline{\text{P}}$PR FPM that is composed by compliant joints with traditional topologies (Fig. 2.23a). Termed as the conventional FPM (Fig. 2.23b), its compliant PR joint is a cantilever beam that has both ends fixed to a conventional compliant $\underline{\text{P}}$ joint. The design of this stage uses the same optimal space distribution for the compliant $\underline{\text{P}}$ and PR joints. Instead of making a physical prototype for the conventional FPM, it is more economical to conduct the comparison via FEA. To have a fairer comparison, we have designed both FPMs to have one identical actuating compliance, and thus we have selected the compliance about the z-axis to be identical. For the conventional FPM, the flexure thickness of the traditional PR joints is selected as 0.6 mm to match the compliance about the z-axis of the optimized FPM.

By inverting the matrix in Eq. (2.26), the compliance matrix of the optimized FPM is:

$$\mathbf{C}_{\text{opt,ee},6\times6} = \begin{bmatrix} 3.55\times10^{-5} & & & & & \\ 0 & 3.55\times10^{-5} & & & \textbf{SYM} & \\ 0 & 0 & 1.12\times10^{-6} & & & \\ 0 & -3.61\times10^{-6} & 0 & 4.06\times10^{-4} & & \\ 3.61\times10^{-6} & 0 & 0 & 0 & 4.06\times10^{-4} & \\ 0 & 0 & 0 & 0 & 0 & 2.42\times10^{-2} \end{bmatrix}. \tag{2.27}$$

Using a similar FEA solver, the compliance matrix of the conventional FPM, $\mathbf{C}_{\text{con, ee}}$, is given as:

$$\mathbf{C}_{\text{con,ee},6\times 6} = \begin{bmatrix} 1.86\times 10^{-5} & & & & & \\ 0 & 1.86\times 10^{-5} & & & \textbf{SYM} & \\ 0 & 0 & 1.96\times 10^{-6} & & & \\ 0 & -7.1\times 10^{-6} & 0 & 5.41\times 10^{-4} & & \\ 7.1\times 10^{-6} & 0 & 0 & 0 & 5.41\times 10^{-4} & \\ 0 & 0 & 0 & 0 & 0 & 2.42\times 10^{-2} \end{bmatrix}. \tag{2.28}$$

Subsequently, the ratio between Eqs. (2.27) and (2.28) is

$$\mathbf{R}_{\text{comp}} = \mathbf{C}_{\text{opt,ee}} \odot \mathbf{C}_{\text{con,ee}} = \mathbf{diag}\begin{bmatrix} 1.91 & 1.91 & 0.57 & 0.75 & 0.75 & 1 \end{bmatrix}, \tag{2.29}$$

where $\odot$ represents the element-wise divisor operation. The ratio between $\mathbf{C}_{\text{opt, ee}}$ and $\mathbf{C}_{\text{con,ee}}$ in Eq. (2.29) have only considered the diagonal components as they are more critical. Here, the values of $R_{\text{comp},11}$ and $R_{\text{comp},22}$ are 1.91 (around 2) and this suggests that the actuating compliance of the optimized FPM is almost 2 times better than its conventional counterpart. Physically, this comparison suggests that the translational actuating compliance along the x- and y-axes of the optimized FPM are almost two times greater than the conventional FPM. Note that $R_{\text{comp},66}$ is 1 because both FPMs have the same actuating compliance about the z-axis. On the other hand, $R_{\text{comp},33}$, $R_{\text{comp},44}$ and $R_{\text{comp},55}$ are all less than 1. This comparison suggests that the off-axis stiffness along the translational z-axis of the optimized FPM is almost twice of the conventional FPM. It also suggests that the off-axis stiffness about the x- and y-axes of the optimized FPM are higher than the conventional FPM. In summary, this comparison shows that the stiffness characteristic of the optimized FPM is superior than a similar conventional FPM.

Experimental results

A prototype of the optimized FPM was developed as shown in Fig. 2.24a. To validate the accuracy of the predicted compliance matrix in Eq. (2.27), we would evaluate the actual stiffness characteristic of the prototype experimentally. In these experiments, the deflections of the FPM would be recorded by a high resolution 3-Dimensional (3D) scanner (GOM, model: ATOS Triple scan) as shown in Fig. 2.24b. The deflections of the FPM would be induced by the picomotors and these loadings were simultaneously recorded by a 6-axes Force/Torque (F/T) sensor (ATI, model: MINI40; resolution: 0.01N or Nm). The F/T sensor was mounted to the end-effector and covered by a precise cut square cover. The square cover served as a reference datum for the picomotors' loading points and scanning landmark for the 3D scanner. Note that the recorded deflections were images of the corresponding motions of the square cover induced by the external loadings.

The FPM's end-effector had three actuating compliances, i.e. C_{xx} - the translation displacement along the x-axis due to F_x loading, C_{yy} - the translation displacement along the y-axis due to F_y loading, and $C_{\theta_z\theta_z}$ - the angular displacement about the z-axis due to M_z loading. Figure 2.25(a) plots the experimental C_{xx}. From the collected data points,the gradient of the best fit line in Fig. 2.25(a) showed that this compliance was 3.8×10^5 m/N. As compared to the C_{xx} of $\mathbf{C}_{\text{opt, ee}}$, the deviation is only 8.6%. The experimental results for C_{yy} were also plotted in Fig. 2.25(b). Using the gradient of the best fit line, this compliance was estimated to be 3.48×10^5m/N. When compared to the C_{yy} of $\mathbf{C}_{\text{opt, ee}}$, the deviation is only 2%. Lastly, from Fig. 2.25(c), the $C_{\theta_z\theta_z}$ compliance was identified as 2.63×10^2 rad/Nm. By comparing with $C_{\theta_z\theta_z}$ of $\mathbf{C}_{\text{opt,ee}}$, the deviation is also small (8.7%).

The off-axis stiffness of the FPM were also investigated experimentally. Unfortunately, the rotational displacement about the x- and y-axes were too small to be recorded by the 3D scanner. Hence, we would only present the experimental data for the compliance along the z-axis - C_{zz}. These experimental results were plotted in Fig. 2.25(d) and the experimental C_{zz} was estimated to be 1.20×10^6 m/N. As compared to the C_{zz} of $\mathbf{C}_{\text{opt,ee}}$, the deviation was 7.1%. Although $C_{\theta_x\theta_x}$ and $C_{\theta_y\theta_y}$ could not be validated via this investigation, the collected experimental results and various comparisons with theoretical predictions were sufficient to suggest that the predicted

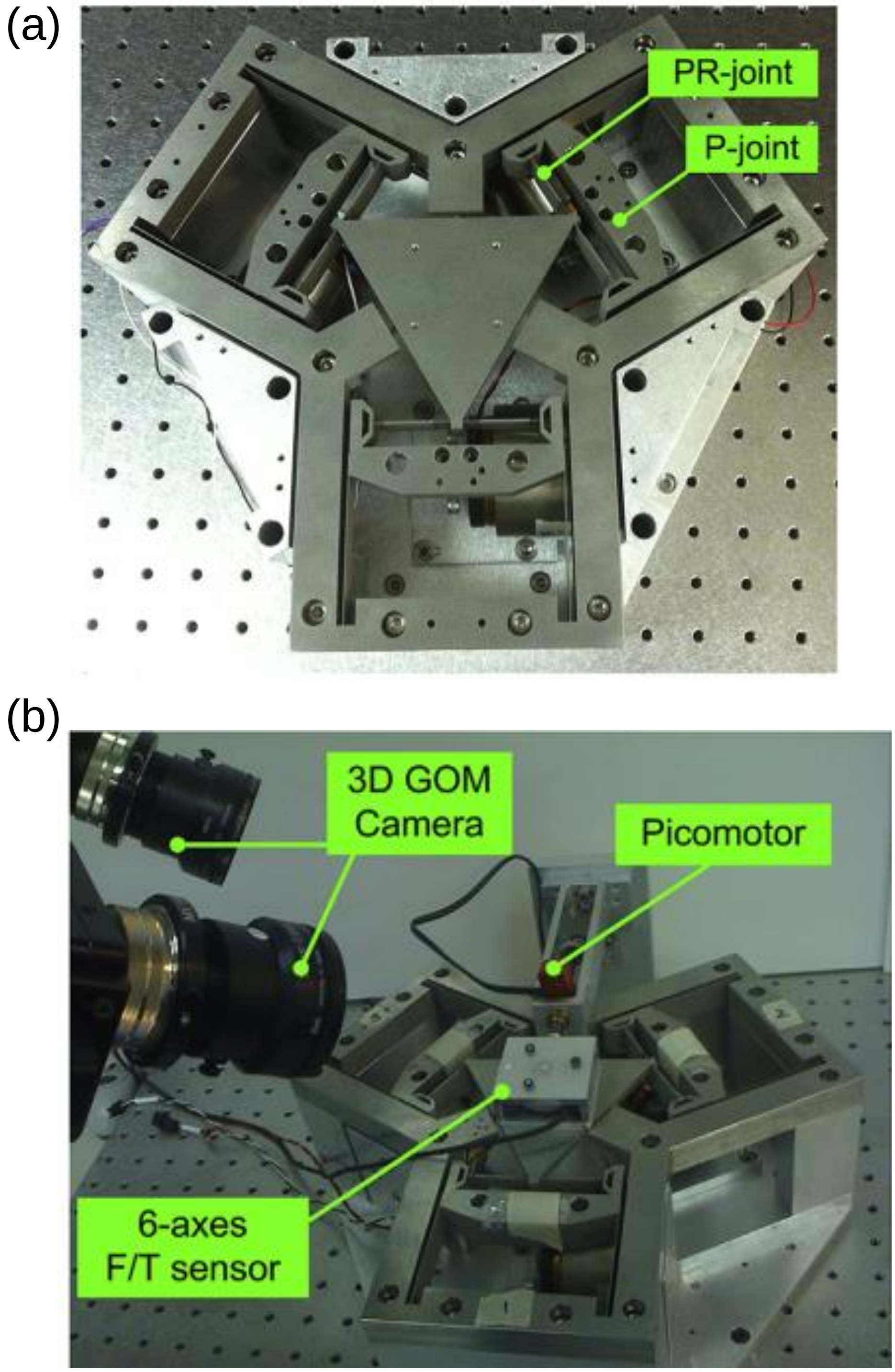

Figure 2.24: (a) A prototype of the optimized 3PPR FPM and (b) the experimental setup to evaluate the stiffness of the FPM. The 3D GOM camera was used to record the end-effector's deflections. The external loads were induced by the picomotor and the loads were recorded by the 6-axes F/T sensor.

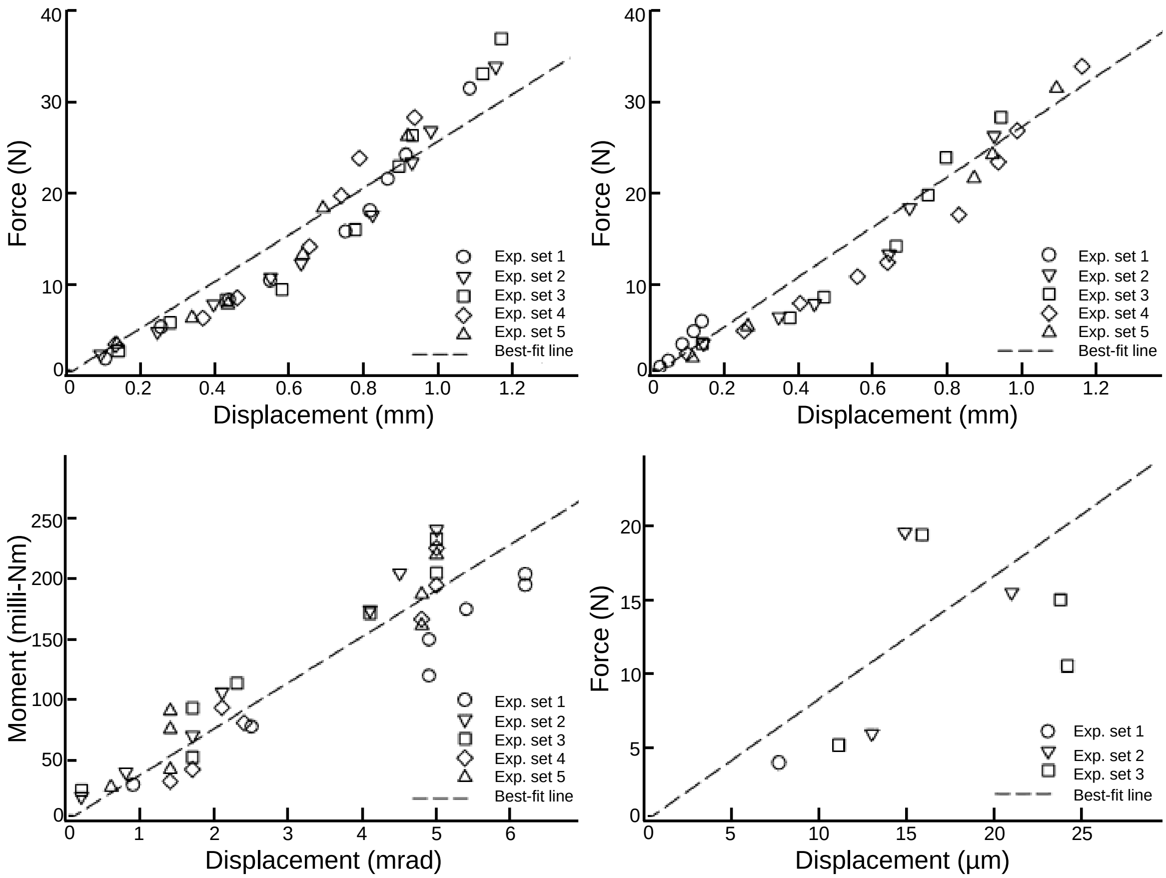

Figure 2.25: (a) Experimental results of the FPM's compliance along the x-axis due to F_x loading. (b) Experimental results of the FPM's compliance along the y-axis due to F_y loading. (c) Experimental results of the FPM's compliance about the z-axis due to M_z loading. (d) Experimental results of the FPM's compliance along the z-axis due to F_z loading.

stiffness characteristic agreed with the actual stiffness characteristic of the developed prototype.

2.4 Summary

This chapter has investigated the effectiveness and feasibility of the proposed topological optimization algorithm - the mechanism-based approach. This is carried out by first using the algorithm to create a μ-gripper, and a $\underline{\mathrm{P}}$ and a PR compliant joint. The obtained flexure mechanisms have feasible designs as there are neither disconnected solid elements nor ambiguous 'grey' elements within them. Furthermore, the convergence plots also indicate that the optimization processes are able to converge. The obtained μ-gripper has shown improvement over an intuitive design, illustrating the potential of the proposed algorithm. For the compliant joints, after they have been synthesized, they were eventually assembled into a 3$\underline{\text{P}}$PR FPM that can deliver a X-Y-θ motion. The effectiveness of the joints are evaluated by comparing it with a similar 3$\underline{\text{P}}$PR FPM that is assembled by traditional compliant joints. By comparing the stiffness ratios of these two FPMs via FEA, it has been shown that the FPM with optimized joints exhibits superior stiffness ratios. Our experimental results suggested that this FEA comparison was credible because the deviations between the actual and predicted stiffness for the optimized FPM were less than 9%. Thus, the advantages of the mechanism-based approach can be summarized as:

- The generated topology does not have disconnected solid elements
- The optimization procedure was done in a discrete manner, thus there are no ambiguous ”grey” elements
- Convergence plot indicates that the algorithm can converge and evolve gradually
- By using a global optimization solver, G.A., the mechanism-based approach has a higher probability to arrive a global solution compared to other gradient-based techniques
- The topology of the flexural mechanism is not fixed by the seed, even the ‘topology’ of the seed can be changed
- By using two curves to represent one link of the seed, it is possible to add holes within the linkage representation

The disadvantage of this algorithm is that the optimization procedure requires more computational power and time. However, as the design process is generally conducted as off-line programming, computational time is not a critical factor.

Chapter 3

Two-Dimensional Integrated Design Methodology for Structurally Optimal Flexural Mechanism

This chapter introduces the first design methodology that can synthesize multi-degrees-of-freedom FPMs with optimal stiffness and dynamic properties. This proposed methodology will be demonstrated on another $X-Y-\theta_z$ centimeter-scale FPM. However, instead of pre-specifying the sub-chains' topology, we will use the proposed methodology to determine the optimal topology, shape and size for the sub-chains. The proposed methodology is discussed in section 3.1 while a generic dynamic model will be derived in section 3.2. By using the methodology and model, section 3.3 will use the mechanism-based approach presented in the previous chapter to synthesize a $X - Y - \theta_z$ FPM. The properties of this FPM will be evaluated experimentally in section 3.4 and a summary will be provided in section 3.5.

3.1 Design Methdology

A universal design methodology for synthesizing multi-degrees-of-freedom FPMs with optimal dynamic and stiffness properties will be shown here. We hypothesized that this can be achieved if the mechanism-based approach can be utilized to optimize the topology, shape and size for the sub-chains of a FPM.

The required steps to construct such a FPM can be divided into three steps as shown in Fig. 3.1. The FPM's design requirements, such as its required degrees-of-freedom and size constraints, are listed in step 1. Based on the desired degrees-of-freedom, step 2 uses the rigid-body-replacement method to synthesize the FPM's overall topology. This can be achieved by using the design guidelines for parallel robots to determine the required number and type of sub-chains [114, 115]. Step 2 is essential as it simplifies the formulations to implement structural optimization techniques on a flexural mechanism with multi-degrees-of-freedom.

Subsequently, based on the FPM's size constraints, step 3 designs the sub-chains by identifying their optimal topology, shape and size sequentially. This is achieved by using the mechanism-based approach to automatically synthesize the sub-chains as a whole. The sub-chains' topology and shape are first identified by undergoing two optimizations that maximize the FPM's stiffness ratios, as shown in steps 3(a) and (b). Note that these two steps do not include inertia effects as their objective is to select an optimal configuration for the FPM to achieve its desired kinematics.

Based on the obtained topology and shape, step 3(c) will determine the sub-chains' size by optimizing the FPM's dynamic properties. As the stiffness ratios of the FPM may be compromised in step 3(c), suitable stiffness constraints should be applied. For example, by considering the desired workspace and actuation capabilities, the maximum allowable actuating stiffness for the FPM can be determined. This computation can be achieved by using similar kinetostatic analyses to those performed in [9, 116]. Likewise, by using the maximum allowable actuating stiffness and minimum required stiffness ratios, the minimum allowable off-axis stiffness can be computed.

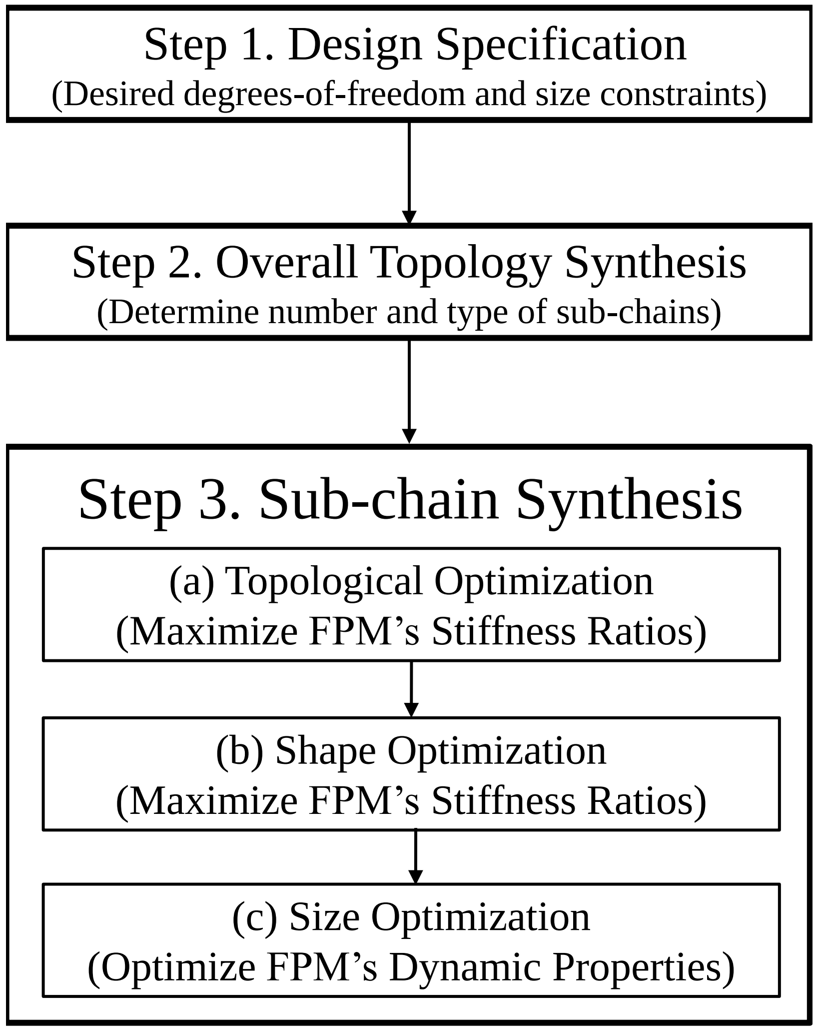

Figure 3.1: The synthesis steps: Based on the desired kinematic requirements, the overall topology of FPM will be identified. This is followed by identifying the optimal topology, shape and size of the sub-chains sequentially. The topological and shape optimizations will maximize the FPM's stiffness ratios while the size optimization will optimize the dynamic properties of the FPM.

Although the synthesis process resembles the building block approach [81], there is one distinct difference. Similar to the kinematic approach, the building block method aims to identify feasible topologies for the flexural mechanism. Thus, there may be multiple feasible topologies, and the selected topology may not have optimal performance. The proposed methodology, however, aims to identify an optimal topology, shape and size for the FPMs' sub-chains such that the FPM's dynamic and stiffness properties can be optimized.

3.2 A Generic Dynamic Model for FPMs

In order to execute the dynamic optimization process shown in step 3(c) in Fig. 3.1, a generic model that can accurately predict an arbitrary FPM's dynamic properties have to be derived. An analytical closed-form model, however, would be too difficult to derive if the geometries of the sub-chains are too complex. Alternatively, if a full FEA is implemented, the entire optimization process would be too computationally expensive. In view of this, a new semi-analytical dynamic model is developed to facilitate the dynamic optimization process for FPMs. The procedure to derive the dynamic model for the FPMs' end-effector can be divided into two stages:

- Stage 1: Obtain the lump mass and stiffness matrices that describe the rigid-body motion of the sub-chains' loading point via simplifying the full FEA model. Note that the loading point of the sub-chains is also their connecting point to the end-effector.
- Stage 2: Use the lump mass and stiffness matrices of the sub-chains to obtain the equations of motion for the FPM's end-effector via the Lagrangian method.

Stage 1 can be carried out by first discretizing each sub-chain into a mesh of finite elements. The FEA structural stiffness matrix for the j^{th} sub-chain can be expressed as $\mathbf{K}_{\text{SC},n\times n,j} = \sum_{i=1}^{\text{all elements}} \mathbf{K}_{\text{FE},i}$. Likewise, its structural FEA mass matrix, $\mathbf{M}_{\text{SC},n\times n,j}$ can be obtained by assembling each finite element's mass matrices, $\mathbf{M}_{\text{FE},i}$. By extracting essential qualities from $\mathbf{M}_{\text{SC},n\times n,j}$, the lump mass matrix $\mathbf{M}_{\text{SC},6\times 6,j}$ can be determined. The extracting process is commonly known as dynamic condensation in FEA. There are several known dynamic condensation techniques such as the Guyan reduction [117], IRS [118] and the SEREP [119] methods but they generally conserve the motion in their FEA nodes instead of the rigid-body motion of the structure. Thus, a modified dynamic condensation method that has similar characteristics as the Guyan reduction is presented in the subsequent sub-section.

Once $\mathbf{M}_{\text{SC},6\times6,j}$ is identified, stage 2 determines the FPM's effective lumped 6×6 mass matrix, $\mathbf{M}_{\text{ee},6\times6}$, by using the Lagrangian equation. The matrix $\mathbf{M}_{\text{ee},6\times6}$ would account for the amalgamated inertia properties of the central platform, $\mathbf{M}_{\text{platform},6\times6}$, and the sub-chains. The lump stiffness of the end-effector, $\mathbf{K}_{\text{ee},6\times6}$, can be obtained by using Eq.s (3.17) and (3.18) respectively. Subsequently, based on the obtained $\mathbf{M}_{\text{ee},6\times6}$ and $\mathbf{K}_{\text{ee},6\times6}$, the six lowest natural frequencies of the FPM can be determined.

3.2.1 Stage 1 of the semi-analytical dynamic model

The presented model is general for any FPM that has l non-identical parallel sub-chains as shown in Fig. 3.2. The j^{th} sub-chain will be discretized into a mesh of finite elements. The mass matrix of the i^{th} finite element, $\mathbf{M}_{\text{FE},i}$, and the assembled mass matrix, $\mathbf{M}_{\text{SC},n\times n,j}$, can be expressed as:

$$\mathbf{M}_{\text{FE},i} = \iiint \rho\, \mathbf{N}^{\text{T}}\mathbf{N}\text{d}V, \quad \mathbf{M}_{\text{SC},n\times n,j} = \sum_{i=1}^{\text{all elements}} \mathbf{M}_{\text{FE},i}. \tag{3.1}$$

The matrix $\mathbf{N}$ represents the shape function matrix in FEA while the variable, ρ, represents the density of the finite element. The wrench, $\mathbf{w}_{\text{SC},6\times1,j}$, exerted on the loading point of the j^{th} sub-chain can be described in the FEA format,$\mathbf{w}_{\text{SC},n\times1,j}$, by the span of the basis $[\mathbf{f}_x, \mathbf{f}_y, \mathbf{f}_z, \mathbf{m}_x, \mathbf{m}_y, \mathbf{m}_z]$:

$$\mathbf{w}_{\text{SC},n\times1,j} = q_1\mathbf{f}_x + q_2\mathbf{f}_y + q_3\mathbf{f}_z + q_4\mathbf{m}_x + q_5\mathbf{m}_y + q_6\mathbf{m}_z. \tag{3.2}$$

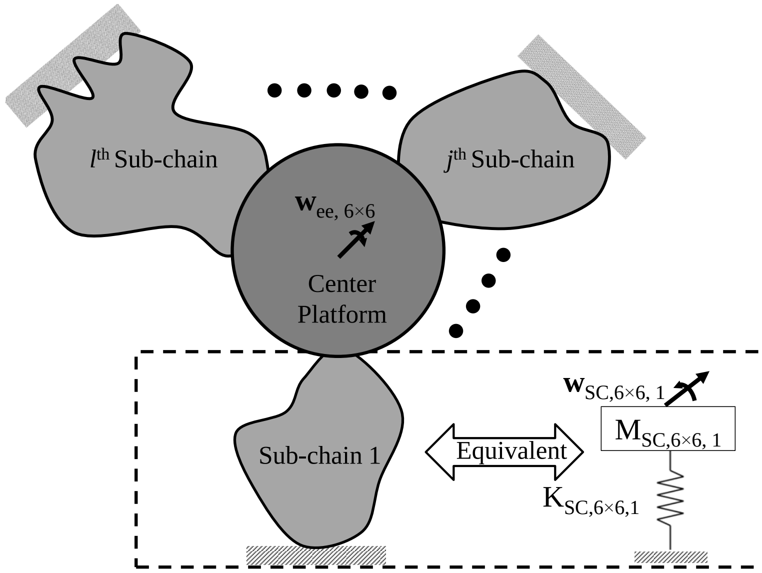

Figure 3.2: A generic FPM that has l arbitrary, parallel sub-chains attached to the central platform (represented by the circle). In the general configuration, the end-effector of the FPM is subjected to an arbitrary external wrench $\mathbf{w}_{\text{ee},6\times6}$. The wrench exerted on the j^{th} sub-chain by the rigid platform is represented by the variable $\mathbf{w}_{\text{SC},6\times6,j}$. Each sub-chain can be represented by a corresponding 6×6 mass and stiffness matrix.

The corresponding nodal deformation, $\mathbf{u}_{\text{SC},n\times1,j}$, can be described as:

$$\begin{aligned}\mathbf{u}_{\text{SC},n\times1,j} &= \mathbf{K}^{-1}_{\text{SC},n\times n,j}\mathbf{w}_{\text{SC},n\times1,j} = \mathbf{U}_{\text{SC},n\times6}\mathbf{q}, \text{ where} \\ \mathbf{U}_{\text{SC},n\times6,j} &= \mathbf{K}^{-1}_{\text{SC},n\times n,j}[\mathbf{f}_x \quad \mathbf{f}_y \quad \mathbf{f}_z \quad \mathbf{m}_x \quad \mathbf{m}_y \quad \mathbf{m}_z],\end{aligned} \tag{3.3}$$

and the vector $\mathbf{q} = [q_1 \;\; q_2 \;\; q_3 \;\; q_4 \;\; q_5 \;\; q_6]^{\text{T}}$. Since $\mathbf{U}_{\text{SC},n\times6,j}$ is independent of time, the rate of change of the nodal deformation with respect to time, $\dot{\mathbf{u}}_{\text{SC},n\times1,j}$, can be expressed by:

$$\dot{\mathbf{u}}_{\text{SC},n\times1,j} = \mathbf{U}_{\text{SC},n\times6,j}\dot{\mathbf{q}}. \tag{3.4}$$

Thus, the kinetic energy of the j^{th} sub-chain, T_j, is $T_j = \frac{1}{2}\dot{\mathbf{u}}^{\text{T}}_{\text{SC},n\times1,j}\mathbf{M}_{\text{SC},n\times n,j}\dot{\mathbf{u}}_{\text{SC},n\times1,j}$. In order to obtain an equivalent lump mass matrix of the j^{th} sub-chain, $\mathbf{M}_{\text{SC},6\times6,j}$, the kinetic energy of the lump mass model has to be equal to the kinetic energy of the j^{th} sub-chain in the FEA format:

$$
\begin{aligned}
T_j &= \frac{1}{2}\dot{\mathbf{u}}^{\mathrm{T}}_{\mathrm{SC},n\times 1,j}\mathbf{M}_{\mathrm{SC},n\times n,j}\dot{\mathbf{u}}_{\mathrm{SC},n\times 1,j} \\
&= \frac{1}{2}\dot{\mathbf{u}}^{\mathrm{T}}_{\mathrm{SC},6\times 1,j}\mathbf{M}_{\mathrm{SC},6\times 6,j}\dot{\mathbf{u}}_{\mathrm{SC},6\times 1,j}.
\end{aligned} \tag{3.5}
$$

The vectors $\mathbf{u}_{\mathrm{SC},6\times 1,j}$ and $\dot{\mathbf{u}}_{\mathrm{SC},6\times 1,j}$ represent the rigid-body deflection of the j^{th} sub-chain's loading point and its rate of change with time, respectively. Based on the compliance matrix, $\mathbf{u}_{\mathrm{SC},6\times 1,j}$ and $\dot{\mathbf{u}}_{\mathrm{SC},6\times 1,j}$ can be expressed as:

$$
\mathbf{u}_{\mathrm{SC},6\times 1,j} = \mathbf{C}_{\mathrm{SC},6\times 6,j}\mathbf{q}, \quad \dot{\mathbf{u}}_{\mathrm{SC},6\times 1,j} = \mathbf{C}_{\mathrm{SC},6\times 6,j}\dot{\mathbf{q}}. \tag{3.6}
$$

By substituting Eq. (3.4) and Eq. (3.6) into Eq. (3.5), and comparing the lump mass matrix with the FEA mass matrix, the lump mass matrix of the j^{th} sub-chain is expressed as:

$$
\mathbf{M}_{\mathrm{SC},6\times 6,j} = \mathbf{C}^{-\mathrm{T}}_{\mathrm{SC},6\times 6,j}\mathbf{U}^{\mathrm{T}}_{\mathrm{SC},n\times 6,j}\mathbf{M}_{\mathrm{SC},j}\mathbf{U}_{\mathrm{SC},n\times 6}\mathbf{C}^{-1}_{\mathrm{SC},6\times 6,j}. \tag{3.7}
$$

The six lowest natural frequencies of the sub-chain can be obtained by using the lump mass and compliance matrices. In order to validate the effectiveness of the derived lump mass matrix, the six lowest natural frequencies of 20 arbitrary structures are evaluated with these lump matrices. Subsequently, these results are compared with the ones obtained from a full FEA analysis. It is found that although the lump matrices model is not able to conserve all six lowest frequencies of the structure, the first three to four lowest natural frequencies can be conserved reasonably well. This is especially true for the fundamental natural frequency where the deviation between the lumped model and a full FEA is always less than 3%. Table 3.1 shows two examples of such comparisons. It should be noted that the presented dynamic condensation method has similar characteristics compared to the Guyan reduction method. For example, this method can also accurately preserve several lowest natural frequencies that correspond to translational mode shapes. Due to its resemblance to the Guyan reduction method, this method may not be able to preserve natural frequencies that correspond with rotational mode shapes. However, this dynamic condensation method is sufficient for this thesis as we can optimize a fundamental natural frequency that corresponds to a translational mode shape. Note that if each sub-chain's fundamental natural frequency can be conserved, the fundamental natural frequency of the FPM can be predicted accurately.

Table 3.1: The six lowest natural frequencies of two random structures that are predicted by the lumped matrices model are shown in the center column. The right column shows the six lowest frequencies obtained via a full FEA respectively. Although the lumped matrices model cannot preserve all six modes of natural frequencies, the first few modes of the natural frequencies of the structure had been fairly well approximated. This is especially true for the fundamental natural frequencies that are encased in the rectangular boxes.

Examples	Model (Hz)	Full FEA (Hz)
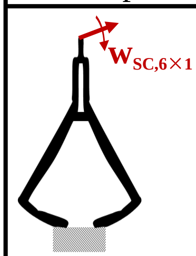	$\begin{pmatrix} \boxed{1,301} \\ 1,743 \\ 3,183 \\ 16,571 \\ 25,168 \\ 59,323 \end{pmatrix}$	$\begin{pmatrix} \boxed{1,296} \\ 1,593 \\ 3,083 \\ 5,421 \\ 12,464 \\ 13,170 \end{pmatrix}$
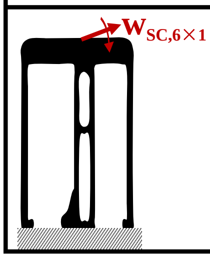	$\begin{pmatrix} \boxed{3,912} \\ 7,029 \\ 7,085 \\ 12,450 \\ 33,615 \\ 48,166 \end{pmatrix}$	$\begin{pmatrix} \boxed{3,912} \\ 7,078 \\ 9,497 \\ 13,266 \\ 68,483 \\ 212,132 \end{pmatrix}$

3.2.2 Stage 2 of the semi-analytical dynamic model

The equations of motions for the FPM can be determined via the Lagrangian method. This can be achieved by deriving the total kinetic energy, strain energy, and work done on the FPM. The total kinetic energy of the FPM, T_{total}, can be described as:

$$T_{\text{total}} = \frac{1}{2}\{\dot{\mathbf{r}}^{\mathrm{T}}_{\text{ee},6\times1}\mathbf{M}_{\text{platform},6\times6}\dot{\mathbf{r}}_{\text{ee},6\times1} + \sum_{j=1}^{l}\dot{\mathbf{u}}^{\mathrm{T}}_{\text{SC},6\times1,j}\mathbf{M}_{\text{SC},6\times6,j}\dot{\mathbf{u}}_{\text{SC},6\times1,j}\}. \tag{3.8}$$

The variables, $\dot{\mathbf{r}}_{\text{ee},6\times1}$ and $\mathbf{M}_{\text{platform},6\times6}$, refers to the platform's twist and inertia, respectively. The relationship of $\dot{\mathbf{r}}_{\text{ee},6\times1}$ and the twist of each sub-chain's loading point can be described as:

$$\dot{\mathbf{r}}_{\text{ee},6\times1} = \mathbf{J}_j \dot{\mathbf{u}}_{\text{SC},6\times1,j}. \tag{3.9}$$

By substituting Eq. (3.9) into Eq. (3.8), the total kinetic energy can be expressed as:

$$T_{\text{total}} = \frac{1}{2}\dot{\mathbf{r}}^{\text{T}}_{\text{ee},6\times1}\{\mathbf{M}_{\text{platform},6\times6} + \sum_{j=1}^{l}\mathbf{J}_j^{\text{-T}}\mathbf{M}_{\text{SC},6\times6,j}\mathbf{J}_j^{\text{-1}}\}\dot{\mathbf{r}}_{\text{ee},6\times1}. \tag{3.10}$$

The total strain energy, S_{total}, can be expressed as:

$$\begin{aligned} S_{\text{total}} &= \frac{1}{2}\sum_{j=1}^{l}\mathbf{u}^{\text{T}}_{\text{SC},6\times1,j}\mathbf{K}_{\text{SC},6\times6,j}\mathbf{u}_{\text{SC},6\times1,j} \\ &= \frac{1}{2}\mathbf{r}^{\text{T}}_{\text{ee},6\times1}\{\sum_{j=1}^{l}\mathbf{J}_j^{-\text{T}}\mathbf{K}_{\text{SC},6\times6,j}\mathbf{J}_j^{-1}\}\mathbf{r}_{\text{ee},6\times1}. \end{aligned} \tag{3.11}$$

The work done, W, induced by the external wrench, $\mathbf{w}_{\text{ee},6\times1}$ can be expressed as:

$$W = \mathbf{w}^{\text{T}}_{\text{ee},6\times1}\mathbf{r}_{\text{ee},6\times1}. \tag{3.12}$$

Thus, by applying the Lagrangian equation with respect to the spatial coordinates of $\mathbf{r}_{\text{ee},6\times1}$, the equations of motion for the FPM can be described as:

$$
\begin{aligned}
\mathbf{M}_{\text{ee},6\times6}\ddot{\mathbf{r}}_{\text{ee},6\times1} + \mathbf{K}_{\text{ee},6\times6}\mathbf{r}_{\text{ee},6\times1} &= \mathbf{w}_{\text{ee},6\times1}, \text{ where} \\
\mathbf{K}_{\text{ee},6\times6} &= \sum_{j=1}^{l} \mathbf{J}_j^{-\text{T}}\mathbf{K}_{\text{SC},6\times6,j}\ \mathbf{J}_j^{-1}, \\
\mathbf{M}_{\text{ee},6\times6} = \mathbf{M}_{\text{platform},6\times6} &+ \sum_{j=1}^{l} \mathbf{J}_j^{-\text{T}}\mathbf{M}_{\text{SC},6\times6,j}\ \mathbf{J}_j^{-1}, \text{ and} \\
\mathbf{M}_{\text{SC},6\times6,j} = \mathbf{C}_{\text{SC},6\times6,j}^{-\text{T}}&\mathbf{U}_{\text{SC},n\times6,j}^{\text{T}}\mathbf{M}_{\text{SC},j}\mathbf{U}_{\text{SC},n\times6}\mathbf{C}_{\text{SC},6\times6,j}^{-1}.
\end{aligned}
\tag{3.13}
$$

The six lowest natural frequencies of the FPM can be determined by solving the eigenvalues, ω_n, of the following equation:

$$
|-\omega_n^2\mathbf{M}_{\text{ee},6\times6} + \mathbf{K}_{\text{ee},6\times6}| = 0. \tag{3.14}
$$

3.3 Synthesis of a $X-Y-\theta_z$ FPM

Using the mechanism-based approach and the generic dynamic model, the proposed design methodology will be illustrated via the synthesis of a $X-Y-\theta_z$ FPM. Aluminum is used for the FPM and its Young's modulus and Poisson ratio are assumed to be 71 GPa and 0.33, respectively. The design requirements for this FPM are:

- A desired workspace of 1.2 mm$\times 1.2$ mm$\times 6°$.
- Optimize the stiffness ratios of the FPM (at least > 80).
- Maximize the FPM's bandwidth (at least fundamental natural frequency > 60 Hz).

The minimum allowable stiffness ratios and bandwidth were selected to ensure that there is at least a 30% improvement over similar flexural mechanisms [7, 8, 12, 49].

3.3.1 Overall topology synthesis

The overall topology of the FPM is determined by using the rigid-body-replacement method. As mentioned in Chapter 4, there are three possible parallel robot configurations that can realize the required $X - Y - \theta_z$ planar motion. They are the 3-legged-Prismatic-Prismatic-Revolute, 3-legged-Prismatic-Revolute-Revolute and 3-legged-Revolute-Revolute-Revolute configurations. Despite having different combination of joints, all the three configurations have three 3-degrees-of-freedom sub-chains. Thus, the selected configuration for this FPM also has three identical, 3-degrees-of-freedom sub-chains to articulate a rigid end-effector. The sub-chains were arranged in a rotary symmetrical manner so that the payload can be divided equally. This configuration is shown in the left portion of Fig. 3.3 where the sub-chains are represented by springs with stiffness properties in all 6-axes. In contrast with Chapter 4, however, we do not specify the topology of the sub-chains. Instead we will use the mechanism-based approach to obtain the optimal topology for the sub-chains.

The design domain of a sub-chain is constrained within a $50\ \text{mm} \times 50\ \text{mm}$ area with a plate thickness of 20 mm. Note that the plate thickness is selected to be 20 mm because it gets increasingly difficult to fabricate flexures with more than 20 mm plate thickness. The loading point of the sub-chain is indicated by the location where it is subjected to an arbitrary wrench, $\mathbf{w}_{\text{SC},6\times1}$, by the rigid platform as shown in Fig. 3.3. The bottom portion of the design domain is fixed to the ground.

The design of the sub-chains is determined by undergoing three optimization processes in the following subsections. The static and dynamic analyses of the FPM, are performed with FEA. The selected mesh density always satisfies two conditions. Firstly, it enables each optimization process to complete within 4-6 hours. Secondly, the mesh density can predict the behavior of the sub-chain accurately. This is validated by using the mesh to pre-evaluate the mechanical behavior of several non-uniform beams before the optimization processes.

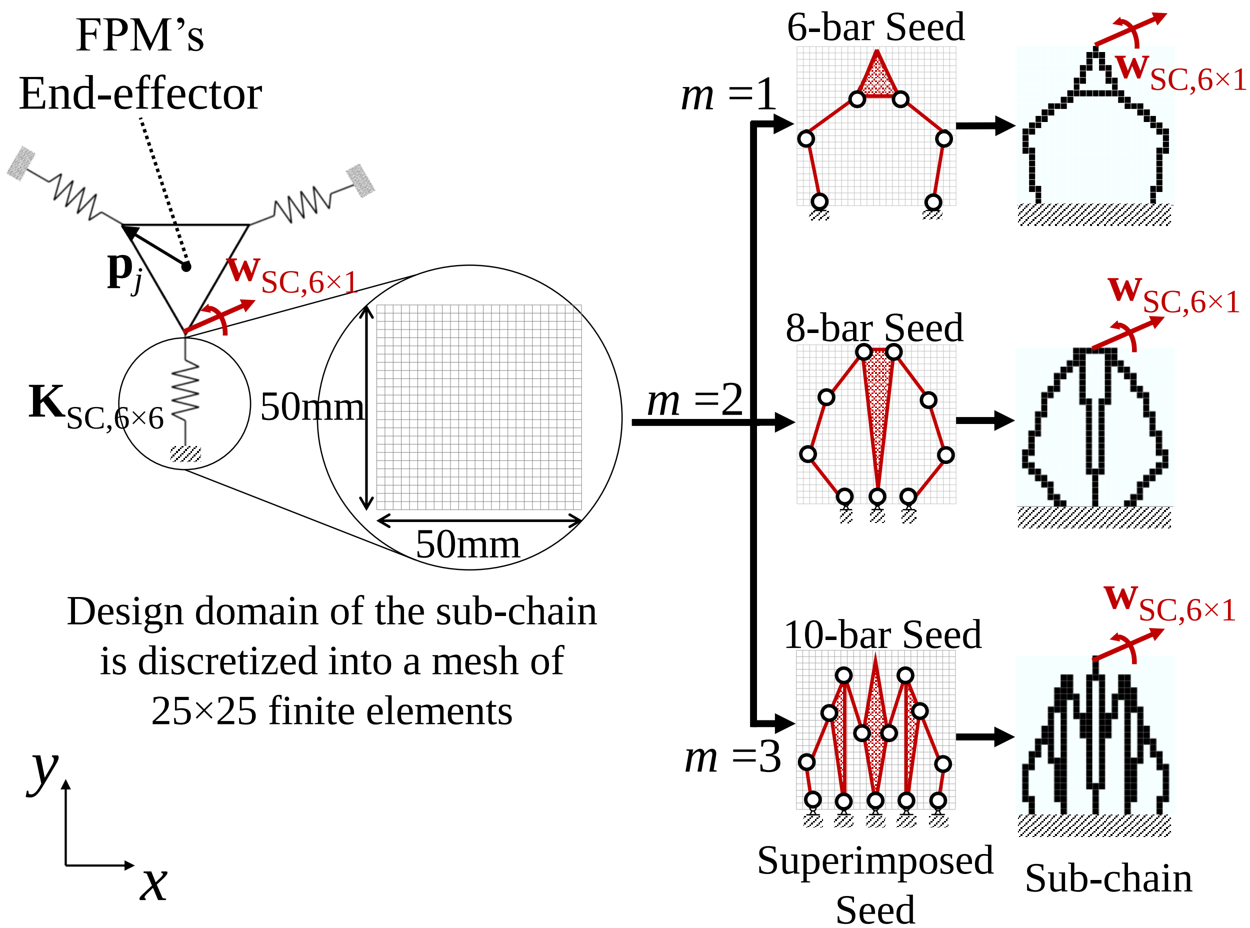

Figure 3.3: The conceptual design of the $X - Y - \theta_z$ FPM and the procedure to implement the mechanism-based approach. The FPM's rigid platform is represented by the triangle shown at the extreme left and the end-effector is located at the center of the platform. The end-effector is articulated by three identical sub-chains and the design domain of each sub-chain is discretized into a mesh of 25×25 identical finite elements. Based on the discrete variable m, a seed will be selected to generate a sub-chain. A sub-chain is created by converting the finite elements, which are in contact with the selected seed, into solid elements. The loading point of the sub-chain is indicated by the location where it is subjected to an arbitrary wrench, $\mathbf{w}_{SC,6\times1}$, by the platform. The bottom portion of the sub-chain is fixed to the ground.

3.3.2 Topological optimization for sub-chains

The optimal topology for the sub-chains that can maximize the FPM's stiffness ratios is determined by using the mechanism-based approach. Thus, the design domain of each sub-chain is discretized into a mesh of finite elements, 25×25 identical 20-node quadratic elements, as shown in Fig. 3.3. Each element can only exist as either solid or void, and initially they are all void.

Subsequently, as each sub-chain has 3-degrees-of-freedom, we select three classical 3-degrees-of-freedom mechanisms with the simplest closed-loop configurations: the 6-, 8- and 10-bar linkages as the seeds. Closed-loop mechanisms are chosen as they have more complicated configurations than their open-loop counterparts, and if required they can evolve into serially-connected structures.

As there is more than one available seed, a discrete design variable, m, is used to select a seed that will be superimposed onto the void design domain. The superimposed seed will create a sub-chain by converting the finite elements that are in contact with it into solid elements (refer to Chapter 3 for the first way of mapping to represent the links), as shown on the right portion of Fig. 3.3. In order to minimize the FPM's off-axis parasitic motions, the seeds are always constrained to be symmetrical. The position and orientation of the seed's links are determined by the design variables - the position of the links' tip. Thus, in this optimization, m and the position of the links' tip are encoded as the genetic material in the genetic algorithm. Note that the topology of the seed can be changed if any link length of the seed approaches to zero during the optimization process.

Once a sub-chain has been created, its stiffness properties are determined via FEA. The stiffness matrices for the i^{th} finite element, $\mathbf{K}_{\text{FE},i}$, and the j^{th} sub-chain, $\mathbf{K}_{\text{SC},n\times n,j}$, are given as:

$$\mathbf{K}_{\text{FE},i} = \iiint \mathbf{B}^{\text{T}}\mathbf{D}\mathbf{B}\,\mathrm{d}V, \quad \mathbf{K}_{\text{SC},n\times n,j} = \sum_{i=1}^{\text{all elements}} s_i \mathbf{K}_{\text{FE},i}. \tag{3.15}$$

For convenience, the matrices $\mathbf{B}$ and $\mathbf{D}$ are restated to be the deformation matrix in FEA and compliance matrix in solid mechanics, respectively. Likewise, the variables s and V represent the state and volume of each finite element, respectively. If element i is void, a small number (10^{-6}) is assigned to s_i, instead of 0, to prevent numerical instability. If the element is solid, $s_i = 1$. The variable, $n \gg 6$, represents the dimension of $\mathbf{K}_{\text{SC},n\times n,j}$. The resultant FEA governing equation is:

$$\mathbf{K}_{\text{SC},n\times n,j}\mathbf{u}_{\text{SC},n\times 1,j} = \mathbf{f}_{\text{SC},n\times 1,j}. \tag{3.16}$$

The vectors $\mathbf{u}_{\text{SC},n\times 1,j}$ and $\mathbf{f}_{\text{SC},n\times 1,j}$ represent the nodal deformations and nodal force loadings of the j^{th} sub-chain, respectively. The stiffness properties of the j^{th} sub-chain can be determined by evaluating the loading point's rigid-body deflection when it is subjected to six orthogonal unit loads. These loads are expressed in the FEA format: $\mathbf{f}_x$, $\mathbf{f}_y$, $\mathbf{f}_z$, $\mathbf{m}_x$, $\mathbf{m}_y$ and $\mathbf{m}_z$. The loadings $\mathbf{f}_x$, $\mathbf{f}_y$ and $\mathbf{f}_z$ represent unit force loadings in the x, y and z directions, respectively. Likewise, the loadings $\mathbf{m}_x$, $\mathbf{m}_y$ and $\mathbf{m}_z$ represent unit torque loadings in the x, y and z directions, respectively. The 6×6 compliance matrix for the j^{th} sub-chain, $\mathbf{C}_{\text{SC},6\times 6,j}$, can be expressed as:

$$\begin{aligned} \mathbf{C}_{\text{SC},6\times 6,j} &= \mathbf{A}\mathbf{U}_{\text{SC},n\times 6,j}, \text{ where} \\ \mathbf{U}_{\text{SC},n\times 6,j} &= \mathbf{K}^{-1}_{\text{SC},n\times n,j}[\mathbf{f}_x \quad \mathbf{f}_y \quad \mathbf{f}_z \quad \mathbf{m}_x \quad \mathbf{m}_y \quad \mathbf{m}_z]. \end{aligned} \tag{3.17}$$

The six columns of the matrix $\mathbf{U}_{\text{SC},n\times 6,j}$ represent the nodal deflections induced by corresponding loadings. The matrix, $\mathbf{A}$, extracts relevant nodal deflections to determine the rigid-body deflection of the loading point. The first three rows of $\mathbf{C}_{\text{SC},6\times 6,j}$ represent the translational deflection while the last three rows represent the rotary deflection. The 6×6 stiffness matrix of the j^{th} sub-chain, $\mathbf{K}_{\text{SC},6\times 6,j}$, can be obtained by inverting $\mathbf{C}_{\text{SC},6\times 6,j}$. This FEA is found to be accurate although the void elements are represented with $s_i = 10^{-6}$ instead of 0. This was checked by first creating multiple random sub-chains and evaluate their stiffness properties by using $s_i = 10^{-6}$ for the void elements. Subsequently, the stiffness properties of these sub-chains were re-evaluated by reducing $s_i = 10^{-9}$ for the void elements. The deviation between these two types of analyses is found to be less than 2% for all these random sub-chains.

Once the sub-chains' stiffness properties are identified, the end-effector's 6×6 stiffness matrix, $\mathbf{K}_{\text{ee},6\times6}$, can be expressed as:

$$\mathbf{K}_{\text{ee},6\times6} = \sum_{j=1}^{3} \{\mathbf{J}_j^{-\text{T}} \mathbf{K}_{\text{SC},6\times6,j} \mathbf{J}_j^{-1}\}, \quad \mathbf{J}_j = \begin{bmatrix} \mathbf{I}_{3\times3} & \hat{\mathbf{p}}_j \\ \mathbf{0}_{3\times3} & \mathbf{I}_{3\times3} \end{bmatrix}. \tag{3.18}$$

The matrix, $\mathbf{J}_j$, represents the Jacobian matrix for the j^{th} sub-chain. The 3×3 skew-symmetric matrix, $\hat{\mathbf{p}}_j$, represents the position vector from the end-effector to the j^{th} sub-chain as illustrated in Fig. 3.3. Note that before Eq. (3.18) is executed, the coordinate frame of all the $\mathbf{K}_{\text{SC},6\times6,j}$ are expressed in the global coordinate frame that is shown in Fig 3.3.

The stiffness ratios of $\mathbf{K}_{\text{ee},6\times6}$ are maximized by evolving the sub-chains' topology via this optimization problem:

$$\begin{aligned} \text{minimize} \quad f &= \frac{K_{xx} K_{yy} K_{\theta z \theta z}}{K_{zz} K_{\theta x \theta x} K_{\theta y \theta y}} \\ \text{subject to:} \quad & \mathbf{K}_{\text{SC},n\times n,j} \mathbf{u}_{\text{SC},n\times1,j} = \mathbf{f}_{\text{SC},n\times1,j}. \end{aligned} \tag{3.19}$$

The equality constraint represents the FEA governing equation. After using genetic algorithm to evolve a population of 100 chromosomes via 40 generations, the optimal topology for the sub-chains is identified and shown in Fig. 3.4(h). The evolutionary process is illustrated in Fig. 3.4 and this optimization process is shown to converge as the best and mean fitness plots in Fig. 3.5 converge to the same value. The total computational time is about four hours and the obtained topology is simple.

A simple topology, however, does not suggest that complicated topologies should be excluded during the synthesis process. Note that the solution is not known a priori, and it would be beneficial to increase the optimization search space by including these complicated topologies. It should also be noted that although the search space can be increased by having more seeds,

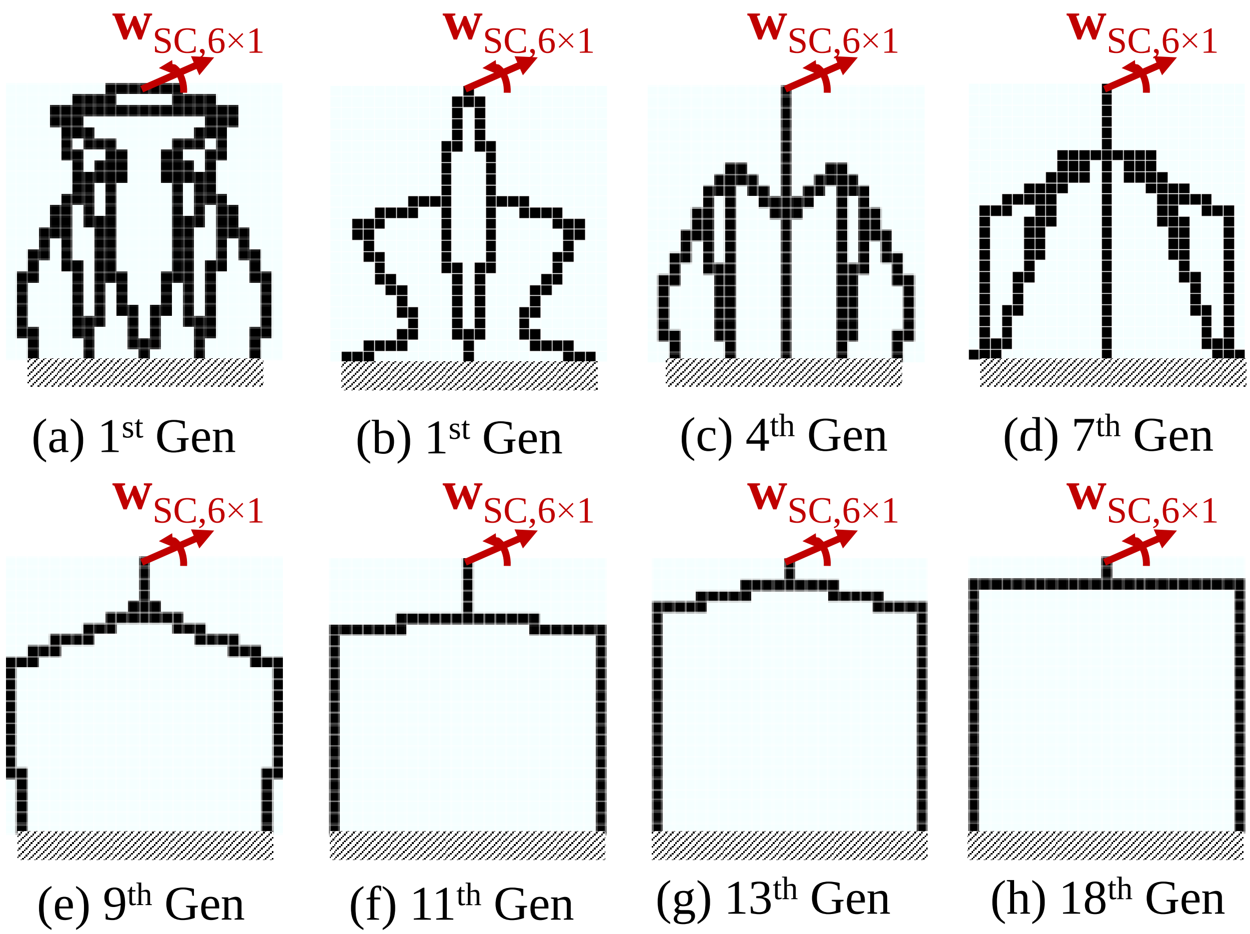

Figure 3.4: The evolutionary process to obtain the sub-chains' optimal topology. (a) and (b) are sample chromosomes in the first generation while (c) - (h) shows the solutions obtained in various generations. The final solution, (h), is obtained in the 18^{th} generation.

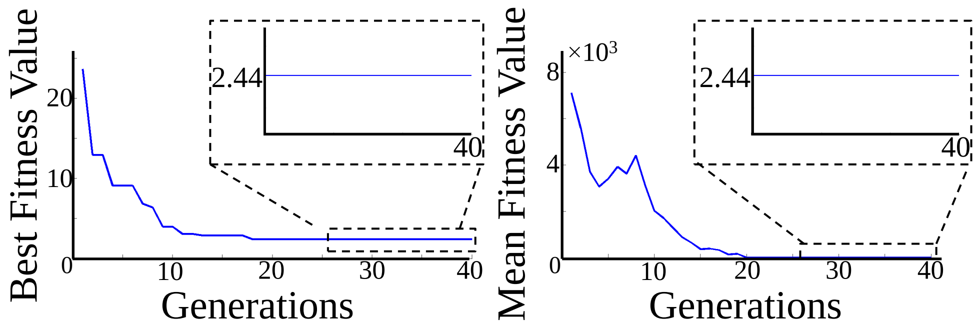

Figure 3.5: The convergence plots for the topological optimization. The optimization process had converged as the best fitness and the mean fitness plots eventually converge to the same value.

this will also require more computational cost and time. Thus, by considering the computational cost, we only select three seeds.

3.3.3 Shape optimization for sub-chains

The stiffness ratio of the FPM can be further enhanced by letting the optimal topology of the sub-chain to undergo a shape optimization. This sub-section shows how the curvature of each link in Fig. 3.4(h) is optimized.

Similar to the previous optimization process, the design domain of the sub-chains is first discretized into a mesh of 50×50 identical 8-node bi-linear finite elements as shown in Fig. 3.6(a). All the elements can either be solid or void and they are initially all selected as void here. The optimal topology obtained in Fig. 3.4(h) is then used as a seed to superimpose onto the void mesh of elements as shown in Fig. 3.6(b). The seed's link lengths in this optimization, however, would remain constant. Furthermore, instead of using straight lines, each link of the seed is represented by an area bounded by a straight line and a cubic curve as shown in Fig. 3.6(c)-(d) (refer to Chapter 3 for second way of mapping for the links). Note that we have excluded the harmonic curves to reduce computational time. As the sub-chains are geometrically symmetrical, this shape mapping would only be required to carry out on the left-half plane of the seed. Elements that are in contact with the seed are selected as solid elements. The features on the right-half plane are obtained by making a reflection about the symmetrical axis as shown in Fig. 3.6(e). This essentially creates a sub-chain as shown in Fig. 3.6(f). The stiffness properties of the FPM's end-effector are then evaluated via equations (3.15) to (3.18).

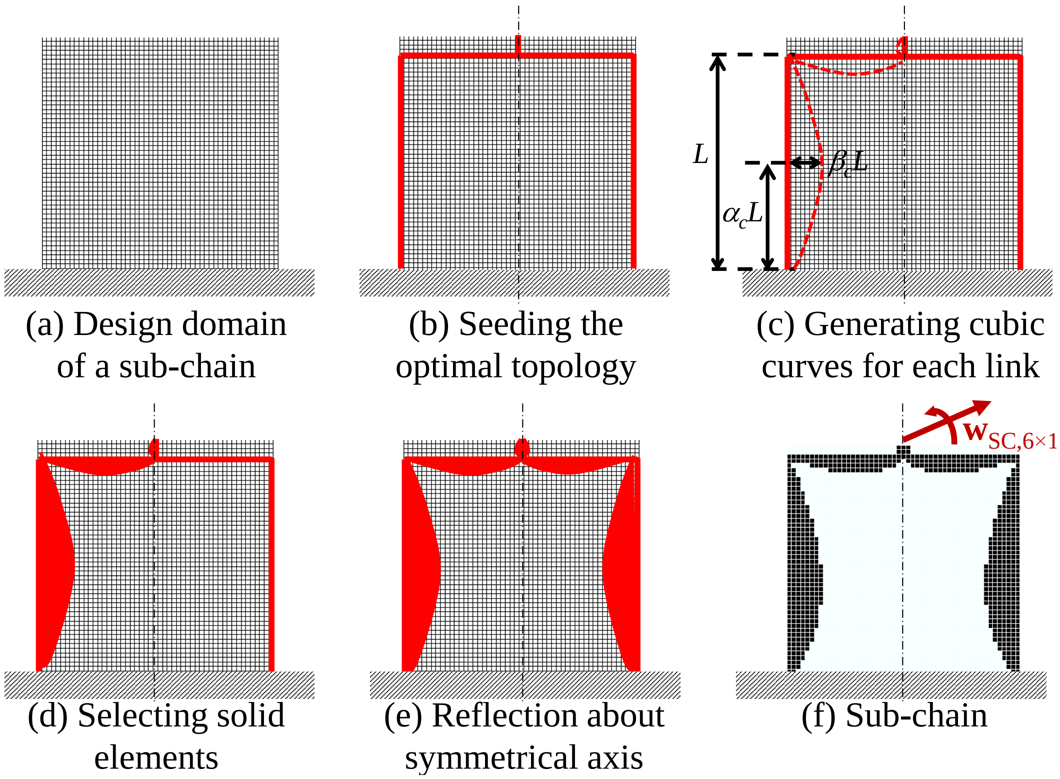

Figure 3.6: The procedure to implement shape optimization. (a) The design domain is discretized into a mesh of 50 $\times$ 50 identical finite elements which can be either solid or void. All of the elements are initially selected as void. (b) The optimal topology in Fig. 3.4(h) is superimposed onto the mesh. (c) Each link of the seed that is located on the left feature of the seed will produce an additional cubic curve. The location and height of the curve's stationary point are specified by the design variables α_c and β_c, respectively. (d) All the finite elements which are in contact with the area bounded by the cubic curve and the link are selected as solid elements. (e) A structure is formed by reflecting the left features about the symmetrical axis. (f) The generated sub-chain.

The profile of the curve is specified with three parameters, L, α and β as shown in Fig. 3.6(c). The parameter L represents the link length and it is predetermined by the previous optimization process. The parameters α_c and β_c are the design variables that specify the location and height of the stationary point of the curve, respectively. By varying these design variables, the seed's links can generate different curvatures. Thus, in this optimization, each chromosome in the G.A. encodes the curve parameters, α_c and β_c, as their genetic materials. Although the design variables are different, the fitness function and constraints for the shape optimization are also formulated by Eq. (3.19).

The optimal shape is shown in Fig. 3.7(c) after G.A. evolves the curve parameters with 70 chromosomes via 50 generations. The evolutionary process is illustrated in Fig. 3.7. The optimization process is shown to converge as the best and mean fitness plots in Fig. 3.8 converge to the same value. The computational time is about 6 hours.

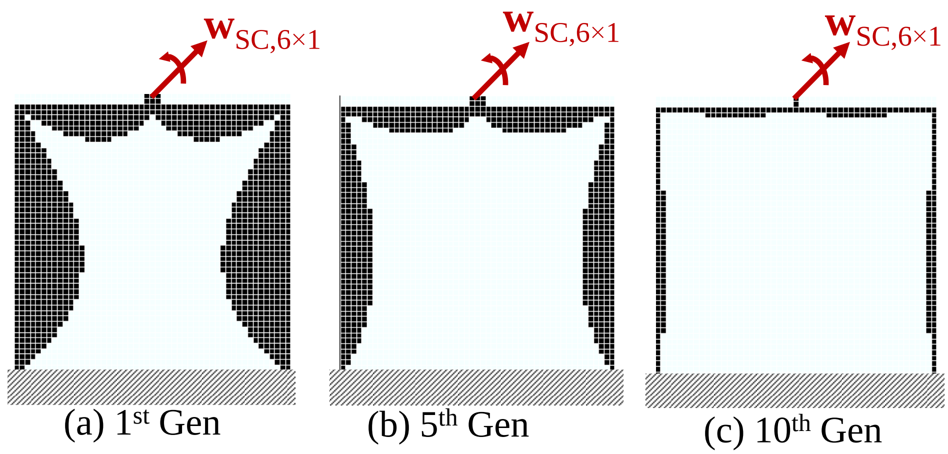

Figure 3.7: The evolutionary process to obtain the sub-chains' optimal shape based on its optimal topology. (a), (b) and (c) show the solutions obtained in the 1^{st}, 5^{th} and 10^{th} generations, respectively. The final solution is obtained in the 10^{th} generation.

It is found that the values of β_c for all the optimized cubic curves are small. Thus, the resultant shape for each link resembles a rectangle. However, despite having simple shapes, it does not suggest that the cubic curves are unnecessary. This is because the solution is not known a priori and if the cubic curves are removed, the search space for the shape optimization is inadvertently

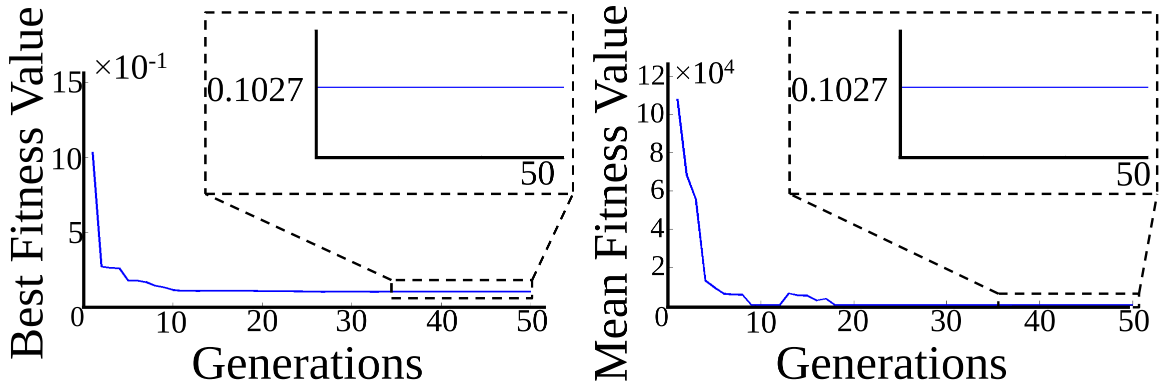

Figure 3.8: The convergence plots for the shape optimization. The optimization process is shown to converge as the best fitness and the mean fitness plots eventually converge to the same value.

reduced.

3.3.4 Size optimization for sub-chains

The dynamic properties of the FPM will be optimized by using the obtained sub-chains to undergo a final size optimization. Specifically, this sub-section will optimize the flexural length and thickness of the sub-chains. Unlike previous optimizations, this optimization includes the inertia effects of the FPM as shown in Fig. 3.9. The inertias of the platform and the j^{th} sub-chain are represented by the matrices $\mathbf{M}_{\text{platform},6\times 6}$ and $\mathbf{M}_{\text{SC},6\times 6,j}$, respectively. Each $\mathbf{M}_{\text{SC},6\times 6,j}$ can be determined by the model provided in section 5.2.

The design variables, listed as t_i, are shown in Fig. 3.10(a). Thus, in this optimization, the chromosomes in genetic algorithm would encode the values of these design variables as their genetic material.

Each sub-chain is discretized into a mesh of 340 20-node quadratic finite elements. The FEA mass matrices of the i^{th} finite element, $\mathbf{M}_{\text{FE},i}$, and j^{th} sub-chain, $\mathbf{M}_{\text{SC},n\times n,j}$, are given as:

$$\mathbf{M}_{\text{FE},i} = \iiint \rho \, \mathbf{N}^{\text{T}}\mathbf{N} \, \mathrm{d}V, \quad \mathbf{M}_{\text{SC},n\times n,j} = \sum_{i=1}^{\text{all elements}} \mathbf{M}_{\text{FE},i}. \tag{3.20}$$

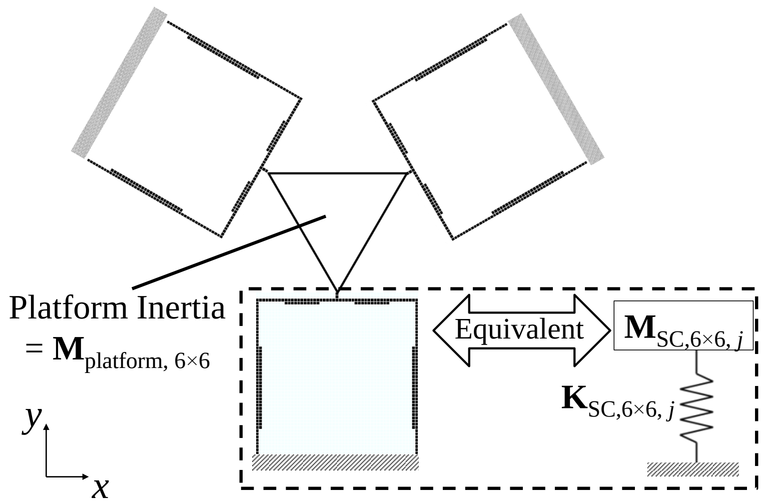

Figure 3.9: A schematic representative of the FPM's dynamic model. The platform inertia is represented by the mass matrix, $\mathbf{M}_{\text{platform},6\times6}$ while the inertia and stiffness matrices of each sub-chain can be represented as $\mathbf{M}_{\text{SC},6\times6,j}$ and $\mathbf{K}_{\text{SC},6\times6,j}$, respectively.

The matrix, **N**, represents the shape function of the finite element while the variable, ρ, represents the density of the element. The mass matrices, $\mathbf{M}_{\text{SC},6\times6,j}$, is given as:

$$\mathbf{M}_{\text{SC},6\times6,j} = \mathbf{C}^{-\text{T}}_{\text{SC},6\times6,j}\mathbf{U}^{\text{T}}_{\text{SC},n\times6,j}\mathbf{M}_{\text{SC},n\times n,j}\mathbf{U}_{\text{SC},n\times6}\mathbf{C}^{-1}_{\text{SC},6\times6,j}. \tag{3.21}$$

Using Eq. (3.21) and the Lagrangian method, the end-effector's equivalent inertia matrix, $\mathbf{M}_{\text{ee},6\times6}$, is:

$$\mathbf{M}_{\text{ee},6\times6} = \mathbf{M}_{\text{platform},6\times6} + \sum_{j=1}^{3}\mathbf{J}_j^{-\text{T}}\mathbf{M}_{\text{SC},6\times6,j}\ \mathbf{J}_j^{-1}. \tag{3.22}$$

Although the FPM has many natural frequencies, we will only maximize its fundamental natural frequency (bandwidth) as a proof-of-concept. It should, however, be noted that it is also possible to optimize the natural frequency of higher vibrational modes. The bandwidth, $\omega_{n,1}$, can be maximized via this optimization:

$$
\begin{aligned}
\text{minimize} f_1 &= \frac{1}{\omega_{n,1}} \\
\text{subjected to: } &\left| -\omega_n^2 \mathbf{M}_{\text{ee},6\times6} + \mathbf{K}_{\text{ee},6\times6} \right| = 0 \\
K_{xx} \leq 2.0 \times 10^4 \text{ N/m}, \, &K_{yy} \leq 2.0 \times 10^4 \text{ N/m}, \\
K_{zz} \geq 1.6 \times 10^6 \text{ N/m}, \, &K_{\theta x \theta x} \geq 1.2 \times 10^3 \text{ Nm/rad}, \\
K_{\theta y \theta y} \geq 1.2 \times 10^3 \text{ Nm/rad}, \, &K_{\theta z \theta z} \leq 15 \text{ Nm/rad}.
\end{aligned}
\tag{3.23}
$$

The six lowest natural frequencies of the FPM can be determined by solving the eigenvalues, ω_n, in the equality constraint shown in Eq. (3.23). In order to achieve the required workspace with three actuators that can supply a maximum of 8 N, the maximum allowable actuating stiffness K_{xx}, K_{yy} and $K_{\theta z \theta z}$ can be determined. This computation can be achieved by using similar kinetostatic analyses that were demonstrated in [9, 116]. Furthermore, based on the required stiffness ratios (> 80), the minimum allowable off-axis stiffness, K_{zz}, $K_{\theta x \theta x}$ and $K_{\theta y \theta y}$, can be computed. Note that the stiffness ratios are feasible as they are within the 'upper bound' limits of the FPM. These 'upper bound' limits are determined by undergoing a size optimization with the fitness function and constraints listed in Eq. (3.19) instead of Eq. (3.23).

The optimal FPM is obtained, as shown in Fig. 3.10(b), after genetic algorithm evolves a population of 100 chromosomes via 100 generations. The jagged edges of the design have been smoothened to prevent stress concentration. The optimization process is shown to converge as the best and mean fitness plots in Fig. 3.11 converge to the same value. The total computational time is about 5 hours and the simulated stiffness properties of the FPM are:

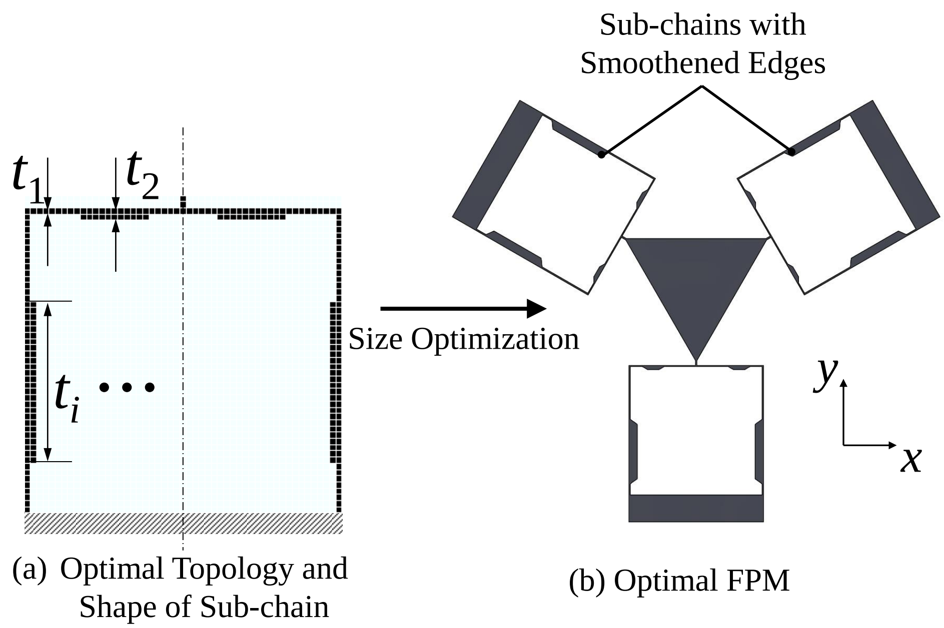

Figure 3.10: The procedure to implement size optimization on the FPM. By undergoing another size optimization on the sub-chain shown in (a), the optimal FPM is obtained in (b).

$$\mathbf{K}_{\text{ee},6\times 6} = \begin{bmatrix} 2.0\times 10^4 & & & & & \\ 0 & 2.0\times 10^4 & & & \textbf{SYM} & \\ 0 & 0 & 2.6\times 10^6 & & & \\ 0 & -545 & 0 & 1.3\times 10^3 & & \\ 545 & 0 & 0 & 0 & 1.3\times 10^3 & \\ 0 & 0 & 0 & 0 & 0 & 12 \end{bmatrix}. \tag{3.24}$$

The obtained K_{xx}, K_{yy}, K_{zz}, $K_{\theta x\theta x}$, $K_{\theta y\theta y}$, $K_{\theta z\theta z}$ are 2.0×10^4 N/m, 2.0×10^4 N/m, 2.6×10^6 N/m, 1.3×10^3 Nm/rad, 1.3×10^3 Nm/rad and 12 Nm/rad, respectively. The translational and rotational stiffness ratios are $K_{zz}/K_{xx} = K_{zz}/K_{yy} = 130$ and $K_{\theta x\theta x}/K_{\theta z\theta z} = K_{\theta y\theta y}/K_{\theta z\theta z} = 108$, respectively. The simulated bandwidth for the FPM is 117 Hz and it corresponds to the x-axis translational mode shape. Due to the FPM's rotary symmetrical configuration, the second

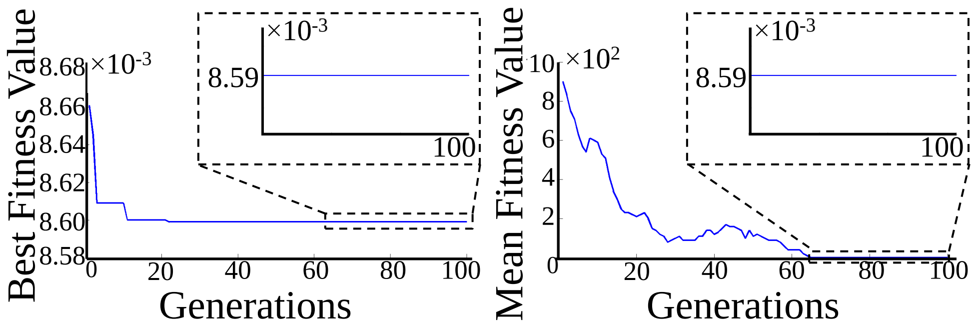

Figure 3.11: The convergence plots for the size optimization. The optimization process converges as the best fitness and the mean fitness plots eventually converge to the same value.

lowest natural frequency is also equal to 117 Hz and it corresponds to the y-axis translational mode shape.

Stress analyses are conducted via Comsol simulations after the size optimization is completed and the jagged edges smoothened. These analyses are conducted by first computing the required wrench on the FPM's end-effector, $\mathbf{w}_{\mathrm{ee},6\times6}$, such that the FPM can achieve its desired workspace. This is computed by pre-multiplying the stiffness matrix in Eq. (3.24) to the maximum travel range of the desired workspace. Subsequently, the FPM's Von Mises stress induced by $\mathbf{w}_{\mathrm{ee},6\times6}$ is determined. Simulation results indicate that the maximum induced Von Mises stress is 126 MPa and it is lower than the yield stress and fatigue stress of the FPM. This implies that the FPM has approximately 10^8 lifecycles [120]. Note that we assume that the FPM can be constructed with aluminium 7075-T6, and its yield stress and fatigue stress are approximated to be 450 MPa and 159 MPa, respectively.

While it is possible to include fatigue and yield stress constraints in Eq. (3.23) during the optimization process, we have excluded such stress analyses to reduce computational costs.

3.3.5 Discussion

The obtained FPM had achieved stiffness ratios that were greater than 100, and a high bandwidth of 117 Hz. These properties have satisfied the required design criteria that are listed in the beginning of Section 3. The targeted workspace of the FPM can also be theoretically achieved as the actuating stiffness had been constrained based on the actuators' capabilities (as shown in Eq. (3.23)). Furthermore, as the maximum induced Von Mises stress is lower than the FPM's fatigue stress, this implies that the FPM can repeat approximately 10^8 cycles.

The obtained stiffness ratios had shown significant improvement over existing centimeter-scale flexural mechanisms with 3-degrees-of-freedom. The stiffness ratios of these flexural mechanisms are typically between $0.5 - 50$ [7, 8, 9, 12, 13, 14, 49, 50]. The stiffness ratios are also much more superior than the 3$\underline{\text{P}}$PR FPM in Chapter 4 because the topology and shape of the sub-chains have been optimized. Furthermore, the obtained bandwidth also has significant improvement over existing flexural mechanisms, which have translational and rotational deflections greater than 0.5 mm and $0.5°$, respectively. The bandwidth of these flexural mechanisms typically does not exceed 45 Hz [7, 8, 12, 49].

The configuration of the obtained FPM resembles the classical 3-legged-Prismatic-Prismatic-Revolute architecture. The two parallel vertical beams resemble a prismatic joint that slides horizontally, as shown in Fig. 3.12(a). The combination of the horizontal beam and the top vertical beam resemble the second prismatic joint and a revolute joint that provide vertical and rotational motions. These deformation characteristics are illustrated in Fig. 3.12(b) and Fig. 3.12(c), respectively.

Despite having a simple topology and shape for the FPM's sub-chains, it should be noted that this design is unique from other $X - Y - \theta_z$ FPMs in the literature. There may, however, exist more optimal solutions if more seeds, and higher order polynomial curves are used in the topological and shape optimizations, respectively. However, this would in turn require more computational time and cost.

Lastly, different topologies and shapes may be obtained if the fitness function in Eq. (3.19) is changed. This can be achieved by altering the stiffness components' indices where the optimization processes would place higher emphasis for components with higher indices.

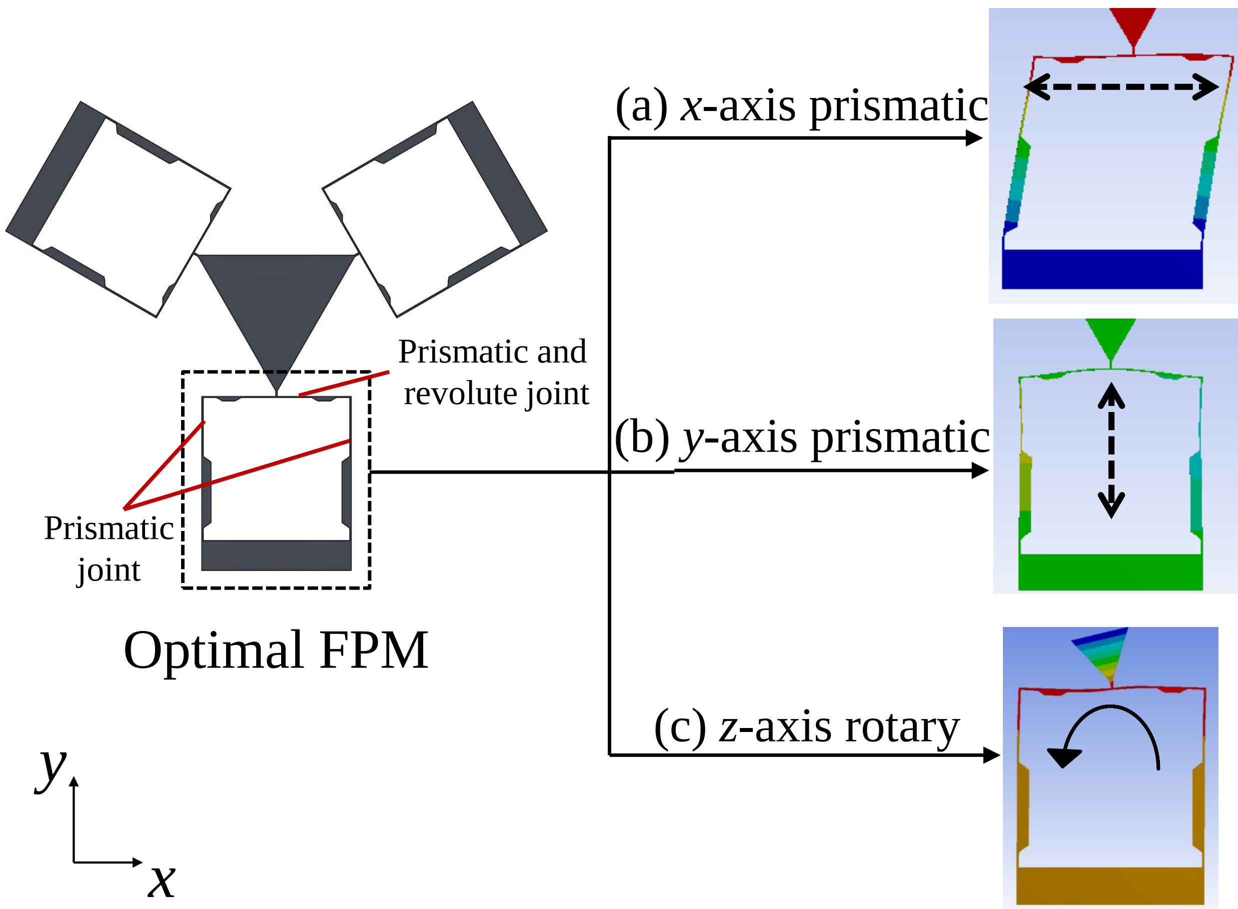

Figure 3.12: The obtained FPM resembles a 3-legged-Prismatic-Prismatic-Revolute configuration. The compliant joint motions of the sub-chains are shown on the right.

3.4 Experiments

As a proof-of-concept, a cheaper material, aluminum 6061, is used to construct our prototype. Its Young's modulus is 69 GPa and it is slightly lower than the simulated Young's modulus (71 GPa). Furthermore, due to manufacturing errors, the dimensions of the prototype are slightly different from the conceptual design shown in Fig. 3.10. By accounting for such changes, the FPM's updated simulated stiffness and dynamic properties are shown in Tables 3.2 and 3.3, respectively.

Two types of experiments, the stiffness and dynamic experiments were conducted on the prototype. The stiffness tests evaluated the stiffness properties and workspace of the FPM while the dynamic test evaluated its bandwidth. All these experiments were conducted on an anti-vibration table.

3.4.1 Stiffness experiments

Actuating Stiffness Evaluation

The FPM was connected to a linear positioner via a rigid rod. When the linear positioner applied a pushing force to the FPM, the deflection and pushing force on the FPM were measured by a micrometer and a load cell, respectively. Note that the stiffness of the rigid rod was at least 1000 times greater than the FPM's actuating stiffness. Thus, when the rigid rod was placed serially with the FPM, the deflections caused by the rigid rod were negligible. As the FPM had 3 degrees-of-freedom, three actuating stiffness - the x-axis force loading, y-axis force loading and z-axis moment loadings were evaluated. This experimental setup was shown in Fig. 3.13 by using the y-axis force loading as an illustration. The linear positioner was placed collinearly with the end-effector's y-axis. Similarly, the x-axis force loading was carried out by rotating the positioner 90° so that the positioner was aligned with the end-effector's x-axis. In the z-axis moment loadings, the positioner had an offset distance along the y-axis from the x-axis force

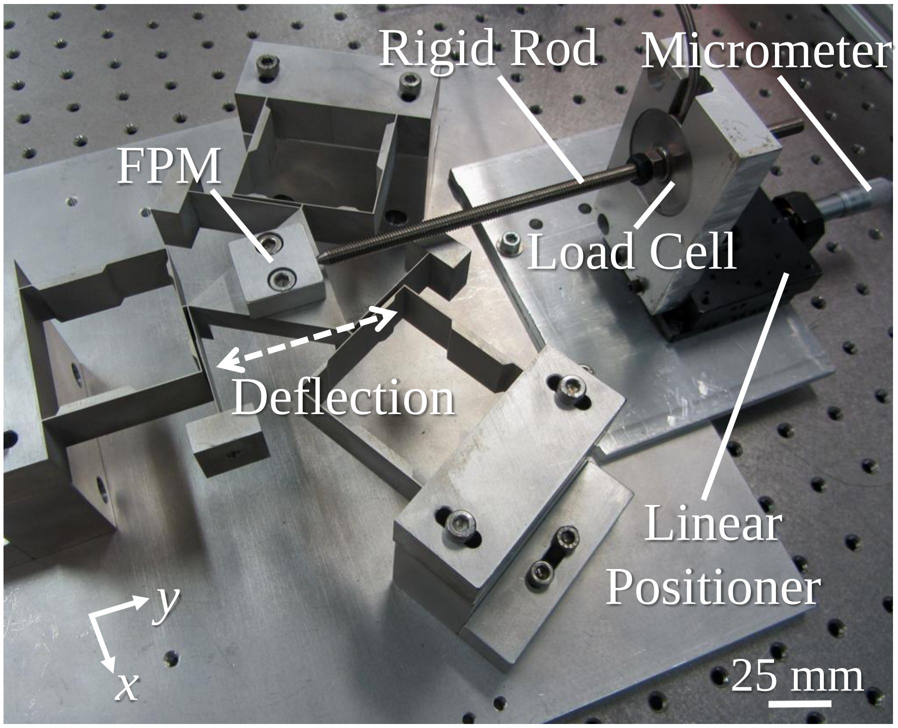

Figure 3.13: The experimental setup for evaluating the actuating stiffness of the FPM. A linear positioner is used to apply a pushing force to the FPM via a rigid rod. The linear deflection and applied force are measured by a micrometer and a load cell, respectively.

loading configuration. This allowed the positioner to apply z-axis torques to the FPM.

For each experiment, three sets of five data points were collected. The compiled data were represented by the plots shown in Fig. 3.15(a), (b) and (c). Based on the slope of the best fit lines, the experimentally obtained stiffness for the x-axis force loading, y-axis force loading and z-axis torque loading were 1.89×10^4 N/m, 1.84×10^4 N/m and 10.8 Nm/rad, respectively. These results agree with the simulation results, where the corresponding stiffness are predicted to be 1.86×10^4 N/m, 1.86×10^4 N/m and 11.4 Nm/rad, respectively. The differences between the simulation results and experimental results were within 5% deviation.

Note that the pushing force would also induce an off-axis torque because the loading point of this force had a 5 mm z-axis length offset above its end-effector. However, the deflection induced by this off-axis torque was negligible. As an example, when a 1 N x-axis force was applied on the FPM, this force would also generate a 0.005 Nm torque in the y-axis. Based on the FPM's simulated stiffness properties, the translational deflection along the x-axis that was induced by the y-axis torque and x-axis force were 0.08 μm and 50 μm, respectively. In comparison, the deflection induced by the y-axis torque was 625 times less than the deflection induced by the x-axis force and thus could be neglected.

Off-axis Stiffness Evaluation

The rotational off-axis stiffness, $K_{\theta x \theta x}$ and $K_{\theta y \theta y}$, cannot be determined experimentally as their deflections were too small to be detected with our available equipments. Thus, the z-axis force loading, K_{zz}, was the only evaluated off-axis stiffness. Dead weights were placed on the FPM's platform to apply z-axis forces. The corresponding deflection was measured by a linear probe that had a resolution of 2 μm. Five sets of three data points were collected and the complied data was represented in Fig. 3.15(d). Based on the slope of the best fit line, the experimental stiffness value was 2.41×10^6 N/m. This result agreed with the simulation results, where the K_{zz} stiffness was predicted to be 2.5×10^6 N/m. The deviation between the experimental results and simulation results was within 4%.

Workspace Evaluation

The achievable workspace for the FPM was evaluated by using three 1-degree-of-freedom, bi-directional, linear actuators. As a proof-of-concept, the actuators were connected to the FPM's end-effector via simple beams as indicated in Fig. 3.14. Each beam was designed to have low bending stiffness along the directions indicated in Fig. 3.12(b) and (c), and high stiffness in other directions. When the actuators were connected to the beams, the beams' low stiffness directions functioned like the sub-chains' passive compliant joints. Based on Comsol's FEA simulations, the contribution of these stiffness had less than 5% effects on the stiffness properties indicated in Table 3.2. The beams' stiffness along the direction indicated in Fig. 3.12(a) was high so that the beams was able to move with the actuators as a rigid body. This direction served as the

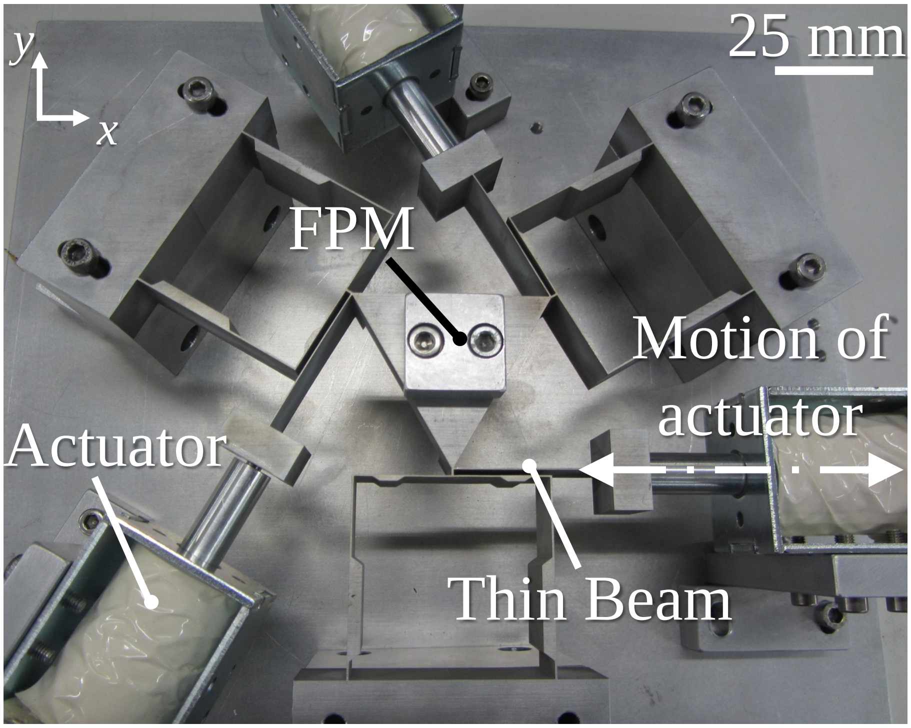

Figure 3.14: The end-effector of the FPM is directly driven by three 1-degree-of-freedom, linear actuators that are connected via simple beams. As an example, the motion of one of these actuators is indicated by the dash-dot arrow. As the end-effector has more than 1-degree-of-freedom, the motions that are unachievable by the actuators, are compensated by the compliance of the thin beams. An open-loop actuation of the prototype is shown in the supplementary video.

active compliant joint for each sub-chain. Furthermore, when the actuators were connected to the beams, the reduction in the FPM's open-loop bandwidth was less than 6% even when the moving mass of the actuators were considered. This analysis was also performed via Comsol's FEA simulations. The reduction in the open-loop bandwidth was low because the actuators had constrained one end of the beams such that they were only allowed to move along the active joint direction. This boundary condition helped to preserve the open-loop bandwidth of the FPM. Lastly, the dimensions of the thin beams were calculated to prevent buckling and other failure modes.

By driving the FPM with the actuators that could supply a maximum force of 8 N, it was found experimentally that the FPM was able to achieve its targeted workspace of 1.2 mm$\times$1.2 mm$\times$ 6°. The actuated deflection of the FPM was measured by a linear probe and a supplementary video illustrated simple open-loop actuation on the FPM.

3.4.2 Dynamic experiments

Based on the FEA in Section 3.4, the bandwidth of the FPM (without actuators) can be determined by evaluating the natural frequency that corresponded to either the x-axis translational or y-axis translational mode shapes. Thus, the FPM's end-effector was subjected to a knock along the y-axis to simulate an input impulse. The y-axis acceleration of the FPM was measured by an accelerometer. By using a double integration with respect to time, the FPM's displacement-time response was obtained. The frequency response of the FPM was obtained using a Fourier transform on the displacement-time response. The process was repeated six times and the average frequency response of the FPM was shown in Fig. 3.15(e). The bandwidth of the FPM was approximated by its resonance frequency, which was 102 Hz.

Similarly, the natural frequency that corresponded to the x-axis translational mode shape was determined by simulating an impulse along the x-axis. This process was repeated 6 times and the average frequency response was shown in Fig. 3.15(f). The resonance frequency for this mode shape was found to be 102.5 Hz. Lastly, the frequency response for the z-axis rotational mode shape was determined by first simulating an impulse that was parallel to the x-axis but with an offset distance, L_1, along the y-axis. This would create a torque impulse along the z-axis. As the accelerometer was placed parallel to the y-axis but with an offset distance, L_2, along the x-axis, it could determine the angular acceleration by dividing the measured acceleration with L_2. The experimental setup that evaluated the z-axis rotational mode shape was shown in Fig. 3.16. Note that the accelerometer would only measure the tangential acceleration as its orientation was perpendicular to the attached point's centripetal acceleration. This experiment was repeated 6 times and the average frequency response for the rotary z-axis mode shape was shown in Fig. 3.15(g). The resonance frequency was found to be 104.7 Hz.

These experimental results agreed with Comsol simulations as the predicted natural frequen-

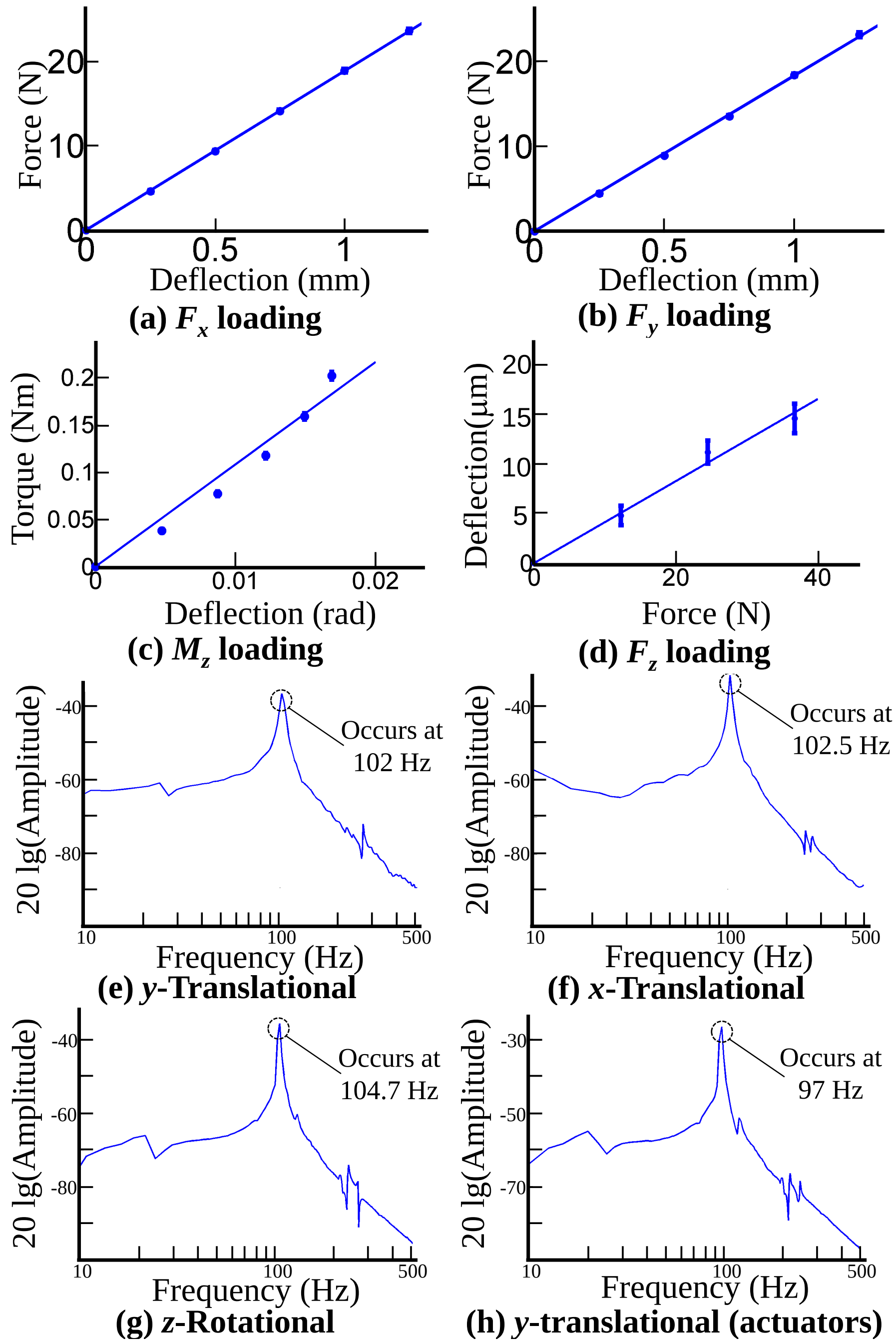

Figure 3.15: (a), (b), (c) and (d) are the experimental results for the F_x, F_y, M_z and F_z loading, respectively. The actuating stiffness experiments that are shown in (a), (b) and (c) have three sets of five data points. The off-axis stiffness experiment data that is shown in (d) have five sets of three data points. Based on the slope of the plots, the experimental K_{xx}, K_{yy}, $K_{\theta z \theta z}$ and K_{zz} stiffness of the FPM are 1.89×10^4 N/m, 1.84×10^4 N/m, 10.8 Nm/rad and 2.41×10^6 N/m, respectively. (e), (f) and (g) are the Bode plots that correspond to the FPM's translational y- and x-axes, and rotational z-axis mode shapes, respectively. Their corresponding resonance frequencies are 102 Hz, 102.5 Hz and 104.7 Hz, respectively. (h) The experimental frequency response of the FPM when it was connected to the actuators. The resonance frequency occurred at 97 Hz.

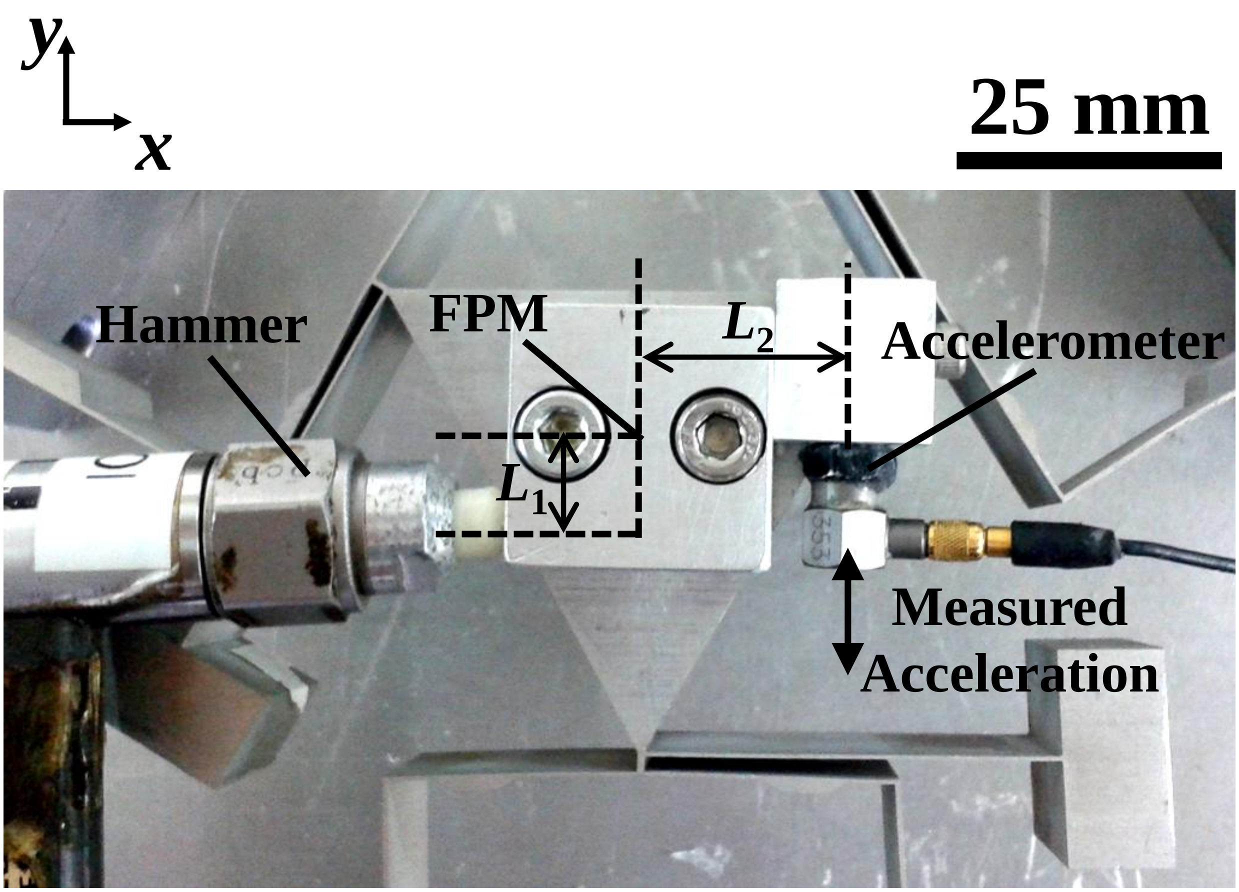

Figure 3.16: The experimental setup for evaluating the frequency response that corresponds to the z-axis rotational mode shape. A torque impulse is applied to the FPM by using the hammer to generate an impulse that is parallel to the x-axis but with an offset length of L_1 along the y-axis. As the accelerometer is placed parallel to the y-axis but with an offset length of L_2 along the x-axis, it measures the angular acceleration of the FPM by dividing the measured tangential acceleration with L_2.

Table 3.2: An overview of the FPM's stiffness properties where the simulation results are compared with the experimental data. The second and third rows represent the translational stiffness ratios while the fourth and fifth rows represent the rotational stiffness ratios of the FPM.

Stiffness Properties	Simulation	Experimental Data
K_{zz}/K_{xx}	134	128
K_{zz}/K_{yy}	134	131
$K_{\theta x\theta x}/K_{\theta z\theta z}$	111	—
$K_{\theta y\theta y}/K_{\theta z\theta z}$	111	—
K_{xx} (N/m)	1.86×10^4	1.89×10^4
K_{yy} (N/m)	1.86×10^4	1.84×10^4
K_{zz} (N/m)	2.5×10^6	2.41×10^6
$K_{\theta x\theta x}$ (Nm/rad)	1.26×10^3	—
$K_{\theta y\theta y}$ (Nm/rad)	1.26×10^3	—
$K_{\theta z\theta z}$ (Nm/rad)	11.4	10.8

cies in the translational x- and y-axes, and rotational z-axis were 111 Hz, 111 Hz and 115 Hz, respectively. The deviation between the experimental data and simulation predictions was within 9%. Note that there was a discrepancy in comparing the measured resonance frequencies $(= \omega_n\sqrt{1-2\zeta^2})$ with the predicted natural frequencies, ω_n, as damping effects were ignored in the latter situation. Although this friction was small, a small deviation between the resonance and natural frequencies should still be expected. The variable ζ referred to the damping ratio resultant by air friction.

Similar experiments were also performed on the FPM when it was attached to the actuators. The obtained bandwidth was 97 Hz, and the frequency response was shown in Fig. 3.15(h). This agreed with the Comsol FEA simulation, where the additional moving mass of the actuators had less than 6% effects on the FPM's open-loop bandwidth. The frequency responses of higher order mode shapes were not evaluated experimentally as their natural frequencies exceeded the working range of our available sensors.

Table 3.3: An overview of the FPM's dynamic properties where the simulation results are compared with the experimental data. The first column indicates the corresponding mode shape while the second and last column represent the simulation predictions and experimental data, respectively.

Mode Shape	Simulation	Experimental Data
y-Translational (Hz)	111	102
x-Translational (Hz)	111	102.5
z-Rotational (Hz)	115	104.7
z-Translational (Hz)	890	—
x-Rotational (Hz)	910	—
y-Rotational (Hz)	910	—

3.4.3 Discussion

Tables 3.2 and 3.3 compare the FPM's experimental stiffness and dynamic properties with its simulation results, respectively. The stiffness and dynamic experimental data agreed with the simulation results as their deviations were within 5% and 9%, respectively. These deviations could be caused by other manufacturing errors that were difficult to account for. The dynamic experimental errors were larger because there was a discrepancy in comparing the resonance frequency with the natural frequency. Note that due to damping effects, the resonance frequency was always slightly lower than the natural frequency.

3.5 Summary

In this chapter, we have introduced the generic design methodology that can integrate both the kinematic and structural optimization approaches. In order to implement this methodology, we have also proposed a generic dynamic model that can accurately predict the fundamental natural frequency of a FPM with arbitrary geometries. Using the dynamic model and the mechanism-based approach, the proposed design methodology uses a structural optimization approach to optimize the topology, shape and size of a FPM's sub-chains. This is in contrast with existing kinematic approaches where the sub-chains are only subjected to size optimizations. It is found that by including topological and shape optimizations, the FPM's dynamic and stiffness properties can be improved significantly.

A FPM that has optimal sub-chains can be synthesized by first using the kinematic approach to determine its overall topology. Subsequently, a structural optimization method is applied to synthesize the sub-chains of the FPM by determining their optimal topology, shape and size sequentially. The topological and shape optimizations aim to select an optimal configuration for the FPM to realize its desired kinematics. This is achieved by formulating optimization problems that can maximize the stiffness ratios of the FPM. Based on the optimal topology and shape, a size optimization is then used to optimize the FPM's dynamic properties.

The proposed synthesis approach is illustrated via designing a planar $X - Y - \theta_z$ FPM. This FPM is evaluated experimentally to have a large workspace of 1.2 mm $\times$ 1.2 mm $\times$ $6°$, bandwidth of 102 Hz, and stiffness ratios above 120. The improvement in stiffness ratio is significant compared to existing centimeter-scale flexural mechanisms with 3-degrees-of-freedom. The stiffness ratios of these flexural mechanisms are typically between $0.5 - 50$ [7, 8, 9, 12, 13, 14, 49, 50]. Furthermore, the bandwidth of existing large workspace flexural mechanisms, which have translational and rotational deflections greater than 0.5 mm and $0.5°$ respectively, do not exceed 45 Hz [7, 8, 12, 49]. From the synthesized FPM, we have demonstrated the benefits of performing topological and shape optimizations on the sub-chains. It should be noted that there is no loss of generality in applying the proposed approach to optimize the natural frequency of higher vibrational modes. We envision that the proposed design methodology can be used universally to create multi-degrees-of-freedom FPMs that have optimal dynamic and stiffness properties.

Chapter 4

Shape-Programmable Magnetic Soft Robots

This chapter proposes the second design methodology, which enables scientists and engineers to program miniature soft robots for desirable time-varying shapes with high spatial and temporal resolutions. We demonstrate the proposed methodology by first introducing the theory and the overview of the methodology in section 4.1. Subsequently, we show the proposed fabrication technique that allows a non-uniform magnetization profile to be programmed in both directions and magnitude in section 4.2. The proposed methodology and fabrication technique are then applied to create various small-scale soft robots in sections 4.3 and 4.4. Lastly, section 4.5 will provide a summary for the chapter.

4.1 Theory and Methodology

Here we present the generic theory and overview of our proposed methodology that allows scientists and engineers to program miniature soft robots with desirable time-varying shapes. The programming steps are sufficiently robust to be applied across materials with arbitrary geometries and they are summarized in Fig. 4.1. Following the steps in Fig. 4.1, we first specify the

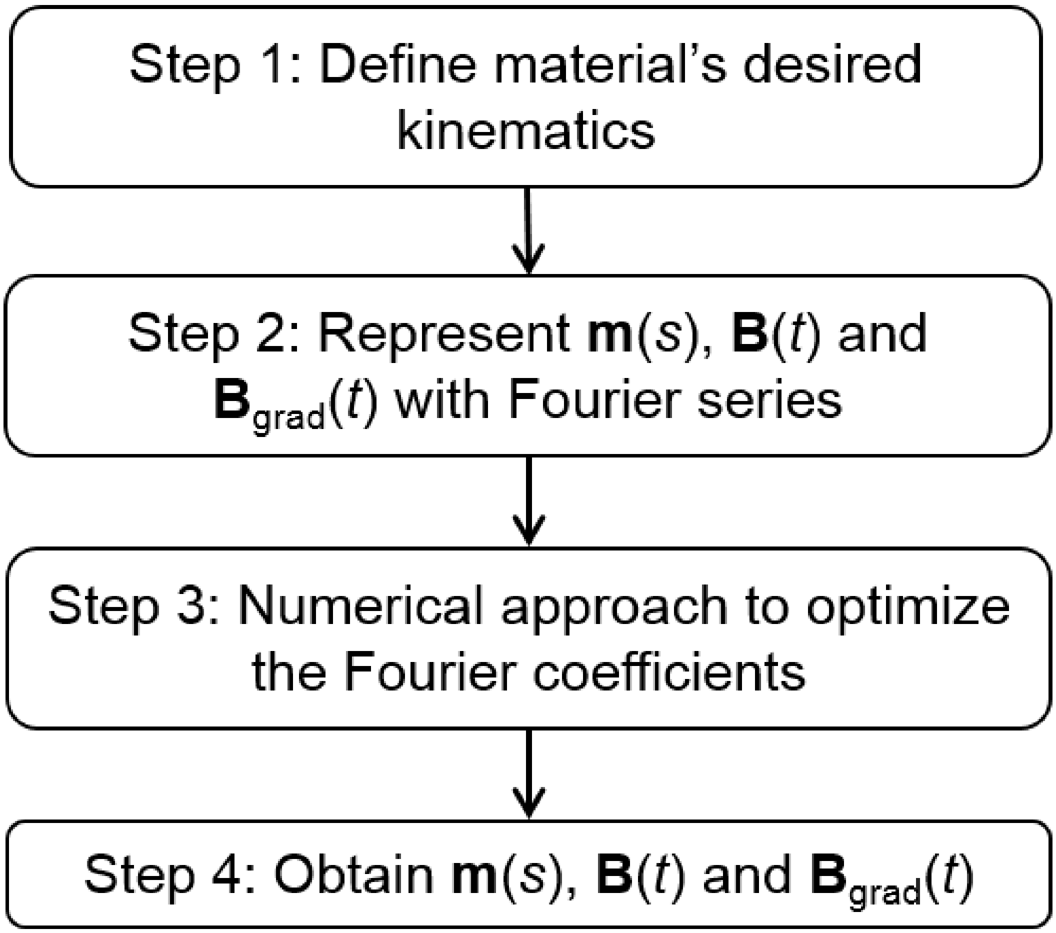

Figure 4.1: The generic programming steps required to create desirable time-varying shapes. The first step is to define the robot's desired kinematics or time-varying shapes. Subsequently, **m**(s), **B** and $\mathbf{B}_{grad}$ are represented with corresponding Fourier series. An optimization process is then implemented to determine optimal Fourier coefficients for the magnetic actuation.

desired time-varying displacement fields (u, v, w) for the materials where u, v and w represent the translational deflections along the x-, y- and z-axis, respectively. Based on these deflections, the time-varying deformation gradient tensor, **F**, and strains can be computed. The resultant time-varying strains across the materials are given as

$$\begin{aligned} e_{ij} &= \frac{1}{2}(u_{i,j} + u_{j,i}) \\ \omega_{ij} &= \frac{1}{2}(u_{i,j} - u_{j,i}) \\ \epsilon_{ij} = e_{ij} + \frac{1}{2}(e_{ik} &+ \omega_{ik})(e_{kj} + \omega_{kj}) \end{aligned} \tag{4.1}$$

where ϵ_{ij} is the component of the Lagrangian strain tensor and the subscripts indicate the Cartesian directions, i.e., $i,\ j,\ k\ =\ 1, 2, 3$. The above equations are written in index notation for convenience. The relationship between the strains and stresses within the materials can be expressed by

$$\mathbf{S} = \mathbf{D}\boldsymbol{\epsilon} \tag{4.2}$$

where **S** is the stress tensor in Lagrangian description, i.e., the second Piola-Kirchhoff stress (2nd PK stress), and **D** is a 9×9 matrix of the coefficients determined by the material properties.

After we determine the stress distribution within the materials, we establish the quasi-static analysis. Because it is more desirable to perform the quasi-static analysis in Eulerian description, we convert the 2nd-PK stress into the Cauchy stress in the Eulerian description as

$$\boldsymbol{\sigma} = J^{-1}\mathbf{F} \cdot \mathbf{S} \cdot \mathbf{F}^{\mathrm{T}} \tag{4.3}$$

where $J = \det(\mathbf{F})$. According to the theory for electromagnetic-elastic solids [121], the quasi-static equations can be written in index notation as

$$
\begin{aligned}
\sigma_{kl,l} + f_l &= 0 \\
(\sigma_{kl} - \sigma_{lk}) + \tau_i &= 0
\end{aligned}
\tag{4.4}
$$

where $\sigma_{kl,l}$ is the component of the Cauchy stress tensor and f_i and τ_i are the external body force and torque per unit volume in the i^{th}-direction, respectively. The external body forces and torques per volume that are applied from the magnetic field, **B**, are functions of the local magnetization vector, **m**:

$$
\begin{aligned}
\boldsymbol{\tau}_m &= \mathbf{m} \times \mathbf{B} \\
\mathbf{f}_m &= (\mathbf{m} \cdot \bigtriangledown)\mathbf{B}
\end{aligned}
\tag{4.5}
$$

When Eq. (4.5) is expressed in index notation, it becomes

$$
\begin{aligned}
f_i &= m_i B_{i,j} \\
\tau_i = B_k m_l - B_l m_k &= \epsilon_{kli} m_l B_k.
\end{aligned}
\tag{4.6}
$$

Because we must account for the change in the magnetization profile after the material has deformed, we must map the magnetization profile from its initial un-deformed state to the current deformed state. As **m** is defined as the magnetization per unit volume, its magnitude varies similarly to the density of a body that undergoes a deformation. Thus, **m** can be defined as

$$
\mathbf{m} = \frac{d\mathbf{M}}{dV} \tag{4.7}
$$

where $d\mathbf{M}$ is magnetic moment within the volume of dV. When a deformation occurs, the magnetic moment changes its orientation, and the magnitude of the volume is also changed:

$$
\begin{aligned}
d\mathbf{M}' &= Rd\mathbf{M} \\
dV' &= JdV
\end{aligned}
\tag{4.8}
$$

where R is the rotational component of **F**, which can be found by the polar decomposition of **F**. Therefore, the magnetization vector under deformation can be written as

$$
\mathbf{m}' = \frac{d\mathbf{M}'}{dV'} = \frac{Rd\mathbf{M}}{JdV} = \frac{R}{J}\mathbf{m}. \tag{4.9}
$$

This implies that the magnetic torque/forces in the deformed state can be expressed as $\boldsymbol{\tau}'_m = \mathbf{m}' \times \mathbf{B}$ and $\boldsymbol{f}'_m = (\mathbf{m}' \cdot \nabla)\mathbf{B}$. By substituting these variables back into Eqs. (4.4) and (4.6), we obtain the equilibrium equations expressed explicitly with the magnetic torques and forces. To generalize the approach to solve for these magnetic torques and forces, we use a corresponding spatial set of Fourier series to represent the magnetization profile and a temporal set of Fourier series to represent the magnetic fields (step 2 in Fig. 4.1). Subsequently, we will employ an optimization approach to determine the optimal Fourier coefficients (step 3 in Fig. 4.1). This determines the **m** and **B** necessary to achieve the time-varying shapes for a programmable material with non-planar geometries (step 4 in Fig. 4.1). The benefit of using Fourier series to represent $\mathbf{m}(s)$ and $\mathbf{B}(t)$ is that they are inclusive of all possible mathematical functions. Thus, this enables our proposed programming method to be highly versatile, and it can be used as a generic approach. We will show the details of our optimization formulations via programming large deflecting beams in the next sub-section.

4.1.1 Programmable beams

While the presented theory in the previous sub-section is generic for materials with arbitrary geometries, our current fabrication technique is limited to programming two-dimensional beams. Thus, we will simplify the theory to suit beams with large or small bending deflections here. In

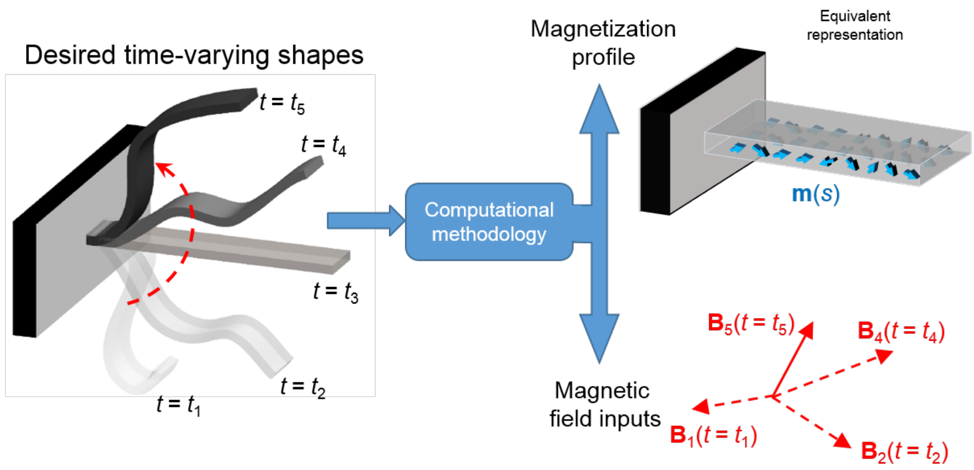

Figure 4.2: The computational methodology used to magnetically program soft elastomeric composite materials with complex time-varying shapesWe illustrate this concept with a straight beam that can be programmed to achieve the desired shapes shown on the left. Our proposed approach uses numerical simulations to automatically determine the necessary magnetization profile, $\mathbf{m}(s)$, and magnetic field control inputs, $\mathbf{B}(t)$, for the material (shown on the right). The given $\mathbf{m}(s)$ and $\mathbf{B}(t)$ are only used as an illustration.

particular, the critical steps to acquire the necessary magnetization profiles and actuating magnetic fields are provided (see Fig. 4.2 for an illustration).

Although the boundary conditions for the beams are highly important and will be discussed in the next sub-section, we simplify our discussion by starting with these boundary conditions: the beam is fixed at $s = 0$ and has a free end at $s = L$ (Fig. 4.3(i)). Using these boundary conditions and without any loss in generality, we describe the bending deflections of the beam with a global frame that has its z-axis parallel to the beams bending axis.

Because we assume that the shape of the beam is known across all time frames, the torque balance equation for an arbitrary infinitesimal element that is shown in Fig. 4.3(ii) at a given time, t, can be expressed as

$$\tau_m A + v\cos\theta - h\sin\theta = -\frac{\partial M_b}{\partial s}. \tag{4.10}$$

The variable M_b represents the beams bending moment, and h and v correspond to the x- and y-axis internal forces within the beam, respectively. The other variables τ_m and A represent

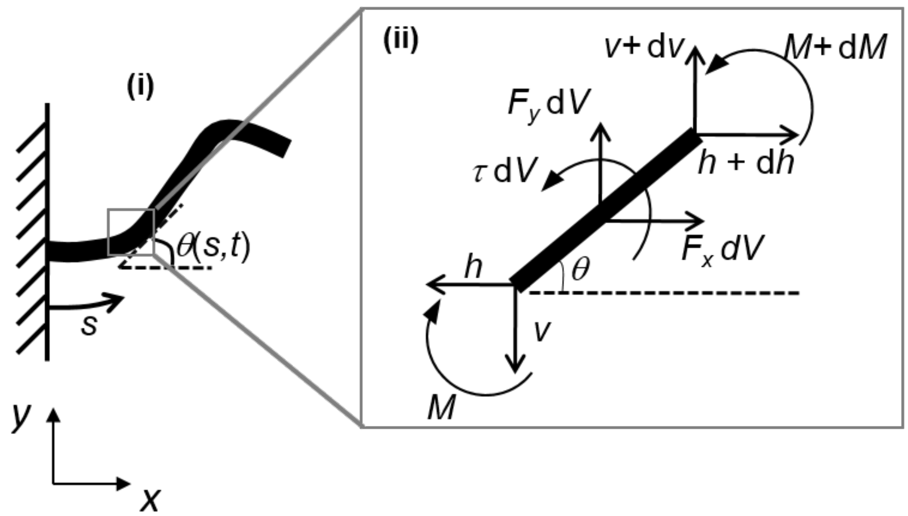

Figure 4.3: Analysis for a large deflecting beam that has an arbitrary deflection. Based on the desired deflection in (i), a quasi-static analysis can be conducted on (ii). The beam is fixed at $s = 0$ and has a free-end at $s = L$.

the applied magnetic torque and the cross-sectional area of the beam, respectively. In a similar manner, the force balance equations of the infinitesimal element can be expressed as

$$F_x = -\frac{1}{A}\frac{\partial h}{\partial s},\ F_x = -\frac{1}{A}\frac{\partial v}{\partial s}, \tag{4.11}$$

where F_x and F_y represent the applied magnetic forces in the x- and y-axes, respectively.

Thus, by using the Euler-Bernoulli equation and substituting Eq. (4.11) into Eq. (4.10), the desired deflections can be expressed explicitly by the actuating magnetic forces and torques as follows:

$$\tau_m A + \left(\int_s^L F_y \mathrm{d}s\right)\cos\theta - \left(\int_s^L F_x \mathrm{d}s\right)\sin\theta = -\frac{\partial M_b}{\partial s} \tag{4.12}$$

The applied magnetic forces and torques are dictated by the magnetization profile and actuating magnetic fields, and their relationships can be mathematically described as

$$\tau_m = [0 \quad 0 \quad 1]\left(\mathbf{R}(s,t)\mathbf{m}(s) \times \mathbf{B}(t)\right) \tag{4.13}$$

The rotational matrix, $\mathbf{R}(s,t)$, is used to account for the orientation change in the magnetization profile due to the beam's large deflection, and it is given as

$$\mathbf{R} = \begin{bmatrix} \cos\theta & -\sin\theta & 0 \\ \sin\theta & \cos\theta & 0 \\ 0 & 0 & 1 \end{bmatrix} \tag{4.14}$$

As described earlier, in contrast to other previous magnetic programming studies, we do not use human intuition to derive the necessary $\mathbf{m}(s)$ and $\mathbf{B}(t)$. Instead, we use computers to automatically generate them by first representing them with corresponding Fourier series:

$$\mathbf{m}(s) = \begin{bmatrix} \sum_{i=0}^{n}\{a_i\cos(i\omega_s s) + b_i\sin(i\omega_s s)\} \\ \sum_{i=0}^{n}\{c_i\cos(i\omega_s s) + d_i\sin(i\omega_s s)\} \\ 0 \end{bmatrix}, \mathbf{B}(t) = \begin{bmatrix} \sum_{j=0}^{m}\{\alpha_j\cos(j\omega_t t) + \beta_j\sin(j\omega_t t)\} \\ \sum_{j=0}^{m}\{\gamma_j\cos(j\omega_t t) + \eta_j\sin(j\omega_t t)\} \\ 0 \end{bmatrix},$$

$$\begin{bmatrix} \frac{\partial B_x}{\partial x} \\ \frac{\partial B_y}{\partial x} \\ \frac{\partial B_y}{\partial y} \end{bmatrix} = \begin{bmatrix} \sum_{j=0}^{m}\{\epsilon_j\cos(j\omega_t t) + \delta_j\sin(j\omega_t t)\} \\ \sum_{j=0}^{m}\{\lambda_j\cos(j\omega_t t) + \mu_j\sin(j\omega_t t)\} \\ \sum_{j=0}^{m}\{\rho_j\cos(j\omega_t t) + \sigma_j\sin(j\omega_t t)\} \end{bmatrix}. \tag{4.15}$$

Thus, by substituting the fitting functions in Eq. (4.15) into Eq. (4.10), we can rewrite this equation as

$$
\begin{aligned}
\sum_{i=0}^{n}\sum_{j=0}^{m}\{[a_i\gamma_j - c_i\alpha_j]\cos(\theta)\cos(i\omega_s s)\cos(j\omega_t t)+\\
... - [d_i\eta_j + b_i\beta_j]\sin(\theta)\sin(i\omega_s s)\cos(j\omega_t t)\}\\
+\cos\theta\sum_{i=0}^{n}\sum_{j=0}^{m}\{[a_i\lambda_j + c_i\rho_j]\int_s^L \cos(\theta)\cos(i\omega_s s)\cos(j\omega_t t)\mathrm{d}s+\\
... - [b_i\sigma_j - d_i\mu_j]\int_s^L \sin(\theta)\sin(i\omega_s s)\cos(j\omega_t t)\mathrm{d}s\}\\
-\sin\theta\sum_{i=0}^{n}\sum_{j=0}^{m}\{[a_i\epsilon_j + c_i\lambda_j]\int_s^L \cos(\theta)\cos(i\omega_s s)\cos(j\omega_t t)\mathrm{d}s+\\
... - [b_i\mu_j - d_i\delta_j]\int_s^L \sin(\theta)\sin(i\omega_s s)\cos(j\omega_t t)\mathrm{d}s\} = -\frac{EI}{A}\frac{\partial^2\theta}{\partial s^2}
\end{aligned}
\tag{4.16}
$$

where the left side of the equation is a linear combination of the products of the Fourier coefficients. We use a computational approach to determine the optimal values of the Fourier coefficients so Eq. (4.16) can be satisfied. First, we discretize the motion of the beam into p number of time frames, i.e., $t = t_0; t = t_1; \ldots ; t = t_p$. Similarly, in each time frame, the length of the beam is divided into q number of segments, i.e., $s = s_0; s = s_1; \ldots ; s = s_q = L$. Thus, we create q new equations for each time frame by substituting different values of s across the entire beam length into Eq. (4.16). By assembling all of the equations across all time frames, there are a total of $p \times q$ equations that are linearly dependent on the products of the one-dimensional Fourier coefficients. This can be written in matrix form as

$$
\mathbf{Ku} = \mathbf{M}_b \tag{4.17}
$$

Subsequently, we solve for the optimal Fourier coefficients by performing the following optimization process:

$$
\begin{aligned}
\text{minimize} \;\; & f = (\mathbf{Ku} - \mathbf{M}_b)^T \mathbf{Q} (\mathbf{Ku} - \mathbf{M}_b) \\
\text{subject to:} \;\; & |\mathbf{m}(s)| \le m_{\max} \\
& |\mathbf{B}(t)| \le B_{\max}.
\end{aligned}
\tag{4.18}
$$

where $\mathbf{Q}$ is a matrix that gives different weightings/importance to different time frames/shapes. The time frames that are deemed to be more important have higher weightings. Physically, the optimization process in Eq. (4.18) minimizes the difference between the magnetic actuation and the required first derivative of the bending moment within the beam. This optimization process is solved numerically by using solvers, such as a genetic algorithm and gradient-based solvers. More information pertaining to the nature of these solvers can be found in [122, 123].

After the optimization solvers determined the optimal Fourier coefficients, the necessary $\mathbf{m}(s)$ and $\mathbf{B}(t)$ required to achieve the desired time-varying shapes were determined.

4.1.2 Boundary conditions

To achieve the desired time-varying shapes, the boundary conditions of the materials must always be satisfied. Generally, there are two types of boundary conditions: the fixed and free ends of the robots (see Fig. 4.4A as an illustration for beams). For the fixed ends, the desired kinematics, such as their desired deflections must be zero at all time-instants. On the other hand, as it is difficult to create magnetic torques and forces at the free ends, the bending moment and shearing forces must be constrained to be zero at these locations. However, because not all time-varying shapes have a zero bending moment and shearing force at their free ends, we introduce a method that can overcome this limitation.

Our proposed method is to extend the desired dimensions of the materials artificially. Subsequently, the bending moment and shearing forces of the beam at the artificial extension is

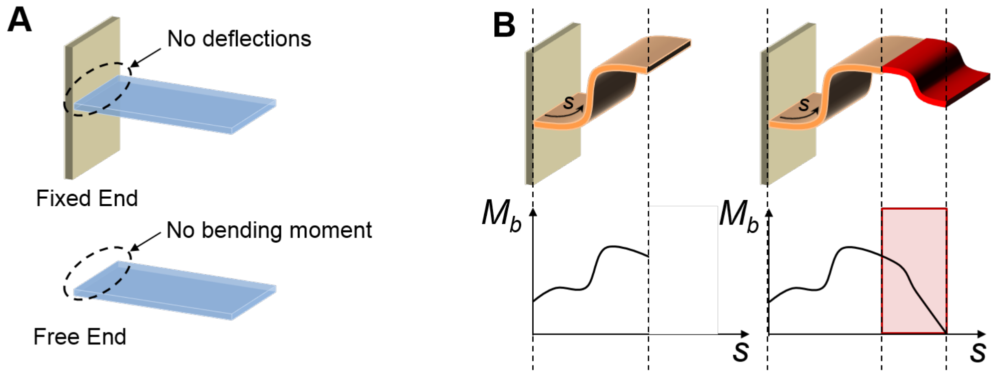

Figure 4.4: Necessary boundary conditions for time-varying shapes. A. The conditions used to obey the boundary conditions. For a fixed end, there should not be any deflections. By contrast, there should be no bending moment at the free end. B. Creation of an artificial extension to satisfy the boundary conditions for the free-ends. At all of the time instants, the bending moment at the free end should be zero, as achieved by introducing an artificial extended free-end (indicated by the red portions). The bending moment along this artificial extension was fitted by a polynomial function so that its bending moment at the free end was always zero.

gradually reduced to zero by using a polynomial fitting curve (Fig. 4.4B). We can determine the necessary magnetization profile for this extension to satisfy the free-end boundary condition by including the artificial extension into the Fourier series representation of $\mathbf{m}(s)$.

4.2 Fabrication Technique

Here, we present the fabrication technique to create the desired magnetization profile for a programmable beam. The required steps are illustrated in Fig. 4.5.

The programmable magnetic soft composite material consists of two components: a passive component and an active component that can be stimulated by magnetic excitation. The active component is created by embedding fine neodymium-iron-boron (NdFeB) particles that have an average size of 5 m (MQFP, Magnequench) into a soft silicone rubber (Ecoflex 00-10, Smooth-on, Inc.). The volume ratio for the NdFeB particles and Ecoflex 00-10 is 0.15:1. However, the passive component is created by embedding aluminum (Al) powder with an average particle size of 5 m into the same type of silicone rubber with the same volume ratio. The volume ratio of

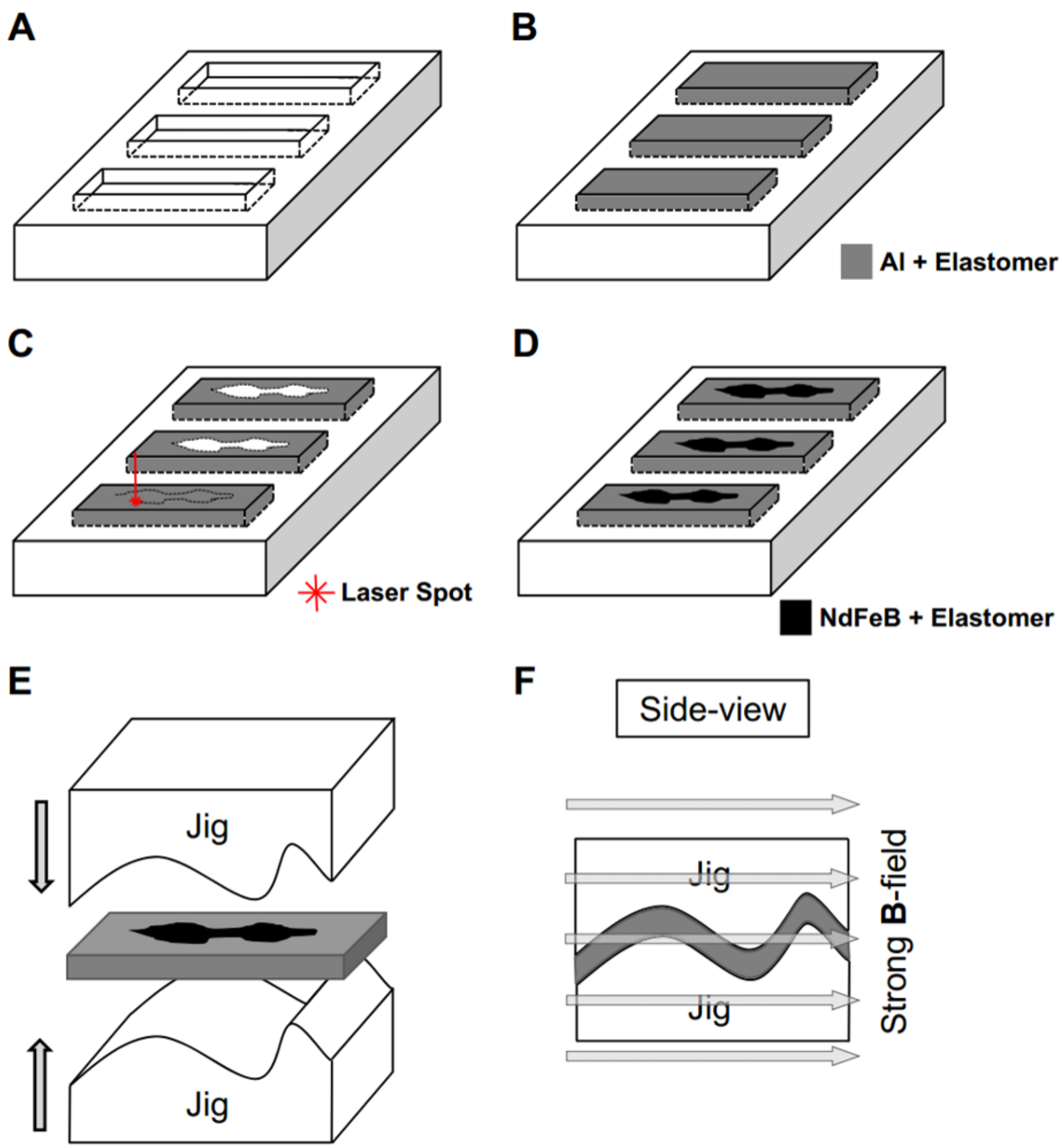

Figure 4.5: The fabrication procedure to create a programmable magnetic soft composite beam. A. A negative mold for the beam. B. The passive component, Al + Ecoflex, was poured into the mold in liquid form and allowed to cure. C. Based on the programmable magnetization profile, a band of non-uniform width was cut out with a laser cutter. D. The active component, NdFeB + Ecoflex, was then poured and cured to replace the band. E. The beam was bent into the jig profile. F. The beam was magnetized with a strong B-field (approximately 1 T).

the active and passive components is selected such that their elastic modulus will match (see Appendix B), providing the composite with a uniform elastic modulus. The relationship between the passive components volume ratio and its resultant elastic modulus was experimentally characterized (see Appendix B). To create a non-uniform magnetization profile that has a varying magnitude, the distribution between the passive and active components must be patterned. The locations that have a higher magnitude of magnetization will have more active components. To achieve this, a two-step micro-molding process was adopted. First, a negative mold that had the desired geometries of the beams was created by computer numerical control machining on an acrylic sheet. The passive component (in liquid form) was first poured into the negative mold and allowed to cure. Once the passive component was fully cured, a laser cutter was used to cut out a band that had a non-uniform width. Subsequently, the active component (in liquid form) was poured into the mold to replace the removed band. The two components formed a composite that had a uniform thickness once the active component was also cured. Due to the non-uniform width of the band, the distribution of the active components could be patterned. This allowed the beam to have a magnetization profile with a varying magnitude when the beam was magnetized by a larges uniform magnetic field (approximately 1 T). The orientation of the desired magnetization profile was created by using jigs to bend/fold the beam during the magnetization process (Fig. 4.6). The curvature of the jigs can be mathematically represented by the following integral:

$$\begin{aligned} x_{\text{jig}}(s) &= \int_0^s \cos(-\phi(s))\mathrm{d}s \\ y_{\text{jig}}(s) &= \int_0^s \sin(-\phi(s))\mathrm{d}s \end{aligned} \tag{4.19}$$

where $\phi = \tan^{-1}(m_y(s)/m_x(s))$, and $\mathbf{m}_x$ and $\mathbf{m}_y$ are the $x-$ and $y-$axis components of $\mathbf{m}(s)$ when the beam is undeformed. The desired jigs were fabricated with the laser cutter. Thus, by magnetizing the beam when it was sandwiched between the jigs, the desired magnetization profile could be obtained after the applied magnetic field and the jigs were removed. The NdFeB

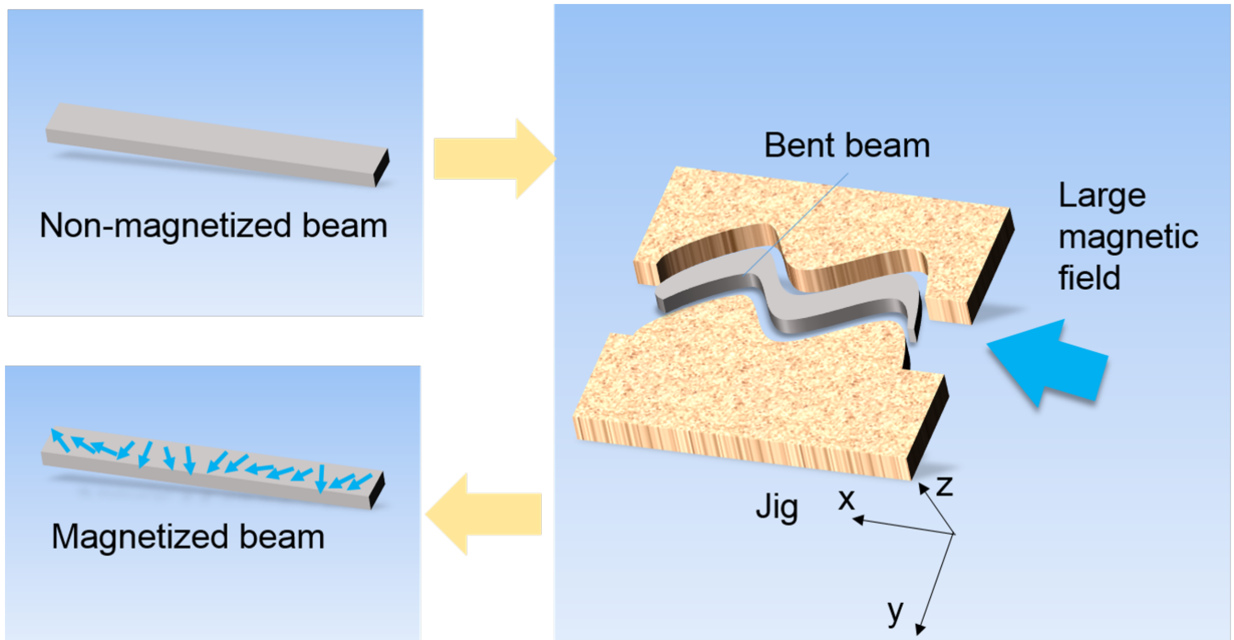

Figure 4.6: Magnetization process of a soft beam. The soft beam was placed in a jig, which was designed based on the magnetization profile from the simulation results. A large external constant uniform magnetic field was applied in the +x direction. The soft beam was magnetically programmed and could still recover to a straight shape after being removed from the jig.

particles that were embedded within the active components were saturated by the large magnetizing field.

4.3 Programmable beams with simple time-varying shapes

For the first experimental demonstration of our shape-programming methodology, a millimeter-scale beam was programmed to create a single shape when it was subjected to a constant **B** (Fig. 4.7A). We showed that, by using the obtained $\mathbf{m}(s)$ from our computational method, the beam achieved its desired cosine function shape when magnetically actuated (Fig. 4.7B).

Next, the effectiveness of our methodology was demonstrated by programming various millimeter-scale beams to create multiple desired shapes. We began with programming a beam that could achieve simple time-varying shapes. For this beam, the time-varying shapes were divided into 100 discrete time frames. In each time frame, the beams curvature was held constant

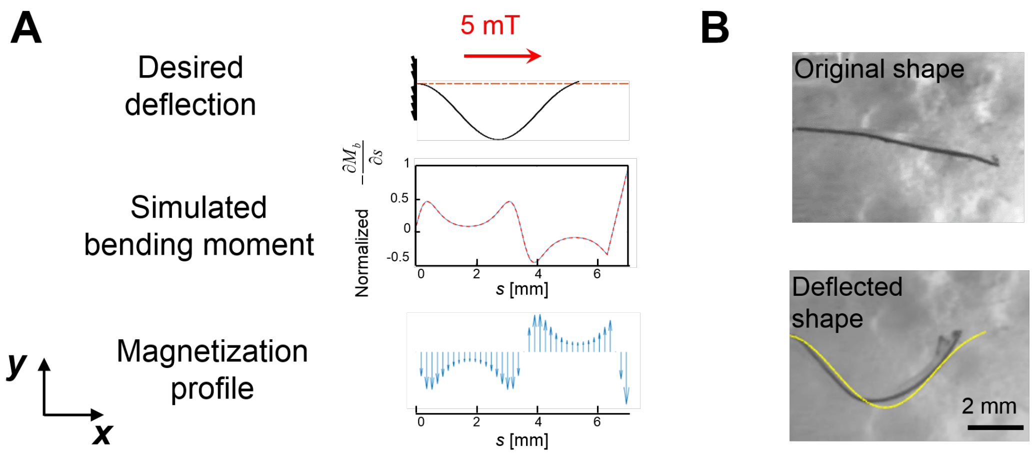

Figure 4.7: A simple proof-of-concept of the proposed method in which a beam is programmed to create a shape resembling a cosine function when it is subjected to a 5 mT uniform magnetic field input. A. Desired shape, and simulated first derivative of the bending moment and necessary magnetization profile along the beam. The simulated first derivative of the bending moment plot has two overlapping curves. The blue curve represents the desired first derivative of the bending moment required to create the desired shape, and the dotted red curve represents the first derivative of the bending moment generated by magnetic actuation. The plotted magnetization profile is along the pre-deformed beam. The obtained experimental results are shown in B. The yellow line represents the desired programmed shape for this demonstration. The beam achieved its programmed shape when it was subjected to a 5 mT magnetic field.

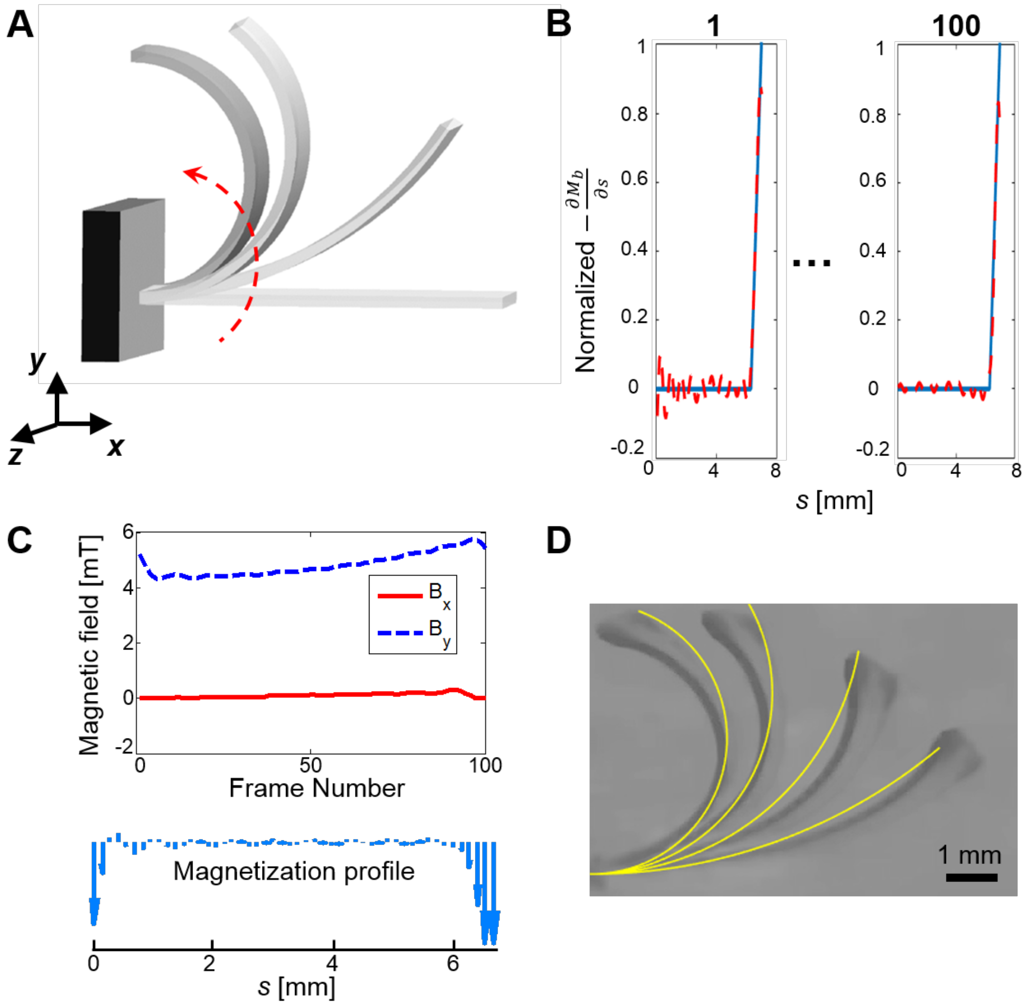

Figure 4.8: Programming soft composite materials that can gradually fold up into a semi-circle. A. Schematic of a soft beam programmed to fold up under magnetic excitation. Although we illustrated this motion with only four shapes, there were a total of 100 distinct shapes throughout this motion. B. Optimization results for the desired first derivative of the bending moment. Each plot represents the desired first derivative of the bending moment of the beam for one time frame. The frame number for each time frame is represented by the number at the top of it. In the simulations, the time difference between each time frame is 0.01 seconds. The blue lines in the time frames represent the desired first derivative of the bending moment, and the dotted red lines represent the obtained first derivative of the bending moment created by the magnetic actuation. The x-axis of each plot represents the length of the beam, which ranges from $s = 0$ mm to 7 mm. C. The required magnetization profile, $\mathbf{m}(s)$, and the magnetic field, $\mathbf{m}(s)$, to achieve the desired time-varying shapes. This magnetization profile is along the pre-deformed straight beam. Using the coordinate system in A as a reference, the variables Bx and By in the magnetic field plot represent the x- and y-axis components of the magnetic field, respectively. D. Snapshots of a single beam curling up under magnetic excitation. The yellow lines represent the corresponding desired time-varying shapes. E. A more quantitative representation for the magnetization profile).

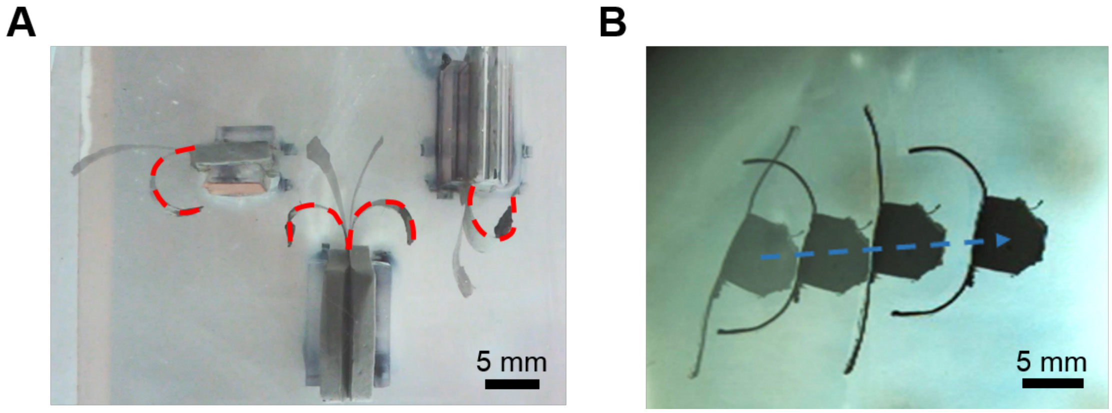

Figure 4.9: "CMU" logo and jellyfish-like robot. A. Four soft beams made of the programmable material are shown deforming into a reversible CMU logo under magnetic excitation. To visualize the logo better, we highlighted the final "CMU" shape with dotted red lines. B. A jellyfish-like robot equipped with two soft tentacles made of the programmable soft composite material. The robot could propel itself on an oil-water interface by bending its tentacles back and forth under magnetic excitation.

throughout its length, gradually increasing between each time frame, until the beam curls into a semi-circle (Fig. 4.8A). Despite having time-varying shapes, we achieved appropriate yet simple $\mathbf{m}(s)$ and $\mathbf{B}(t)$ that satisfied Eq. (4.16) (Fig. 4.8B-C). Using the obtained $\mathbf{m}(s)$ and $\mathbf{B}(t)$, we experimentally manipulated the beam to form the desired shapes (Fig. 4.8D). Because the required magnetization profile and magnetic fields were relatively simple, we extended this concept to simultaneously control multiple beams that had similar motions. By organizing several such beams in specific orientations, we created a reversible three-letter "CMU" logo (Fig. 4.9A). We further extended this concept by using two similar beams to form the tentacles of a jellyfish-like robot, which can swim on an oil-water interface. By controlling the time-varying shapes of the tentacles, we were able to create a power stroke and a recovery stroke. When the speed of the power stroke was greater than that of the recovery stroke, we were able to create net propulsion that allowed the jellyfish-like robot to swim against the slope of the oil-water interface (see Fig. 4.9B). The jellyfish-like robot was also steerable, and the details of such steering strategies will be discussed in section 4.4 subsequently.

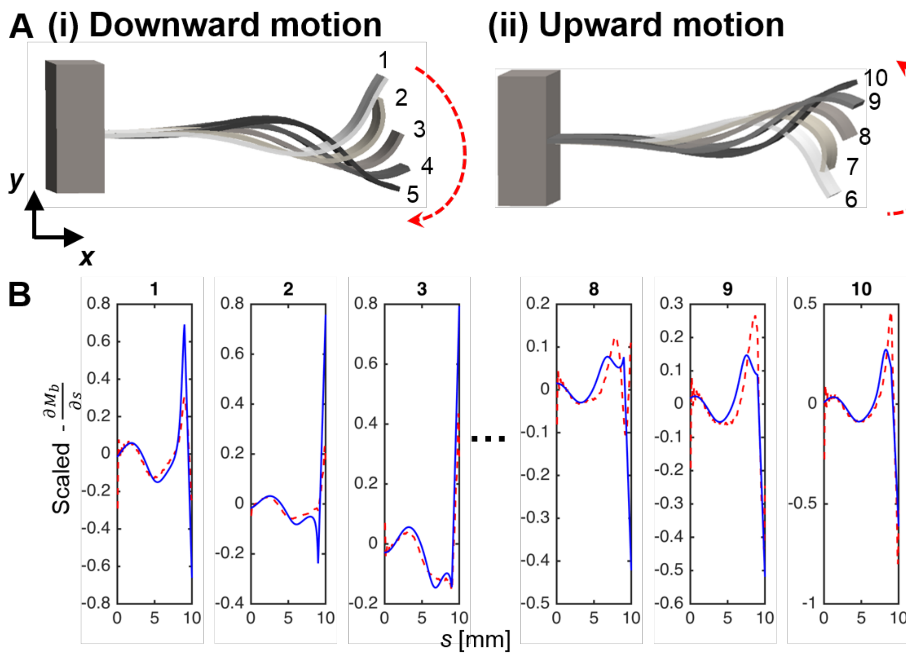

Figure 4.10: Programming a spermatozoid-like undulating soft swimmer: ideal gait and simulation results. A. The desired undulation, which requires a traveling wave with increasing amplitude from the left tip to the right tip. The entire motion can be divided into two strokes: (i) downward motion and (ii) upward motion. The associated time frame for each shape is represented by a corresponding frame number. In the simulations, the time difference between each time frame is 0.1 seconds. B. Optimization results for the desired first-derivative of the bending moment to achieve the undulation. Each plot represents the desired first derivative of the bending moment of the beam for one time frame. The frame number is represented by the number at the top. The blue lines represent the desired first derivative of the bending moment, and the dotted red lines represent the obtained first derivative of the bending moment created by the magnetic actuation. The x-axis for each frame corresponds to the length of the beam, which ranges from $s = 0$ to 10 mm.

4.4 Programmable beams with complex time-varying shapes

Contrary to previous studies for shape-programmable magnetic materials, our methodology is universal and therefore it can also acquire the necessary magnetization profiles and magnetic field control inputs for small-scale materials with complex time-varying shapes. To illustrate this, we created a spermatozoid-like undulating swimmer, as well as an artificial cilium that was able to approximately mimic the complex beating patterns of its biological counterpart. The swimming gait of the spermatozoid-like undulating swimmer has a propagating traveling wave

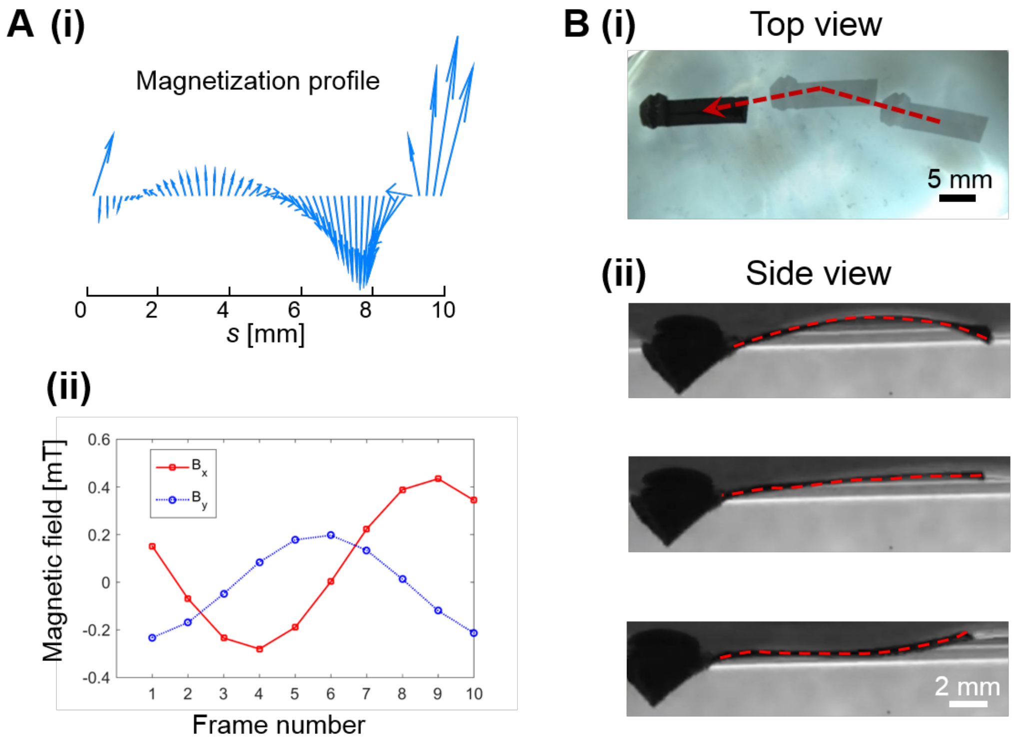

Figure 4.11: Programming a spermatozoid-like undulating soft swimmer: design and experimental results. A. The required magnetization profile and magnetic field for the swimmer. This is the magnetization profile along the pre-deformed beam (see Supplementary Fig. S7 for a more quantitative representation for the magnetization profile). Using the coordinate system in A as a reference, the variables Bx and By in the magnetic field plot represent the x-axis and y-axis components of the magnetic field, respectively. B. Snapshots extracted from the video of the undulating swimmer swimming on an air-water interface (i) top view and (ii) side view of the swimmer.

with amplitudes that gradually increase from the fixed end to the free end (Fig. 4.10A). Despite having such a complex time-varying shape, our computational method allowed us to obtain the necessary $\mathbf{m}(s)$ and $\mathbf{B}(t)$ for creating the desired undulating swimmer (Fig. 4.11A). After fabricating the undulating soft swimmer, we tethered it to visually show the created traveling wave on the swimmers body experimentally. We also demonstrated that the untethered swimmer used its spermatozoid-like undulation to swim on an air-water interface (Fig. 4.11B).

Finally, we created an artificial soft cilium that was able to approximate the complex beating pattern extracted from a biological cilium [124]. This beating pattern can be divided into two

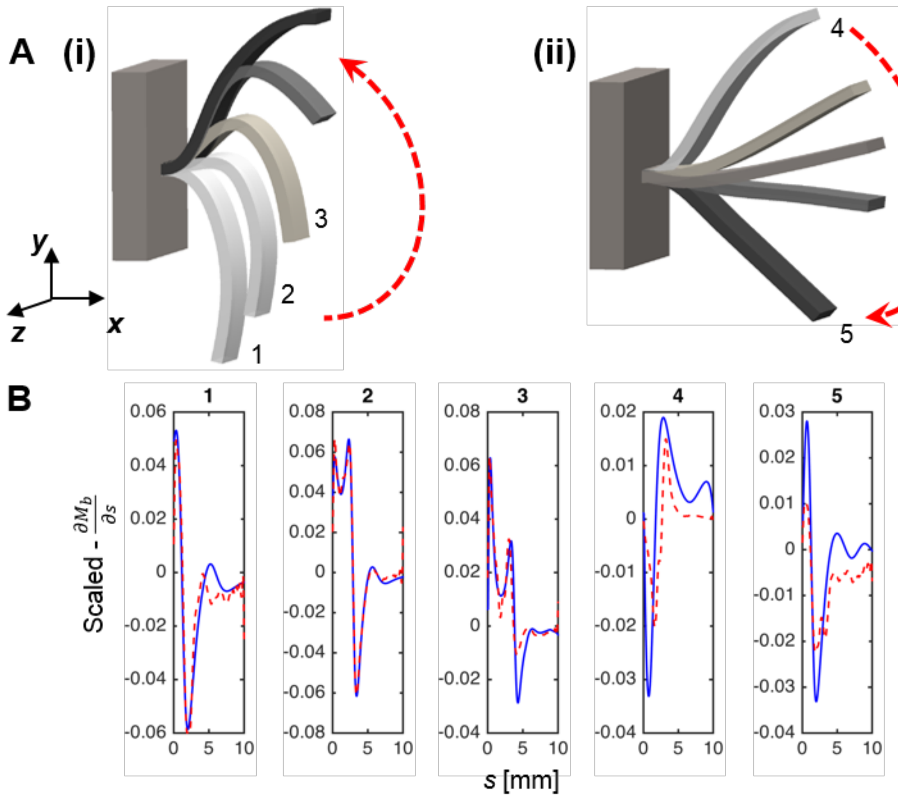

Figure 4.12: Programming an artificial cilium: ideal gait and simulation results. Extracted two-dimensional natural cilia motion as expressed in Cartesian coordinates. The motion pattern includes two strokes: (i) the recovery stroke and (ii) the power stroke. The key time frames used by the artificial cilium are associated with a corresponding frame number. The time difference between each time frame is 0.2 seconds. B. Optimization results for the desired first-derivative of the bending moment to achieve the cilium motion. Each plot represents the desired first derivative of the bending moment of the beam for one time frame. The frame number is represented by the number at the top of it. The blue lines represent the desired first derivative of the bending moment, and the dotted red lines represent the obtained first derivative of the bending moment created by the magnetic actuation. The x-axis for each frame corresponds to the length of the beam, ranging from $s = 0$ to 10 mm. The first three frames were given more weight during the optimization process because they were more important.

strokes the power and the recovery strokes (Fig. 4.12A). Due to the high complexity of the motion, the solution could easily be trapped into a sub-optimal solution if only one optimization process was utilized. Thus, we segregated the programming steps for the artificial cilium into two sequential optimization processes. The first optimization determined the necessary $\mathbf{m}(s)$ and $\mathbf{B}_{\text{rec}}(t)$ for the recovery strokes. The obtained $\mathbf{m}(s)$ was subsequently fed into a second optimization process to determine the required $\mathbf{B}_{\text{pow}}(t)$ for the power strokes. The obtained results are shown in Fig. 4.12B and Fig. 4.13A-B, and the key time-varying shapes that we utilized to closely mimic the complex beating pattern of a biological cilium are shown in Fig. 4.12A. Although other researchers have had some success in creating time-asymmetrical motions for their artificial cilia [125, 126, 127, 128], our artificial cilium is the only one on a millimeter scale that can approximate the motions of a biological cilium.

4.5 Discussion

While the proposed programming method is promising, there are several limitations that need to be addressed in future studies. First, although both $\mathbf{m}(s)$ and $\mathbf{B}(t)$ are represented with their corresponding optimal one-dimensional (1D) Fourier series, the obtained magnetic actuation cannot be represented by a two-dimensional (2D) Fourier series in terms of s and t. This implies that the proposed method cannot produce all possible shapes when $\mathbf{m}(s)$ is time-invariant and $\mathbf{B}(t)$ is position-invariant. However, this limitation may be moderated by developing more powerful electromagnetic coil systems that can allow $\mathbf{B}$ to change spatially, allowing our method to produce a larger range of feasible shapes. While a complete analysis to determine the range of feasible shapes that can be achieved by our method is beyond the scope of this paper, we provide a brief discussion on this topic in section 4.4.2. Second, several metastable shapes may exist for a given control input, and these shapes may cause the programmable material to deform into an undesired shape. Because the selected metastable shape is highly dependent on the previous shape, this limitation can be moderated by using a finer temporal resolution for the shape

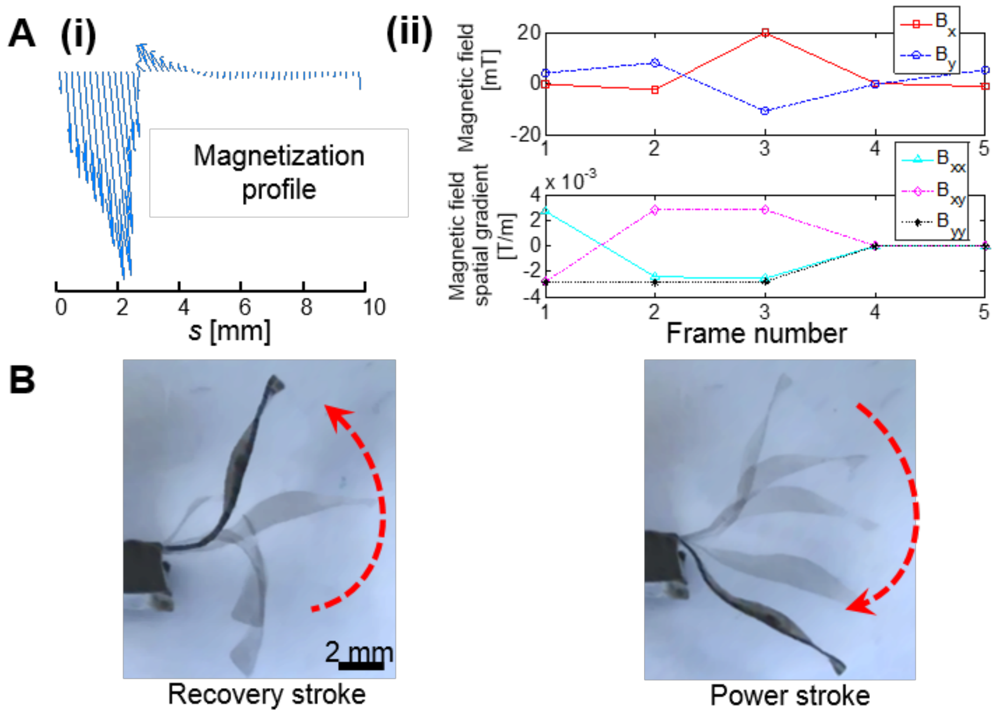

Figure 4.13: Programming an artificial cilium: design and experimental results. A. (i) The required magnetization profile and (ii) the magnetic field and its spatial gradients for the cilium.Using the coordinate system in Fig. 4.12A as a reference, the variables B_x and B_y in the magnetic field plot represent the x-axis and y-axis components of the magnetic field, respectively. The spatial gradients B_{xx}, B_{xy}, and B_{yy} represent $\frac{\partial B_x}{\partial x}$, $\frac{\partial B_y}{\partial x}$, and $\frac{\partial B_y}{\partial y}$, respectively. B. Snapshots extracted from the video of the beating artificial cilium.

trajectories. This moderation reduces the deviation between the desired shape and the previous shape, making it easier to guide the material to deform into the desired shape. Third, as our proposed method uses a numerical optimization approach, the obtained solution may not be the globally optimal solution. New numerical techniques, such as the one used for the cilium case, can be used to overcome this limitation. Fourth, while we provide a generic theory, our current fabrication techniques are limited from experimentally program materials that are smaller than millimeter-scale or with non-planar three-dimensional geometries. As such, one of our future works is to develop higher resolution three-dimensional microfabrication techniques combined with more precise two- and three-dimensional magnetization profile generation techniques for such experimental purposes.

In the subsequent sub-sections, we will also discuss about the steering strategies for untethered miniature robots, the achievable time-varying shapes for our proposed method and other additional discussions.

4.5.1 Steering Strategies

There are several strategies to steer untethered miniature devices magnetically. We introduce the first steering strategy by using the jellyfish-like robot as an example. To implement this strategy, we intentionally constrained the magnetization profile of the beams to be symmetrical around the y-axis of the robots body frame (see Fig. 4.14A). This allowed the robots net magnetization to always be parallel to its body frames y-axis. The net magnetization of the programmable material, $\mathbf{m}_{\text{net}}$, is given as

$$\mathbf{m}_{\text{net}} = A \int_0^L \mathbf{m}(s)\mathrm{d}s \tag{4.20}$$

Because the net magnetization of the robot always aligns with $\mathbf{B}(t)$, we can vary the directions of $\mathbf{B}(t)$ to control the orientation of the robot. Furthermore, because the required $\mathbf{B}(t)$ to change the shape of the tentacles is always approximately in the same direction, we can con-

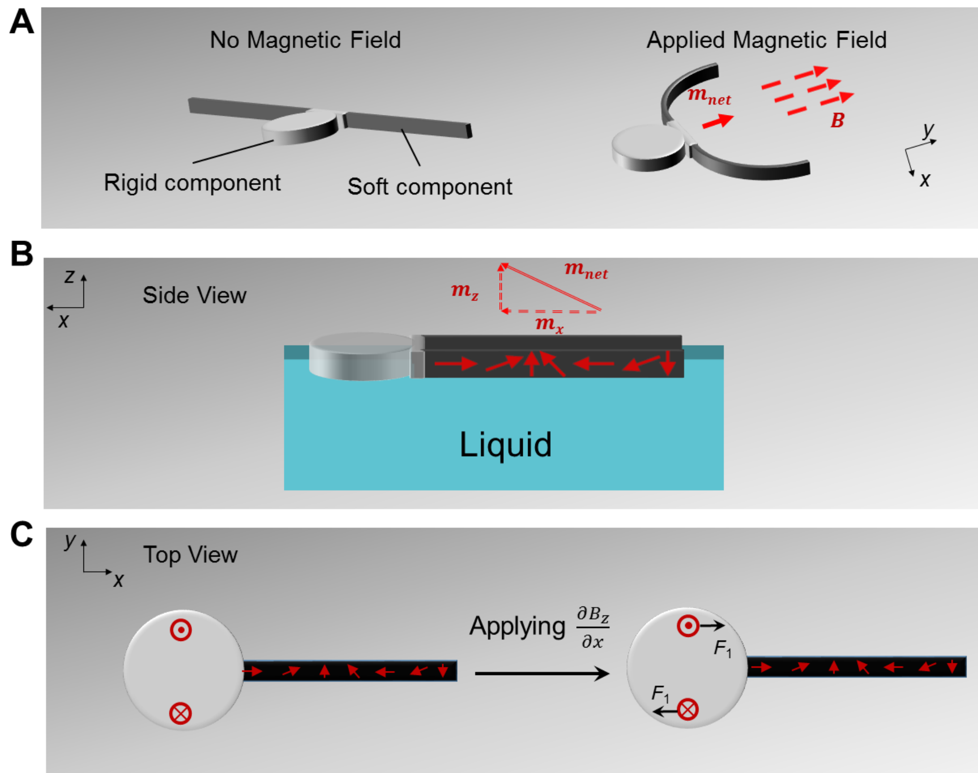

Figure 4.14: Necessary boundary conditions for time-varying shapes. A. The conditions used to obey the boundary conditions. For a fixed end, there should not be any deflections. By contrast, there should be no bending moment at the free end. B. Creation of an artificial extension to satisfy the boundary conditions for the free-ends. At all of the time instants, the bending moment at the free end should be zero, as achieved by introducing an artificial extended free-end (indicated by the red portions). The bending moment along this artificial extension was fitted by a polynomial function so that its bending moment at the free end was always zero.

trol the tentacles shapes by adjusting the magnitude of $\mathbf{B}(t)$ after the robot achieves its desired orientation.

In addition to the first strategy, we present two additional strategies that allow untethered programmable materials to steer in a plane while being able to achieve their desired shape transformations. The second strategy is to constrain certain motions of the programmable material so that it is easier to steer the device. The last strategy is to include a rigid component that can be used to control the devices orientation.

The second strategy can be implemented by placing the material on a liquid interface in which the programmable material is constrained by the surface tension of the fluid. As an illustration, Fig. 4.14B shows the $x - z$ plane of the programmable materials body frame. Due to the surface tension of the fluid, the z-axis components of the net magnetization cannot create rigid-body torques that affect the orientation of the material. Thus, the alignment of the material on the liquid interface is solely dependent on the body frames x-axis component of the net magnetization. Thus, we can control the robots orientation by using an applied $\mathbf{B}(t)$ to align this x-axis component of the net magnetization. We used this strategy to control the orientation of the undulating swimmer.

For the last steering strategy, we can control the orientation of the device by programming the magnetization profile of a rigid component. Multiple feasible magnetization profiles may exist, and an example is shown in Fig. 4.14C. In this case, although the net magnetization for the rigid-component is zero, this component can still provide a rigid-body torque that can steer the orientation of the material. By following the body frame assignment in Fig. 4.14C, a rigid-body torque around the z-axis can be induced on the rigid component when the spatial gradient, $\frac{\partial B_z}{\partial x}$, is applied, allowing the material to steer in the $x - y$ plane. This spatial gradient also induces a z-axis force for the x-axis components of $\mathbf{m}(s)$, and the induced deflections into the plane can be greatly reduced by increasing the stiffness of the beam in that direction. This can be easily achieved by increasing the width of the beam. Thus, it is possible to compensate for any z-axis torque that is induced by the programmable material by controlling the magnitude of the spatial gradient, $\frac{\partial B_z}{\partial x}$. Although we did not implemented this strategy, we demonstrated a similar concept in our previous work to control the orientation of an untethered miniature device [27, 28].

4.5.2 Achievable Time-varying Shapes

Although a complete analysis for determining the number of feasible shapes that are achievable with our method is beyond the scope of this thesis, we provide a brief discussion here. The proposed method cannot produce all possible time-varying shapes for small-scale soft robots because the materials have a time-invariant $\mathbf{m}$ and a global $\mathbf{B}$ that cannot be changed spatially. Thus, the number of programmable shapes for a material depends significantly on the complexity of the shape trajectories. For example, for simple time-varying shapes, such as those shown in Fig. 4.8 and Fig. 4.9, it is possible to create 100 shapes for the entire shape trajectories. However, for extremely complex time-varying shapes, such as those generated by the artificial cilium, we can only plan 5 key shapes for the device. Currently, the only way to determine the number of achievable shapes is to perform the numerical optimization process. If the optimization cannot create the necessary magnetic actuation to match the desired first derivative of the bending moment, the number of shapes must be reduced. This process may have to be iterated several times until it is possible to obtain a good numerical solution. However, we believe that the minimum number of continuous shapes achievable by our proposed method should be two because it is possible to pattern two axes of the magnetization profile independently, i.e., the x- and y-axis components of $\mathbf{m}(s)$.

4.5.3 Additional Discussion

Here, we discuss the possibility of extending the proposed approach to simultaneously determine the magnetization profile for multiple beams and the effects of a $\mathbf{B}$ that can be varied locally in space. Finally, we will discuss about the possibility of changing the speed for the shape transformations in the experiments.

The programming method can determine the magnetization profile for multiple beams simultaneously by using a corresponding set of Fourier series for each beams magnetization profile. For example, if there are r numbers of beams, there will be r sets of Fourier series. Thus, for each time frame, we can create $r \times q$ new equations by substituting different values of s across each beam into Eq. (4.16). By assembling all of the equations across all time frames, there will be a total of $p \times r \times q$ equations that are linearly dependent on the products of the one-dimensional Fourier coefficients. Using the formulations shown in Eq. 4.18, the optimal Fourier coefficients can be determined, thus generating the necessary magnetization profiles for all of the beams.

On the other hand, if $\mathbf{B}$ can be varied locally for l regions, there will be l number of independent $\mathbf{B}$ values, i.e., there will be $\mathbf{B}_1, \mathbf{B}_2, \ldots, \mathbf{B}_l$. Each of these magnetic fields can then be represented by a Fourier series, i.e., there are l sets of them. However, Eq. 4.16 will be slightly modified as we substitute the corresponding $\mathbf{B}$ in each region. In a similar manner, the optimal Fourier coefficients can be solved by Eq. 4.18. The difference in a $\mathbf{B}$ that can be varied locally in space is that it allows the beam to create more feasible motions. Note that a $\mathbf{B}$ that can be varied spatially is easier to be generated for materials in macro-scale because this can be achieved with a much smaller magnitude of magnetic field spatial gradients. The steps to program such macro-scale devices are similar to programming micro-scale devices that have a position-variant $\mathbf{B}$.

Lastly, we discuss about the feasibility of changing the speed for inducing the shape changes. Physically, there is an upper speed limit for the programmable material to change its shape. This limit is dictated by either the speed of the electromagnetic coil system that generates the actuating magnetic fields or the fundamental natural frequency of the material. In our experiments, it is the speed of the electromagnetic system that limits our bandwidth to be 25 Hz. Based on this limitation, we have constrained the fastest component of the Fourier series representing $\mathbf{B}$(t) to be 25 Hz. Reducing the speed for the shape change is, however, much simpler and there is no lower bound for such a change. Thus, for the jellyfish-like robot, we have reduced the speed of the recovery stroke to be approximately 3 times slower than its power stroke.

4.6 Summary

This chapter has introduced a systematic, universal methodology that can enable scientists and engineers to magnetically program desired time-varying shapes for soft materials. In contrast with existing miniature soft robots that have overall dimensions of approximately 1 cm or smaller, our miniature soft robots have the potential to achieve complex time-varying shapes that have high spatial and temporal resolutions. The proposed method was validated with a simple showcase, and we demonstrated its effectiveness by creating a reversible "CMU" logo, a jellyfish-like robot, a spermatozoid-like undulating swimmer and an artificial cilium. Compared to other shape-programmable materials that may require minutes to induce a shape change, our devices can transform into their desired shapes within seconds. This study paves the way for novel miniature devices that are critical in robotics, for smart engineering surfaces or materials, and for biomedical devices. In particular, these miniature devices have great potential to be deployed for unprecedented biomedical applications such as targeted drug delivery as well as minimally invasive surgery.

Chapter 5

Conclusion and Future Works

5.1 Conclusion

In this research, we have presented two new design methodologies for synthesizing optimal compliant mechanisms. The first methodology was created specifically for designing multi-degrees-of-freedom FPMs with optimal stiffness and dynamic properties - overcoming the limitations existed in previous synthesis approaches for flexural mechanisms. In order to implement this methodology, we have developed a new topological optimization algorithm termed the mechanism-based approach, and also a generic semi-analytical dynamic model that can accurately predict the fundamental natural frequencies of FPMs with arbitrary geometries. The effectiveness of the proposed methodology has been illustrated via the synthesis of an optimal $X - Y - \theta_z$ FPM. The significance of our key contributions for this methodology is summarized in the following points:

- **The Development of the Algorithm: The Mechanism-based Approach**

  As many existing topological optimization algorithms may produce infeasible solutions, a new topological optimization algorithm termed the mechanism-based approach has been developed specifically for the proposed design methodology. Based on the required degrees-of-freedom of the compliant mechanism, the mechanism-based approach will first identify various traditional mechanisms that can satisfy this requirement. These mechanisms are termed as seeds and their geometrical characteristics will be used to create the topology of a compliant mechanism. By gradually evolving the seeds' geometrical properties with genetic algorithm, an optimal compliant mechanism will eventually emerge. A notable advantage of the mechanism-based approach is that it will never produce disconnected solid elements because the links of the seed are always physically connected. Furthermore, as the selection of the solid elements is done in a discrete manner, the possibility of having ambiguous "grey" elements is eliminated. Lastly, this algorithm does not overconstrain the topology of the compliant mechanism because it has been shown that even the "topology" of the seeds can be changed. The effectiveness of this algorithm has been evaluated via several case studies, including the development of a μ-gripper, a compliant $\underline{\text{P}}$ joint, and a compliant PR joint that have optimal stiffness characteristics. For all these case studies, it has been shown that these devices are able to exhibit superior stiffness characteristics compared to the ones obtained via intuitive designs. Furthermore, the convergence plots for all of the case studies suggest that the mechanism-based approach has good convergence properties.

- **A Generic Dynamic Model for FPMs**

  In order to have a generic design methodology that can produce FPMs with optimal dynamic properties, the derivation of a universe model that can accurately predict the fundamental natural frequency of a FPM with arbitrary geometries will be required. An analytical model, however, maybe too difficult when the geometries of the sub-chains are too complex. Alternatively, if a full FEA is implemented, the entire optimization process would be too computationally expensive. In view of this, we had proposed a semi-analytical dynamic model where the derivation of the model is divided into two stages. The first stage will use a FEA dynamic condensation to obtain the lump mass and stiffness matrices for the sub-chains. This will be followed by the second stage where the Lagrangian method will use all these lump matrices and the inertia of the end-effector to obtain the equations of motion for the FPM. The accuracy of the model has been evaluated by at least 20 structures with arbitrary geometries. The fundamental natural frequency of these structures obtained by the proposed model has less than 3% deviation compared to a full FEA dynamic model - suggesting high credibility for the model.

- **Design Methodology for Multi-degrees-of-freedom FPMs with Optimal Stiffness and Dynamic Properties**

The proposed design methodology is realized by integrating the benefits of two existing synthesis approaches - the kinematic and the structural optimization approaches. First, the rigid-body-replacement method is used to determine suitable parallel-kinematics configurations for the compliant mechanism. This reduced the complexity of using a structural optimization approach to synthesize a compliant mechanism with multi-degrees-of-freedom - overcoming the previous challenges of existing structural optimization methods. Subsequently, the mechanism-based approach and the generic dynamic model are utilized to synthesize the sub-chains of the FPM by determining their optimal structural topology, shape and size sequentially. By automating this process, the proposed integrated design methodology has the potential to surpass traditional FPMs that are synthesized via the kinematic approach. The effectiveness of the proposed approach is demonstrated via synthesizing a $X - Y - \theta_z$ FPM that has a large workspace of 1.2 mm$\times 1.2$ mm$\times 6°$. This FPM (shown in Fig. 5.1) has significantly better stiffness and dynamic properties over existing 3-degrees-of-freedom, centimeter-scale compliant mechanisms. For example, this FPM can achieve a large translational and rotational stiffness ratio of 130 and 108 respec-

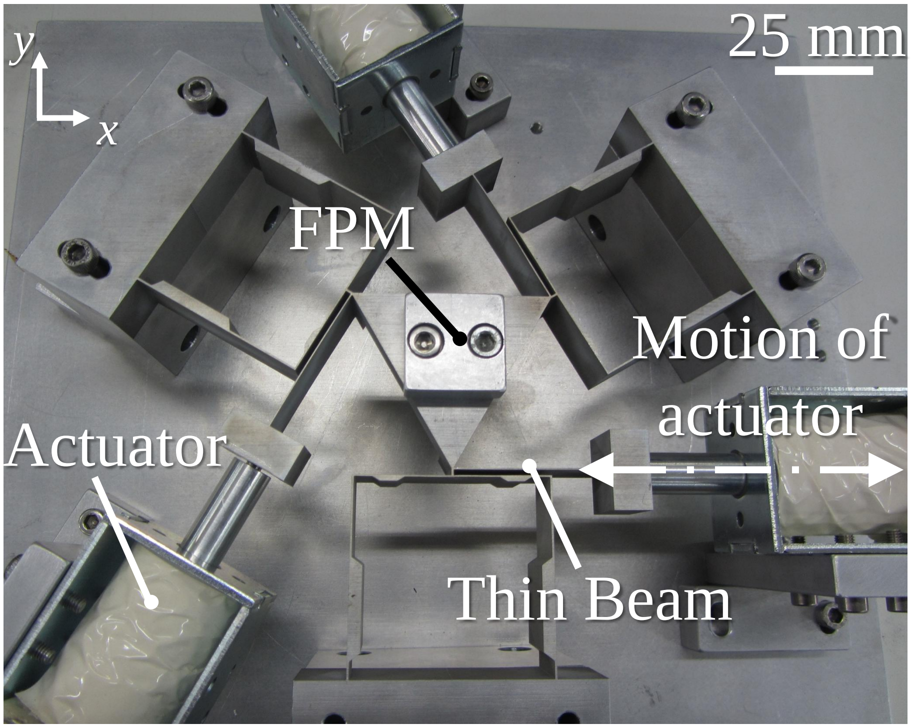

Figure 5.1: The optimal $X - Y - \theta_z$ FPM created by the first design methodology.

tively while existing ones can only achieve 0.5-50. Likewise, the synthesized FPM has a large bandwidth of 117 Hz while other existing large workspace FPMs, which can deflect more than 0.5 mm and 0.5°, can only achieve bandwidths that are lower than 45 Hz. The stiffness and dynamic properties of the FPM have been evaluated experimentally via a prototype. The experimental stiffness properties and bandwidth agree with the simulation results as their deviations are within 5% and 9%, respectively. The proposed FPM can be deployed across a wide range of applications pertaining to biomedical research and various micro/nano-positioning industrial tasks.

The second methodology was created such that it can be a universal method for scientists and engineers to program desirable time-varying shapes with high spatial and temporal resolutions for miniature soft robots that have overall dimensions smaller than 1 cm. We have provided a universal theory, optimization algorithm and fabrication procedure for this methodology. The effectiveness of this programming methodology has been demonstrated via synthesizing several miniature soft robots (tethered and untethered). The significance of this methodology is summarized in the following points:

- **A Universal Shape-Programming Method**

  Our key contribution is to propose a universal programming method that can enable scientists and engineers to magnetically program desired time-varying shapes with high spatial and temporal resolutions for small-scale soft robots. This contribution is highly significant because previous works can only depend on human intuition to guess the necessary magnetization profiles and magnetic fields for their soft robots. As a result, previous works could only program very specific and relatively simple cases, limiting scientists and engineers from fully capitalizing the potential of shape-programmable soft materials. Since we have successfully overcome this limitation, we believe other researchers could use our proposed methodology to develop a wide range of other novel soft programmable active surfaces and devices that are critical in robotics, engineering, and medicine.

- **Design and Development of Jellyfish-like Robot, Spermatozoid-like Robot and Artificial Cilium**

  While this is not our major contribution, we have created a series of high performance devices using our proposed programming method. For example, compared to existing previous works, our artificial cilium and spermatozoid-like robot had been able to create complex time-varying shapes, which allow these soft devices to function in low Reynolds number environments. The creation of these devices suggests that this technology can be further extended to create miniature soft robots, which can potentially realize unprecedented biomedical applications such as targeted drug delivery and minimally invasive surgery.

In summary, this thesis has provided the generic guide for engineers to design optimal compliant mechanisms. The first methodology enables engineers to create multi-degrees-of-freedom FPMs that have optimal stiffness and dynamic properties. We envision that this method will

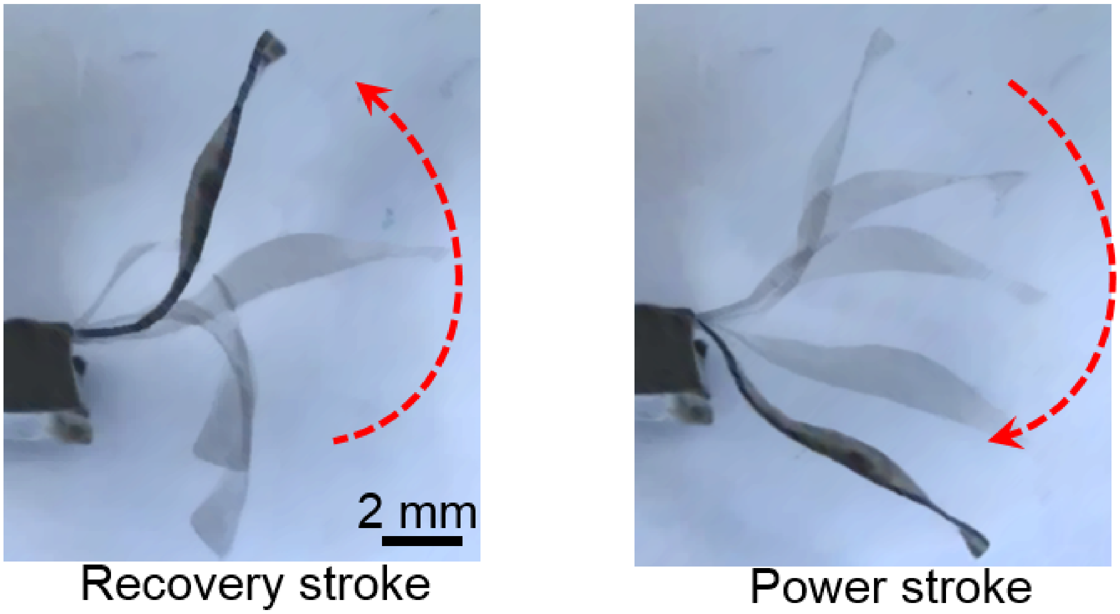

Figure 5.2: The artificial cilium created by the second design methodology.

inspire the design and development of a variety of new high precision machines that have large workspaces, strong capabilities to reject disturbances, and fast transient responses. The second methodology enables scientists and engineers to magnetically program desired time-varying shapes for miniature soft robots. We envision that this methodology can enable other researchers to develop a wide range of other novel soft programmable active surfaces and devices that are critical in robotics, engineering, and medicine.

5.2 Future Works

Although two universal design methodologies for compliant mechanisms have been developed, there remains several aspects in this area that have yet to be explored.

- **Development of other FPMs**

  Currently, the proposed design methodology has only been used to develop a $X - Y - \theta_z$ FPM. It will be interesting, however, to use this methodology to develop other types of planar FPMs like a $X - Y$ precision stage, or other spatial-motioned FPMs like a X–Y–Z or a θ_x–θ_y–Z stage. As the spatial FPMs would require more computational resources, the mechanism-based approach would have to be modified to optimize its computational efficiency for such FPMs.

- **Development of New Control Algorithms**

  It should be noted that control algorithms are also highly important for the flexural mechanisms. Thus, one of our future work is to explore new control algorithms that can optimize the closed-loop characteristics of these machines.

- **Miniature Soft Robots with Non-planar motions**

  While we provide a generic theory, our current fabrication techniques are limited from experimentally program materials that have non-planar deflections. Thus, in order to fully capitalize this technology, a viable future work is to develop higher resolution three-dimensional microfabrication techniques combined with more precise two- and three-dimensional magnetization profile generation techniques that can program these soft robots to achieve non-planar, three-dimensional time-varying shapes.

List of Author's Publication

Journal Publications

1. E. Diller, J. Zhuang, **G. Z. Lum**, M. R. Edwards and M. Sitti, "Continuously distributed magnetization profile for millimeter-scale elastomeric undulatory swimming", *Applied Physics Letter*, vol. 104, no. 174101, April 2014.
2. E. Diller*, J. Giltinan*, **G. Z. Lum***, Y. Zhou and M. Sitti, "Six-degrees-of-freedom remote actuation of magnetic microrobots", *Robotics: Science and Systems*, July 2014. *(Co-First Authors)
3. **G. Z. Lum**, T. J. Teo, G. L. Yang, S. H. Yeo and M. Sitti, "Integrating classical mechanism synthesis and modern topological optimization technique for stiffness-oriented design of three degrees-of-freedom flexure-based parallel mechanisms", *Precision Engineering*, vol. 39, pp. 125-133, January 2015.
4. **G. Z. Lum**, T. J. Teo, G. L. Yang, S. H. Yeo and M. Sitti, "Structural optimization for flexure-based parallel mechanisms - Towards achieving optimal dynamic and stiffness properties", *Precision Engineering*, vol. 42, pp. 195-207, October 2015.
5. E. Diller*, J. Giltinan*, **G. Z. Lum***, Y. Zhou and M. Sitti, "Six-degree-of-freedom magnetic actuation for wireless microrobotics", *International Journal of Robotics Research*, vol. 35, no. 1-3, January 2016, Pages 114-128. *(Co-First Authors)
6. Y. Zhou*, **G. Z. Lum***, S. Sukho, S. Rich and M. Sitti, "Phase change of gallium enables highly reversible and switchable adhesion", *Advanced Materials*, vol. 28, no. 25, May 2016, Pages 5088-5092. *(Co-First Authors)
7. **G. Z. Lum***, Y. Zhou*, X. Dong*, H. Marvi, O. Erin, W. Hu and M. Sitti, "Shape-programmable magnetic soft matter", *Proceedings of National Academy of Sciences*, vol. 13, no. 41, September 2016, Pages E6007-E6015. *(Co-First Authors)

Conference Publications

1. **G. Z. Lum**, T. J. Teo, G. L. Yang, S. H. Yeo and M. Sitti, "Topological optimization for continuum compliant mechanisms via morphological evolution of traditional mechanisms", *4th International Conference on Computational Methods*, Gold Coast, Australia, Nov 2012, pp. 2008-2014.
2. T. J. Teo, **G. Z. Lum**, G. L. Yang, S. H. Yeo and M. Sitti, "Geometrical-based approach for flexure mechanism design", *13th International Conference of European Society for Precision Engineering and Nanotechnology*, Berlin, Germany, May 2013, pp. 184-187.
3. **G. Z. Lum**, T. J. Teo, G. L. Yang, S. H. Yeo and M. Sitti, "A novel hybrid topological and structural optimization method to design a 3-DOF planar motion compliant mechanism", *IEEE/ASME International Conference on Advanced Intelligent Mechatronics*, Wollongong, Australia, July 2013, pp. 247-254.
4. **G. Z. Lum**, E. Diller, and M. Sitti, "Structural optimization method towards synthesis of small scale flexure-based mobile grippers", *IEEE International Conference on Robotics and Automation*, Hong Kong, China, May 2014, pp. 2339-2344.
5. **G. Z. Lum**, M. T. Tuan, T. J. Teo, G. Yang, S.H. Yeo and M. Sitti, "An $XY\theta_z$ flexure mechanism with optimal stiffness properties", *IEEE International Conference on Advanced Intelligent Mechatronics*, Munich, Germany, July 2017, pp. 1103-1110.

Awards

1. Received Third Prize at the 2012 A*STAR-SIMTech Postgraduate Posters Exhibition
2. Finalist for Best Paper Award at the highly prestigious 2014 Robotics: Science and Systems Conference
3. Frontispiece Cover for Advanced Materials, 2016

Appendix A

CAD Drawings for Synthesized Flexural Mechanisms

This section presents the detailed 2-D CAD drawing for the synthesized compliant P and PR joints, the 3$\underline{P}$PR FPM and the optimal $X - Y - \theta_z$ FPM. Except for the 3$\underline{P}$PR FPM, which is constructed by stainless steel, the rest of the flexure mechanisms are made by aluminum. The thickness of the compliant joints are 10 mm while the FPMs' thickness are 20 mm. All of these flexure mechanisms are fabricated by wire-EDM techniques.

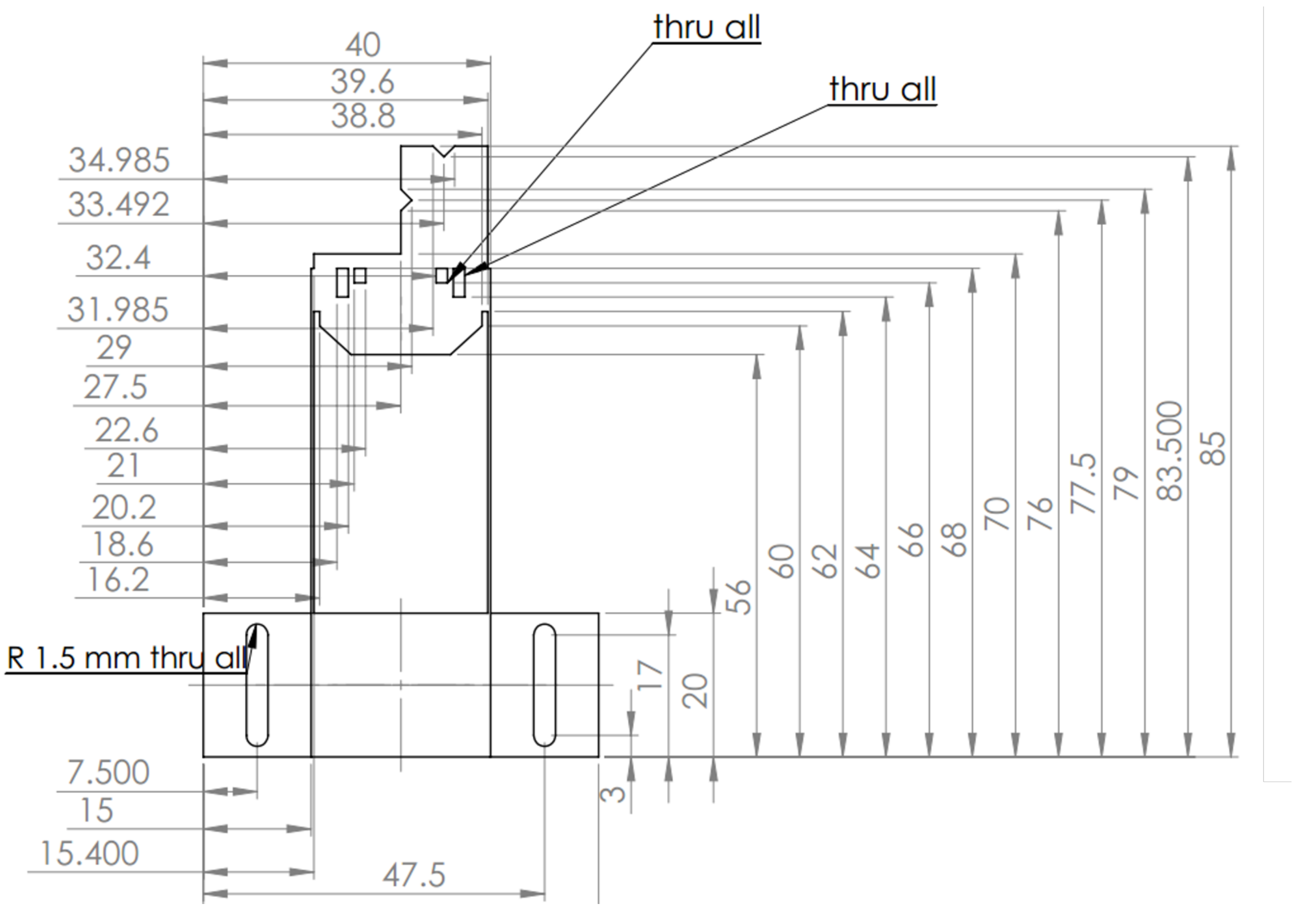

Figure A.1: The 2D CAD drawing for the synthesized compliant P joint. The units for all the dimensions are in millimeters and the thickness of the joint is 10 mm.

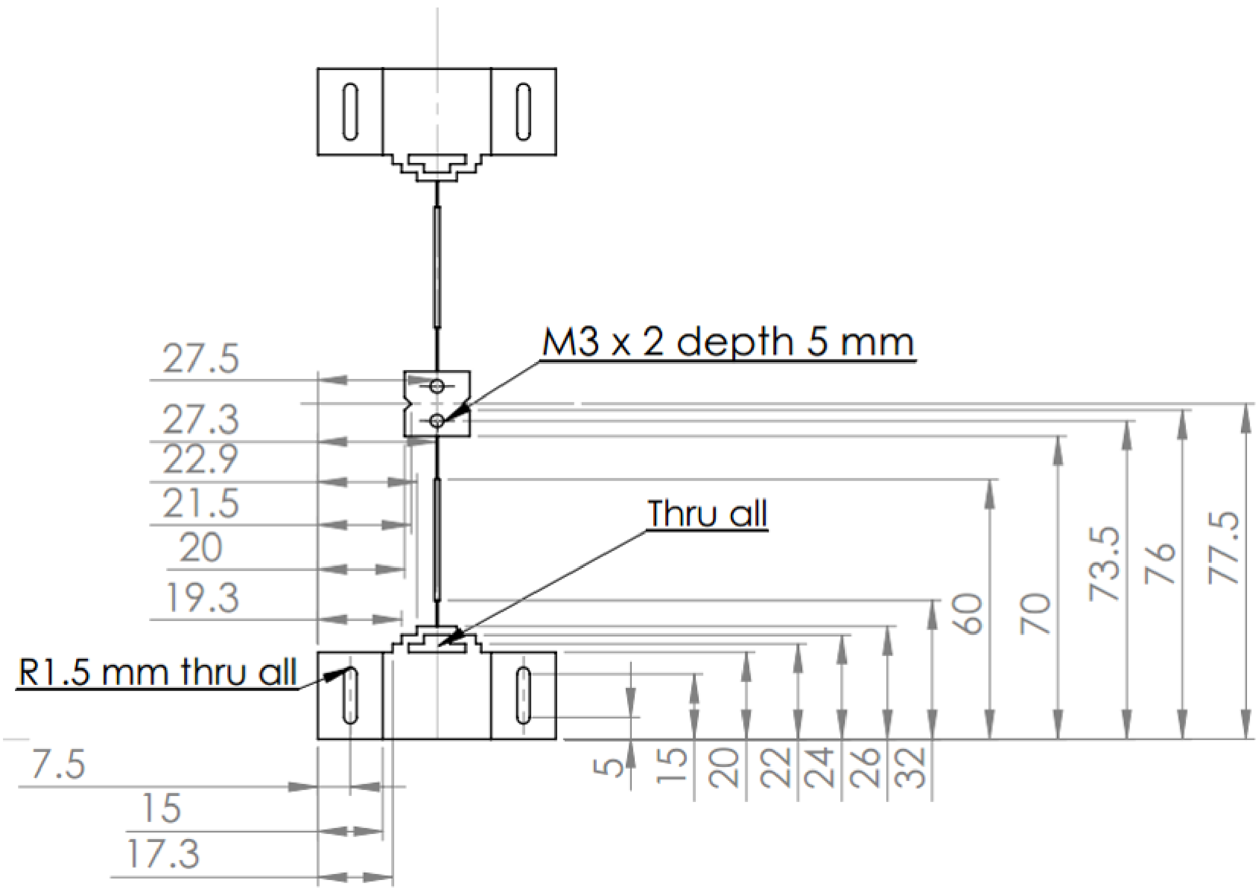

Figure A.2: The 2D CAD drawing for the synthesized compliant PR joint. The units for all the dimensions are in millimeters and the thickness of the joint is 10 mm.

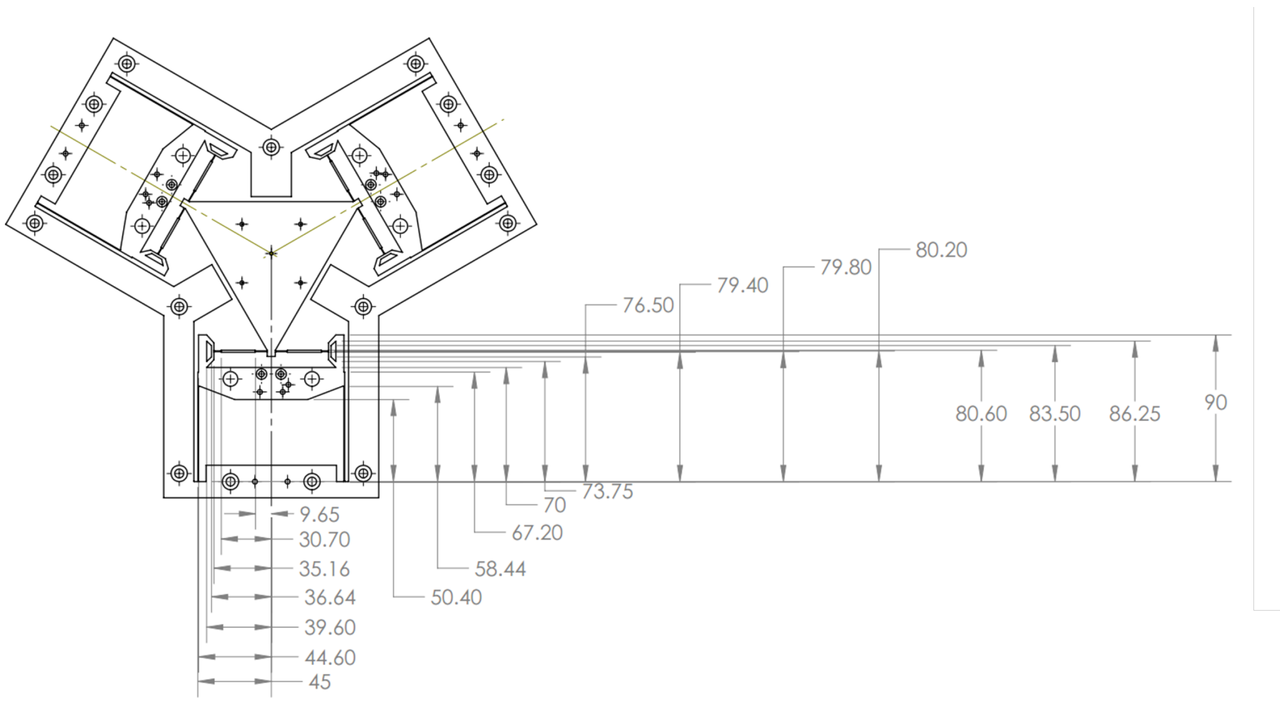

Figure A.3: The 2D CAD drawing for the synthesized 3PPR FPM. The units for all the dimensions are in millimeters and the thickness of the joint is 20 mm.

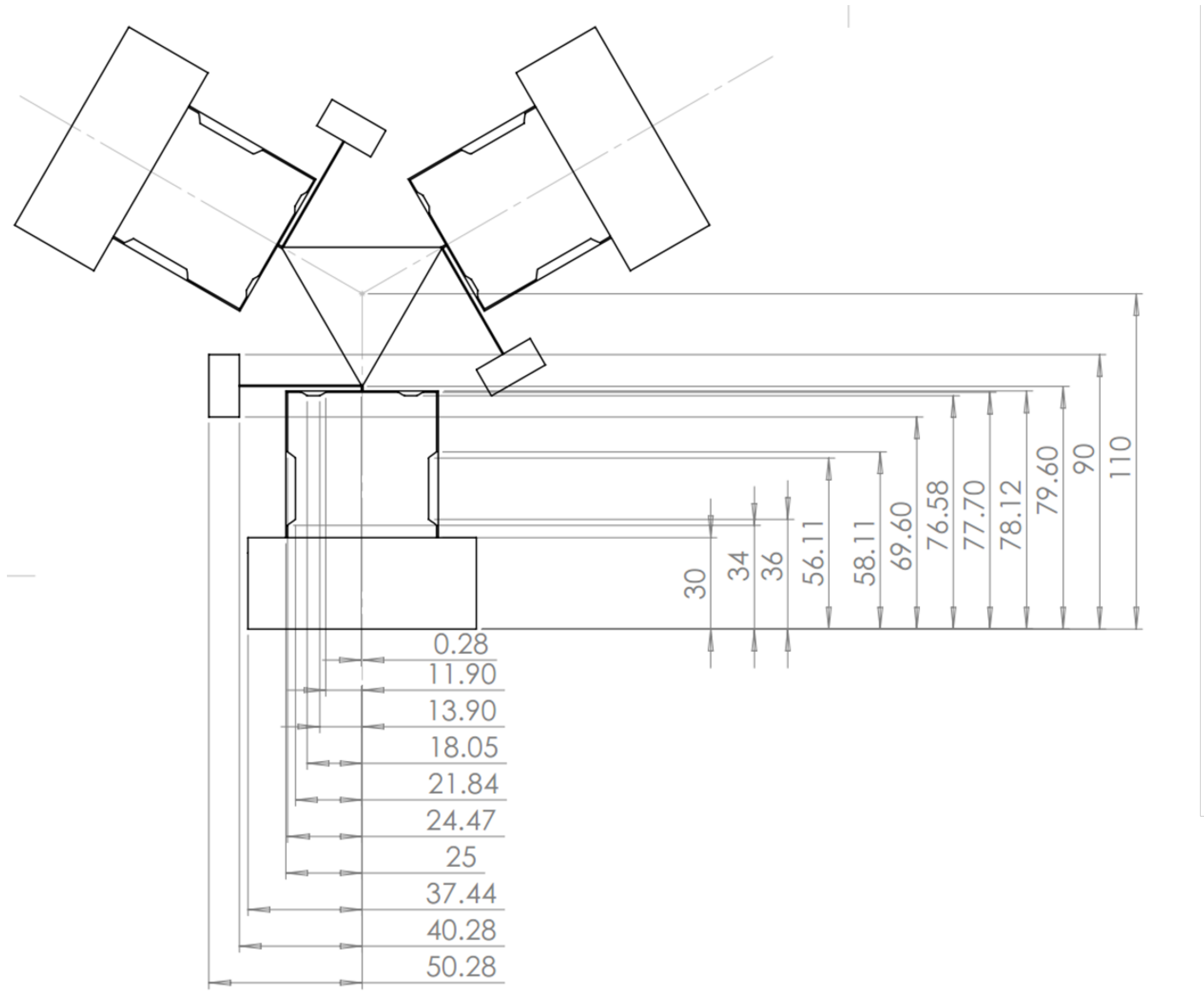

Figure A.4: The 2D CAD drawing for the synthesized optimal $X - Y - \theta_z$ FPM. The units for all the dimensions are in millimeters and the thickness of the joint is 20 mm.

Appendix B

Experimental Procedures for Shape-programmable Magnetic Matter

This section describes the experimental procedures for matching the elastic modulus of the passive and active components. The procedures and setup for the experiments, which evaluate the performance of the programmable materials, are also discussed.

B.1 Matching the Elastic Modulus Properties

Because of the embedded metal particles, the elastic modulus of the composite materials is different from that of pure Ecoflex. The embedded aluminum and NdFeB powders were selected to have the same mean particles size of 5 μm. The volume ratio of the embedded NdFeB powder to Ecoflex in the active component was predetermined; hence, the active components elastic modulus was fixed. Therefore, the elastic modulus of the passive component, Ecoflex with embedded aluminum powder, was tuned by changing the volume ratio of the particles to Ecoflex. The elastic modulus of both the passive and active components was evaluated with a tensile testing machine (Instron 5943, Instron Inc.). Each volume ratio was evaluated with three experiments, and a linear model was fitted to represent the relationship between the elastic modulus and the volume

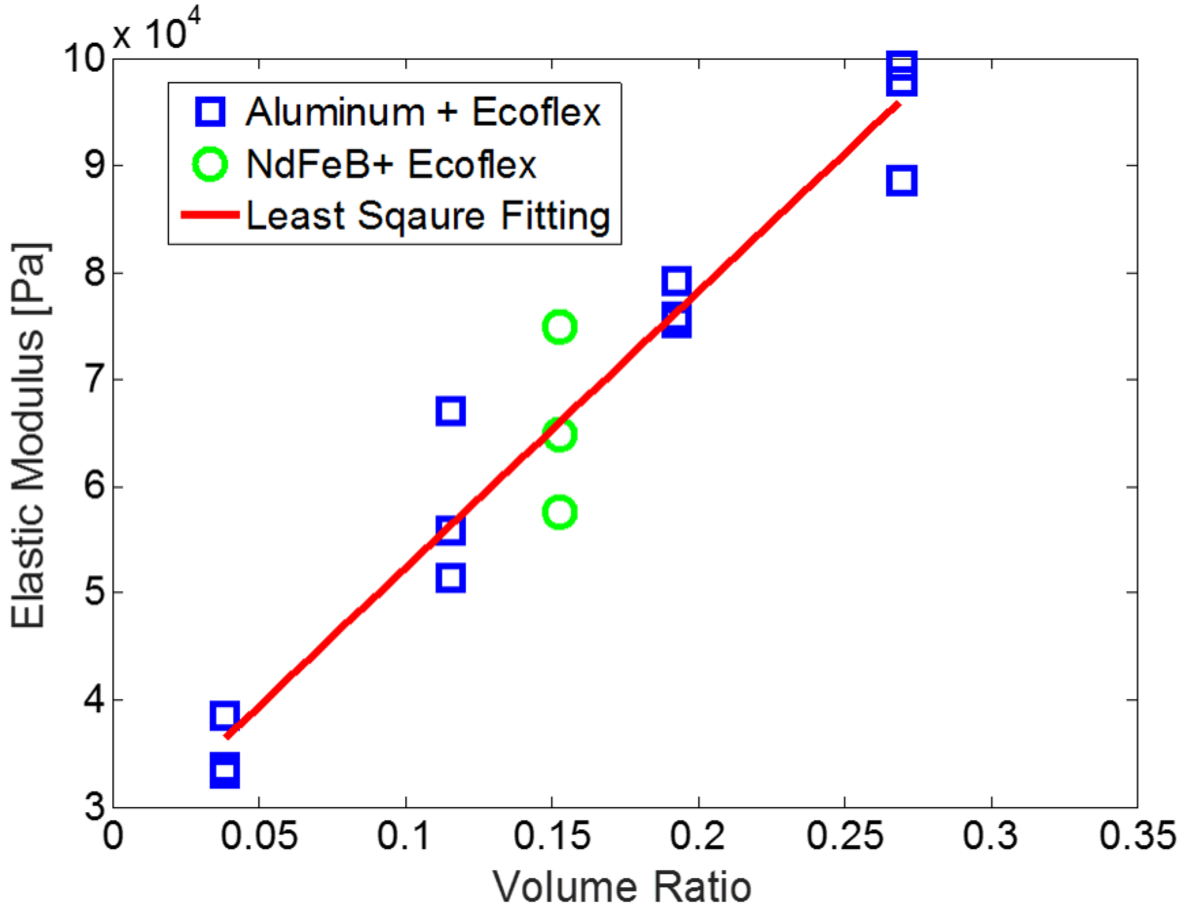

Figure B.1: Tensile test of the mixture of Ecoflex and aluminum with different volume ratios of the aluminum powder. The data for the mixture of Ecoflex and aluminum are represented as pink circles, and the data for the mixture of Ecoflex and NdFeB are represented as green squares. A linear model was fitted with the parameters shown in the figure.

ratio. Based on the fitted model, the necessary volume ratio for the passive components elastic modulus to match the active components was determined (see Fig. B.1). The corresponding mass ratio was obtained by

$$\text{mass ratio} = \frac{\text{density of particle}}{\text{density of Ecoflex}} \times \text{volume ratio} \tag{B.1}$$

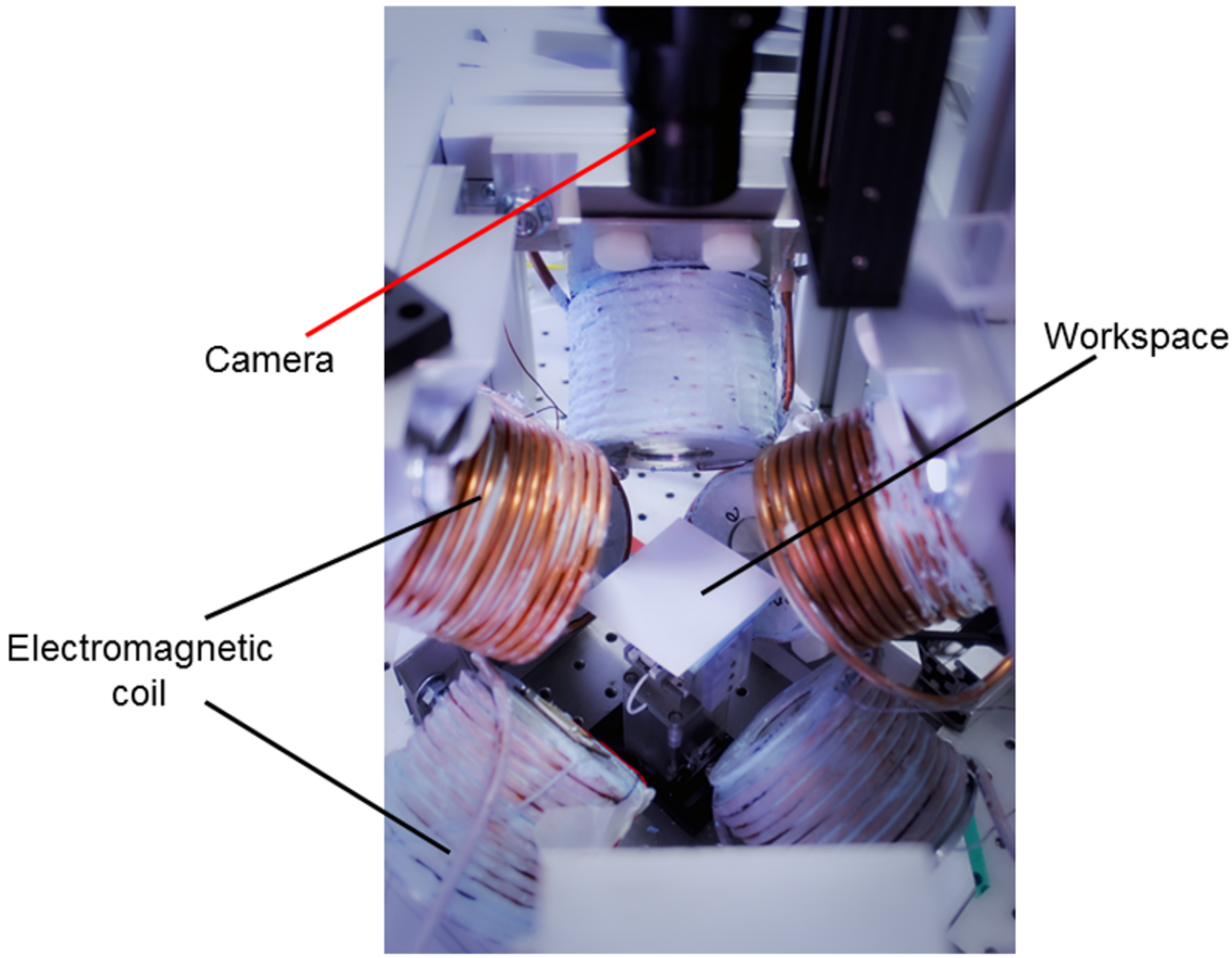

Figure B.2: A custom electromagnetic coil system with eight coils was used to generate the external magnetic field, $\mathbf{B}(t)$. A magnetized beam was placed in a container filled with liquid(s), and the container was in turned placed in the center of the workspace of the electromagnetic coil system. The time-varying shapes of the beams were recorded by the camera.

B.2 Experimental Procedure

The magnetic field and its spatial gradients were generated by an electromagnetic coil system with eight coils, as shown in Fig. B.2. The coil system can be controlled to generate the desired magnetic field and its spatial gradient in the workspace with a uniformity above 95% across a 2 cm $\times$ 2 cm $\times$ 2 cm volume. The mapping from the current in each coil and the resulting magnetic field and spatial gradient can be approximated in a linear form as

$$\mathbf{AI} = [\mathbf{B}^T \quad \mathbf{B}_{\text{grad}}^T]^T \tag{B.2}$$

The matrix $\mathbf{A}$ and vector $\mathbf{I}$ represent the actuation matrix and the currents for each coil, respectively. The magnetic field can be expressed as $\mathbf{B} = [B_x \quad B_y \quad B_z]^T$ in the global frames shown in the figures, and the spatial gradients of B are represented by $\mathbf{B}_{\text{grad}}$. Based on Gausss Law of $\nabla \cdot \mathbf{B} = 0$ and Amperes Law of $\nabla \times \mathbf{B} = \mathbf{0}_{3\times 1}$ there are only five independent components. Because there is more than one combination of Bgrad, we selected the following representation for $\mathbf{B}_{\text{grad}}$:

$$\mathbf{B}_{\text{grad}} = [\frac{\partial B_x}{\partial x} \quad \frac{\partial B_x}{\partial y} \quad \frac{\partial B_y}{\partial y} \quad \frac{\partial B_z}{\partial x} \quad \frac{\partial B_z}{\partial y}]^T. \tag{B.3}$$

We recorded the time-varying shapes of the beam when they are subjected to the simulated magnetic field and its spatial gradients on the programmable beams.

B.3 Parameters for Each Showcase

Here, we provide the parameters used for each showcase, i.e., the dimensions of the beams and the number of Fourier series coefficients, or n and m, respectively. These parameters are summarized in Table B.1.

Table B.1: Parameters for each showcase.

	Cosine	**Jellyfish-like robot**	**Undulating swimmer**	**Artifical cilium**
Length (mm)	7	7	10	10
Width (mm)	5	3	3	3
Thickness (mm)	80	80	240	80
m	-	10	1	10
n	200	10	70	20

The detailed magnetization profile for each device are shown in Fig. B.3.

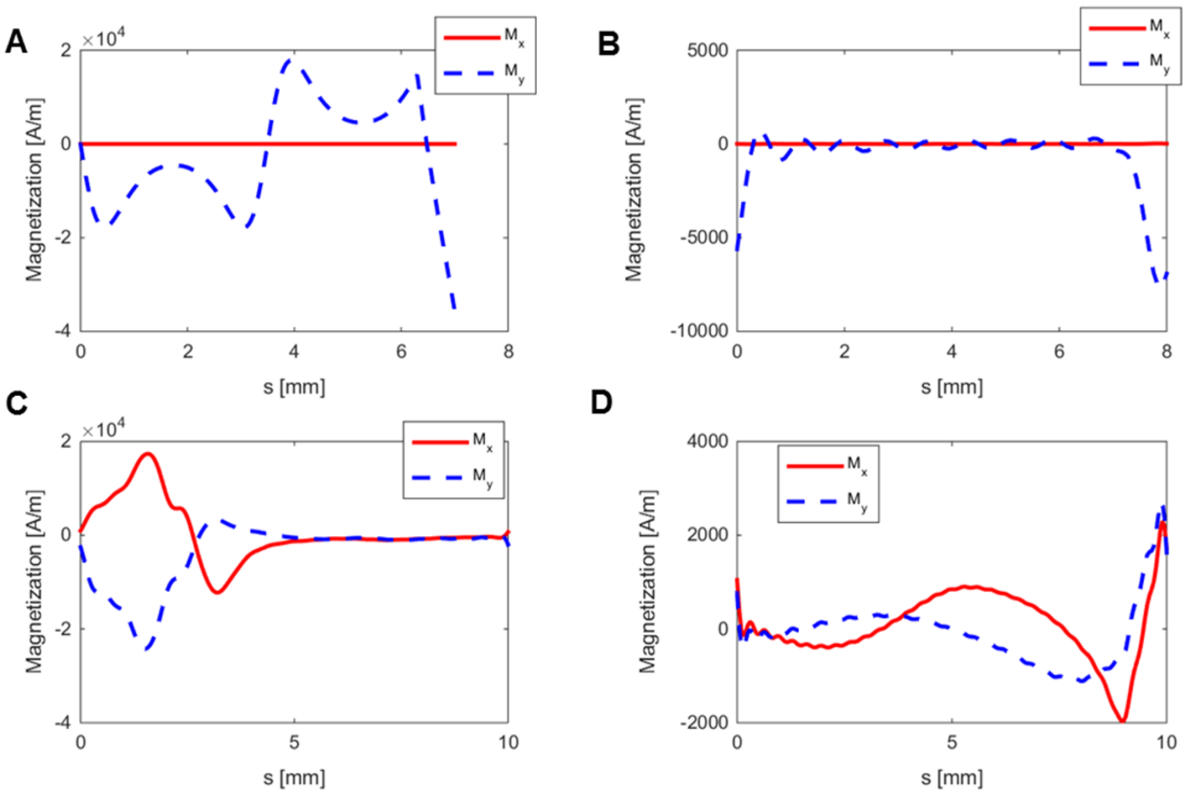

Figure B.3: Quantitative representation for the magnetization profiles for all the showcases when they were un-deformed. A. Magnetization profile for the cosine showcase. B. Magnetization profile for the jellyfish-like robot and reversible “CMU” logo. C. Magnetization profile for the artificial cilium. D. Magnetization profile for the spermatozoid-like undulating swimmer.

References

[1] L. L. Howell, *Compliant mechanisms*. Wiley, 2001. 1.1, 1.2.1

[2] S. T. Smith, *Flexures: elements of elastic mechanisms*. Gordon & Breach, 2000. 1.1, 1.2.1, 1.2.1, 1.4

[3] Y. Bellouard, *Microrobtics: methods and applications*. CRC Press, 2010. 1.1

[4] D. L. Blanding, *Exact constraint: machine design using kinematic principles*. ASME Press, 1999. 1.1, 1.2.1

[5] L. C. Hale, *Principles and techniques for designing precision machines*. PhD Thesis, Massachusetts Institute of Technology, 1999. 1.1, 1.2.1

[6] J. A. Miller, R. Hocken, S. T. Smith, and S. Harb, "X-ray calibrated tunneling system utilizing a dimensionally stable nanometer positioner," *Precision Engineering*, vol. 18, no. 23, pp. 95 – 102, 1996. 1.1

[7] T. J. Teo, G. Yang, and I. M. Chen, "A large deflection and high payload flexure-based parallelmanipulator for uv nanoimprint lithography: part i. modeling and analyses," *Precision Engineering*, vol. 38, pp. 861–871, October 2014. 1.1, 1.6, 1.2.1, 1.2.1, 3.3, 3.3.5, 3.5

[8] T. J. Teo, I. M. Chen, and G. Yang, "A large deflection and high payload flexure-based parallelmanipulator for uv nanoimprint lithography: part ii. stiffness modeling and performance evaluation," *Precision Engineering*, vol. 38, pp. 872–884, October 2014. 1.1,

1.2.1, 1.2.1, 3.3, 3.3.5, 3.5

[9] J. W. Ryu, D. G. Gweon, and K. S. Moon, “Optimal design of a flexure hinge based x–y–θ_z wafer stage,” *Precision Engineering*, vol. 21, pp. 18–28, July 1997. 1.1, 1.2.1, 1.2.1, 3.1, 3.3.4, 3.3.5, 3.5

[10] C. W. Lee and S. W. Kim, “An ultraprecision stage for alignment of wafers in advanced microlithography,” *Precision Engineering*, vol. 21, pp. 113–122, September 1997. 1.1, 1.2.1, 1.2.1

[11] G. Yang, W. Lin, T. Teo, and C. Kiew, “A flexure-based planar parallel nanopositioner with partially decoupled kinematic architecture,” in *EUSPEN International Conference*, (Zurich, Switzerland), pp. 2751–2756, June 2009. 1.1, 1.2.1

[12] H. Kim and D.-G. Gweon, “Development of a compact and long range $x-y-\theta_z$ nanopositioning stage,” *Review of Scientific Instruments*, vol. 83, pp. –, August 2012. 1.1, 1.2.1, 1.7, 1.2.1, 3.3, 3.3.5, 3.5

[13] B. J. Yi, G. Chung, H. Y. Na, W. H. Kim, and I. H. Suh, “Design and experiment of a 3-dof parallel micromechanism utilizing flexure hinges,” *IEEE Transactions on Robotics and Automation*, vol. 19, pp. 604–612, August 2003. 1.1, 1.7, 1.2.1, 3.3.5, 3.5

[14] H.-Y. Kim, D.-H. Ahn, and D.-G. Gweon, “Development of a novel 3-degrees of freedom flexure based positioning system,” *Review of Scientific Instruments*, vol. 83, pp. –, May 2012. 1.1, 1.2.1, 1.2.1, 3.3.5, 3.5

[15] T. Lu, D. C. Handley, Y. K. Yong, and C. Eales, “A three-dof compliant micromotion stage with flexure hinges,” *Industrial Robot: An International Journal*, vol. 31, no. 4, pp. 355–361, 2004. 1.1, 1.2.1

[16] A. A. Eielsen, M. Vagia, J. T. Gravdahl, and K. Y. Pettersen, “Damping and tracking control schemes for nanopositioning,” *IEEE/ASME Transactions on Mechatronics*, vol. 19, no. 2, pp. 432–444, 2014. 1.1

[17] M. N. M. Zubir and B. Shirinzadeh, "Development of a high precision flexure-based microgripper," *Precision Engineering*, vol. 33, no. 4, pp. 362 – 370, 2009. 1.1, 1.2.1

[18] X. Shi, W. Chen, J. Zhang, and W. Chen, "Design, modeling, and simulation of a 2-dof microgripper for grasping and rotating of optical fibers," in *IEEE/ASME International Conference on Advanced Intelligent Mechatronics*, (Wollongong, Australia), pp. 1597–1602, 2013. 1.1, 1.2.1

[19] M. Grossard, C. Rotinat-Libersa, N. Chaillet, and M. Boukallel, "Mechanical and control-oriented design of a monolithic piezoelectric microgripper using a new topological optimization method," *IEEE/ASME Transactions on Mechatronics*, vol. 14, no. 1, pp. 32–45, 2009. 1.1

[20] D. Mukhopadhyay, J. Dong, E. Pengwang, and P. Ferreira, "A soi-mems-based 3-dof planar parallel-kinematics nanopositioning stage," *Sensors and Actuators A: Physical*, vol. 147, pp. 340 – 351, April 2008. 1.1

[21] N. Lobontiu and E. Garcia, "Analytical model of displacement amplification and stiffness optimization for a class of flexure-based compliant mechanisms," *Computers and Structures*, vol. 81, pp. 2797 – 2810, July 2003. 1.1

[22] K. Sharma, I. G. Macwan, L. Zhang, L. Hmurick, and X. Xiong, "Design optimization of mems comb accelerometer," in *in ASEE Zone 1 Conference 2008, United States Military Academy*, (New York, USA), pp. 833–837, July 2008. 1.1

[23] F. Peano and T. Tambosso, "Design and optimization of a mems electret-based capacitive energy scavenger," *Journal of microelectromechanical systems*, vol. 14, pp. 429 – 435, June 2005. 1.1

[24] O. Sigmund, "Design of multiphysics actuators using topology optimization - part i: One-material structures," *Computer Methods in Applied Mechanics and Engineering*, vol. 190, pp. 6577 – 6604, October 2001. 1.1, 1.2.2

[25] O. Sigmund, "Design of multiphysics actuators using topology optimization - part ii: Two-material structures," *Computer Methods in Applied Mechanics and Engineering*, vol. 190, pp. 6605 – 6627, October 2001. 1.1, 1.2.2

[26] M. P. Kummer, J. J. Abbott, B. E. Kratochvil, R. Borer, A. Sengul, and B. J. Nelson, "Octomag: An electromagnetic system for 5-dof wireless micromanipulation," *IEEE Transactions on Robotics*, vol. 26, no. 6, pp. 1006–1017, 2010. 1.1

[27] E. Diller, J. Giltinan, G. Z. Lum, Z. Ye, and M. Sitti, "Six-degree-of-freedom magnetic actuation for wireless microrobotics," *The International Journal of Robotics Research*, vol. 35, no. 1-3, pp. 114–128, 2016. 1.1, 4.5.1

[28] G. Z. L. Z. Y. M. S. Eric Diller, Joshua Giltinan, "Six-degrees-of-freedom remote actuation of magnetic microrobots," in *Robotics: Science and Systems*, Springer, July 2014 2014. 1.1, 4.5.1

[29] E. Diller and M. Sitti, "Three-dimensional programmable assembly by untethered magnetic robotic micro-grippers," *Advanced Functional Materials*, vol. 24, no. 28, pp. 4397–4404, 2014. 1.1

[30] S. Chen and M. Y. Wang, "Designing distributed compliant mechanisms with characteristic stiffness," in *ASME International Design Engineering Technical Conferences and Computers and Information in Engineering Conference*, (Nevada, USA), pp. 33–45, 2008. 1.2.1

[31] M. Y. Wang, "A kinetoelastic approach to continuum compliant mechanism optimization," in *ASME International Design Engineering Technical Conferences and Computers and Information in Engineering Conference*, (New York, USA), pp. 183–195, August 2009. 1.2.1

[32] M. D. Murphy, A. Midha, and L. . L. Howell, "The topological synthesis of compliant mechanisms," *Mechanisms and Machine Theory*, vol. 31, no. 2, pp. 185–199, 1996. 1.2.1

[33] H. H. Pham and I. M. Chen, "Stiffness modeling of flexure parallel mechanism," *Precision Engineering*, vol. 29, no. 4, pp. 467–478, 2005. 1.2.1

[34] L. C. Hale and A. H. Slocum, "Optimal design techniques for kinematic couplings," *Precision Engineering*, vol. 25, no. 2, pp. 114–127, 2001. 1.2.1, 1.2.1

[35] S. Awtar and A. H. Slocum, "Constraint-based design of parallel kinematic xy flexure mechanisms," *ASME Journal of Mechanical Design*, vol. 129, no. 8, pp. 816–830, 2006. 1.2.1, 1.2.1

[36] J. B. Hopkins and M. L. Culpepper, "Synthesis of multi-degree of freedom, parallel flexure system concepts via freedom and constraint topology (fact) - part i: principles," *Precision Engineering*, vol. 34, no. 2, pp. 259–270, 2010. 1.2.1, 1.2

[37] J. B. Hopkins and M. L. Culpepper, "Synthesis of multi-degree of freedom, parallel flexure system concepts via freedom and constraint topology (fact) - part ii: practice," *Precision Engineering*, vol. 34, no. 2, pp. 271–278, 2010. 1.2.1

[38] J. B. Hopkins and M. L. Culpepper, "Synthesis of precision serial flexure systems using freedom and constraint topologies (fact)," *Precision Engineering*, vol. 35, no. 4, pp. 638–649, 2011. 1.2.1

[39] H. J. Su, D. V. Dorozhkin, and J. M. Vance, "A screw theory approach for the type synthesis of compliant mechanisms with flexures," in *International Design Engineering Technical Conferences & Computers and Information in Engineering Conference*, (California, USA), pp. DETC2009–86684, September 2009. 1.2.1

[40] J. A. Gallego and J. Herder, "Synthesis methods in compliant mechanisms: An overview," in *in ASME International Design Engineering Technical Conferences and Computers and Information in Engineering Conference*, (California, USA), pp. 193–214, 2010. 1.2.1, 1.6, 1.2.2

[41] Y. Tian, B. Shirinzadeh, D. Zhang, and Y. Zhong, "Three flexure hinges for compli-

ant mechanism designs based on dimensionless graph analysis," *Precision Engineering*, vol. 34, no. 1, pp. 92 – 100, 2010. CIRP-CAT 2007. 1.2.1, 1.2.1, 1.4

[42] S. Polit and J. Dong, "Development of a high-bandwidth xy nanopositioning stage for high-rate micro-/nanomanufacturing," *Mechatronics, IEEE/ASME Transactions on*, vol. 16, pp. 724–733, Aug 2011. 1.2.1

[43] Y. Li and Q. Xu, "Design and analysis of a totally decoupled flexure-based xy parallel micromanipulator," *Robotics, IEEE Transactions on*, vol. 25, pp. 645–657, June 2009. 1.2.1

[44] Q. Xu, "Design and development of a compact flexure-based xy precision positioning system with centimeter range," *Industrial Electronics, IEEE Transactions on*, vol. 61, pp. 893–903, Feb 2014. 1.2.1

[45] Q. Yao, J. Dong, and P. Ferreira, "Design, analysis, fabrication and testing of a parallel-kinematic micropositioning {XY} stage," *International Journal of Machine Tools and Manufacture*, vol. 47, no. 6, pp. 946 – 961, 2007. 1.2.1

[46] X. Tang, I.-M. Chen, and Q. Li, "Design and nonlinear modeling of a large-displacement xyz flexure parallel mechanism with decoupled kinematic structure," *Review of Scientific Instruments*, vol. 77, no. 11, pp. –, 2006. 1.2.1

[47] D. Zhu and Y. Feng, "A spatial 3-dof translational compliant parallel manipulator," in *International Conference on Mechanical Engineering and Green Manufacturing*, (Hunan, China), pp. 143–147, 2010. 1.2.1

[48] Y. Li and Q. Xu, "A totally decoupled piezo-driven xyz flexure parallel micropositioning stage for micro/nanomanipulation," *Automation Science and Engineering, IEEE Transactions on*, vol. 8, pp. 265–279, April 2011. 1.2.1

[49] G. Yang, T. J. Teo, I.-M. Chen, and W. Lin, "Analysis and design of a 3-dof flexure-based zero-torsion parallel manipulator for nano-alignment applications," in *IEEE International*

Conference on Robotics and Automation, (Shanghai, China), pp. 2751–2756, May 2011. 1.2.1, 3.3, 3.3.5, 3.5

[50] Y. Tian, B. Shirinzadeh, and D. Zhang, "Design and dynamics of 3-dof flexure-based parallel mechanism," *Microelectronics Engineering*, vol. 87, pp. 230–241, February 2010. 1.2.1, 3.3.5, 3.5

[51] J. Zhan and X. Zhang, "Topological optimization of multiple inputs and multiple outputs compliant mechanisms using the ground structure," in *IEEE/ASME International Conference on Advance Intelligent Mechatronics*, (Singapore, Singapore), pp. 833–837, July 2009. 1.2.2, 1.2.2

[52] N. F. Wang and K. Tai, "Design of 2-dof compliant mechanisms to form grip-and-move manipulators for 2d workspace," *Journal of Mechanical Design*, vol. 132, no. 3, pp. 0310071–0310079, 2010. 1.2.2, 1.2.2, 1.2.2

[53] M. P. Bendse and N. Kikuchi, "Generating optimal topologies in structural design using a homogenization method," *Computer Methods in Applied Mechanics and Engineering*, vol. 71, no. 2, pp. 197–224, 1988. 1.2.2, 1.2.2

[54] S. Shuib, M. I. Z. Ridazwan, and A. H. Kadarman, "Methodology of compliant mechanisms and it current developments in applications: A review," vol. 4, pp. 160–167, 2007. 1.2.2, 1.2.2

[55] M. P. Bendse and O. Sigmund, *Topology optimization: theory, methods, and applications*. Springer, 2003. 1.2.2, 1.2.2, 1.2.2

[56] O. Sigmund and J. Petersson, "Numerical instabilities in topology optimization: A survey on procedures dealing with checkerboards, mesh-dependencies and local minima," *Structural Optimization*, vol. 16, no. 1, pp. 68–75, 1998. 1.2.2

[57] S. Ananiev, "On equivalence between optimality criteria and projected gradient methods with application to topoloy optimization problem," *Multibody System Dynamics*, vol. 13,

no. 1, pp. 25–38, 2005. 1.2.2, 1.2.2

[58] N. P. Garcia-Lopez, M. Sanchez-Silva, A. L. Medaglia, and A. Chateauneuf, "A hybrid topology optimization methodology combining simulated annealing and simp," *Computers and Structures*, vol. 89, no. 15-16, pp. 1512–1522, 2011. 1.2.2

[59] X. Liu, Z. Li, L. Wang, and J. Wang, "Solving topology optimization problems by the guide-weight method," *Frontiers of Mechanical Engineering*, vol. 6, no. 1, pp. 136–150, 2011. 1.2.2

[60] H. Panganiban, G. W. Jang, and T. J. Chung, "Topology optimization of pressure-actuated compliant mechanisms," *Finite Elements in Analysis and Design*, vol. 46, no. 3, pp. 238–246, 2010. 1.2.2

[61] J. Lin, Z. Luo, and L. Tong, "A new multi-objective programming scheme for topology optimization of compliant mechanisms," *Structural and Multidisciplinary Optimization*, vol. 40, no. 1-6, pp. 241–255, 2010. 1.2.2

[62] J. Zhan, X. Zhang, and J. Hu, "Maximization of values of simple and multiple eigenfrequencies of continuum structures using topology optimization," in *International Conference on Measuring Technology and Mechatronics Automation*, (Hunan, China), pp. 833–837, 2009. 1.2.2

[63] Y. M. Xie and G. P. Steven, *Evolutionary structural optimization*. Springer, 1997. 1.2.2, 1.2.2

[64] X. Huang and Y. M. Xie, "A further review of eso type methods for topology optimization," *Structural and Multidisciplinary Optimization*, vol. 41, no. 5, pp. 671–683, 2010. 1.2.2, 1.2.2

[65] X. Huang and Y. M. Xie, "Evolutionary topology optimization of continuum structures including design dependent self-weight loads," *Finite Elements in Analysis and Design*, vol. 47, no. 8, pp. 942–948, 2011. 1.2.2, 1.2.2

[66] K. Tai and T. H. Chee, "Design of structures and compliant mechanisms by evolutionary optimization of morphological representations of topology," *Journal of Mechanical Design*, vol. 122, no. 4, pp. 560–566, 2000. 1.2.2, 1.13, 1.2.2

[67] K. Tai and S. Akhtar, "Structural topology optimization using a genetic algorithm with a morphological geometric representation scheme," *Structural and Multidisciplinary Optimization*, vol. 30, no. 2, pp. 113–127, 2005. 1.2.2, 1.2.2

[68] N. F. Wang and K. Tai, "Design of grip-and-move manipulators using symmetric path generating compliant mechanisms," *Journal of Mechanical Design*, vol. 130, no. 11, pp. 1123051–1123059, 2008. 1.2.2, 1.2.2

[69] N. F. Wang and K. Tai, "Target matching problems and an adaptive constraint strategy for multiobjective design optimizations using genetic algorithms," *Computers and Structures*, vol. 88, no. 19-20, pp. 1064–1073, 2010. 1.2.2, 1.2.2, 1.2.2

[70] N. F. Wang and Y. W. Yang, "Structural design optimization subjected to uncertainty using fat bezier curve," *Computer Methods in Applied Mechanics and Engineering*, vol. 199, no. 1-4, pp. 210–219, 2009. 1.2.2

[71] M. Y. Wang, X. Wang, and D. Guo, "A level set method for structural topology optimization," *Computer Methods in Applied Mechanics and Engineering*, vol. 192, no. 1-2, pp. 227–246, 2003. 1.2.2, 1.2.2

[72] X. Wang, Y. Mei, and M. Y. Wang, "Incorporating topological derivatives into level set methods for structural topology optimization," in *10th AIAA/ISSMO Multidisciplinary Analysis and Optiization Conference*, (New York, USA), pp. 2923–2932, 2004. 1.2.2, 1.2.2

[73] X. Wang, M. Wang, and D. Guo, "Structural shape and topology optimization in a level-set-based framework of region representation," *Structural and Multidisciplinary Optimization*, vol. 27, no. 1-2, pp. 1–19, 2004. 1.2.2, 1.2.2

[74] P. Wei and M. Y. Wang, “Piecewise constant level set method for structural topology optimization,” *International Journal for Numerical Methods in Engineering*, vol. 78, no. 4, pp. 379–402, 2009. 1.2.2, 1.2.2

[75] J. Zhan and X. Zhang, “Topology optimization of compliant mechanisms with geometrical nonlinearities using the ground structure approach,” *Chinese Journal of Mechanical Engineering*, vol. 24, no. 2, pp. 257–263, 2011. 1.2.2, 1.2.2

[76] A. Asadpoure, M. Tootkaboni, and J. K. Guest, “Robust topology optimization of structures with uncertainties in stiffness,” *Computers and Structures*, vol. 89, no. 11-12, pp. 1131–1141, 2011. 1.2.2, 1.2.2

[77] D. S. Ramrakhyani, M. I. Frecker, and G. A. Lesieutre, “Hinged beam elements for the topology design of compliant mechanisms using ground structure approach,” *Structural and Multidisciplinary Optimization*, vol. 37, no. 6, pp. 557–567, 2009. 1.2.2, 1.2.2

[78] M. Sauter, G. Kress, M. Giger, and P. Ermanni, “Complex-shaped beam element and graph-based optimization of compliant mechanisms,” *Structural and Multidisciplinary Optimization*, vol. 36, no. 4, pp. 429–442, 2008. 1.2.2, 1.2.2

[79] P. Martinez, P. Marti, and O. M. Querin, “Growth method for size, topology and geometry optimization of truss structures,” *Structural and Multidisciplinary Optimization*, vol. 33, no. 1, pp. 13–26, 2007. 1.2.2, 1.2.2

[80] W. Achtziger and M. Stolpe, “Truss topology optimization with discrete design variables - guaranteed global optimality and benchmark examples,” *Structural and Multidisciplinary Optimization*, vol. 34, no. 1, pp. 1–20, 2007. 1.2.2, 1.2.2

[81] C. J. Kim, Y.-M. Moon, and S. Kota, “A building block approach to the conceptual synthesis of compliant mechanisms utilizing compliance and stiffness ellopsoids,” *Journal of Mechanical Design*, vol. 130, no. 2, pp. 022308–1, 2008. 1.2.2, 1.2.2, 3.1

[82] P. Bernardoni, P. Bidaud, C. Bidard, and F. Gosselin, “A new compliant mechanism design

methodology based on flexible building blocks," Society of Photo-Optical Instrumentation Engineers (SPIE) Conference Series, (France), pp. 244–254, July 2004. 1.2.2, 1.2.2

[83] G. I. N. Rozvany, "A critical review of established methods of structural topology optimization," *Structural and multidisciplinary optimization*, vol. 37, no. 3, pp. 217–237, 2009. 1.2.2

[84] M. J. Jakiela, C. Chapman, J. Duda, A. Adewuya, and K. Saitou, "Continuum structural topology design with genetic algorithms," *Computer Methods in Applied Mechanics and Engineering*, vol. 186, no. 2-4, pp. 339–356, 2000. 1.2.2

[85] S. Felton, M. Tolley, E. Demaine, D. Rus, and R. Wood, "A method for building self-folding machines," *Science*, vol. 345, no. 6197, pp. 644–646, 2014. 1.2.3, 1.15

[86] E. Hawkes, B. An, N. M. Benbernou, H. Tanaka, S. Kim, E. D. Demaine, D. Rus, and R. J. Wood, "Programmable matter by folding," *Proceedings of the National Academy of Sciences*, vol. 107, no. 28, pp. 12441–12445, 2010. 1.2.3, 1.15

[87] S. Miyashita, S. Guitron, M. Ludersdorfer, C. R. Sung, and D. Rus, "An untethered miniature origami robot that self-folds, walks, swims, and degrades," in *2015 IEEE International Conference on Robotics and Automation (ICRA)*, pp. 1490–1496. 1.2.3, 1.15, 1.2.3

[88] R. Mohr, K. Kratz, T. Weigel, M. Lucka-Gabor, M. Moneke, and A. Lendlein, "Initiation of shape-memory effect by inductive heating of magnetic nanoparticles in thermoplastic polymers," *Proceedings of the National Academy of Sciences of the United States of America*, vol. 103, no. 10, pp. 3540–3545, 2006. 1.2.3, 1.2.3

[89] J.-H. Na, A. A. Evans, J. Bae, M. C. Chiappelli, C. D. Santangelo, R. J. Lang, T. C. Hull, and R. C. Hayward, "Programming reversibly self-folding origami with micropatterned photo-crosslinkable polymer trilayers," *Advanced Materials*, vol. 27, no. 1, pp. 79–85, 2015. 1.2.3, 1.15, 1.2.3

[90] T. Xie, "Tunable polymer multi-shape memory effect," *Nature*, vol. 464, no. 7286,

pp. 267–270, 2010. 1.2.3, 1.2.3

[91] Y. Liu, J. K. Boyles, J. Genzer, and M. D. Dickey, "Self-folding of polymer sheets using local light absorption," *Soft Matter*, vol. 8, no. 6, pp. 1764–1769, 2012. 1.2.3, 1.2.3

[92] J. Mu, C. Hou, H. Wang, Y. Li, Q. Zhang, and M. Zhu, "Origami-inspired active graphene-based paper for programmable instant self-folding walking devices," *Science Advances*, vol. 1, no. 10, 2015. 1.2.3, 1.15, 1.2.3

[93] R. M. Erb, J. S. Sander, R. Grisch, and A. R. Studart, "Self-shaping composites with programmable bioinspired microstructures," *Nat Commun*, vol. 4, p. 1712, 2013. 1.2.3, 1.2.3

[94] K.-U. Jeong, J.-H. Jang, D.-Y. Kim, C. Nah, J. H. Lee, M.-H. Lee, H.-J. Sun, C.-L. Wang, S. Z. D. Cheng, and E. L. Thomas, "Three-dimensional actuators transformed from the programmed two-dimensional structures via bending, twisting and folding mechanisms," *Journal of Materials Chemistry*, vol. 21, no. 19, pp. 6824–6830, 2011. 1.2.3

[95] S. Maeda, Y. Hara, T. Sakai, R. Yoshida, and S. Hashimoto, "Self-walking gel," *Advanced Materials*, vol. 19, no. 21, pp. 3480–3484, 2007. 1.2.3, 1.2.3

[96] H. Therien-Aubin, M. Moshe, E. Sharon, and E. Kumacheva, "Shape transformations of soft matter governed by bi-axial stresses," *Soft Matter*, vol. 11, no. 23, pp. 4600–4605, 2015. 1.2.3, 1.2.3

[97] Z. Wei, Z. Jia, J. Athas, C. Wang, S. R. Raghavan, T. Li, and Z. Nie, "Hybrid hydrogel sheets that undergo pre-programmed shape transformations," *Soft Matter*, vol. 10, no. 41, pp. 8157–8162, 2014. 1.2.3, 1.2.3

[98] C. Ye, S. V. Nikolov, R. Calabrese, A. Dindar, A. Alexeev, B. Kippelen, D. L. Kaplan, and V. V. Tsukruk, "Self-(un)rolling biopolymer microstructures: Rings, tubules, and helical tubules from the same material," *Angewandte Chemie International Edition*, vol. 54, no. 29, pp. 8490–8493, 2015. 1.2.3, 1.2.3

[99] R. V. Martinez, C. R. Fish, X. Chen, and G. M. Whitesides, "Elastomeric origami: Programmable paper-elastomer composites as pneumatic actuators," *Advanced Functional Materials*, vol. 22, no. 7, pp. 1376–1384, 2012. 1.2.3

[100] D. Rus and M. T. Tolley, "Design, fabrication and control of soft robots," *Nature*, vol. 521, no. 7553, pp. 467–475, 2015. 1.2.3

[101] E. Diller, J. Zhuang, G. Zhan Lum, M. R. Edwards, and M. Sitti, "Continuously distributed magnetization profile for millimeter-scale elastomeric undulatory swimming," *Applied Physics Letters*, vol. 104, no. 17, p. 174101, 2014. 1.2.3, 1.15, 1.2.3

[102] S. L. Juan Roche, Paris Von Lockette, "Study of hard-and soft- magnetorheological elastomers (mre's) actuation capabilities," in *Proceedings of the 2011 COMSOL Conference*. 1.2.3, 1.2.3

[103] A. Crivaro, R. Sheridan, M. Frecker, T. W. Simpson, and P. Von Lockette, "Bistable compliant mechanism using magneto active elastomer actuation," *Journal of Intelligent Material Systems and Structures*, 2015. 1.2.3, 1.2.3

[104] M. Zrnyi, L. Barsi, and A. Bki, "Ferrogel: a new magneto-controlled elastic medium," *Polymer Gels and Networks*, vol. 5, no. 5, pp. 415–427, 1997. 1.2.3, 1.2.3

[105] M. Zrnyi, D. Szab, and H.-G. Kilian, "Kinetics of the shape change of magnetic field sensitive polymer gels," *Polymer Gels and Networks*, vol. 6, no. 6, pp. 441–454. 1.2.3, 1.2.3

[106] R. Dreyfus, J. Baudry, M. L. Roper, M. Fermigier, H. A. Stone, and J. Bibette, "Microscopic artificial swimmers," *Nature*, vol. 437, no. 7060, pp. 862–865, 2005. 1.2.3

[107] B. Jang, E. Gutman, N. Stucki, B. F. Seitz, P. D. Wendel-Garca, T. Newton, J. Pokki, O. Ergeneman, S. Pan, Y. Or, and B. J. Nelson, "Undulatory locomotion of magnetic multilink nanoswimmers," *Nano Letters*, vol. 15, no. 7, pp. 4829–4833, 2015. 1.2.3, 1.2.3

[108] M. Khoo and C. Liu, "Micro magnetic silicone elastomer membrane actuator," *Sensors*

and Actuators A: Physical, vol. 89, no. 3, pp. 259–266, 2001. 1.2.3, 1.2.3

[109] J. Kim, S. E. Chung, S.-E. Choi, H. Lee, J. Kim, and S. Kwon, "Programming magnetic anisotropy in polymeric microactuators," *Nat Mater*, vol. 10, no. 10, pp. 747–752, 2011. 1.2.3, 1.2.3

[110] R. T. Olsson, M. A. S. Azizi Samir, G. Salazar Alvarez, BelovaL, StromV, L. A. Berglund, IkkalaO, NoguesJ, and U. W. Gedde, "Making flexible magnetic aerogels and stiff magnetic nanopaper using cellulose nanofibrils as templates," *Nat Nano*, vol. 5, no. 8, pp. 584–588, 2010. 1.2.3, 1.2.3

[111] G. Piotr, T. Pietro, B. W. Douglas, S. Francesc, and M. W. George, "Propulsion of flexible polymer structures in a rotating magnetic field," *Journal of Physics: Condensed Matter*, vol. 21, no. 20, p. 204110, 2009. 1.2.3, 1.2.3

[112] T. Qiu, S. Palagi, and P. Fischer, "3d-printed soft microrobot for swimming in biological fluids," in *2015 37th Annual International Conference of the IEEE Engineering in Medicine and Biology Society (EMBC)*, pp. 4922–4925. 1.2.3, 1.2.3

[113] C. E. Wilson, J. P. Sadler, and W. J. Michels, *Kinematics and dynamics of machinery*. Pearson Education, 2003. 2.2

[114] X. Kong and C. Gosselin, *Type synthesis of parallel mechanisms*. Springer, 2007. 3.1

[115] J. P. Merlet, *Parallel Robot*. Kluwer Academic Publishers, 2000. 3.1

[116] H.-H. Pham and I.-M. Chen, "Stiffness modeling of flexure parallel mechanism," *Precision Engineering*, vol. 29, pp. 467–478, March 2005. 3.1, 3.3.4

[117] R. Guyan, "Reduction of stiffness and mass matrices," *AIAA Journal*, vol. 3, no. 2, p. 380, 1965. 3.2

[118] J. O'Callahan, "A procedure for an improved reduced system (irs) model," in *Seventh International Modal Analysis Conference*, (Las Vegas, USA), pp. 17–21, 1989. 3.2

[119] J. O'Callahan, P. Avitabile, and R. Riemer, "System equivalent reduction expansion pro-

cess (serep)," in *Seventh International Modal Analysis Conference*, (Las Vegas, USA), pp. 29–37, 1989. 3.2

[120] T. J. Teo, G. Yang, and I.-M. Chen, *Compliant Manipulators*. Handbook of Manufacturing Engineering and Technology, Springer, 2014. 3.3.4

[121] A. C. Kiral E., Eringen, *Constitutive equations of non-linear electromagnetic elastic crystals.* Springer-Verlag, New York, 1990. 4.1

[122] L. B. Booker, D. E. Goldberg, and J. H. Holland, "Classifier systems and genetic algorithms," *Artificial Intelligence*, vol. 40, no. 1, pp. 235–282, 1989. 4.1.1

[123] L. C. Boyd, S., *Convex optimization*. Cambridge Univ Press, 2004. 4.1.1

[124] C. Motion. 4.4

[125] C. L. van Oosten, C. W. M. Bastiaansen, and D. J. Broer, "Printed artificial cilia from liquid-crystal network actuators modularly driven by light," *Nat Mater*, vol. 8, no. 8, pp. 677–682, 2009. 10.1038/nmat2487. 4.4

[126] A. R. Shields, B. L. Fiser, B. A. Evans, M. R. Falvo, S. Washburn, and R. Superfine, "Biomimetic cilia arrays generate simultaneous pumping and mixing regimes," *Proceedings of the National Academy of Sciences*, vol. 107, no. 36, pp. 15670–15675, 2010. 4.4

[127] M. Vilfan, A. Potonik, B. Kavi, N. Osterman, I. Poberaj, A. Vilfan, and D. Babi, "Self-assembled artificial cilia," *Proceedings of the National Academy of Sciences*, vol. 107, no. 5, pp. 1844–1847, 2010. 4.4

[128] D. Zhang, W. Wang, F. Peng, J. Kou, Y. Ni, C. Lu, and Z. Xu, "A bio-inspired inner-motile photocatalyst film: a magnetically actuated artificial cilia photocatalyst," *Nanoscale*, vol. 6, no. 10, pp. 5516–5525, 2014. 4.4